NPS EC-91-005

NAVAL POSTGRADUATE SCHOOL
Monterey, California

DISSERTATION

RECOVERING SIGNALS
FROM
OPTICAL FIBER
INTERFEROMETRIC SENSORS

by

Charles B. Cameron

June, 1991

Dissertation Advisor: Steven L. Garrett

Approved for public release: distribution is unlimited.

Prepared for:

Naval Sea Systems Command
Washington, DC

Naval Postgraduate School
Monterey, CA

NAVAL POSTGRADUATE SCHOOL
Monterey, California

Rear Admiral R. W. West
Superintendent

Dr. H. Shull
Provost

The work reported herein was supported by and prepared for the Naval Sea Systems Command, Washington, DC, and for the Naval Postgraduate School, Monterey, California.

Principal author for this report was

UNCLASSIFIED
SECURITY CLASSIFICATION OF THIS PAGE

REPORT DOCUMENTATION PAGE

Form Approved
OMB No 0704 0188

1a REPORT SECURITY CLASSIFICATION
UNCLASSIFIED

1b RESTRICTIVE MARKINGS

2a SECURITY CLASSIFICATION AUTHORITY
Multiple Sources

3 DISTRIBUTION / AVAILABILITY OF REPORT
Approved for public release; distribution is unlimited

2b DECLASSIFICATION / DOWNGRADING SCHEDULE

4 PERFORMING ORGANIZATION REPORT NUMBER(S)
NPS EC-91-005

5 MONITORING ORGANIZATION REPORT NUMBER(S)
NPS EC-91-005

6a NAME OF PERFORMING ORGANIZATION
Naval Postgraduate School

6b OFFICE SYMBOL (If applicable)
PH/Gx

7a NAME OF MONITORING ORGANIZATION
Naval Postgraduate School

6c. ADDRESS (City, State, and ZIP Code)
Monterey, CA 93943-5000

7b ADDRESS (City, State, and ZIP Code)
Monterey, CA 93943-5000

8a NAME OF FUNDING / SPONSORING ORGANIZATION
1) Naval Sea Systems Command
2) Naval Postgraduate School

8b OFFICE SYMBOL (If applicable)
06UR4

9 PROCUREMENT INSTRUMENT IDENTIFICATION NUMBER
N0002491AFE84NX

8c. ADDRESS (City, State, and ZIP Code)
1) Washington, DC
2) Monterey, CA 93943-5000

10 SOURCE OF FUNDING NUMBERS

PROGRAM ELEMENT NO	PROJECT NO	TASK NO	WORK UNIT ACCESSION NO

11 TITLE (Include Security Classification)
RECOVERING SIGNALS FROM OPTICAL FIBER INTERFEROMETRIC SENSORS

12 PERSONAL AUTHOR(S)
CAMERON, Charles B.

13a TYPE OF REPORT	13b TIME COVERED	14 DATE OF REPORT (Year, Month, Day)	15 PAGE COUNT
Ph.D. Dissertation	FROM _____ TO _____	June 1991	403

16 SUPPLEMENTARY NOTATION
The views expressed in this thesis are those of the author and do not reflect the official policy or position of the Department of Defense or the U. S. Government.

17 COSATI CODES		
FIELD	GROUP	SUB-GROUP

18 SUBJECT TERMS (Continue on reverse if necessary and identify by block number)
Demodulation, optical fiber, fiber optic, sensors, passive homodyne demodulation, symmetric demodulation, asymmetric demodulation, fringe-rate demodulation.

19 ABSTRACT (Continue on reverse if necessary and identify by block number)

This dissertation examines three methods of recovering signals cheaply from one class of highly sensitive Optical Fiber Interferometric Sensors (OFIS). This class of sensors consists of a laser light source; a 2×2 optical fiber coupler to split the beam in two; a differential transducer which converts a signal of interest into optical phase shift in the laser light transmitted through the two optical fibers in the interferometer; and a 3×3 optical fiber coupler which recombines the two beams, producing interference which can be detected electronically. The three outputs can be operated on symmetrically or asymmetrically to recover the signal of interest. The use of the 3×3 coupler permits Passive Homodyne Demodulation of the phase-modulated signals provided by the interferometer without feedback control or modulation of the laser itself and without requiring the use of electronics within the interferometer. One of the three methods discussed in this dissertation performs symmetric demodulation with analog electronics. Another uses analog-to-digital conversion of the signals and performs asymmetric demodulation in digital hardware. The third method discussed uses asymmetric fringe-rate demodulation. The three methods are characterized by their harmonic distortion, minimum detectable signal, bandwidth, dynamic range, noise, complexity, and approximate cost.

20 DISTRIBUTION / AVAILABILITY OF ABSTRACT
☒ UNCLASSIFIED/UNLIMITED ☐ SAME AS RPT ☐ DTIC USERS

21 ABSTRACT SECURITY CLASSIFICATION
UNCLASSIFIED

22a NAME OF RESPONSIBLE INDIVIDUAL
STEVEN GARRETT

22b TELEPHONE (Include Area Code)
(408) 646-2540

22c OFFICE SYMBOL
PH/Gx

DD Form 1473, JUN 86 *Previous editions are obsolete*
S/N 0102-LF-014-6603

SECURITY CLASSIFICATION OF THIS PAGE
UNCLASSIFIED

Approved for public release: distribution is unlimited.

Recovering Signals
from
Optical Fiber Interferometric Sensors

by

Charles B. Cameron
Lieutenant Commander, United States Navy
B.Sc., University of Toronto, 1977
M.S.E.E., Naval Postgraduate School, 1989
Electrical Engineer, Naval Postgraduate School, 1989

Submitted in partial fulfillment
of the requirements for the degree of

DOCTOR OF PHILOSOPHY IN ELECTRICAL ENGINEERING

from the

NAVAL POSTGRADUATE SCHOOL
June 1991

ABSTRACT

This dissertation examines three methods of recovering signals cheaply from one class of highly sensitive Optical Fiber Interferometric Sensors (OFIS). This class of sensors consists of a laser light source; a 2×2 optical fiber coupler to split the beam in two; a differential transducer which converts a signal of interest into optical phase shift in the laser light transmitted through the two optical fibers in the interferometer; and a 3×3 optical fiber coupler which recombines the two beams, producing interference which can be detected electronically. The three outputs can be operated on symmetrically or asymmetrically to recover the signal of interest. The use of the 3×3 coupler permits Passive Homodyne Demodulation of the phase-modulated signals provided by the interferometer without feedback control or modulation of the laser itself and without requiring the use of electronics within the interferometer. One of the three methods discussed in this dissertation performs symmetric demodulation with analog electronics. Another uses analog-to-digital conversion of the signals and performs asymmetric demodulation in digital hardware. The third method discussed uses asymmetric fringe-rate demodulation. The three methods are characterized by their harmonic distortion, minimum detectable signal, bandwidth, dynamic range, noise, complexity, and approximate cost.

TABLE OF CONTENTS

I. OPTICAL FIBER SENSORS 1
A. APPLICATIONS OF OPTICAL FIBER SENSORS 1
B. THE NEED FOR LOW-COST SENSORS 1
C. PRINCIPLES OF OPERATION OF OPTICAL FIBER SENSORS 3
1. Amplitude Modulation 4
2. Polarization Modulation 5
3. Phase Modulation 6
D. OPTICAL FIBER INTERFEROMETRIC SENSORS 7
1. Principles of Operation 7
2. Schemes for Recovering Signals 8
a. Phase Generated Carrier Homodyne Demodulation 8
b. Synthetic Heterodyne Demodulation 12
c. Fringe-Rate Demodulation 12
d. Homodyne Demodulation 13
3. The Use of 3×3 Couplers to Facilitate Signal Recovery 14

II. SCOPE OF THE RESEARCH 15
A. OBJECTIVES OF THE RESEARCH 15
B. ORGANIZATION OF THE DISSERTATION 15
C. MEASURES OF THE PERFORMANCE OF THE DEMODULATOR 18

III. THEORY OF 3×3 MACH-ZENDER OPTICAL FIBER INTERFEROMETERS 20

A. KEY RESULT OF THE THEORY 20
B. DERIVATION OF THE KEY RESULT OF THE THEORY 26
C. SUMMARY 59

IV. CONSTRUCTION OF A 3×3 OPTICAL FIBER INTERFEROMETRIC SENSOR 60
A. APPLICABILITY OF THIS SENSOR 60
B. DETAILS OF CONSTRUCTION 61
C. SCALE FACTOR OF THE INTERFEROMETER 67
D. SUMMARY 67

V. DESIGN OF A FRINGE-RATE DEMODULATOR 72
A. INTRODUCTION 72
B. THEORY 72
C. DESIGN 79
D. SUMMARY 89

VI. PERFORMANCE OF THE FRINGE-RATE DEMODULATOR 90
A. OVERVIEW 90
B. SCALE FACTOR 90
C. BANDWIDTH 97
D. MAXIMUM ACCEPTABLE SIGNAL 100
E. MINIMUM DETECTABLE SIGNAL 105
F. DYNAMIC RANGE 105
G. COMPLEXITY 107
H. APPROXIMATE COST 107
I. SUMMARY 109

VII. ASYMMETRIC DEMODULATION 110
A. OBTAINING THE SINE OF THE SIGNAL OF INTEREST 110

B. THE ALGORITHM 111
C. SUMMARY 113

VIII. SYMMETRIC DEMODULATION 114
A. THE INTERFEROMETRIC OUTPUTS WITH AND WITHOUT DISTORTION 114
B. MEASURING THE PHASE ANGLE BETWEEN INTERFEROMETRIC OUTPUTS 118
C. RECOVERING THE SIGNAL OF INTEREST 120

IX. DESIGN OF A SYMMETRIC ANALOG DEMODULATOR 133
A. THE RECEIVERS 135
B. WAVEFORMS 146
C. SUMMARY 151

X. MEASURING NOISE 153
A. HOW TO MEASURE NOISE 153
B. HP3561A DYNAMIC SIGNAL ANALYZER 153
C. EG&G PRINCETON APPLIED RESEARCH MODEL 5210 LOCK-IN AMPLIFIER 154
D. ANALOG INTERFEROMETRIC SIMULATORS 154
E. AN INVERTING AMPLIFIER 155
1. Noise sources $e_s^{\dagger}$ and $e_{RI}^{\dagger}$ 156
2. Noise source $e_{R2}^{\dagger}$ 157
3. Noise source $e_n^{\dagger}$ 157
4. Noise source $i_n^{\dagger}$ 157
5. Total noise 157

XI. PERFORMANCE OF THE SYMMETRIC ANALOG DEMODULATOR 160
A. OVERVIEW 160
B. SCALE FACTOR 161
C. BANDWIDTH 175
D. MAXIMUM ACCEPTABLE SIGNAL 182
E. NOISE FLOOR 193
F. DYNAMIC RANGE 200
G. COMPLEXITY 202
H. APPROXIMATE COST 202
I. SUMMARY 203

XII. DESIGN OF AN ASYMMETRIC DIGITAL DEMODULATOR 205
A. BACKGROUND 205
B. DETAILED DESIGN 208
C. SUMMARY 223

XIII. PERFORMANCE OF THE ASYMMETRIC DIGITAL DEMODULATOR 225
A. OVERVIEW 225
B. SCALE FACTOR 226
C. BANDWIDTH 226
D. MAXIMUM ACCEPTABLE SIGNAL 231
E. NOISE FLOOR 234
F. DYNAMIC RANGE 237
G. COMPLEXITY 243
H. APPROXIMATE COST 245
I. SUMMARY 245

XIV. CONCLUSION AND RECOMMENDATIONS 248

APPENDIX A. MISCELLANY 253
A. LEMMA 253
B. THEOREM 255
C. THEOREM 256
D. EQUIVALENT NOISE BANDWIDTH 258
E. ANALYSIS OF A COMPARATOR WITH HYSTERESIS 261
F. ANALYSIS OF A CIRCUIT FOR INTEGRATION AND DIFFERENTIATION 265
G. OBTAINING LARGE RESISTANCES WITH A TEE-NETWORK 275

APPENDIX B. THEORY OF OPTICAL FIBER COUPLERS 279
A. KEY RESULT OF THE THEORY 279
B. MAXWELL'S EQUATIONS 280
C. APPLICATION OF MAXWELL'S EQUATIONS TO AN ARBITRARY MEDIUM 282
D. FINDING THE TRANSVERSE FIELDS IN AN ARBITRARY MEDIUM 288
E. Z-COMPONENT OF THE FIELD IN AN ARBITRARY MEDIUM 290
F. COMPLETE FIELD IN AN ARBITRARY MEDIUM 293
G. SOLUTION IN PARALLEL UNIFORM OPTICAL FIBERS 295

APPENDIX C. AN ANALOG INTERFEROMETRIC SIMULATOR 297
A. CIRCUIT DESCRIPTION 297
B. MEASUREMENT OF THE SCALE FACTOR 301

APPENDIX D. A DIGITAL INTERFEROMETRIC SIMULATOR 303

APPENDIX E. BEHAVIOR OF THE BESSEL FUNCTION 307

APPENDIX F. NOISE ANALYSIS, SYMMETRIC ANALOG DEMODULATOR 311

A. RECEIVERS WITH LOWPASS FILTERING 314

B. INVERTING SCALING ADDERS 318

C. INVERTING SCALING ADDERS WITH LOWPASS FILTERING 321

D. DIFFERENTIATORS AND INTEGRATORS 321

E. INTEGRATORS WITH TEE-NETWORKS IN THE FEEDBACK 324

F. ANALOG MULTIPLIERS 332

G. ANALOG DIVIDERS 336

H. CALCULATING THE NOISE: RECEIVERS 337

I. CALCULATING THE NOISE: SUMMING AMPLIFIER U4A .. 339

J. CALCULATING THE NOISE: SUBTRACTORS U5A, U6A, U7A 340

K. CALCULATING THE NOISE: DIFFERENTIATORS U5B, U6B, U7B 340

L. CALCULATING THE NOISE: CROSS-MULTIPLIERS U11, U12, U13 341

M. CALCULATING THE NOISE: SQUARING MULTIPLIERS U8, U9, U10 342

N. CALCULATING THE NOISE: SCALING ADDER U14A 343

O. CALCULATING THE NOISE: SCALING ADDER U4B 343

P. CALCULATING THE NOISE: THE DIVIDER U15 344

Q. CALCULATING THE NOISE: THE INTEGRATOR U14B 345

R. SUMMARY 346

LIST OF REFERENCES 347

BIBLIOGRAPHY 349

INITIAL DISTRIBUTION LIST 353

LIST OF TABLES

Table I Advantages and disadvantages of optical fibers sensors. 2

Table II Split-ratios of the Sifam Model Special 33S 82C 3×3 optical fiber coupler (S/N 01150). 63

Table III Measurements to determine the amount of optical phase shift output by the interferometer for a given voltage on the signal generator (one through 40 closures of the Lissajous pattern.) 69

Table IV Measurements to determine the amount of optical phase shift output by the interferometer for a given voltage on the signal generator (41 through 79 closures of the Lissajous pattern). 70

Table V Summary of observations showing the output voltage of the LM2917N Voltage-to-Frequency Converter as a function of input frequency. 96

Table VI Measurements to obtain the scale factor of the Fringe-Rate Demodulator (f=50, 100, and 150 Hz). 98

Table VII Measurements to obtain the scale factor of the Fringe-Rate Demodulator (f=200, 250, and 300 Hz). 99

Table VIII These data show the bandwidth of the Fringe Rate Demodulator at various levels of input phase amplitude. 100

Table IX Interpolation to determine the maximum phase amplitude resulting in 4% total harmonic distortion from the Fringe Rate Demodulator for several frequencies. 104

Table X Dynamic range of the Fringe Rate Demodulator. 106

Table XI Calculation of the cost of the integrated circuits used in the Fringe Rate Demodulator. 108

Table XII Measurements of the noise of the Analog Interferometric Simulators, taken on the Model 5210 Lock-In Amplifier. 155

Table XIII Comparison of predicted and observed noise levels from an inverting amplifier. 159

Table XIV Inaccuracies in the output of the HP3314A Function Generator when small amplitudes are specified. 165
Table XV These data show that the Gertsch Model 480 Ratio Standard can accurately scale an input voltage of 10 mV to as little as 1 μV. 168
Table XVI Measurements to obtain the scale factor of the Symmetric Analog Demodulator. 173
Table XVII These data show some examples of combinations of frequency and amplitude which cause the divisor input to the DIV100 to saturate, resulting in a loss of control of the output amplitude. 174
Table XVIII These data rule out the hypothesis that the rise in scale factor with small combinations of amplitude and frequency can be due to a failure of the denominator input of the DIV100 to stay within range. 175
Table XIX These are the peak input phase shifts required to force the Symmetric Analog Demodulator output to exceed 4% total harmonic distortion. 187
Table XX Measurements to obtain the noise floor of the Symmetric Analog Demodulator (23-110 Hz). Data marked with an asterisk (*) were not included in the least-squares fit. 194
Table XXI Measurements to obtain the noise floor of the Symmetric Analog Demodulator (200 Hz - 1.00 kHz). 196
Table XXII Least squares fit of the logarithm of phase input to the Symmetric Analog Demodulator to achieve a given ratio *S/N* of signal to noise. 197
Table XXIII Computation of the phase noise spectral density for the Symmetric Analog Demodulator. 198
Table XXIV Calculation of the cost of the integrated circuits used in the Symmetric Analog Demodulator. 203
Table XXV Determination of the scale factor of the Asymmetric Digital Demodulator for frequencies of 50 Hz and 100 Hz. 227
Table XXVI Determination of the scale factor of the Asymmetric Digital Demodulator for frequencies of 150 Hz and 200 Hz. 228

Table XXVII Determination of the scale factor of the Asymmetric Digital Demodulator for frequencies of 250 Hz and 300 Hz. 229
Table XXVIII Total harmonic distortion (in %) of the Asymmetric Digital Demodulator as a function of input optical phase shift and frequency (phase shift from 6.22 rad to 33.7 rad). 234
Table XXIX Total harmonic distortion (in %) of the Asymmetric Digital Demodulator as a function of input optical phase shift and frequency (phase shift from 50.8 rad to 137 rad). 235
Table XXX Total harmonic distortion (in %) of the Asymmetric Digital Demodulator as a function of input optical phase shift and frequency (phase shift from 154 rad to 239 rad). 236
Table XXXI Maximum phase amplitude acceptable to the Asymmetric Digital Demodulator, given as a function of input frequency, based on accepting 4% total harmonic distortion. 237
Table XXXII Measurements of the noise floor of the Asymmetric Digital Demodulator for frequencies from 19 Hz to 97 Hz. 239
Table XXXIII Measurements of the noise floor of the Asymmetric Digital Demodulator for frequencies from 195 Hz to 2 kHz. 240
Table XXXIV Least squares fit of the logarithm of the phase input A_{LH} to the Asymmetric Digital Demodulator to achieve a given ratio S/N of signal to noise. 241
Table XXXV The noise floor of the Asymmetric Digital Demodulator. 241
Table XXXVI Calculation of the cost of the integrated circuits used in the Asymmetric Digital Demodulator. 246
Table XXXVII Summary of the performance of each of the three demodulators described in this dissertation. 252
Table XXXVIII Error in the magnitude of the gain of the differentiating circuit as a function of the ratio of signal frequency to pole frequency. 272
Table XXXIX Error in the phase of the gain of the differentiating circuit as a function of the ratio of signal frequency to pole frequency. 273

Table XL Error in the magnitude of the gain of the integrating circuit as a function of the ratio of signal frequency to pole frequency. 275
Table XLI Measurements to determine the scale factor of the three Analog Interferometric Simulators we used. 302

LIST OF FIGURES

Figure 1 Variation of the angle of rotation of polarization in quartz as a function of temperature. Adapted from Busurin, *et al.* [Ref. 6, p. 614] . . . 5

Figure 2 Mach-Zender Optical Fiber Interferometer with 2×2 optical fiber couplers at input and output. 21

Figure 3 Michelson Optical Fiber Interferometer with a single 2×2 optical fiber coupler for input and output. 21

Figure 4 Schematic of a Mach-Zender optical fiber interferometer with a 2×2 coupler at the input and a 3×3 coupler at the output. 22

Figure 5 Schematic of a Mach-Zender optical fiber interferometer with a 3×3 coupler at the input and a 3×3 coupler at the output. 22

Figure 6 Michelson Optical Fiber Interferometer with a single 3×3 optical fiber coupler for input and output. 23

Figure 7 Simulation of an interferometric output with a peak phase amplitude of 5π radians. 25

Figure 8 Another simulation of interferometric output for a sinusoidal stimulus of amplitude $A = 10.5\pi$ radians. 26

Figure 9 Physical layout of an optical fiber interferometric sensor of voltages. . . . 62

Figure 10 Detail of the assembly of the piezoelectric cylinders with fiber wrapped around them. 63

Figure 11 Apparatus used to obtain constant tension in the fiber wrapped on the cylinders. The fibers were wrapped by hand. 64

Figure 12 Upper trace: oscilloscope display of three interferometric outputs resulting from a sinusoidal stimulus (also shown) of amplitude 2.79 rad. Lower trace: two interferometric outputs on an XY plot generate a Lissajous figure. 68

Figure 13 Block diagram of a Fringe Rate Demodulator. 75

Figure 14 Karnaugh map of logic needed to generate *LL*. 78

Figure 15 Comparator circuit used to convert bipolar interferometric outputs to binary levels of 0 or V_H. 80
Figure 16 Schematic drawing of the Fringe Rate Demodulator. The receivers, transimpedance amplifiers, and comparators are omitted from this drawing. 82
Figure 17 A Tee-network can be used to obtain large resistances. 88
Figure 18 Graph of the output voltage of the LM2917N Frequency-to-Voltage Converter as a function of input frequency. 94
Figure 19 Graph of the output voltage of the LM2917N Frequency-to-Voltage Converter as a function on input frequency. This figure shows the same data as in Figure 18, but here it is plotted logarithmically on both axes. 95
Figure 20 Instrumentation used to obtain the output voltage of the LM2917N Frequency-to-Voltage Converter as a function of input frequency. 95
Figure 21 Instrumentation used to measure the scale factor of the Fringe Rate Demodulator. 97
Figure 22 Contour plot of the total harmonic distortion in the Fringe Rate Demodulator as a function of frequency and phase amplitude. 102
Figure 23 Perspective view of a surface plot of the total harmonic distortion in the Fringe Rate Demodulator as a function of frequency and phase amplitude. 103
Figure 24 Block diagram of the symmetric demodulation algorithm. 115
Figure 25 Simulation of an interferometric output with a peak phase amplitude of 5π radians. 116
Figure 26 Interferometric outputs for $A=\pi$ rad. Upper traces: no distortion. Lower traces: distortion present. Left side: amplitude *v.* time. Right side: Lissajous figure. 117
Figure 27 Simulations of the derivatives of the three interferometric outputs. . . . 122
Figure 28 Phasor diagram depicting the operation of the asymmetric demodulation technique. 124

Figure 29 Phasor diagram depicting the operation of the symmetric demodulation technique. 125
Figure 30 Simulations of the differences between the three possible pairings of derivatives of the interferometric outputs. The stimulus has amplitude $A=5\pi$ radians. 128
Figure 31 Plots of the products of one signal with the difference between the derivatives of the other two signals. 130
Figure 32 The result of adding up the three products of signals with differences of derivatives. Superimposed on it is the original stimulus of amplitude $A=5\pi$ radians. 131
Figure 33 Schematic diagram of an implementation of the symmetric analog demodulation technique in analog electronics. Power-supply bypass capacitors are omitted in this diagram. 134
Figure 34 Design of a Differentiator. A compromise is necessary in setting the gain of the differentiator to avoid exceeding the gain-bandwidth product of the amplifier, an AD712 in this case. 142
Figure 35 Three outputs of the optical fiber interferometric sensor with the 100 Hz sinusoidal stimulus superimposed. Upper photograph: $A=33.7$ rad. Lower photograph: $A=67.9$ rad. 147
Figure 36 Derivatives of three outputs of the optical fiber interferometric sensor with the 100 Hz sinusoidal stimulus superimposed. Upper photograph: $A=33.7$ rad. Lower photograph: $A=67.9$ rad. 148
Figure 37 Products of each output with the difference between the derivatives of the other two; the 100 Hz sinusoidal stimulus is superimposed. Upper photograph: $A=33.7$ rad. Lower photograph: $A=67.9$ rad. 149
Figure 38 Symmetric Analogue Demodulator output, $f=100$ Hz, $A=137$ rad. Upper photograph, upper trace: undistorted input; lower trace, demodulator output. Lower photograph: FFT of demodulator output with 5% THD present. 150
Figure 39 Noise sources in an inverting amplifier. 156

Figure 40 Graph of the ratio V_{OUT}/V_{IN} shown in Table XIV. 166
Figure 41 This instrumentation was used to verify that the Gertsch Model 480 Ratio Standard could provide accurately scaled replicas of the signals from the HP3314A Function Generator. 167
Figure 42 Setup used to measure the scale factor f_D of the Symmetric Analog Demodulator. 169
Figure 43 Instrumentation for an experiment to test whether the increase in scale factor at low combinations of amplitude and frequency could be due to a failure of the DIV100's divider input to stay within acceptable limits. 171
Figure 44 Instrumentation used to measure the small-signal bandwidth of the Analog Electronic Simulators. 179
Figure 45 Small-signal bandwidth of the Analog Interferometric Simulators. The upper trace is the magnitude of the gain; the lower trace is its phase. The gain is down by 3dB at f = 1 MHz. 181
Figure 46 Block diagram of instrumentation for determining the small-signal bandwidth of the Symmetric Analog Demodulator. 182
Figure 47 Measured bandwidth of the Symmetric Analog Demodulator (113 kHz for small signals). In descending order of bandwidth, the phase inputs to the demodulator were 219 mrad, 690 mrad, 2.17 rad, 5.54 rad, and 9.28 rad. 183
Figure 48 Block diagram of instrumentation for measuring the bandwidth of the Symmetric Analog Demodulator when the input is from the combination of power supply and optical fiber interferometer. 184
Figure 49 Five oscilloscope traces of increasingly distorted sinusoidal waveforms (lower traces) with an undistorted waveform for comparison (upper traces). 186
Figure 50 This instrumentation was used to measure the phase shift required to exceed 4% total harmonic distortion in the output of the Symmetric Analog Demodulator. 188

Figure 51 Peak phase shift into the Symmetric Analog Demodulator necessary to exceed 4% total harmonic distortion. 189
Figure 52 Contour plot of the Harmonic Distortion in the output of the Symmetric Analog Demodulator as a function of frequency and amplitude of the signal of interest. 191
Figure 53 Surface plot of the Harmonic Distortion in the output of the Symmetric Analog Demodulator as a function of frequency and amplitude of the signal of interest. 192
Figure 54 Plot of the phase noise spectral density of the Symmetric Analog Demodulator as a function of frequency of the signal of interest. The spectral density indicates the minimum discernible signal in a one hertz bandwidth. 199
Figure 55 The dynamic range of the Symmetric Analog Demodulator when the output is viewed in a 1 Hz bandwidth. 201
Figure 56 Schematic of the Asymmetric Digital Demodulator. This section converts two of the interferometric outputs to digital form and creates an in-phase and a quadrature signal from them. 209
Figure 57 Schematic of the Asymmetric Digital Demodulator. This section finds differences between consecutive samples, cross-multiplies one signal with the difference from the other signal, and subtracts one from the other. . . 210
Figure 58 Schematic of the Asymmetric Digital Demodulator. This section performs an integration of the derivative of the signal of interest which was created in the preceding section. 211
Figure 59 Schematic drawing of the Asymmetric Digital Demodulator. This section is the digital-to-analog converter which creates an analog reconstruction of the output of the digital circuitry. 212
Figure 60 Block diagram showing how to obtain the in-phase and quadrature wave forms without overflow. 214

Figure 61 Block diagram showing the asymmetric demodulation algorithm when the data are digital words taken at successive sampling instants *t-1*, *t*, *t+1*, *etc.* 217
Figure 62 Graph of the scale factor of the Asymmetric Digital Demodulator at 200 Hz as a function of input phase amplitude. 230
Figure 63 Contour plot showing combinations of input optical phase shift and frequency which yield the same amount of total harmonic distortion in the Asymmetric Digital Demodulator. 232
Figure 64 Surface plot showing the total harmonic distortion in the Asymmetric Digital Demodulator as a function of various combinations of input optical phase shift and frequency 233
Figure 65 Maximum phase amplitude acceptable to the Asymmetric Digital Demodulator as a function of input frequency. 238
Figure 66 The noise floor of the Asymmetric Digital Demodulator as a function of frequency. 242
Figure 67 The dynamic range of the Asymmetric Digital Demodulator. The upper limit is taken to be where 4% total harmonic distortion results. The lower level is the noise floor in a one hertz bandwidth. 243
Figure 68 Breadboard implementation of the Asymmetric Digital Demodulator. The circuit on the right-hand side of the upper photograph is the same as that on the left-hand side in the lower photograph. 244
Figure 69 Schematic diagram of a comparator with hysteresis. 262
Figure 70 A general circuit for differentiation, integration, and bandpass filtering. 267
Figure 71 A Tee-network can be used to obtain large resistances. 276
Figure 72 Block diagram of the Analog Interferometric Simulator. 298
Figure 73 Schematic drawing of the Analog Interferometric Simulator. 299
Figure 74 Block diagram of a Digital Quadrature Phase Modulation Simulator. 304

Figure 75 Karnaugh map of logic needed to generate in-phase *I* and quadrature *Q* data for the Digital Quadrature Phase Shift Modulator. 305
Figure 76 The Bessel functions $J_n(10)$ and $J_n(50)$ as functions of n. 308
Figure 77 The Bessel functions $J_n(90)$ and $J_n(100)$ as functions of n. 309
Figure 78 The Bessel functions $J_n(150)$ and $J_n(200)$ as functions of n. 310
Figure 79 General schematic of an optical receiver using a photodiode and a transimpedance amplifier with lowpass filtering. 315
Figure 80 Noise from the transimpedance amplifier considering just the thermal noise from the feedback resistor. 317
Figure 81 Schematic drawing of a summing amplifier with noise sources included. 319
Figure 82 Schematic diagram of a scaling inverting adder with lowpass filtering. 323
Figure 83 Schematic drawing of the standard circuit we use for differentiation and integration with noise sources shown. 324
Figure 84 Schematic of an integrator with a Tee-network in the feedback and with all noise sources shown. 325

TABLE OF SYMBOLS

In this dissertation we use units from the *Système International d'Unités*, or SI. For a good description of this system, see Appendix B in Hayt [Ref. 1, pp. 501-506]. A table of prefixes to units in this system is given at the end of the table of symbols. Generally we use *italics* to denote scalar variables, bold to denote vector variables, and ordinary type to denote units. For example, x is a scalar variable, $\mathbf{x}$ is a vector variable, and s is the abbreviation for "second".

Symbol	Definition
A	The amplitude of the signal of interest when it is a simple sinusoid of the form $A \sin(\omega t)$. Its units vary with the context: it may be measured in units of the signal of interest, or in radians of phase shift created in the optical fiber interferometric sensor when the signal of interest impinges on the sensor. For example, in an acoustic sensor it could be measured in pascals (Pa). After demodulation of a phase-modulated signal, A could be measured in volts.
$\mathbf{B}$	The magnetic flux density. It is measured in tesla (T) or, equivalently, webers per square meter (W / m^2). In fundamental SI units, one tesla is the ratio of kilograms to the product of coulombs and seconds, or 1 T = 1 kg / (C s).

Symbol	Definition
c	The speed of light, which was redefined in 1983 to have the value 2.99792458×10^8 meters per second (m / s).
C	One coulomb, the fundamental unit of charge in SI units.
D	The central value around which the output of the optical fiber interferometric sensor fluctuates. Its units vary with the context: it may be measured in watts of optical power, or, after the light strikes a photodiode, in amperes of current, or, after passage of that current through a transimpedance amplifier, in volts.
D	The electric flux density, measured in units of coulombs per square meter.
E	The amplitude of the output of the optical fiber interferometric sensor. Its units vary with the context in the same manner as the units of D described above.
E	The electric field intensity, measured in units of volts per coulomb (V / C). In fundamental SI units, this is equivalent to kilogram meters per coulomb per second squared (kg m / C s^2).
f	The conventional frequency of the signal of interest, measured in hertz (Hz).
F_I	The scale factor of the Optical Fiber Interferometer with a power amplifier of gain 10 providing the input voltage signal. This is the conversion factor between the peak input to the power amplifier in volts and the output in radians of peak phase shift.

Symbol	Definition
$F_{S,EFF}$	The scale factor of the Analog Interferometric Simulators. This is the conversion factor between the peak input in volts and the output in radians of peak phase shift.
$F_{S,AD}$	The scale factor of the Symmetric Analog Demodulator. This is the conversion factor between the input in radians of phase shift and the output in volts.
F	One farad, the SI unit of capacitance. One farad is equal to one volt per coulomb (V / C), or, in fundamental units, the product of kilograms and cubic meters divided by the product of seconds squared and coulombs squared [(kg m^3) / (s^2 C^2)].
H	One henry, the SI unit of inductance. One henry is equal to one weber per ampere (Wb / A), or, in fundamental units, the product of kilograms and meters squared divided by coulombs squared [(kg m^2) / C^2]
H	The magnetic field intensity measured in units of amperes per meter (A / m).
Hz	One hertz, the SI unit of frequency. One hertz is defined to be one cycle per second (s^{-1}). Since one cycle comprises 2π rad, 1 Hz = 2π rad/s.

Symbol	Definition
j	The imaginary number usually called i by mathematicians and physicists. It is called j by electrical engineers in order to avoid confusion with the conventional use of the symbol i for electrical current. $$j = \sqrt{-1}$$
J	The current density, measured in amperes per square meter (A / m^2).
k	Boltzmann's constant, with a value of 1.38×10^{-23} J/K.
K	One kelvin, the unit of thermodynamic temperature. Until the 13th General Conference on Weights and Measures changed the name in 1967, this was called the degree Kelvin (°K). The degree Celsius measures the same interval of temperature, but the Celsius scale has a different origin: 0°C = 273.16 K. [Ref. 2. p. F-100]
kg	One kilogram, the fundamental SI unit of mass.
m	One meter, the fundamental SI unit of length.
rad	One radian. There are 2π rad in a circle.
Re	The real part of the quantity which follows. For example, if z is a complex quantity, then $$\mathbf{Re}[z] = \mathbf{Re}[x + jy] = x.$$

Symbol	Definition
s	One second, the fundamental SI unit of time.
S	One siemen, the ratio of amperes to volts (A / V). (Formerly the siemen was often called a mho and either the symbol $\mho$ or Ω^{-1} was used to represent it.) In fundamental SI units, one siemen equals the product of seconds and coulombs squared divided by the product of kilograms and cubic meters [(s C^2) / (kg m^3)].
t	The time in seconds (s).
T	The period of one oscillation of the signal of interest. T is measured in units of seconds (s). It is related to the conventional frequency f by $$T = \frac{1}{f}.$$
x_k	The kth output of the optical fiber interferometric sensor. In an interferometer using 3×3 optical fiber couplers at the output, k can take on the values 1, 2, or 3. In such an interferometer, $$x_k = D + E\cos\left[\xi - (k-1)\frac{2\pi}{3} + \phi\right].$$ The other symbols in this expression are defined elsewhere in this table.
ϵ	The permittivity of a given substance, measured in farads per meter (F / m). In isotropic materials, it is a scalar constant. In anisotropic materials, it is a tensor. [Ref. 1, p. 149]

Symbol	Definition
ϵ_0	The (dielectric) permittivity of free space. This physical constant has the value 8.854×10^{-12} farads per meter (F / m).
μ	The permeability of a given substance, measured in henrys per meter (H / m). In isotropic materials, it is a scalar constant. In anisotropic materials, it is a tensor. [Ref. 1, p. 315]
μ_0	The permeability of free space. This physical constant is defined to have the value $4\pi\times10^{-7}$ henrys per meter (H / m).
π	The ratio between the circumference of a circle and its diameter. There are 2π rad in a circle.
ξ	This symbol represents a signal of interest. It is a function of time, and so can also be written as $\xi(t)$. Frequently in this dissertation we assume ξ is a simple sinusoid with amplitude A and natural frequency ω, so $$\xi(t) = A \sin(\omega t).$$ This assumption simplifies certain mathematical manipulations, but in general, if ξ is periodic, it may be represented as a Fourier series consisting of many frequencies of various amplitudes.
σ	The (electrical) conductivity, measured in units of siemens per meter (S / m).

Symbol	Definition
ϕ	The phase shift in the output of the optical fiber interferometric sensor due to various, miscellaneous causes excluding the cause which the sensor was designed to detect. For example, in an acoustic sensor, fluctuations in phase due to changes in temperature would be lumped in with ϕ. Although written as a constant, ϕ is not necessarily fixed. If it is not fixed, we generally write it as $\phi(t)$. Often, however, its frequency of variation is well below the frequency range of the signal of interest. In this case, we call ϕ "quasi-static". For example, temperature and pressure usually vary much more slowly than acoustic waves and so the changes in phase induced by changes in temperature or pressure are quasi-static compared to changes in phase induced by acoustic waves.
ψ	The phase shift in a general sinusoid. We use this symbol rather than ϕ only to avoid the impression that some phase shift under discussion is necessarily a phase shift induced in an interferometer.
ω	The natural frequency in units of radians per second (s^{-1}). It is related to the conventional frequency f in hertz (Hz) by $\omega = 2\pi f$.
*	Used as a superscript to indicate the complex conjugate of a quantity. For example, if $z = x + jy$, then $z^* = x - jy$.
†	Used as a superscript to indicate that a quantity is a spectral density. For example, $e^\dagger$ could symbolize a voltage spectral density in volts per root hertz ($V/\sqrt{Hz}$).

Symbol	Definition
$\parallel$	Used to signify the parallel combination of two impedances. For example, the impedance of Z_1 and Z_2 taken in parallel can be computed as $$Z_1 \parallel Z_2 = \frac{1}{\frac{1}{Z_1}+\frac{1}{Z_2}} = \frac{Z_1 Z_2}{Z_1 + Z_2}.$$
$\wedge$	Used to signify the logical AND of two logical quantities. For example, the AND of A and B is written $A \wedge B$. The result of the operation $A \wedge B$ is TRUE if $A=B=$TRUE and FALSE otherwise.
$\vee$	Used to signify the logical OR of two logical quantities. For example, the OR of A and B is written $A \vee B$. The result of the operation $A \vee B$ is TRUE unless $A=B=$FALSE, in which case the result is FALSE.
$\oplus$	Used to signify the logical EXCLUSIVE-OR of two logical quantities. For example, the EXCLUSIVE-OR of A and B is written $A \oplus B$. The result of the operation $A \oplus B$ is TRUE if $A \neq B$ and FALSE otherwise.
$\approx$	Used to signify that one quantity is approximately equal to another. For example, if $A \approx B$, then A and B are roughly the same.

Symbol	Definition
«	Used to signify that one quantity is very much less than another. For example, if $A \ll B$, then A is very much less than B. This is a somewhat vague expression; it simply means that in a comparison, A is negligible compared to B. Some authors interpret $A \ll B$ to mean that $A \leq B/10$.

STANDARD PREFIXES USED WITH SI UNITS

This table is adapted from Hayt [Ref. 1, p. 506].

Prefix	Abbrev-iation	Meaning	Prefix	Abbrev-iation	Meaning
atto-	a-	10^{-18}	deka-	da-	10^{1}
femto-	f-	10^{-15}	hecto-	h-	10^{2}
pico-	p-	10^{-12}	kilo-	k-	10^{3}
nano-	n-	10^{-9}	mega-	M-	10^{6}
micro-	μ-	10^{-6}	giga-	G-	10^{9}
milli-	m-	10^{-3}	tera-	T-	10^{12}
centi-	c-	10^{-2}	peta-	P-	10^{15}
deci-	d-	10^{-1}	exa-	E-	10^{18}

GLOSSARY

AC Alternating current.

AC COUPLING Electronic devices can be connected to one another either by AC coupling or by DC coupling. In AC coupling, the lowest frequencies are removed from a signal before it is passed to the following stage. Some instruments, the HP3561A Dynamic Signal Analyzer for example, have a selectable option to permit the user to select the mode of coupling he prefers.

A/D Analog-to-digital converter. A/D converters generate an analog signal from a sequence of digital words. An analog signal can assume a continuous range of amplitudes, whereas a digital word can represent only a discrete number of amplitudes. Consequently, only some of the possible analog signal levels can be generated. The abrupt changes in output level which result from changes in the magnitude of the input word generate high-frequency noise in the output, which is usually filtered by a low-pass filter in order to mitigate this effect. A/D converters are characterized by the range of analog voltages over which they can operate, by the number of bits which they use to represent the voltage, and by the time it takes them to perform a conversion.

D/A converters generate a digital word representing the magnitude of an analog signal. An analog signal can assume a continuous range of amplitudes, whereas a digital word can represent only a discrete number of amplitudes, so the conversion process introduces quantization errors. D/A converters are characterized by the range of analog voltages which they can generate, by the number of bits which they use to represent the voltage, and by the time it takes them to perform a conversion.

AM Amplitude modulation. The amplitude of a sine wave can be changed as a function of time, *i.e.*, it can be modulated.

Application-Specific Integrated Circuit (ASIC) It is increasingly common for many complex electronic functions to be combined onto a single integrated circuit on a silicon (or other) substrate. These custom-designed circuits are known by the acronym ASIC. The digital implementation of the demodulator, in particular, would benefit greatly from the use of application-specific integrated circuits since it requires the largest number of interconnections, and, so, is the most complicated of the demodulators considered in this dissertation.

Coherent light The coherence of a source of electromagnetic radiation is a measure of how pure its wavelength is, or equivalently, how narrow its bandwidth is. In reality, there are no perfectly coherent sources: all sources have a finite (non-zero) band of component wavelengths. However, it is convenient to compare a real source to an ideal (coherent) one. There are two aspects to coherence. Firstly, we generally require that any two photons coming from the source have the same frequency. Secondly, we require that the phase of a photon depend only on its distance from the source. To measure coherence, we can split light from the source into two beams, permit each beam to travel along separate paths of known length, and then permit these two beams to recombine. The electric fields of each of the two beams add vectorially. If they happen to be of equal magnitudes and opposite directions, then they sum to zero, and the result is zero optical power. Conversely, if they point in the same direction, then the sum of their amplitudes and the corresponding power is non-zero. In general, the sum will be intermediate between these.

The only optical detectors currently available detect optical power, not electric field strength and direction, because optical frequencies are too high for current electronics to keep up with. Now if the difference in the two path lengths is large enough, then the two beams are no longer synchronized, which is another way of saying that they are no

longer coherent. Upon recombination, no recognizable pattern of bright and dark "fringes" is detectable. All that appears is a smear of essentially constant brightness. The minimum path difference necessary to produce this effect is called the coherence length of the light source. The amount of time it takes light to propagate over this path difference is called the coherence time of the light source. The light from the sun and from incandescent and fluorescent lamps is incoherent: there is no path difference so small as to permit an interference pattern to be visible. Laser light, in contrast, exhibits some coherence. Different laser sources have different degrees of coherence, that is, different coherence lengths. The semiconductor lasers used in the research described in this paper have coherence lengths on the order of a few centimeters.

D/A Digital-to-analog converter. D/A converters generate a digital word representing the magnitude of an analog signal. An analog signal can assume a continuous range of amplitudes, whereas a digital word can represent only a discrete number of amplitudes. Consequently, the conversion process introduces quantization errors. It is possible for signals of more than one frequency to generate the same output sequence, a phenomenon known as *aliasing*. To eliminate this effect, frequencies exceeding the *Nyquist frequency* (half of the sampling frequency) must be removed prior to conversion. This is generally done by passing the analog signal through a low-pass filter before sending it to the D/A converter. D/A converters are characterized by the range of analog voltages which they can generate, by the number of bits which they use to represent the voltage, and by the time it takes them to perform a conversion.

DC Direct current.

DC Coupling Electronic devices can be connected either by AC coupling or by DC coupling. With DC coupling, all frequency components of a signal (even those of zero frequency) are passed to the following stage.

DECADE In the expression *per decade increase of frequency*, we mean *for every ten-fold increase in frequency*.

DQPMS (DIGITAL QUADRATURE PHASE MODULATION SIMULATOR) This is an interferometric signal simulator we designed and built using a mixture of analog and digital circuitry. It produces in-phase and quadrature signals which resemble the outputs of an optical fiber interferometric sensor terminated with a 2×2 optical fiber coupler, rather than a 3×3 coupler. However, the waves are squared-off, not smoothly varying. (As is the case with all digital signals, some overshoot always exists, and it takes some time for the signal to settle at the new level after a transition, but these effects can usually be neglected.)

DSP Digital Signal Processor. These are integrated circuits which perform a dedicated signal-processing function. They are similar to the more general-purpose microprocessor.

EG&G PRINCETON APPLIED RESEARCH MODEL 5210 LOCK-IN AMPLIFIER This lock-in amplifier permits very small signals to be detected synchronously. It provides variable time constants, sensitivities, and filter skirts with either −6 Db or −12 Db per octave change in frequency.

EMI Electromagnetic interference. Electric and magnetic fields can propagate through space. As a consequence, despite the fact that these fields are attenuated as they propagate, and even though their sources may be quite some distance away, electrically responsive elements can be affected by them. EMI can also penetrate through to a system through power supplies, if they are connected to the power mains, and from other, less obvious, mechanisms. The latter include optical effects (such as the noise induced in diodes by fluorescent lighting), acoustic coupling, vibration, and even thermal fluctuations.

FRINGE The output of an interferometric sensor is a sequence of bright and dark light. If the recombined waves undergo a shift of 2π radians (one wavelength), a complete cycle from bright to dark and back to bright will occur. This is called one *fringe*. To obtain one fringe, the amplitude of the stimulus must be π radians, which results in a total excursion in phase of $\pm\pi$ radians. It is possible for the direction of the phase shift to change in the middle of such a cycle, and in this case we speak of a *sub-fringe*. A sub-fringe is a shift of less than 2π radians (phase amplitude less than π radians), or less than one wavelength of light. For example, if the wavelength λ of the light in a vacuum is 830 nm and the change Δl in relative path lengths within the two legs of the interferometer is 3 μm, then the interferometric output will undergo $2\pi n\Delta l/\lambda = 33.6$ rad of phase shift, which is 5.4 fringes. Here, we have taken the index of refraction $n=1.48$, which is a typical value for glass.

HP3314A FUNCTION GENERATOR This device can generate sinusoids, triangular waves, or square waves, as well as more complicated waveforms. The user can command a desired signal amplitude, frequency, phase shift relative to some reference, and a DC offset. We found that the commanded signal amplitude was inaccurate at low levels. Using the Gertsch Model 480 Ratio Standard to reduce a strong output from the HP3314A to the desired low level was much more accurate.

HP3456A DIGITAL VOLTMETER This digital voltmeter provides up to six digits of accuracy. It has an averaging capability. The number N specifies the number of readings which the HP3456A takes before computing an average. Individual readings are averaged over a number of intervals of the power line cycle. With 60 Hz operation, one cycle is 1/60 s = 16.7 ms. We typically specified either 10 or 100 power line cycles per reading in making noise measurements, depending on how erratic the measured signal was. As the period of observation lengthens, the variance of the average computed by the instrument diminishes, although the variance in the signal itself (which the instrument also computes) is unaffected.

HP3561A Dynamic Signal Analyzer This device is capable of performing a Fast Fourier Transform (FFT) on its input. The resultant display of amplitude vs. frequency makes analysis of the spectral content of a signal quite straightforward. The device has a mode for computing noise on a basis which is normalized for the bandwidth. This means that the measured amplitude is divided by the square root of the bandwidth in which that amplitude was measured. Unfortunately, the display does not make this fact highly evident. The device can measure frequencies of up to 100 kHz. It adjusts its dynamic range as needed. It can perform averages, too.

HP4194A Impedance-Gain/Phase Analyzer This instrument makes the measurement of gain and phase of a electronic system very easy. The range of frequencies one wishes to have applied to the system under test can be specified. The output signal is applied to the system under test and the output of that system is applied to the test input of the HP4194A. The difference in magnitude and phase can be plotted with either linear or logarithmic scales. This device can generate similar plots of the impedance of a system under test, and can calculate the equivalent parameters of resistance, capacitance, and inductance for a variety of models such as a series connection of a resistor, capacitor and inductor.

Incoherent light Incoherent light is that in which the phase of one wave of light is not related to the phase of another wave except by some random difference. The most common example of incoherent light is that from the sun. Of course, if the two waves do not have the same frequency, then they are generally not regarded as coherent even if their frequencies are commensurate: they have to have equal frequencies *and* their phases must not bear a random relationship to one another before they can be regarded as coherent waves.

Input Phase Shift A demodulator of interferometric sensor outputs is a device which senses optical phase shift and generates a voltage proportional to the phase shift. In sensing-applications, the quantity of interest is more apt to be a measure of pressure (in

pascals), distance (in meters), temperature (in kelvins) and so on. The function of the transducer is to convert this physical phenomenon, the signal of interest, into an equivalent differential phase shift of the light within the two legs of the interferometer.

In the case of optical fiber sensors, this usually is done by causing the signal of interest to strain the glass fibers in direct proportion to the amplitude of the signal. This makes the amount of phase shift directly proportional to the amplitude of the phenomenon being measured. This in turn means that the output of the demodulator is directly proportional to the amplitude of the signal of interest. In short, the phase shift is a measure of the signal of interest, no matter what that signal might be.

JFET Junction Field-Effect Transistor. A unipolar transistor in which the current flowing between two terminals of the device is controlled by the electric field applied to a third terminal.

LASER This is an acronym standing for *Light Amplification by the Stimulated Emission of Radiation*. The essence of laser operation is that the atoms in a substance are excited by some form of "pumping" action so that there are more of them in an excited state than in the usual, relaxed state. When any such atom relaxes into the state of lower energy, it emits a photon. Such emission occurs spontaneously, by chance. When this photon interacts with another excited atom, it can cause this second atom to relax to the lower state too, during which process the second atom also emits a photon. This process is known as stimulated emission. The significant fact is that the original photon is not absorbed in the interaction, but continues onward, and the new photon has the same frequency, phase, and direction of propagation as the first photon. Because the supply of excited atoms is kept artificially high by pumping, the process can repeat itself over and over again. A resonant cavity usually partly or completely surrounds the emissive material, and it ensures that the process occurs often enough for a useful level of amplification to occur. (Some lasers provide sufficient amplification without a resonator.) The consequence is an intense beam of coherent photons. A partially transmissive

element, such as a partially silvered mirror, permits the beam to escape from the resonant cavity, if one is used. The term *laser* has come to refer to the process itself, to the device in which the process takes place, and to the beam produced by the device.

MASER This is an acronym standing for *Microwave Amplification by the Stimulated Emission of Radiation*. Apart from the fact that the electromagnetic radiation emitted by the maser process is in the microwave region of the spectrum, rather than in the visible region, the process is exactly the same as was described above under the heading **LASER**. Historically, the maser was invented before the laser.

MAXIMUM PERMISSIBLE SIGNAL (MPS) The largest amplitude of the signal of interest which can be processed by a demodulator without introducing undue distortion. Some latitude exists in establishing the amount of distortion which is regarded as acceptable.

MINIMUM DETECTABLE SIGNAL (MDS) The smallest amplitude of the signal of interest which can be distinguished from noise. This is the level of signal which provides a signal-to-noise ratio of 1 (0 dB). For a particular purpose, a higher or lower ratio of signal-to-noise ratio may be appropriate. For example, communications systems typically need more than 10 or 20 dB between signal and noise.

OPTICAL FIBER COUPLERS These devices take the place of partially silvered mirrors and prisms, which were the only means of splitting light beams and recombining them in interferometers in the days before optical fibers had been invented. They are manufactured by laying two or more fibers parallel to one another and fusing them together. The geometry of the arrangement and the length of the fused section both are crucial in determining the characteristics of the coupler. Two common examples of these couplers are *2×2 couplers* and *3×3 couplers*. The 2×2 coupler brings two fibers into close contact; hence it has two inputs and two outputs. Either end of the coupler can function either as input or as output; in other words, the 2×2 coupler is bidirectional.

The 3×3 coupler brings three fibers into close contact. Hence it has three inputs and three inputs, and it, too, is bidirectional.

PLA (Programmable Logic Array) An integrated circuit which contains flip-flops for storing bits of data and which has programmable logic. In the variant of this that we use, an Altera EP310, one can designate which pins are inputs, which are outputs, and how the outputs should be derived from the inputs. One can also make this particular PLA operate in a synchronous (clocked) or asynchronous (unclocked) mode. Using a PLA is a convenient way to reduce numerous discrete-logic integrated circuits to a single chip. The EP310 can be erased (by exposure to ultraviolet light) and reprogrammed, making it an excellent choice for prototype systems.

Phase Rate The multiplicative product of the phase of the output of an interferometric sensor and its frequency. It is measured in radians per second and is an indication of the highest frequency components present in the interferometric output. The chief limitation on acceptable phase rate is the bandwidth of the demodulator. If the signal is differentiated, the phase rate appears as a factor in the magnitude of the derivative, and so the possibility of saturating amplifiers also arises if phase rate is too high. This is the second principal limitation on acceptable phase rate.

Polarization Angle The light from many lasers is linearly polarized. As it passes through an interferometric sensor, the polarization direction changes due to several uncontrollable factors. One of these is twisting of the fibers themselves. As a result, the light which is recombined at the output of the interferometer often does not have the optimum polarization. The optimum polarization occurs when both interfering beams are polarized in a parallel direction, the specific direction being irrelevant.

When two beams of light have entirely orthogonal polarizations and no components of parallel polarization, no interference results. This would result in an output of uniform intensity. In practice, we have never observed this. The implication is that the light in

our interferometer is not purely linear in its polarization. The Sharp LT015 laser diode is linearly polarized in a ratio of 5:1 for 1 mW output power, 100:1 for 10 mW output power, and 250:1 for 30 mW output power [Ref. 3], which is consistent with our observations. So even though the visibility of the interference pattern does indeed wander with time, it never vanishes totally. This has a beneficial effect on all the demodulators we consider in this dissertation, for it means that there always is *some* signal to process, which would not be the case if the interference pattern were wholly absent.

RMS Root-mean-squared. In general, the root-mean-square of a function $v(t)$ is

$$v_{RMS} = \sqrt{\lim_{T\to\infty} \frac{1}{T}\int_0^T v^2(t)\,dt}.$$

When $v(t)$ is a periodic signal with period T, then we obtain the same result without taking the limit, and the RMS value is given by

$$v_{RMS} = \sqrt{\frac{1}{T}\int_0^T v^2(t)\,dt}.$$

If $v(t) = A\sin(\omega t)$, or $v(t) = A\cos(\omega t)$, then its RMS value is $A/\sqrt{2}$.

SPST Single pole, single throw. A type of switch which can connect two terminals together or leave them open.

TEK2430 DIGITAL OSCILLOSCOPE This device has two input channels. It digitizes the inputs and stores them in memory. This means that a display can be frozen, and the scales of time and amplitude can be altered to provide increased resolution. It has a mode in which Channel 1 can be displayed along the horizontal axis and Channel 2 can be displayed along the vertical axis, permitting the display of Lissajous patterns. This

makes accurate measurements of the phase angle between two signals possible, since a variety of measurement functions is provided, including voltage, time, and frequency.

TTL (TRANSISTOR-TRANSISTOR LOGIC) A particular family of digital logic integrated circuits. Signals can take on only two valid voltage levels. The low state is at roughly 0 V. The high state is at roughly 3.3 V. The supply voltage is at +5 V. [Ref. 4]

VCO (VOLTAGE CONTROLLED OSCILLATOR) A circuit which outputs a sinusoidal, square wave, or triangular wave whose frequency is directly proportional to the input voltage. The EXAR Archer XR2206 is an example of a VCO, and is the one we employed in the design of the Digital Quadrature Phase Modulation Simulator (DQPMS).

ACKNOWLEDGEMENT

It is common to see acknowledgements in books or documents such as this and to wonder whether they are merely *pro forma*, obligatory sentiments or, in contrast, are wholly sincere. Seldom can one be sure from the wording alone. To reduce the possibility of doubt, then, let me say emphatically that I owe an enormous debt of gratitude to my wife, Diane, for all that she has done to lessen the burden of everyday affairs falling upon my shoulders. She has taken it up herself not through any liking of the work, but solely for my benefit, and I am truly thankful to her for it.

I also am indebted to two others for all they have done for me throughout my lifetime: my parents Wilda May Cameron and William Walter Cameron. I am especially grateful to them for teaching me the value of education, even when there is no obvious application of the knowledge acquired, for one often arises later in circumstances which cannot be foreseen.

On the technical side of the work described herein, I would be remiss if I did not also acknowledge my advisor, Dr. Steve Garrett. He has taught me more than he is likely ever to realize about science and about the methods of scientific inquiry. His boundless enthusiasm have been an inspiration to me.

One other deserves special mention. Dr. Robert Keolian has the ability to see matters with a clarity that I wish I shared. For his generosity in giving of his time and for the ideas that made the idea of symmetric demodulation a reality I am most grateful.

I also would very much like to thank Dr. John Powers, Dr. Sherif Michael, Dr. Tri T. Ha, and Dr. Don Gaver for serving on my Ph. D. Committee.

Finally, thanks also are due to the Naval Sea Systems Command and the Naval Postgraduate School Direct Funded Research Program for their financial support, without which this research could not have been done.

I. OPTICAL FIBER SENSORS

A. APPLICATIONS OF OPTICAL FIBER SENSORS

That anything at all can be detected with strands of glass fiber comes as a complete surprise to the average person. One readily thinks of glass as a useful substance for windows and for beverage containers. That silicon, the raw material from which glass is made, is now the most widely-used substance in fabricating integrated circuits is known to many. The widespread introduction of optical fibers into the telecommunications industry has of course made the existence of optical fibers a matter of common knowledge. Many consumers even have seen their use by artists to make exotic lamps. Their use as sensors, however, is largely unknown to the ordinary citizen and seldom mentioned in the popular press.

Yet optical fiber sensors have attracted considerable interest in the scientific and technological community since 1977. They have been used successfully to sense a variety of phenomena, including acoustic fields, temperature, magnetic fields, displacement, fluid level, torque, current, strain, pressure, acceleration, rotation, and seismic activity. [Ref. 5, p. 626] Apart from the apparent versatility of application of optical fibers as sensors, a number of other reasons for this great interest are shown in the list of their advantageous characteristics presented in Table I. Some disadvantages to the use of optical fibers are also given in the table.

B. THE NEED FOR LOW-COST SENSORS

Of particular interest to the United States Navy is the possibility of using optical fiber sensors as highly sensitive underwater hydrophones. This interest has been a principal, underlying motivation behind the research into optical fiber sensors currently in progress at the Naval Postgraduate School, as well as at the Naval Research Laboratory. In a time of great fiscal constraint, indeed, at any time, the Navy is very

Table I Advantages and disadvantages of optical fibers sensors.

Advantages	
1	Optical fibers are lighter in weight than metal. Therefore a length of optical fiber require much less structural support than a comparable length of metal wire.
2	Optical fibers are made from sand, which potentially could make them much cheaper than metal wires.
3	Losses in optical fiber are very low.
4	Optieal fibers are immune to electromagnetic interference (EMI). This makes them suitable for use in "noisy" environments.
5	Optical fibers are geometrically versatile. They can be stretched out, coiled up, and embedded in epoxy, plastic, or composite materials very readily.
6	Glass is immune to the effects of many chemicals which corrode metals. Consequently optical fibers ean sometimes be used in environments which would be harmful to metal wires.
7	Sensors made from optical fibers are compatible with optical fiber communications systems.
8	Power consumption is very low in optical fibers.
9	Large separations between sensor and detector are feasible.

Disadvantages	
1	As of the time of writing (1991), optical signal processing is not as highly developed as electronic signal proeessing, so conversion of optical signals to electronic form is usually required. Thus a purely optical system is generally impractical. One could expect costs to be lower if mixed processing were unneecssary.
2	Connecting optieal fibers together requires splicing, and reflections and losses invariably occur at the splices. These effects may be small if slices are performed by fusing the glass strands together, but joining glass fibers together by this means is much less convenient than soldering metal wires together.
3	Tapping into an optical fiber requires the use of optical fiber couplers, and these devices are more eostly, less convenient, larger, and heavier than the soldered conneetions permissible with metal wires.
4	Optical fibers are more delicate than metal wires. Although glass is an amorphous crystal and ean be stretched to a limited degree, it will break mueh more readily than metal wires of comparable diameter if its radius of curvature is made too small.

concerned about the immense cost of much of the modern technology used in military applications. In particular, it is infeasible to deploy large numbers of underwater hydrophones if their price is exorbitant.

In addition to the cost of the sensor itself, there is a cost associated with extracting information from it about the phenomenon it has detected. It is of little utility to have inexpensive sensors if the means to recover the signals of interest is not correspondingly cheap.

The purpose of this research is to describe three inexpensive ways to recover signals from very sensitive optical fiber interferometric sensors. Whether the signals are derived from acoustic sensors, accelerometers, seismometers, or any other kind of optical interferometric sensor, the signals can be recovered in the identical, inexpensive manner presented in this dissertation.

C. PRINCIPLES OF OPERATION OF OPTICAL FIBER SENSORS

Since awareness of optical fiber sensing is not yet widespread, it is the purpose of this section to examine in general terms the means by which optical fibers can be made to act as sensors of physical phenomena. The phenomenon under consideration may have a natural origin, as in the case of seismic waves, or it may have a man-made origin, as in the case of noises emitted by a submarine. In either case, we shall refer to the phenomenon which we want to detect as the "signal of interest".

Detection of some signal of interest by an optical fiber sensor can be done if we transmit light through the fiber and if we somehow modify the light within the fiber. This step is called the *modulation* of the optical (light) wave by the signal of interest. Of course, merely altering the light within the fiber may be necessary, but it is hardly sufficient. Our goal is to examine the modified light when it finally emerges from the optical fiber and to infer from it what must have been the stimulus, that is, the quantity of interest to us. This latter step is the *demodulation* of the optical wave.[1] A general

---

[1] We often speak loosely of demodulating the *signal* since it is the signal which interests us, not the optical wave itself. This is not strictly accurate, however.

goal in the design of sensors is to ensure that only the signal of interest induces the modulating effect. As this is a matter pertaining to the design of transducers for specific applications, we shall not discuss this in detail.

There are three fundamental aspects of light which can be modified to encode the information we are interested in detecting. These are amplitude, polarization, and phase. While it is possible to modulate all three aspects of light simultaneously, typically only one of them is modulated. Some workers in this field also speak of modifying the wavelength, the length of the delay in receiving a response to a pulse, or the spatial position of the received radiation [Ref. 6, p. 596]. We shall regard these latter three as essentially the same as modifying the phase of the light.

1. Amplitude Modulation

The quantity being sensed can be made to modulate the *amplitude* of coherent or incoherent light transmitted through the fiber. (Recall that the amplitude of light is the amplitude of the continually changing electric and magnetic fields that comprise light.) In one example of this method, external pressure is applied to the fibers and induces small bends in it. These so-called *micro-bends* change the transmission characteristics within the fiber, and this, in turn, changes the amplitude of the light within the fiber. Upon the emergence of the light from the optical fiber, the change in amplitude is manifested as a change in intensity. [Ref. 6: pp. 600-601] Standard methods of electronic amplitude demodulation permit recovery of the signal inducing the changes in intensity, *e.g.*, the acoustic field being measured.

A primary drawback to the use of amplitude modulation is the variation in the intensity of the output of the light source with variations in temperature, aging, and other causes. Compensation for changes in temperature is feasible, but it adds to the complexity and the cost of these systems. Compensation for other causes of the variations in the intensity of the light is not so easy. In any case, the variations distort the output, as anyone who has ever listened to AM radio during a thunderstorm will attest.

2. Polarization Modulation

The quantity being sensed can be made to modulate the *polarization* of the light within the fiber. By detecting the change, it is possible to recover the signal. As an example of the use of this form of light modulation, quartz will rotate the plane of polarization of a beam of light [Ref. 6, p. 614]. The amount of rotation is linearly dependent on temperature, as shown in Figure 1. One could therefore design a sensor of temperature by taking advantage of this effect and observing the amount of rotation of the polarization which a light wave underwent. A disadvantage of this particular

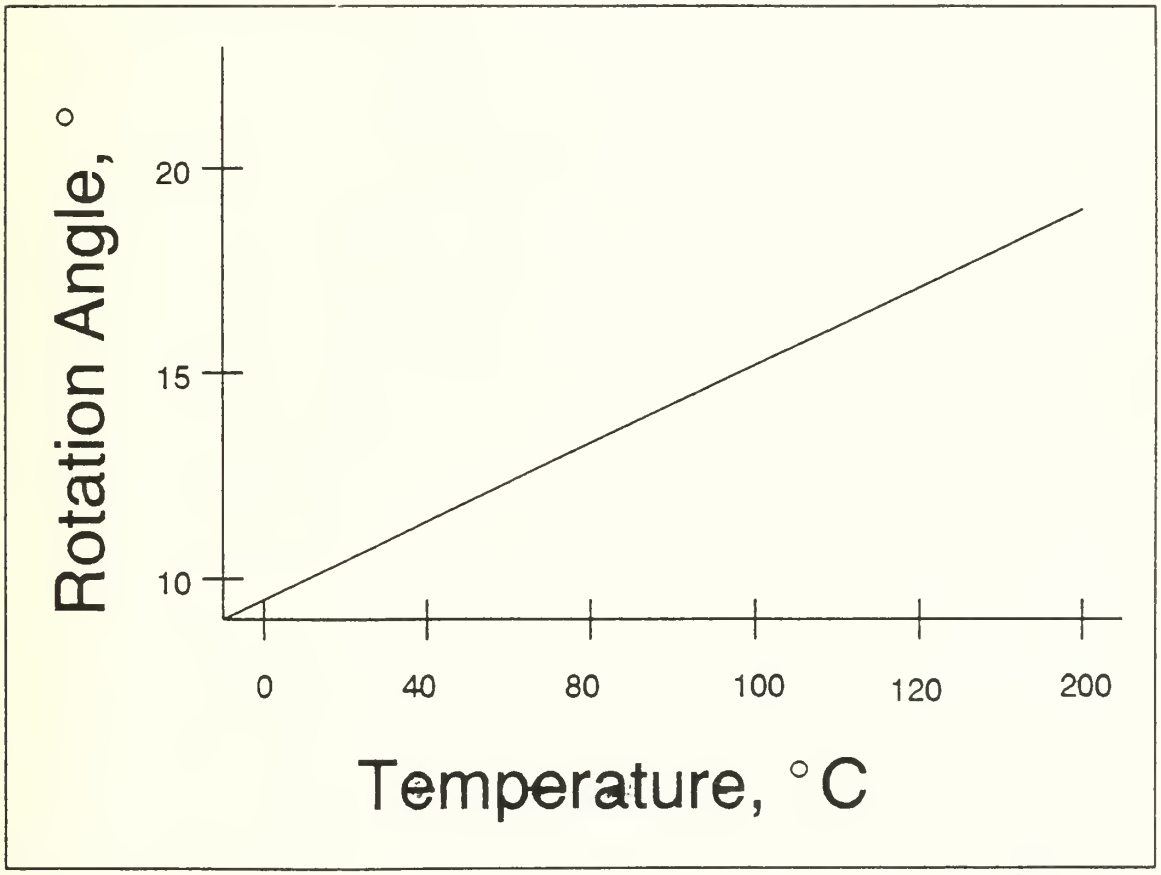

Figure 1 Variation of the angle of rotation of polarization in quartz as a function of temperature. Adapted from Busurin, *et al.* [Ref. 6, p. 614]

example is that the light must leave the fiber and then enter it once more. The optical fiber is reduced to being a mere conduit for the signal and is not really itself a sensor.

A more general disadvantage of polarization modulation is the tendency of the optical fibers to get twisted, altering the polarization of the light emitted from the fiber. To counter this, one can use polarization-preserving optical fiber, but it costs more than ordinary fiber. The use of polarization controlling devices is another possible solution, but these operate by twisting the fiber by an amount which corrects an error in polarization. Simple polarization controllers do not detect the amount of the error, nor do they prevent the fibers from twisting further and so spoiling the corrective effect. More elaborate controllers do detect the error and attempt to keep it constant, but they are correspondingly more costly to use.

3. Phase Modulation

The field being sensed can be made to modulate the *phase* of the light within the fiber. This is most easily done by arranging the fibers so that they are stretched or relaxed by changes in the signal of interest. If the length of a fiber changes by one wavelength λ, there will be 2π radians of phase shift in the light reaching the furthest end of the fiber. Since a wavelength of light is very small (830 nm in a vacuum or 560 nm in the glass for the infrared laser diodes used in this research), measuring phase shifts of one radian is equivalent to measuring changes of length of only

$$\frac{\lambda}{2\pi} = \frac{560 \text{ nm}}{2\pi} = 90 \text{ nm}. \qquad (1)$$

It is possible to measure considerably less than 1 radian without great difficulty, and with care, phase shifts on the order of as little as 1 μrad [Ref. 7, p. 1652] can be detected during an observation lasting one second. Clearly, one does not need to stretch the glass very much to create an easily observable effect. Since there are many phenomena of nature which can be induced to stretch the optical fibers, even a little bit,

by applying a strain to them, optical fibers make very sensitive and versatile detectors of a great many different phenomena.

D. OPTICAL FIBER INTERFEROMETRIC SENSORS

Of the three general methods of modulation applicable to the design of optical fiber sensors, one stands head and shoulders above the others in its ability to detect small signals. This is the method of phase modulation. For this method to be useful, a method of measuring the phase shift must be found. This section discusses how this can be done.

1. Principles of Operation

The difference in phase between two coherent beams of light can be detected by interferometric techniques, which are the most sensitive techniques known for measuring changes in distance (optical path length) [Ref. 6, p. 606; and Ref. 5, p. 661]. No sensors exist for directly measuring the electric or magnetic fields of an optical signal. The reason for this is that visible, and even infrared, radiation have frequencies much higher than those sustainable in any electronics available today. For example, the slightly infrared light emitted by the laser diodes used in our research has a wavelength of 830 nm. The frequency of this light is 361 THz (3.61×10^{14} Hz), well beyond the maximum bandwidth of our fastest electronic components.

We do, however, have detectors which can measure the intensity of light, and, if the intensity varies with time, they can detect this variation, provided that it does not vary too fast. For example, photodiodes with bandwidths of many GHz (10^9 Hz) are now available.

The oscillating phase shifts created by many phenomena have a sufficiently low frequency content to be easily detectable by photodiodes if they can only be converted to variations in the intensity of the light. To perform such a conversion, coherent light is passed through two fibers. Together, the two fibers constitute the arms of an interferometer. The field being measured is made to induce a difference in the phase of

the light in each arm by applying a strain to them, but in opposite directions.[2] When the light waves are recombined, they interfere both constructively and destructively. The resulting pattern of light and dark "fringes" contains information about the original signal.

Whether the output contains *enough* information to recover the signal depends on the means by which the light is recombined. We shall elaborate on this key point presently.

2. Schemes for Recovering Signals

Numerous schemes have been devised for recovering signals from optical fiber interferometric sensors. Several of these are described here.

a. Phase Generated Carrier Homodyne Demodulation

One method of demodulating a phase-modulated interferometric output is that called Phase Generated Carrier Homodyne Demodulation [Ref. 8]. This scheme is also known as Pseudo-Heterodyne Demodulation. In this technique, the current which drives the laser source is modulated in amplitude. The result of this is to create a modulation of the laser's output power and wavelength. If there is a difference in the length of the two legs of the interferometer, the change in wavelength manifests

---

[2] It is possible to arrange matters so that only one fiber is affected by the field of interest. This is an inferior approach since in practice it is impossible to avoid having extraneous effects such as temperature or pressure create length differences between the two fibers. The result is a sensor which detects both the quantity of interest and other quantities which one would prefer to have suppressed. The rejection of these unwanted quantities is best achieved by using a push-pull arrangement in which *unwanted* effects are applied equally to each arm, whereas the *desired* effect induces opposite effects in each arm. The output yields enhancement of the desired quantity and rejection of the unwanted quantities.

itself as a change in phase at the output.[3] This guarantees the presence of a fundamental frequency in the received signal, namely, the frequency of the current modulation.

The modulation frequency and its harmonics each carry in their sidebands a replica of the phase-modulated signal created when the signal of interest impinges on the sensor. Two of these replicas are isolated by the use of bandpass filters. Proper control of the strength of the modulation also guarantees that each of these replicas has the same strength. The receiver uses these tones as inputs to two mixers. The output of this signal processing is a pair of signals. One contains a voltage signal proportional to the trigonometric sine of the signal of interest. The other contains that signal's cosine. That is, if $s(t)$ is the signal of interest expressed in units of induced optical phase shift, the two outputs are

$$x_1(t) = A_1 \sin[s(t)] \tag{2}$$

and

$$x_2(t) = A_2 \cos[s(t)]. \tag{3}$$

One can sum these signals, obtaining a signal like a conventional phase-modulated signal, namely

$$x_1(t) + x_2(t) = \sqrt{A_1^2 + A_2^2}\, \sin\left[s(t) + \tan^{-1}\left(\frac{A_2}{A_1}\right)\right]. \tag{4}$$

This signal can be demodulated using techniques which are standard in the communications field, the goal being to extract the varying phase term $s(t)$. Usually the fixed phase term, the one dependent on A_1 and A_2, would be discarded. However, in forming the sum of $x_1(t)$ and $x_2(t)$, we effectively discard one signal, since we are left with only a single

---

[3] In the absence of a difference in the path lengths, this is not the case. The larger the difference in path length, the larger the phase shift caused by a modulated wave length. [Ref. 7, p. 1652]

sinusoid. The absence of an orthogonal signal (the cosinusoid) causes an ambiguity in trying to recover the phase, which, after all, is simply the argument of the sine function.

For example, if the sine given in Equation (4) has the instantaneous value 1/2, we cannot tell whether the phase angle is 30° or 150°. If we knew the cosine, it would either be $\sqrt{3}/2$ for a phase angle of 30° or $-\sqrt{3}/2$ for a phase angle of 150°. Even with both the sine and the cosine, however, we need more information to distinguish between the four primary quadrants (−180° to +180°) and all other quadrants. If the phase amplitude can fall outside this range, we must keep track of the history of the wanderings of the phase angle in order to know in which quadrant it presently lies.

Keeping track of these wanderings still does not eliminate the need for both the sine and the cosine. The reason for this is that, in general, we do not know the waveform in advance. Suppose we have only the sine. Then it becomes impossible to distinguish between a signal of interest which, after rising in phase amplitude, hesitates briefly at 90° before continuing to grow, and one which hesitates briefly at this same point before beginning to diminish in amplitude.

As an alternative to the standard methods of phase recovery, one can use a method which will be explained in Chapter VII. In this method, the sine and cosine information can both be used in such a way as to recover their mutual argument, *i.e.*, the signal of interest. This method implicitly keeps track of the wanderings of the phase angle outside the four primary quadrants, and so it is capable of demodulating very large phase amplitudes.

There are three principal drawbacks to Phase-Generated Carrier Demodulation.

1. A mismatch in the lengths of the two legs of the interferometer is mandatory. Without the mismatch, the fluctuations in the output wavelength of the laser do not induce fluctuations in phase shift at the output of the interferometer. The inclusion of a mismatch in length has an adverse effect on the coherence of the light emerging from each leg, which shows up as a reduction in fringe visibility, the contrast between bright and dark at the output. This is equivalent to a reduction in the ratio of signal-to-noise. Also, phase noise from the laser source,

already present in both legs of the interferometer, is effectively enhanced by a mismatch in length into differential phase noise upon recombination of the two beams into an interference pattern. Thus it contaminates the interference pattern created by the signal of interest.

2. The phase modulated signal generated by the signal of interest appears as sidebands around the modulation frequency and each of its harmonics. The separation of these harmonics places a limit on the bandwidth of the signal of interest which can be sustained. In fact, only half of the modulation frequency is available as signal bandwidth. If this frequency limitation is exceeded, the upper sideband around the modulation frequency mixes with the lower sideband around its second harmonic, creating distortion in the demodulation process. Since the amplitude of the signal of interest determines its bandwidth, there is therefore a limit on its strength due to the choice of modulation frequency. The demodulator itself must operate over a bandwidth at least five times larger than this permissible signal bandwidth, in order to encompass the upper sidebands of both the modulation frequency and its second harmonic. In Dandridge [Ref. 7], a peak of about one radian in the signal of interest was permissible. In 1982, there were no optical fiber interferometric sensors capable of creating much bigger phase shifts than this, so the use of the Phase Generated Carrier scheme was convenient. The situation is now different. Sensors capable of generating very large phase shifts are available. A demodulator whose entire bandwidth is devoted to handling the signal of interest is preferable to one which needs additional bandwidth due to the choice of demodulation scheme.

3. To achieve large dynamic range with a sensor which is limited to peak phase shifts of less than about one radian requires successful processing of peak phase shifts far below one radian. To achieve a dynamic range of, say, 100 dB when the peak signal is on the order of one radian requires that signals of under 10 μrad be demodulated. Such small phase shifts correspond to very small changes in intensity of the interference pattern at the output of the interferometer. Such small intensity changes are contaminated by noise, so much attention must be paid to the demodulator in order that it may separate the signal from the noise. This tends to make such demodulators expensive. It also makes necessary the use of more costly laser sources with small amounts of phase noise in order to reduce the severity of the effect. At the end of its travel down a fiber, the beam's phase oscillates because the number of wavelengths which fit into the fiber keeps on changing. To increase the operating range with phase-generated carrier demodulation, the modulation frequency must be increased with the consequent adverse effect on bandwidth mentioned in the previous paragraph.

b. Synthetic Heterodyne Demodulation

This techniques bears a great resemblance to the Phase Generated Carrier Demodulation scheme just discussed. It differs principally in that rather than creating a phase shift in the carrier by modulating the laser current, the phase shift is modulated with a piezoelectric cylinder around which one leg of the interferometer is wrapped and to which a sinusoidal voltage signal is applied [Ref. 9, p. 695].

The principal drawback to this scheme is the need to introduce electronics into the interferometer. Since a primary objective in using optical fiber sensors is to eliminate electronics from the sensor, this requirement defeats the purpose.

Another drawback is the different treatment of each leg of the interferometer. This loss of symmetry reduces the rejection of unwanted signals such as changes in pressure or temperature since they are likely to act differently on that leg of the interferometer which contains the piezoelectric cylinder. Once two complete sidebands of the interferometric output have been isolated, the demodulation proceeds as with the Phase Generated Carrier method.

c. Fringe-Rate Demodulation

When large amounts of phase shift are provided by an interferometric sensor, another technique becomes feasible. This technique comes in two variants. One is called fringe-counting, the other is called fringe-rate demodulation [Ref. 10, 11]. These approaches rely on the transitions of interferometric outputs across some central value.

In the fringe-counting variation, the transitions are counted digitally in a given period of time. The instantaneous ratio of count to time is the frequency of the phase-modulated interference pattern. By integrating this number over time, the phase can be recovered. Of course, it is impossible to obtain an instantaneous count, so one must in practice wait a short time to produce at least one count.

In the fringe-rate variation, the transitions are used as inputs to a frequency-to-voltage converter. In a sense, the converter is itself a counter. However, it does not perform a precise count of crossings per unit time. Instead, each transition

triggers a boosting of the output by causing an increment of charge to be pumped onto a capacitor. The passage of time, conversely, causes the output to droop since the capacitor is drained of its accumulated charge through a resistor. The combination of these two tendencies is a voltage which is proportional to the frequency. Again, integration of the result permits recovery of the phase information.

When signals are weak, however, there are *no* transitions at all. The minimum detectable signal is that necessary to create at least one transition. This signal is on the order of π radians peak phase shift. When signals are still only a little stronger than this threshold, an erratic output from the charge pump due to the incremental nature of the charge which is added to the capacitor whenever a transition occurs can be objectionable. This noise is lessened when large signals of interest are present.

d. Homodyne Demodulation

Whereas the synthetic heterodyne technique has generally been limited to less than π radians peak phase shift, the fringe-counting and fringe-rate techniques stop working *below* π radians peak phase shift. To bridge this region, we can use a number of *homodyne* demodulation techniques.[4] These methods all are predicated on the use of orthogonal components of the phase-modulated signal obtained from the interferometer without using heterodyne methods.

Normally, an interferometer has only one output. Optical fiber interferometric sensors usually have two, since they employ 2×2 optical fiber couplers to combine the two legs of the interferometer into an interference pattern. From the law of conservation of energy, it is easy to see that the two outputs must be 180° out of phase from one another: when one is dark, the energy must all be present in the other output and *vice versa*. There are no orthogonal components in the outputs, and for this

---

[4] The word *homodyne* literally means "similar power". That is, there is no mixing with a reference frequency in the receiver, as with *heterodyne* ("different power") techniques. The term *homodyne* is more commonly used to mean that only one frequency is present, whereas *heterodyne* usually means that more than one frequency is present. Since photons of different frequencies contain different quantities of energy, the two meanings for each term are completely consistent with one another.

reason, heterodyning in the various forms described above has been used to obtain orthogonal components artificially as sidebands to the carrier frequency.

3. The Use of 3×3 Couplers to Facilitate Signal Recovery

There is a way to modify the output stage of the interferometer to obtain orthogonal components directly. To achieve this, we can use a 3×3 optical fiber coupler to create the outputs of the interferometer. The two legs of the interferometer now are used to generate three interferometric outputs which do contain orthogonal components. The details of this will be discussed extensively in Chapter III. Methods of extracting the amount of optical phase shift present in the interferometric outputs will then occupy our attention throughout the rest of this dissertation. Suffice it to say, for the present, that with a 3×3 optical fiber coupler at the output, recovery of the signal is feasible without the drawbacks listed for the other techniques of demodulation already discussed.

II. SCOPE OF THE RESEARCH

A. OBJECTIVES OF THE RESEARCH

In the previous chapter, we considered the motivation behind the general research into optical fiber sensors. We stated that the use of optical fiber *interferometric* sensors, in particular, which apply the techniques of interferometry to the use of phase-modulating optical fiber sensors, could produce extremely sensitive sensors. The use of 3×3 couplers at the output of the interferometer, we said, could permit us to obtain orthogonal signals from which the signal of interest could be recovered, without elaborate modulation of laser current on the one hand and without inserting modulating elements into one leg of the interferometer.

It was the goal of our research to investigate three methods of recovering signals of interest from optical fiber interferometric sensors with 3×3 couplers at the output. It is the goal of this dissertation to present the results of this research.

The sensors we are interested in are capable of generating phase shifts of thousands of radians and more. In principle, a sensor producing even greater phase shifts should permit recovery of smaller and smaller signals, until thermal and other sources of noise become significant. The phenomena sensed by the sensor are of secondary importance in this research. The chief requirement is that the phase shift they induce in a sensor be linearly proportional to their amplitude.

B. ORGANIZATION OF THE DISSERTATION

In this section, we outline the organization of the rest of this dissertation in order to help the reader grasp the results of the research. To explain this sensibly, it will be useful to consider the situation at the outset of the research.

In the summer of 1989, when we began this research, we did not yet have any optical fiber interferometric sensors with 3×3 optical fiber couplers at the output for the simple reason that they were not yet commercially available. Their appearance was then imminent, but in order not to be dependent on their arrival to commence the research, we resorted to simulating interferometric signals in order to begin to address the requirements of demodulation. We used two such simulators, one of which was of our own design and construction. These are described in the appendices to this dissertation.

In Appendix B, we present relevant portions of the theory of optical fiber couplers. This lays the foundation for Chapter III, in which we show how 3×3 couplers can be incorporated into a Mach-Zender optical fiber interferometric sensor. The purpose of this is to make it clear how the use of 3×3 couplers produces interferometric outputs which contain both the sine and the cosine of the optical phase shift induced by signal of interest. Dandridge [Ref. 7] showed how one could recover the signal of interest, once its sine and cosine had been isolated. In Chapter VII we explain his method, which we refer to as asymmetric demodulation.

By the summer of 1990, the 3×3 couplers had arrived and we quickly sought to produce an optical interferometer to replace the simulators. Although parallel research was going on by other members of our research group into the design of hydrophones, there were still no practical sensors with 3×3 couplers at the output. Consequently, the author designed an optical fiber interferometer to sense voltage signals, as these could easily be generated in the laboratory. The construction of this sensor is described in Chapter IV.

The easiest demodulation method investigated in this research is the Fringe-Rate Demodulation scheme described by Crooker [Ref. 10] and Crooker and Garrett [Ref. 11]. The design of the Fringe-Rate Demodulator is the subject of Chapter V. Some modifications have been made to the scheme originally discussed in Crooker, and these are detailed here. In Chapter VI, we present experimental measurements of the performance of the Fringe Rate Demodulator.

To demodulate interferometric outputs with peak phase shifts of magnitudes extending both above and below π radians, we have invented a new demodulation

technique which we call *symmetric demodulation*. The author wishes to give credit to Dr. Robert Keolian and to Dr. Steven Garrett for the discussions that made this invention possible. The method of this new demodulation scheme is explained in Chapter VIII. In Chapter IX we describe the design of an analog implementation of this new algorithm, the Symmetric Analog Demodulator.

A key difference between the Symmetric Analog Demodulator and the Fringe Rate Demodulator is that the latter cannot properly handle phase shifts of less than approximately $\pi/2$ radians (more, in practice). The former can handle signals all the way down to the demodulator's noise level. In order to describe the performance of the Symmetric Analog Demodulator, then, we must consider its noise floor. Therefore, in Chapter X we digress briefly to describe how we measure low signal levels and noise in the laboratory. We also describe some of the theory that permits us to predict noise. The close match between theory and observation provides a high degree of confidence in the noise measurements included in the next chapter, Chapter XI, which describes the performance of the Symmetric Analog Demodulator using all the criteria mentioned earlier in Chapter VI on the performance of the Fringe Rate Demodulator, as well as its noise level. The noise of the Fringe Rate Demodulator was not quantified because signals of less than $\pi/2$ radians in amplitude cannot successfully be demodulated by it anyway.

The use of digital signal processing techniques has become increasingly common in recent years because of the continuing reductions in cost and increasing capabilities of microprocessors. Such techniques can be applied to signals recovered from optical fiber interferometric sensors, too. To demonstrate this, we describe in Chapter XII the design of an Asymmetric Digital Demodulator which implements the asymmetric demodulation scheme of Dandridge [Ref. 7], described in Chapter VII of this dissertation. Our design employs discrete digital logic with digital signal processing integrated circuits and a pipelined architecture which exhibits an ability to process signals at a speed limited only by that of the analog-to-digital converters it uses. The performance of the Asymmetric Digital Demodulator is described in Chapter XIII. The performance is characterized in

the same manner as was done in Chapters VI and XI dealing with the performance of the Fringe Rate Demodulator and the Symmetric Analog Demodulator, respectively.

The final chapter in this dissertation, Chapter XIV, presents a synopsis of the results and discusses areas for further research and improvements in the demodulation schemes presented earlier.

In the appendices we provide mathematical details omitted from the main body of the dissertation in an attempt to make it somewhat more readable, although there is ample mathematics in the body of the dissertation already! We also include analyses of both the interferometric simulators we used early in the course of our research; analysis of a simple analog circuit capable of performing integration, differentiation, and bandpass filtering (a circuit which we used repeatedly in the design of the Symmetric Analog Demodulator); and a detailed analysis of the noise in the Symmetric Analog Demodulator.

C. MEASURES OF THE PERFORMANCE OF THE DEMODULATOR

As mentioned above, three chapters of this dissertation are devoted to presenting measurements of the performance of the demodulators we have built, namely the Fringe Rate Demodulator, the Symmetric Analog Demodulator, and the Asymmetric Digital Demodulator. For the sake of completeness, we complete this chapter on the scope of the research with a list of the criteria by which we assessed the performance of the demodulators. These are:

1. the stability of the scale factor, which expresses the voltage out of the demodulator per radian of input optical phase shift;

2. the small-signal bandwidth;

3. the maximum permissible signal (MPS), which is the greatest phase shift which can be demodulated correctly without an unacceptable level of total harmonic distortion;

4. the minimum detectable signal (MDS), which is the smallest peak phase shift which can be detected. It is defined as being equal to the noise threshold (in a

one hertz bandwidth) which is output by the demodulator. This noise threshold is expressed in terms of input phase shift. This definition of minimum detectable signal is inappropriate for the Fringe Rate Demodulator, since it cannot handle signals of less than $\pi/2$ radians;

5. the dynamic range, which is the difference between MDS and MPS;

6. complexity of the circuit; and

7. component cost.

We have attempted to account for differences between the predicted and observed performance.

III. THEORY OF 3×3 MACH-ZENDER OPTICAL FIBER INTERFEROMETERS

A. KEY RESULT OF THE THEORY

In this chapter we derive a mathematical prediction of the performance of an optical fiber interferometer in the Mach-Zender configuration. The Mach-Zender configuration is distinguished from the Michelson configuration in that the two optical paths in the interferometer are only traversed once by light, rather than twice. The implication of this for an optical fiber interferometer is that there must be two optical fiber couplers: one for the input and a second for the output.

In general, Mach-Zender interferometers produce more output power than do Michelson interferometers because they do not rely on reflection for light to be output. On the other hand, Michelson interferometers are twice as sensitive as Mach-Zender interferometers because the light is twice subject to the phase shift induced by the transducer, once for each pass through the interferometer. They are cheaper, too, since only one optical fiber coupler is required, instead of two.

Figure 2 is a schematic drawing of a Mach-Zender optical fiber interferometric sensor with 2×2 optical fiber couplers at both the input and the output. Figure 3 is a schematic drawing of a Michelson optical fiber interferometric sensor with a single 2×2 optical fiber couplers serving as both the input and the output. The drawback to the use of 2×2 couplers is that the two interferometric outputs are 180° out of phase from each other, and so there is insufficient information in them faithfully to reconstruct the signal of interest. In the case of the 2×2 Michelson configuration, there is only one output, and the inability to reconstruct the input is more blatant, although no more real.

To take advantage of passive homodyne demodulation techniques, we can use a 3×3 coupler at the output. Figure 4 shows a Mach-Zender optical fiber interferometric sensor with a 2×2 optical fiber coupler at the input and a 3×3 optical fiber coupler at the output. Figure 5 shows a Mach-Zender optical fiber interferometric sensor with a

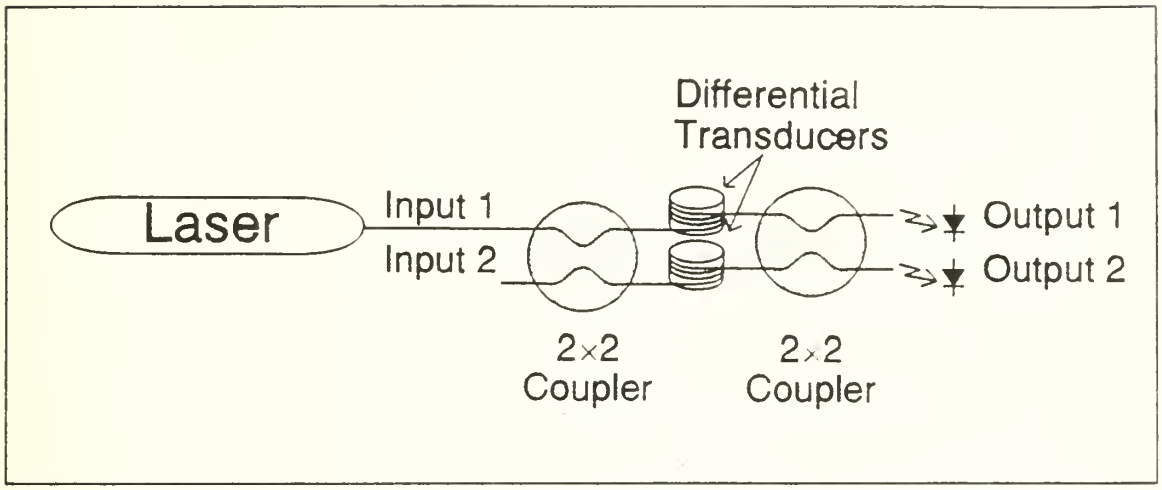

Figure 2 Mach-Zender Optical Fiber Interferometer with 2×2 optical fiber couplers at input and output.

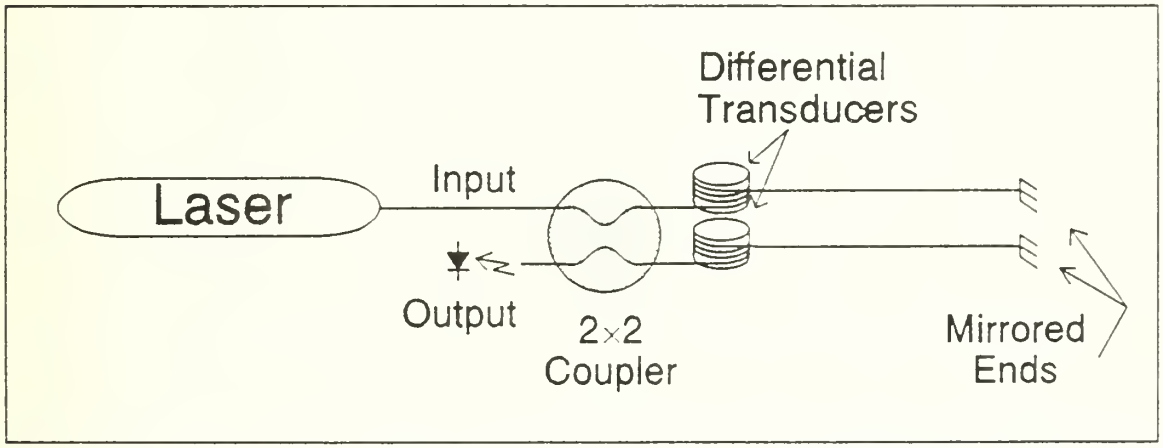

Figure 3 Michelson Optical Fiber Interferometer with a single 2×2 optical fiber coupler for input and output.

3×3 optical fiber coupler at the input and a 3×3 optical fiber coupler at the output. One could also construct a Michelson interferometer with a 3×3 coupler serving both as input and output. In this case, there would be only two outputs available, since one of the three strands of glass in the coupler is devoted to the input. This situation is depicted in Figure 6.

The purpose of the derivation in this chapter is to obtain a theoretical model of the optical power in the output generated by a Mach-Zender optical fiber interferometric sensor like those in Figure 4 and Figure 5. Of these two, that using the 2×2 coupler at

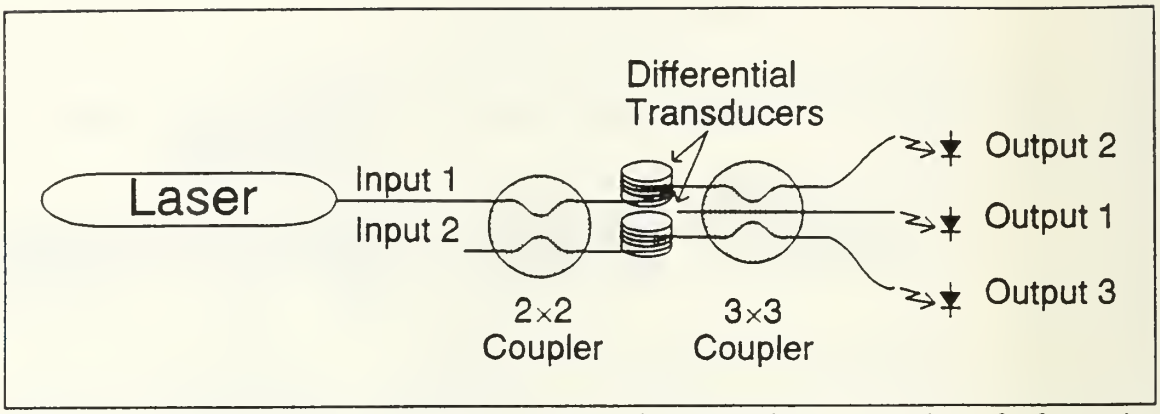

Figure 4 Schematic of a Mach-Zender optical fiber interferometer with a 2×2 coupler at the input and a 3×3 coupler at the output.

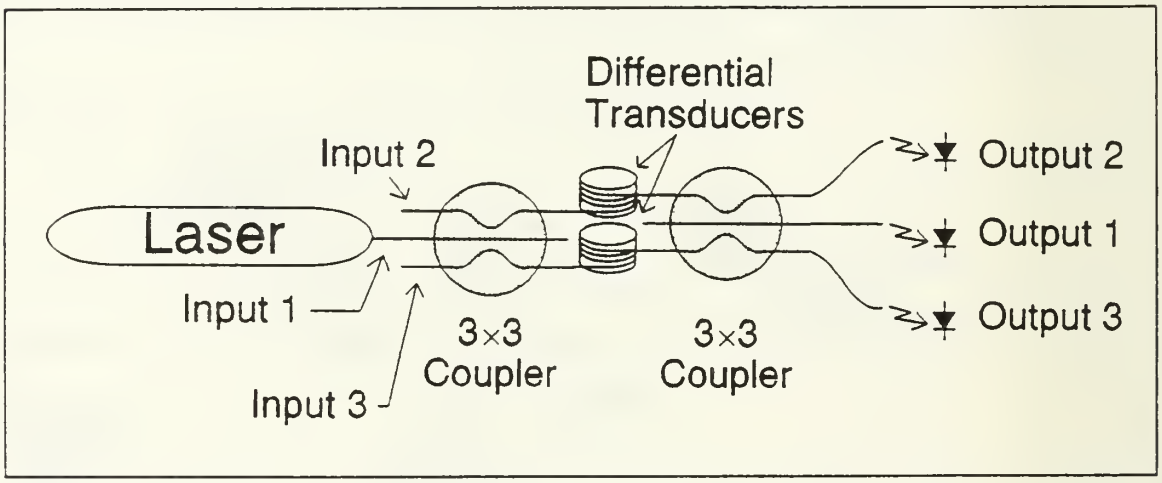

Figure 5 Schematic of a Mach-Zender optical fiber interferometer with a 3×3 coupler at the input and a 3×3 coupler at the output.

the input is more efficient. As we shall show, this yields a 1.76 dB improvement in output power.

The model we derive in detail in the balance of this chapter is given by Equation (5).

$$\frac{|a_k(L)|^2}{2} = D + E\cos\left[\xi(t) + \phi(t) - (k-1)\frac{2}{3}\pi\right]. \tag{5}$$

We shall complete the derivation of the model described in Equation (5) for the interferometer whose input is a 2×2 coupler, that of Figure 4. The completion of the model for the interferometer whose input is a 3×3 coupler, that of Figure 5, proceeds

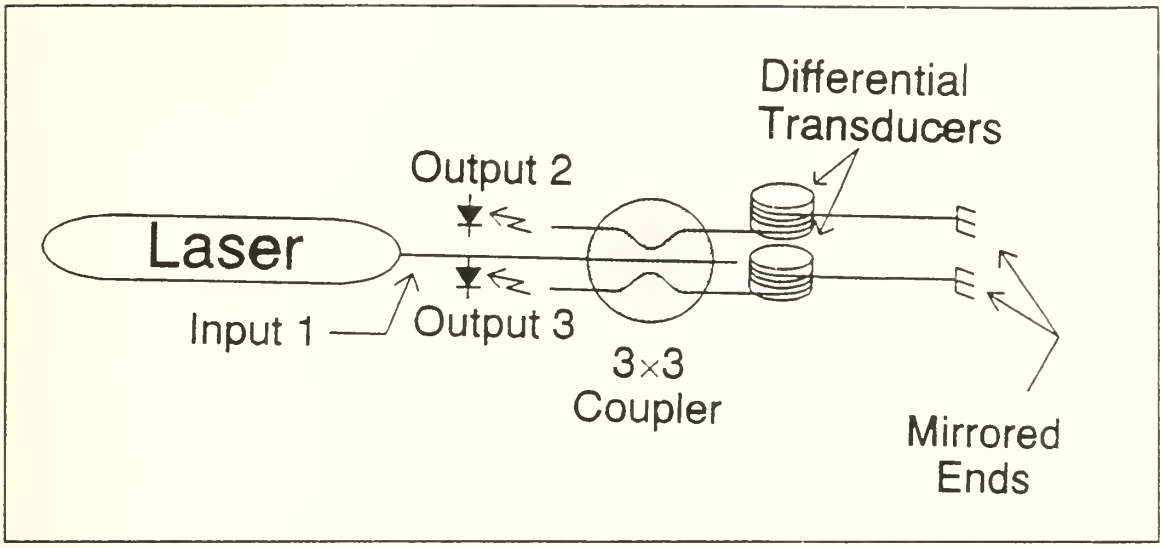

Figure 6 Michelson Optical Fiber Interferometer with a single 3×3 optical fiber coupler for input and output.

upon very similar lines, most of which are supplied in this chapter.

In Equation (5), k is an index which can take on the values 1, 2, or 3. It specifies which of the three outputs is being considered. D represents a central value, around which the outputs of the interferometer can fluctuate by $\pm E$, at most. Whether or not they actually reach the two extrema at $D+E$ and $D-E$ depends on the signal $\xi(t)$. If it has a very small amplitude, then the cosine will not vary much and so the extreme values will not, in general, be achieved. On the other hand, if ξ has a very large amplitude, more than $\pm\pi$ radians, in particular, then the signals are guaranteed to reach both extrema, possibly many times for each cycle of ξ. The term $\phi(t)$ is contributed to the phase by phenomena which are of no interest to us.

In an acoustics application, for example, we would prefer that acoustic waves impinging on the interferometric sensor be the only phenomena to induce a phase shift in the light within the interferometer. Acoustic waves are the signals of interest in this application, and we represent them by $\xi(t)$. Temperature changes also can induce phase shifts within the interferometer, although we do not desire this effect. Thus they contribute to the unwanted phase shift, $\phi(t)$. We often find that the frequency of $\phi(t)$ is much less than the frequency band of the signal of interest, which makes its elimination somewhat easier. With proper construction of the transducer, unwanted effects can be

made to produce the same effect on both legs of the interferometer, and this helps to suppress $\phi(t)$, too. In any event, we shall often suppress this term for mathematical convenience, and because it can be removed by filtering, but it is never truly absent.

In Figure 7 we show graphs of three samples of the kind of outputs described by Equation (5). These graphs were drawn by computer. Superimposed over the three interferometric outputs is a plot of the stimulus itself, $\xi(t)=A\sin(2\pi ft)$. This graph is not to the same scale as the other three; it is centered vertically over the middle output for convenience. For the purpose of illustration, we chose to let the signal of interest be a pure tone (a sinusoid) with phase amplitude $A=5\pi$ radians. The plot does not show the scale of time along the horizontal axis, and so the choice of the frequency f is not specified. By suitable scaling of the time axis, the plot will look the same no matter what f might be. The three plots are offset from one another vertically only to make them easy to see. The model specifies that they will all really be centered around the same central value D.

The choice of amplitude A dictates the amplitude of ξ, of course, but it also dictates the number of fringes (complete cycles of 2π radians, or multiples of π in A) in the three outputs between each successive extremum of ξ.

As the stimulus passes through zero (its midpoint), it changes at its most rapid rate. Simultaneously, the outputs achieve their highest instantaneous frequencies. When the stimulus stops changing (when it reaches an extremum), the outputs also stop changing and their instantaneous frequency drops to zero. The phase shift is directly proportional to ξ. The instantaneous frequency of the interferometric outputs is given by the rate of change of ξ. A Fourier series for the interferometric outputs is presented in Equation (282) on page 177.

In Figure 8 we show another set of sample graphs. They differ from those of Figure 7 only in the different choice for the amplitude of the stimulus, $A=10.5\pi$ radians. Note that there are more fringes in this second example than in the first. Yet the locations of the points where the instantaneous frequency reaches its maximum and where it reaches zero have not changed, since these depend only on the frequency f of the stimulus.

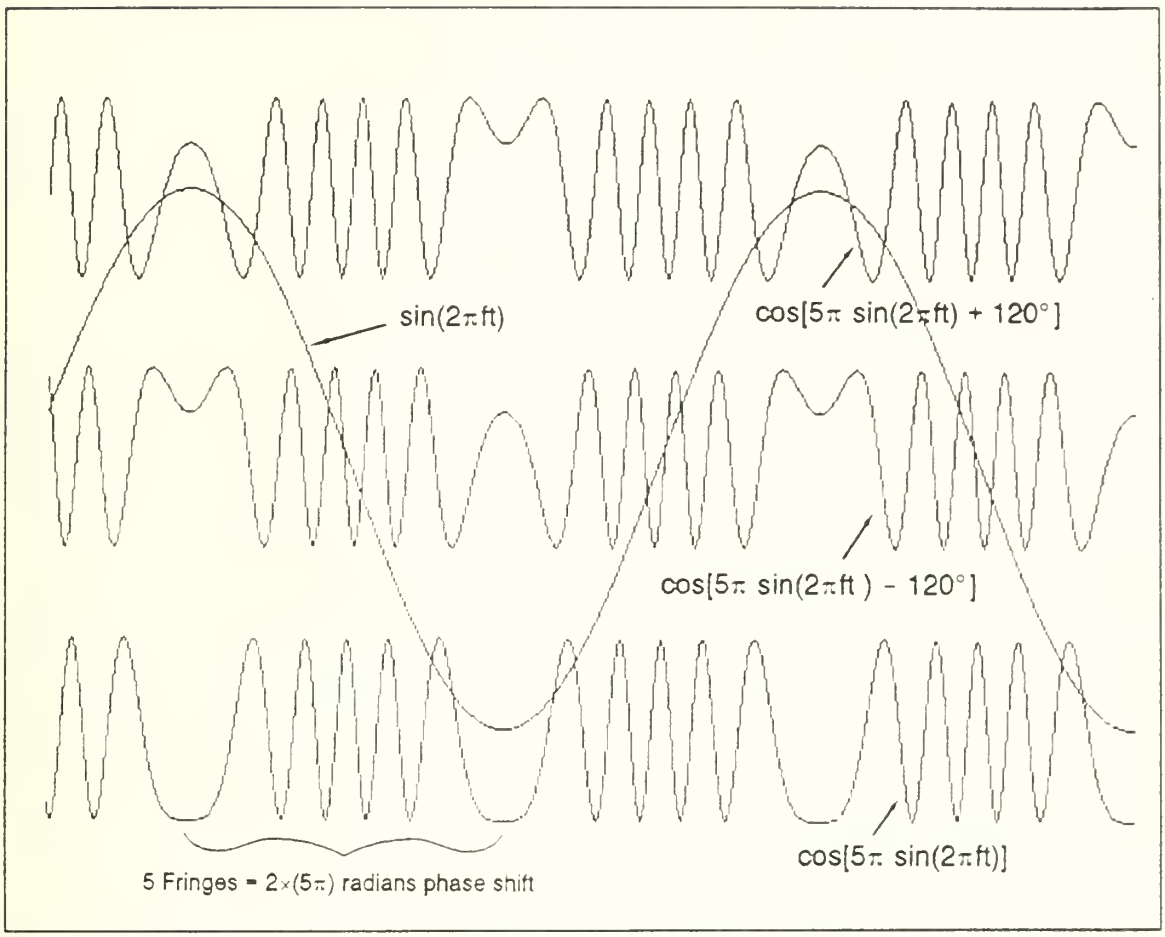

Figure 7 Simulation of an interferometric output with a peak phase amplitude of 5π radians.

It is worth discussing the units of ξ at this point. In the previous paragraph, we treated ξ as measured in radians. ξ is indicative of the amount of strain on the glass in the optical fiber interferometer. The signal of interest, no matter what its natural units, produces differential strain in the two legs of the interferometer, with a consequent differential optical path length. The number of wavelengths of differential path length corresponds to the number of multiples of 2π radians of phase shift induced in the interferometric output.

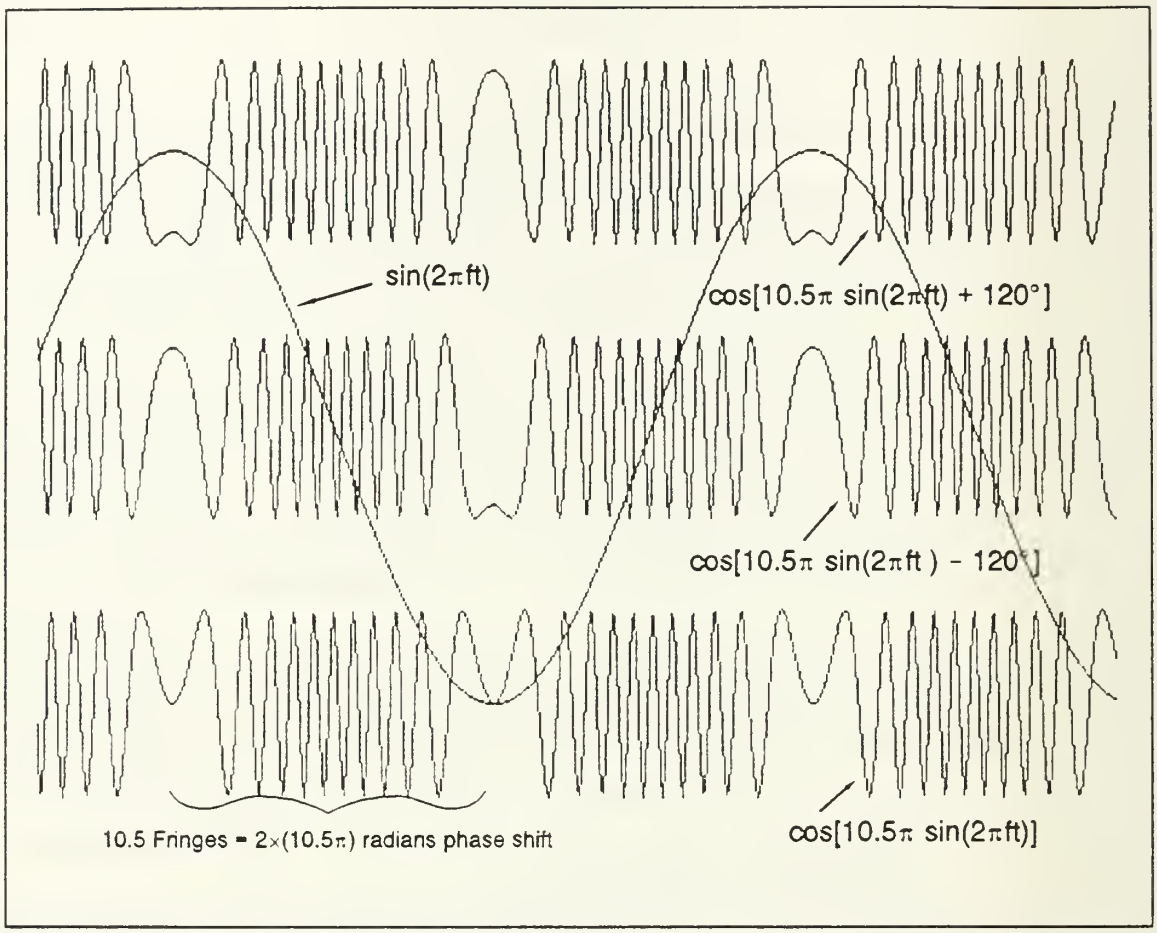

Figure 8 Another simulation of interferometric output for a sinusoidal stimulus of amplitude $A = 10.5\pi$ radians.

B. DERIVATION OF THE KEY RESULT OF THE THEORY

The differential equations which describe the amplitudes of the phasors within the 2×2 and 3×3 couplers are given in Sheem [Ref. 12, p. 3865; and Ref. 13, p. 869]. Before presenting the differential equations themselves, we first establish some notation.

The fibers will be denoted by numbers 1 and 2 for the 2×2 case and 1, 2, and 3 for the 3×3 case. We shall denote electrical field intensities by phasor amplitudes. The electrical field phasor $a_k(z)$ within fiber k is a function of position z measured from the point where light enters the coupler. For instance, $a_1(z)$ is the electric field in optical

fiber 1 at a distance z from the entry point. The differential equations include coupling coefficients K_{ij} between fibers i and j.[5] For example, K_{12} is the coupling coefficient between optical fibers 1 and 2 within a coupler. For the 2×2 case, the differential equations given by Sheem are

$$\frac{da_1(z)}{dz} + jK_{12}a_2(z) = 0 \tag{6}$$

and

$$\frac{da_2(z)}{dz} + jK_{12}a_1(z) = 0. \tag{7}$$

For the 3×3 case, they are very similar:

$$\frac{da_1(z)}{dz} + jK_{12}a_2(z) + jK_{13}a_3(z) = 0 \tag{8}$$

$$\frac{da_2(z)}{dz} + jK_{23}a_3(z) + jK_{21}a_1(z) = 0, \tag{9}$$

and

$$\frac{da_3(z)}{dz} + jK_{31}a_1(z) + jK_{32}a_2(z) = 0. \tag{10}$$

If we compare these equations with the general result given in Equation (420) in Appendix B on page 279, we may note two differences. Firstly, Sheem [Refs. 12 and 13] renames Snyder's [Ref. 20] coupling coefficients C_{ij} and brings them to the left-hand side of the equations as K_{ij}. This is a minor difference in notation, which we shall nonetheless adopt in order to keep this chapter's developments similar to Sheem's.

A more important difference is the dropping of the term $j\beta_j a_j$ in Equation (420) on page 279. The effect of the missing term is zero in the case where the three fibers are identical. [Ref. 14] That they all are identical is a reasonable approximation in a

---

[5] We assume that $K_{ij} = K_{ji}$ for all combinations of i and j.

3×3 optical fiber coupler. This chapter provides details of the solution of the differential equations where this approximation is valid.

It will be noted that in equations (6) and (7) there is little point in appending subscripts to the coupling coefficient K_{12}, so we shall replace it with coupling coefficient K and rewrite these equations as

$$\frac{da_1(z)}{dz} + jKa_2(z) = 0 \tag{11}$$

and

$$\frac{da_2(z)}{dz} + jKa_1(z) = 0. \tag{12}$$

Also, in equations (8) through (10) there are three distinct coupling coefficients, K_{12}, K_{23}, and K_{31}. Strictly speaking, the coupling between each pair of optical fibers in a 3×3 coupler may be different. However, in order to make the mathematics tractable, we shall assume that the coefficients all are equal to the same value, K.[6] This would obviously be a valid assumption for three fibers arranged equidistant from each other, as if at the vertices of an equilateral triangle. However, it is not valid for three fibers aligned in a plane. As it turns out, this assumption leads to a good description of the actual behavior of the interferometers we have built in the laboratory. A more elaborate theory could be created treating the coupling coefficients as random variables dependent on the position z, something we have not found necessary to get useful results, but which might assist in optimization of a practical system.

Replacing all coefficients K_{ij} by K, equations (8) through (10) simplify to

$$\frac{da_1(z)}{dz} + jKa_2(z) + jKa_3(z) = 0, \tag{13}$$

---

[6] Not necessarily equal to the K in equations (11) and (12).

$$\frac{da_2(z)}{dz} + jKa_3(z) + jKa_1(z) = 0, \tag{14}$$

and

$$\frac{da_3(z)}{dz} + jKa_1(z) + jKa_2(z) = 0. \tag{15}$$

Sheem [Ref. 13, p. 3865] gives the solutions to equations (11) and (12) as

$$a_1(z) = a_1(0)\cos(Kz) - ja_2(0)\sin(Kz) \tag{16}$$

and

$$a_2(z) = a_2(0)\cos(Kz) - ja_1(0)\sin(Kz). \tag{17}$$

We can verify that these are indeed solutions by differentiating equations (16) and (17) and substituting into equations (11) and (12). Because this is straightforward, we omit this verification.

The solution to equations (13) through (15) is also given by Sheem [Ref. 12, p. 869]:

$$a_1(z) = c_1 e^{jKz} + de^{-j2Kz} \tag{18}$$

$$a_2(z) = c_2 e^{jKz} + de^{-j2Kz}, \tag{19}$$

and

$$a_3(z) = c_3 e^{jKz} + de^{-j2Kz} \tag{20}$$

where

$$c_1 + c_2 + c_3 = 0. \tag{21}$$

We can verify that equations (18) through (20) are indeed solutions of differential equations (13) through (15) by taking their derivatives and substituting them into the

differential equations. Because this is straightforward, we omit the verification. Note, however, that Equation (21) is useful in performing the verification.

Equations (11) and (12) for the 2×2 coupler and Equations (18) through (20) for the 3×3 coupler are general. Particular solutions depend on the initial conditions. At the input to our Mach-Zender interferometer, we have

$$a_1(0) = A \tag{22}$$

$$a_2(0) = a_3(0) = 0. \tag{23}$$

This represents the situation where a laser of constant amplitude A injects light into one leg of the fiber and the other leg (in the case of a 2×2 coupler) or both other legs (in the case of a 3×3 coupler) are unilluminated.

We shall analyze both these situations before moving on to the next stage, which entails taking the outputs from either a 2×2 coupler or a 3×3 coupler and using them as inputs to a second coupler, a 3×3 coupler. Either of these configurations comprises a Mach-Zender interferometer with a 3×3 coupler as an output.

First we consider the case where the input to the interferometer consists of a 2×2 coupler. Evaluating Equations (16) and (17) we get

$$a_1(z) = A\cos(Kz) \tag{24}$$

and

$$a_2(z) = -jA\sin(Kz). \tag{25}$$

At the outputs of the coupler, $z=L$ and so the average power represented by these two outputs is given by

$$P_{out_1} = \frac{|\, a_1(L)\,|^2}{2} \tag{26}$$

$$P_{out_1} = \frac{1}{2}a_1(L)a_1^*(L) \tag{27}$$

$$P_{out_1} = \frac{A^2}{2}\cos^2(KL) \tag{28}$$

and

$$P_{out_2} = \frac{|\, a_2(L)\,|^2}{2} \tag{29}$$

$$P_{out_2} = \frac{1}{2}a_2(L)a_2^*(L) \tag{30}$$

$$P_{out_2} = \frac{1}{2}[(-j)A\sin(KL)][jA\sin(KL)] \tag{31}$$

$$P_{out_2} = \frac{A^2}{2}\sin^2(KL). \tag{32}$$

The sum of the average power emitted by each output of the coupler is a constant, as should be expected from the law of conservation of energy if the couplers are assumed to be lossless. (Although couplers are not 100% lossless, this approximation is quite good.)

We next consider the case where the input to the interferometer consists of a 3×3 coupler. We shall suppose that laser light of amplitude A is injected into input 1; inputs 2 and 3 will be left dark. Evaluating equations (18) through (20) at $z=0$ we get

$$a_1(0) = A = c_1 + d \tag{33}$$

$$a_2(0) = 0 = c_2 + d \tag{34}$$

and

$$a_3(0) = 0 = c_3 + d. \tag{35}$$

So

$$c_1 = A - d \tag{36}$$

and

$$c_2 = c_3 = -d. \tag{37}$$

If we sum the three equations (33) through (35) we get

$$\begin{aligned} A &= c_1 + c_2 + c_3 + 3d \\ &= 3d \end{aligned} \tag{38}$$

where we once again have used equation (21). From this, we see that

$$d = \frac{A}{3} \tag{39}$$

and substituting this into equations (36) and (37), we get

$$\begin{aligned} c_1 &= A - d \\ &= A - \frac{A}{3} \\ &= \frac{2}{3}A \end{aligned} \tag{40}$$

and

$$\begin{aligned} c_2 = c_3 &= -d \\ &= -\frac{A}{3}. \end{aligned} \tag{41}$$

Substituting equations (39) through (41) into equations (18) through (20) yields the particular solutions

$$a_1(z) = \frac{2}{3}Ae^{jKz} + \frac{1}{3}Ae^{-j2Kz} \tag{42}$$

$$a_2(z) = -\frac{1}{3}Ae^{jKz} + \frac{1}{3}Ae^{-j2Kz} \tag{43}$$

and

$$\begin{aligned} a_3(z) &= -\frac{1}{3}Ae^{jKz} + \frac{1}{3}Ae^{-j2Kz} \\ &= a_2(z). \end{aligned} \tag{44}$$

Note that outputs 2 and 3 are identical, which intuitively they should be, since they have not yet been distinguished from one another in any way except by the arbitrary assignment of index numbers to them.

The average power contained in output 1 is given by

$$\begin{aligned} P_{out_1} &= \frac{|\, a_1(L)\,|^2}{2} \\ &= \frac{a_1(L)a_1^*(L)}{2}. \end{aligned} \tag{45}$$

Substituting $z = L$ into Equation (42) and rewriting Equation (45) yields

$$\begin{aligned} P_{out_1} &= \frac{1}{2}\frac{A}{3}(2e^{jKL} + e^{-j2KL})\frac{A}{3}(2e^{-jKL} + e^{j2KL}) \\ &= \frac{A^2}{18}(4 + 1 - 2e^{jKL}e^{j2KL} + 2e^{-j2KL}e^{-jKL}) \\ &= \frac{A^2}{18}[5 + 2(e^{j3KL} + e^{-j3KL})]. \end{aligned} \tag{46}$$

We can replace the complex exponentials with trigonometric functions as follows:

$$P_{out_1} = \frac{A^2}{18}\left[5+4\frac{\left(e^{j3KL}+e^{-j3KL}\right)}{2}\right] = \frac{A^2}{18}[5+4\cos(3KL)]. \quad (47)$$

Similarly, the power in outputs 2 and 3 is given by

$$P_{out_2} = P_{out_3} = \frac{|a_2(L)|^2}{2} = \frac{a_2(L)a_2^*(L)}{2} \quad (48)$$

Substituting $z = L$ into Equation (44) gives

$$P_{out_2}=P_{out_3} = \frac{1}{2}\frac{A}{3}\left(-e^{jKL}+e^{-j2KL}\right)\frac{A}{3}\left(-e^{-jKL}+e^{j2KL}\right) = \frac{A^2}{18}\left[1+1-e^{j3KL}-e^{-j3KL}\right] \quad (49)$$

We can replace the complex exponentials with trigonometric functions as follows:

$$P_{out_2}=P_{out_3} = \frac{A^2}{18}\left[2-2\frac{\left(e^{j3KL}+e^{-j3KL}\right)}{2}\right] = \frac{A^2}{9}[1-\cos 3KL]\ . \quad (50)$$

We now have obtained expressions for the output of both a 2×2 coupler and a 3×3 coupler when they are provided with a laser input on only one optical fiber. These are the conditions at the input of the interferometer. Both outputs of the 2×2 coupler will comprise a leg of the interferometer. In the case of the 3×3 coupler, we arbitrarily pick two of the three available outputs of the coupler for the two legs of the interferometer. The third output is not used. To eliminate back reflection into the laser (a cause of instability in the laser and consequent phase noise), we can put the end of the unused fiber into some index matching fluid. Any light emitted from this strand of the output

of the coupler will be transmitted into the fluid, from which it will be more difficult for it to reflect back into the fiber.

We next derive the conditions under which the couplers split the input power evenly over the outputs. To get an even split, we require that the power out of each leg of the interferometer be equal. For a 2×2 coupler, this means that

$$P_{out_1} = P_{out_2}. \tag{51}$$

Substituting Equations (28) and (32) into Equation (51) yields

$$\frac{A^2}{2}\cos^2 KL = \frac{A^2}{2}\sin^2 KL. \tag{52}$$

The common factor $\frac{A^2}{2}$ can be divided into both sides, so

$$\cos^2 KL = \sin^2 KL. \tag{53}$$

This equation is true only when

$$KL = \frac{\pi}{4} + n\frac{\pi}{2} \tag{54}$$

where n is an arbitrary integer. For example, n might be 0, in which case the condition is that $KL = 45°$. Equations (24) and (25) can be rewritten with this choice of n and with $z = L$ as

$$a_{1,out} = \frac{A}{\sqrt{2}} \tag{55}$$

and

$$a_{2,out} = -j\frac{A}{\sqrt{2}} = \frac{A}{\sqrt{2}}e^{-j\frac{\pi}{2}}. \tag{56}$$

Other choices for n will result in different signs, and the net effect will be that $a_{1,out}$ will either lead $a_{2,out}$ by 90° or *vice versa*. This is tantamount to inverting the choice of labels for the two legs of the coupler. When these two signals are shifted in phase by some differential transducer in the arms of the interferometer, this initial static phase difference will cease to be of any consequence at all since it will be augmented by other sources of phase shift. These other sources include a quasi-static phase shift due to temperature, pressure, and other effects, and by a dynamic phase shift due to the physical quantity we really want to measure with our transducer.

Turning now to the question of how to obtain even splitting from a 3×3 coupler, we must have

$$P_{out_1} = P_{out_2} = P_{out_3}. \tag{57}$$

Note from Equation (49) that the power in output legs 2 and 3 is equal since the electric fields in these legs are identical. Setting Equations (47) and (50) equal to one another, we get

$$\frac{A^2}{18}(5 + 4\cos 3KL) = \frac{A^2}{9}(1 - \cos 3KL). \tag{58}$$

Dividing through on both sides by the common factor $A^2/9$ and multiplying both sides by 2 gives

$$5 + 4\cos 3KL = 2(1 - \cos 3KL). \tag{59}$$

Gathering like terms, we get

$$2 - 5 = 4\cos 3KL + 2\cos 3KL \tag{60}$$

$$6\cos 3KL = -3 \tag{61}$$

$$\cos 3KL = -\frac{1}{2} \tag{62}$$

Equation (62) can only be satisfied when

$$3KL = \pi \pm \frac{\pi}{3} + n2\pi \tag{63}$$

$$KL = \frac{\pi}{3} \pm \frac{\pi}{9} + n\frac{2\pi}{3} \tag{64}$$

where n is an arbitrary integer. For example, n might be 0, in which case the conditions are that $KL = 40°$ or $KL = 80°$.

Summarizing what we have to this point, the electric fields from the 2×2 coupler are given by Equations (24) and (25). The corresponding expressions for the power contained in each output are given in Equations (28) and (32). The electric fields from the 3×3 coupler are given by Equations (42) through (44). The corresponding expressions for the power contained in each output are given in Equations (47) and (50).

We shall now consider what happens when the light from the input coupler (either 2×2 or 3×3) travels through the two legs of the interferometer to the output coupler (which is a 3×3 coupler, always). We shall refer to the input to leg k of the output coupler as $a_k(z)$ where z is the distance from the point where leg k enters the output coupler. Note that we have redefined the origin of the z-axis. Earlier, $z=0$ defined the input to the first optical fiber coupler in the interferometer. Now it defines the input to the second coupler, the one which terminates the interferometer.

First let us consider what happens when the laser light is split by a 2×2 input coupler. After travelling along the two legs of the interferometer, the electric fields in

each leg will have undergone some amount of phase shift. Let us suppose that we have configured the interferometer as shown in Figure 4 on page 21.

Output 1 of the input coupler is fed to input 2 of the output coupler. Output 2 of the input coupler is fed to input 3 of the output coupler. Input 1 of the output coupler is left dark. No matter whether the phase in input 2 of the output coupler initially led that in input 3 by 90° or *vice versa*, at the point where the two optical signals enter the 3×3 coupler, we can say that the light in the input to leg 2 of the 3×3 coupler has been shifted through an angle ϕ and that in the input to leg 3 has been shifted through an angle η. Thus, the light waves in these two legs have phasor representations

$$\begin{aligned} a_2(0) &= A\cos(KL)e^{j\phi} \\ &= B_2 e^{j\phi} \end{aligned} \tag{65}$$

and

$$\begin{aligned} a_3(0) &= -jA\sin(KL)e^{j\eta} \\ &= B_3 e^{j\eta} \end{aligned} \tag{66}$$

where

$$B_2 = A\cos(KL) \tag{67}$$

and where

$$B_3 = -jA\sin(KL). \tag{68}$$

Now let us consider the output from a 3×3 input coupler. After travelling along the two legs of the interferometer, the electric fields in each leg will have undergone some amount of phase shift. Let us suppose that we have configured the interferometer as shown in Figure 5 on page 21. Output 2 of the input coupler is fed to input 2 of the output coupler. Output 3 of the input coupler is fed to input 3 of the output coupler. Output 1 of the input coupler is left disconnected and input 1 of the output coupler is left

dark. The light in input 2 of the output coupler initially was in phase with that in input 3, but at the point where the two optical signals enter the 3×3 coupler, their relative phases have been shifted. We can say that the light in the input to leg 2 of the 3×3 coupler has been shifted through an angle ϕ and that in the input to leg 3 has been shifted through an angle η. These shifts are partly due to the quasi-static phase difference induced by temperature, pressure, and other effects and partly due to the dynamic phase shift which we are trying to measure. Multiplying Equation (43) by the phase shift $e^{j\phi}$ gives us the input to the 3×3 coupler. Input 2 of the output coupler thus has phasor representation

$$\begin{aligned} a_2(0) &= \left[-\frac{1}{3}Ae^{jKL} + \frac{1}{3}Ae^{-j2KL}\right]e^{j\phi} \\ &= -\frac{A}{3}\left[e^{jKL} - e^{-j2KL}\right]e^{j\phi}. \end{aligned} \tag{69}$$

We can remove a complex exponential factor thus:

$$\begin{aligned} a_2(0) &= -\frac{A}{3}e^{-j\frac{KL}{2}}\left[e^{j\frac{3KL}{2}} - e^{-j\frac{3KL}{2}}\right]e^{j\phi} \\ &= -j\frac{2A}{3}e^{-j\frac{KL}{2}}\left[\frac{e^{j\frac{3KL}{2}} - e^{-j\frac{3KL}{2}}}{j2}\right]e^{j\phi}. \end{aligned} \tag{70}$$

Finally, we can simplify this by replacing the difference of the two complex exponentials by a trigonometric function.

$$a_2(0) = -j\frac{2A}{3}\sin\left(\frac{3KL}{2}\right)e^{-j\frac{KL}{2}}e^{j\phi} = B_2 e^{j\phi}. \tag{71}$$

In this equation we define

$$B_2 = -j\frac{2A}{3}\sin\left(\frac{3KL}{2}\right)e^{-j\frac{KL}{2}}, \tag{72}$$

which is a different definition than the one we used when a 2×2 coupler served as the input coupler of the interferometer.

In a very similar manner, we can multiply the equation for input number 3 (Equation (44)) by the phase shift which affects it, $e^{j\eta}$. This gives us

$$\begin{aligned} a_3(0) &= \left[-\frac{1}{3}Ae^{jKL} + \frac{1}{3}Ae^{-j2KL}\right]e^{j\eta} \\ &= -j\frac{2A}{3}\sin\left(\frac{3KL}{2}\right)e^{-j\frac{KL}{2}}e^{j\eta} \\ &= B_3 e^{j\eta}. \end{aligned} \tag{73}$$

From this equation, we see that

$$B_3 = B_2. \tag{74}$$

If we compare Equation (65) to Equation (71) and Equation (66) to Equation (73), we see that the form of the inputs to the second optical fiber coupler is the same whether we use a 2×2 coupler or a 3×3 coupler at the input to the interferometer. The only difference is in the definitions of B_2 and B_3 in each case. For the 2×2 coupler at the input, these are defined by Equations (67) and (68); for the 3×3 coupler, they are defined by Equations (72) and (74). In fact, if the input coupler is a 3×3 coupler, then $B_2 = B_3$.

Our next goal is to find the outputs of the 3×3 coupler when two inputs receive light (legs 2 and 3) and one is left dark (leg 1), as illustrated in Figure 4 on page 21 and in Figure 5 on page 21. We will find this output in terms of B_2 and B_3 so that the results may readily be applied to either of two cases: a 2×2 coupler at the input to the interferometer or a 3×3 coupler at the input. Earlier, in discussing what happens at the input coupler, we used L to denote the length of the coupler. We shall continue to use this notation here, but one should not infer that the length of the various couplers in a system must be the same. Later, when we combine equations that include the length of more than one coupler, we shall take care to use symbols that distinguish one length from another.

Because the output coupler is a 3×3 coupler, the electric field phasors are specified by Equations (18) through (20). We would like to find the constants c_k and d in these equations, for then we could evaluate the equations at $z=L$, where the light leaves the terminating 3×3 coupler. Evaluating each of these equations at the point $z=0$, where signals are injected into the coupler and are known, we get

$$a_1(0) = c_1 + d = 0, \tag{75}$$

$$a_2(0) = c_2 + d = B_2 e^{j\phi}. \tag{76}$$

and

$$a_3(0) = c_3 + d = B_3 e^{j\eta}. \tag{77}$$

Summing Equations (75) through (77) gives

$$\begin{aligned} \sum_{k=1}^{3} a_k(0) &= 3d + \sum_{k=1}^{3} c_k \\ &= B_2 e^{j\phi} + B_3 e^{j\eta}. \end{aligned} \tag{78}$$

Making use of Equation (21),

$$\sum_{k=1}^{3} a_k(0) = 3d = B_2 e^{j\phi} + B_3 e^{j\eta}. \tag{79}$$

So

$$d = \frac{1}{3}\left[B_2 e^{j\phi} + B_3 e^{j\eta}\right]. \tag{80}$$

Using Equation (80) in Equations (75) through (77) lets us calculate the constants c_k.

$$c_1 + d = c_1 - \frac{1}{3}\left[B_2 e^{j\phi} + B_3 e^{j\eta}\right] = 0. \tag{81}$$

So

$$c_1 = -\frac{1}{3}\left[B_2 e^{j\phi} + B_3 e^{j\eta}\right]. \tag{82}$$

Also

$$c_2 + d = B_2 e^{j\eta\phi} \tag{83}$$

so

$$\begin{aligned} c_2 &= B_2 e^{j\phi} - \frac{1}{3}\left[B_2 e^{j\phi} + B_3 e^{j\eta}\right] \\ &= \frac{1}{3}\left[2B_2 e^{j\phi} - B_3 e^{j\eta}\right]. \end{aligned} \tag{84}$$

Finally,

$$c_3 + d = B_3 e^{j\eta}. \tag{85}$$

So

$$
\begin{aligned}
c_3 &= B_3 e^{j\eta} - \frac{1}{3}\left[B_2 e^{j\phi} + B_3 e^{j\eta}\right] \\
&= -\frac{1}{3}\left[B_2 e^{j\phi} - 2B_3 e^{j\eta}\right].
\end{aligned}
\tag{86}
$$

We now have obtained expressions for all the constants in Equations (18) through (20). Replacing the constants by these expressions gives us the ability to compute the output power at the end of the coupler, where $z=L$.

$$
a_1(L) = -\frac{1}{3}\left[B_2 e^{j\phi} - B_3 e^{j\eta}\right] e^{jKL} + \frac{1}{3}\left[B_2 e^{j\phi} + B_3 e^{j\eta}\right] e^{-j2KL} \tag{87}
$$

This can be rearranged to give

$$
\begin{aligned}
a_1(L) &= -\frac{B_2}{3} e^{j\phi}\left[e^{-j\frac{KL}{2}}\right]\left[e^{j\frac{3KL}{2}} - e^{-j\frac{3KL}{2}}\right] - \frac{B_3}{3} e^{j\eta} e^{-j\frac{KL}{2}}\left[e^{j\frac{3KL}{2}} - e^{-j\frac{3KL}{2}}\right] \\
&= -j\frac{2}{3}\left[B_2 e^{j\phi} + B_3 e^{j\eta}\right] \sin\left(\frac{3KL}{2}\right) e^{-j\frac{KL}{2}}
\end{aligned}
\tag{88}
$$

The complex conjugate of this is

$$
a_1^*(L) = j\frac{2}{3}\left[B_2^* e^{-j\phi} + B_3^* e^{-j\eta}\right] \sin\left(\frac{3KL}{2}\right) e^{j\frac{KL}{2}}. \tag{89}
$$

We get the power in strand 1 at the output point $z=L$ by multiplying the complex conjugates and dividing by 2.

$$
\begin{aligned}
\frac{|a_1(L)|^2}{2} &= \frac{1}{2} a_1(L) a_1^*(L) \\
&= \frac{1}{2}\left(\frac{2}{3}\right)^2 \left[B_2 B_2^* + B_3 B_3^* + B_2 B_3^* e^{j(\phi-\eta)} + B_2^* B_3 e^{-j(\phi-\eta)}\right] \sin^2\left(\frac{3KL}{2}\right).
\end{aligned}
\tag{90}
$$

The same procedure applied to output 2 gives

$$
\begin{aligned}
a_2(L) &= c_2 e^{jKL} + d e^{-j2KL} \\
&= \frac{1}{3}\left[2B_2 e^{j\phi} - B_3 e^{j\eta}\right] e^{jKL} + \frac{1}{3}\left[B_2 e^{j\phi} + B_3 e^{j\eta}\right] e^{-j2KL}.
\end{aligned}
\tag{91}
$$

This can be rearranged a little to give a marginally improved form.

$$
a_2(L) = \frac{B_2}{3} e^{j\phi}\left[2e^{jKL} + e^{-j2KL}\right] - \frac{B_3}{3} e^{j\eta}\left[e^{jKL} - e^{-j2KL}\right] \tag{92}
$$

The complex conjugate of this is

$$
a_2^*(L) = \frac{B_2^*}{3} e^{-j\phi}\left[2e^{-jKL} - e^{j2KL}\right] - \frac{B_3^*}{3} e^{-j\eta}\left[e^{-jKL} - e^{j2KL}\right]. \tag{93}
$$

The power in this output is

$$
\begin{aligned}
\frac{|a_2(L)|^2}{2} &= \frac{1}{2} a_2(L) a_2^*(L) \\
&= \frac{1}{2}\left\{\left(\frac{1}{3}\right)^2 B_2 B_2^*\left[4+1+2e^{j3KL}+2e^{-j3KL}\right]\right. \\
&\quad - \left(\frac{1}{3}\right)^2 B_3 B_3^*\left[1+1-e^{j3KL}-e^{-j3KL}\right] \\
&\quad - \left(\frac{1}{3}\right)^2 B_2 B_3^* e^{j(\phi-\eta)}\left[2-1-2e^{j3KL}+e^{-j3KL}\right] \\
&\quad \left. - \left(\frac{1}{3}\right)^2 B_2^* B_3 e^{-j(\phi-\eta)}\left[2-1+e^{j3KL}-2e^{-j3KL}\right]\right\}.
\end{aligned}
\tag{94}
$$

We can simplify this expression by replacing certain pairs of complex exponentials with trigonometric equivalents.

$$\frac{|a_2(L)|^2}{2} = \frac{1}{18}\{B_2B_2^*[5+4\cos(3KL)] + 2B_3B_3^*[1-\cos(3KL)] - B_2B_3^*e^{j(\phi-\eta)}[1-2e^{j3KL}+e^{-j3KL}] - B_2^*B_3e^{-j(\phi-\eta)}[1+e^{j3KL}-2e^{-j3KL}]\}. \quad (95)$$

Now we turn to the last of the three outputs, number 3.

$$a_3(L) = c_3e^{jKL} + de^{-j2KL} = -\frac{1}{3}[B_2e^{j\phi} - 2B_3e^{j\eta}]e^{jKL} + \frac{1}{3}[B_2e^{j\phi} + B_3e^{j\eta}]e^{-j2KL}. \quad (96)$$

We can rewrite this as

$$a_3(L) = -\frac{B_2}{3}e^{j\phi}[e^{jKL} - e^{-j2KL}] + \frac{B_3}{3}e^{j\eta}[2e^{jKL} + e^{-j2KL}]. \quad (97)$$

Comparing this with Equation (92), we see that they are identical except that B_2 and B_3 are interchanged, and ϕ and η also are interchanged. This permits us to write the power in output leg 3 by performing the same interchange on Equation (95).

$$\frac{|a_3(L)|^2}{2} = \frac{1}{18}\{2B_2B_2^*[1-\cos(3KL)] + B_3B_3^*[5-4\cos(3KL)] - B_2B_3^*e^{j(\phi-\eta)}[1+e^{j3KL}-2e^{-j3KL}] - B_2^*B_3e^{-j(\phi-\eta)}[1-2e^{j3KL}+e^{-j3KL}]\}. \quad (98)$$

Equations (90), (95), and (98) are general solutions to the power in the three outputs of an optical fiber interferometer with one dark input. Knowing the values of B_2 and B_3 as well as the product of K and L permits one to find specific solutions as functions of ϕ and η.

As mentioned before, once we start to combine results of the analysis of more than one coupler, we must be careful to distinguish between the coupling coefficients K and

the coupling interaction lengths L of each. Our next task is to perform this combination for the two cases where the output 3×3 coupler gets signals from an interferometer with either a 2×2 coupler or a 3×3 coupler at its input. We shall designate as K_i and L_i the parameters which apply to the input coupler, and we shall designate as K_o and L_o the parameters which apply to the output coupler. We shall denote by z_i the position in the input coupler, and as z_o the position in the output coupler.

For the 2×2 coupler at the input to the interferometer, we can therefore rewrite Equations (65) and (66) as

$$B_2 e^{j\phi} = a_2(z_o)\big|_{z_o=0} = A\cos(K_i L_i)e^{j\phi} \tag{99}$$

and

$$B_3 e^{j\eta} = a_3(z_o)\big|_{z_o=0} = -jA\sin(K_i L_i)e^{j\eta}. \tag{100}$$

We now compute the various products of B_k which appear in Equation (90), (95), and (98). By using the trigonometric identity

$$\cos(2\theta) = 2\cos^2(\theta) - 1. \tag{101}$$

we get

$$\begin{aligned} B_2 B_2^* &= A^2\cos^2(K_i L_i) \\ &= \frac{A^2}{2}[\cos(2K_i L_i) + 1]. \end{aligned} \tag{102}$$

By using the trigonometric identity

$$\cos(2\theta) = 1 - 2\sin^2(\theta). \tag{103}$$

we get

$$B_3 B_3^* = A^2 \sin^2(K_t L_t) = \frac{A^2}{2}[1-\cos(2K_t L_t)]. \tag{104}$$

By using the trigonometric identity

$$\sin(2\theta) = 2\sin(\theta)\cos(\theta). \tag{105}$$

we get

$$B_2 B_3^* = jA^2 \sin(K_t L_t)\cos(K_t L_t) = j\frac{A^2}{2}\sin(2K_t L_t). \tag{106}$$

Finally, we can use the same trigonometric identity to get

$$B_2^* B_3 = jA^2 \sin(K_t L_t)\cos(K_t L_t) = -j\frac{A^2}{2}\sin(2K_t L_t). \tag{107}$$

Substituting them into Equation (90) gives

$$\frac{|a_1(L_o)|^2}{2} = \frac{1}{2}\left(\frac{2}{3}\right)^2 \left\{ \begin{array}{l} \frac{A^2}{2}[\cos(2K_t L_t)-1] \\ +\frac{A^2}{2}[1-\cos(2K_t L_t)] \\ +j\frac{A^2}{2}\sin(2K_t L_t)e^{j(\phi-\eta)} \\ -j\frac{A^2}{2}\sin(2K_t L_t)e^{-j(\phi-\eta)} \end{array} \right\} \sin^2\left(\frac{3K_o L_o}{2}\right). \tag{108}$$

In this expression, the braces do not denote a matrix of values. They are used in order to keep the lengthy summation within from sprawling across the page. We shall use braces in this manner whenever it lends clarity to the expressions. We can rewrite the expression as

$$\frac{|a_1(L_o)|^2}{2} = \frac{2}{9}A^2\left\{1 - \sin(2K_iL_i)\left[\frac{e^{j(\phi-\eta)}-e^{-j(\phi-\eta)}}{j2}\right]\right\}\sin^2\left(\frac{3K_oL_o}{2}\right) \tag{109}$$

$$= \frac{A^2}{9}[1-\sin(2K_iL_i)\sin(\phi-\eta)][1-\cos(3K_oL_o)].$$

For the power in the second output leg, we get

$$\frac{|a_2(L_o)|^2}{2} = \frac{A^2}{18}\left\{\begin{array}{l} \frac{1}{2}[\cos(2K_iL_i)+1][5+4\cos(3K_oL_o)] \\ + \frac{1}{2}2[1-\cos(2K_iL_i)][1-\cos(3K_oL_o)] \\ - \frac{j}{2}\sin(2K_iL_i)e^{j(\phi-\eta)}\left[1-2e^{j3K_oL_o}+e^{-j3K_oL_o}\right] \\ + \frac{j}{2}\sin(2K_iL_i)e^{-j(\phi-\eta)}\left[1+e^{j3K_oL_o}-2e^{-j3K_oL_o}\right] \end{array}\right\}. \tag{110}$$

We can remove the factor of 1/2 from within the admittedly forbidding-looking expression within the brackets, multiply out the terms within the brackets, and get ready to replace the complex exponential functions with trigonometric functions.

$$\frac{|a_2(L_o)|^2}{2} = \frac{A^2}{36}\left\{\begin{array}{l} 5\cos(2K_iL_i)+4\cos(3K_oL_o)+5 \\ +4\cos(2K_iL_i)\cos(3K_oL_o)+2-2\cos(2K_iL_i) \\ -2\cos(3K_oL_o)+2\cos(2K_iL_i)\cos(3K_oL_o) \\ +2\sin(2K_iL_i)\left[\frac{e^{j(\phi-\eta)}-e^{-j(\phi-\eta)}}{2j}\right] \\ -4\sin(2K_iL_i)\left[\frac{e^{j(\phi-\eta+3K_oL_o)}-e^{-j(\phi-\eta+3K_oL_o)}}{2j}\right] \\ +2\sin(2K_iL_i)\left[\frac{e^{j(\phi-\eta-3K_oL_o)}-e^{-j(\phi-\eta-3K_oL_o)}}{2j}\right] \end{array}\right\}. \tag{111}$$

Summing like terms within the brackets and factoring some terms gives a simpler, though still quite formidable, form

$$\frac{|a_2(L_o)|^2}{2} = \frac{A^2}{36}\left\{\begin{array}{l} 7+3\cos(2K_iL_i)+2\cos(3K_oL_o)+6\cos(2K_iL_i)\cos(3K_oL_o) \\ +2\sin(2K_iL_i)[\sin(\phi-\eta)-2\sin(\phi-\eta+3K_oL_o)+\sin(\phi-\eta-3K_oL_o)] \end{array}\right\}. \tag{112}$$

This can be further rewritten as

$$\frac{|a_2(L_o)|^2}{2} = \frac{A^2}{36}\left\{\begin{array}{l} 7+3\cos(2K_iL_i)+2\cos(3K_oL_o)+6\cos(2K_iL_i)\cos(3K_oL_o) \\ +2\sin(2K_iL_i)\left[\begin{array}{l}\sin(\phi-\eta) \\ -2\sin(\phi-\eta)\cos(3K_oL_o) \\ -2\cos(\phi-\eta)\sin(3K_oL_o) \\ +\sin(\phi-\eta)\cos(3K_oL_o)-\cos(\phi-\eta) \\ -\cos(\phi-\eta)\sin(3K_oL_o)\end{array}\right]\end{array}\right\} \tag{113}$$

$$= \frac{A^2}{36}\left\{\begin{array}{l} 7+3\cos(2K_iL_i)+2\cos(3K_oL_o)+6\cos(2K_iL_i)\cos(3K_oL_o) \\ +2\sin(2K_iL_i)\left[\begin{array}{l}\sin(\phi-\eta) \\ -\sin(\phi-\eta)\cos(3K_oL_o)-3\cos(\phi-\eta)\sin(3K_oL_o)\end{array}\right]\end{array}\right\}.$$

Now finding the power in the third output leg is just as tedious as it was to find the power in the second output leg. We start with Equation (98), using the products found in Equations (102) through (107).

$$\frac{|a_3(L)|^2}{2} = \frac{A^2}{36}\left\{\begin{array}{l} 2[\cos(2K_iL_i)+1][1-\cos(3K_oL_o)] \\ +[1-\cos(2K_iL_i)][5+4\cos(3K_oL_o)] \\ -j\sin(2K_iL_i)e^{j(\phi-\eta)}\left[1+e^{j3K_oL_o}-2e^{-j3K_oL_o}\right] \\ +j\sin(2K_iL_i)e^{-j(\phi-\eta)}\left[1-2e^{j3K_oL_o}+e^{-j3K_oL_o}\right]\end{array}\right\}. \tag{114}$$

Multiplying this out and replacing the complex exponentials with equivalent trigonometric functions gives

$$\frac{|a_3(L)|^2}{2} = \frac{A^2}{36}\left\{\begin{array}{l} 2\cos(2K_iL_i)-2-2\cos(3K_oL_o)-2\cos(2K_iL_i)\cos(3K_oL_o) \\ +5-5\cos(2K_iL_i)+4\cos(3K_oL_o)-4\cos(2K_iL_i)\cos(3K_oL_o) \\ +\sin(2K_iL_i)\left[2\sin(\phi-\eta)+2\sin(\phi-\eta-3K_oL_o)-4\sin(\phi-\eta-3K_oL_o)\right]\end{array}\right\}. \tag{115}$$

This can be further simplified to

$$\frac{|a_3(L)|^2}{2} = \frac{A^2}{36}\left\{\begin{array}{l} 7-3\cos(2K_iL_i)+2\cos(3K_oL_o)-6\cos(2K_iL_i)\cos(3K_oL_o) \\ +2\sin(2K_iL_i)\left[\begin{array}{l}\sin(\phi-\eta) \\ \quad+\sin(\phi-\eta)\cos(3K_oL_o) \\ \quad+\cos(\phi-\eta)\sin(3K_oL_o) \\ \quad-2\sin(\phi-\eta)\cos(3K_oL_o) \\ \quad+2\cos(\phi-\eta)\sin(3K_oL_o)\end{array}\right] \end{array}\right\}. \tag{116}$$

Finally, we get the equation

$$\frac{|a_3(L)|^2}{2} = \frac{A^2}{36}\left\{\begin{array}{l} 7-3\cos(2K_iL_i)+2\cos(3K_oL_o)-6\cos(2K_iL_i)\cos(3K_oL_o) \\ +2\sin(2K_iL_i)\left[\begin{array}{l}\sin(\phi-\eta) \\ \quad-\sin(\phi-\eta)\cos(3K_oL_o) \\ \quad+3\cos(\phi-\eta)\sin(3K_oL_o)\end{array}\right] \end{array}\right\}. \tag{117}$$

At last we are in the position we have been struggling toward so patiently. We have three expressions for the power from each of the three output legs of the 3×3 coupler at the output of the interferometer. These very complicated expressions are given in Equations (109), (112), and (117). We can apply the conditions derived earlier for couplers which provide even splitting of the power to find several of the sines and cosines in these expressions. First we use Equation (54).

$$\begin{aligned}\cos(2K_iL_i) &= \cos\left[2\left(\frac{\pi}{4}+n\frac{\pi}{2}\right)\right] \\ &= \cos\left[\frac{\pi}{2}+n\pi\right] \\ &=0.\end{aligned} \tag{118}$$

$$\begin{aligned}\sin(2K_iL_i) &= \sin\left[2\left(\frac{\pi}{4} + n\frac{\pi}{2}\right)\right] \\ &= \sin\left[\frac{\pi}{2} + n\pi\right] \\ &= \pm 1.\end{aligned} \tag{119}$$

From Equation (62),

$$\cos(3K_oL_o) = -\frac{1}{2}. \tag{120}$$

From Equation (64),

$$\begin{aligned}\sin(3K_oL_o) &= \sin\left[3\left(\frac{\pi}{3} \pm \frac{\pi}{9} + n\frac{2\pi}{3}\right)\right] \\ &= \sin\left[\pi \pm \frac{\pi}{3} + n2\pi\right] \\ &= \mp\frac{\sqrt{3}}{2}.\end{aligned} \tag{121}$$

If we did not use couplers with evenly split power, or if we used couplers with imperfections that prevented even splitting from occurring, then these four trigonometric quantities would differ, but they still would be fixed numbers and so could be used to find equations describing the output of the interferometer. A useful piece of research would be to investigate the effects of uneven splitting on the equations developed in this chapter.

In order to keep our notation consistent with that of Crooker [Ref. 10, p. 30], we shall define two new angles ξ_a and ξ_b. We shall define

$$\xi_a = \phi - \eta - \frac{\pi}{2} \tag{122}$$

and

$$\xi_b = \phi - \eta - \frac{\pi}{2}. \tag{123}$$

These two definitions amount to two different ways of specifying the origin of the phase, the point where the phase is zero. The reason for adopting these definitions should become clear presently. Substituting Equations (119) and (120) into Equation (109) for the case $\sin(2K_iL_i) = +1$ gives

$$\begin{aligned}
\frac{|a_1(L)|^2}{2} &= \frac{A^2}{9}[1-\sin(\phi-\eta)]\left[1-\left(-\frac{1}{2}\right)\right] \\
&= \frac{A^2}{6}[1-\sin(\phi-\eta)] \\
&= \frac{A^2}{6}\left[1-\sin\left(\xi_a-\frac{\pi}{2}\right)\right] \\
&= \frac{A^2}{6}[1+\cos(\xi_a)].
\end{aligned} \tag{124}$$

If $\sin(2K_iL_i) = -1$, then

$$\begin{aligned}
\frac{|a_1(L)|^2}{2} &= \frac{A^2}{6}[1 + \sin(\phi-\eta)] \\
&= \frac{A^2}{6}\left[1 + \sin\left(\xi_b+\frac{\pi}{2}\right)\right] \\
&= \frac{A^2}{6}[1 + \cos(\xi_b)].
\end{aligned} \tag{125}$$

The definitions of ξ_a and ξ_b were rigged to make sure that the same equation results no matter what the sign of $\sin(2K_iL_i)$. This causes Equations (124) and (125) to match Equation (2.8a) in Crooker [Ref. 10, p. 30] except that where she had a factor of 1/9, we have a factor of 1/6. This represents the 1.76 dB advantage that results from using a 2×2 coupler at the input to the interferometer, rather than a 3×3 coupler.

We can go through the same process for outputs 2 and 3, also. In addition to the two possible signs of $\cos(2K_iL_i)$ that can occur, we must also account for the two possible signs of $\sin(3K_oL_o)$ which can occur, since this expression appears in Equations (112) and (117). First we consider the case where $\sin(2K_iL_i) = +1$ and $\sin(3K_oL_o) = \frac{\sqrt{3}}{2}$. For the power from output 2, we substitute Equations (118) through (121) into Equation (112).

$$\begin{aligned}\frac{|a_2(L)|^2}{2} &= \frac{A^2}{36}\{6 + 2\sin(\phi-\eta) + \sin(\phi-\eta) - 3\sqrt{3}\cos(\phi-\eta)\} \\ &= \frac{A^2}{6}\left\{1 + \frac{1}{2}\sin(\phi-\eta) - \frac{\sqrt{3}}{2}\cos(\phi-\eta)\right\} \\ &= \frac{A^2}{6}\left\{1 - \frac{1}{2}\cos(\xi_a) - \frac{\sqrt{3}}{2}\sin(\xi_a)\right\} \\ &= \frac{A^2}{6}\left\{1 + \cos\left(\xi_a + \frac{2}{3}\pi\right)\right\}.\end{aligned} \tag{126}$$

For the power from output 3, we substitute (118) through (121) into Equation (117).

$$\begin{aligned}\frac{|a_3(L)|^2}{2} &= \frac{A^2}{36}\{7 - 1 + 3\sin(\phi-\eta) + 3\sqrt{3}\cos(\phi-\eta)\} \\ &= \frac{A^2}{6}\left\{1 + \frac{1}{2}\sin(\phi-\eta) - \frac{\sqrt{3}}{2}\cos(\phi-\eta)\right\} \\ &= \frac{A^2}{6}\left\{1 - \frac{1}{2}\cos(\xi_a) + \frac{\sqrt{3}}{2}\sin(\xi_a)\right\} \\ &= \frac{A^2}{6}\left\{1 + \cos\left(\xi_a - \frac{2}{3}\pi\right)\right\}.\end{aligned} \tag{127}$$

Next we consider the change to Equations (126) and (127) when $\sin(3K_oL_o) = -\frac{\sqrt{3}}{2}$.

$$\frac{|a_2(L)|^2}{2} = \frac{A^2}{6}\left\{1 - \frac{1}{2}\cos(\xi_a) + \frac{\sqrt{3}}{2}\sin(\xi_a)\right\}$$
$$= \frac{A^2}{6}\left\{1 + \cos\left(\xi_a - \frac{2}{3}\pi\right)\right\}. \quad (128)$$

$$\frac{|a_3(L)|^2}{2} = \frac{A^2}{6}\left\{1 - \frac{1}{2}\cos(\xi_a) - \frac{\sqrt{3}}{2}\sin(\xi_a)\right\}$$
$$= \frac{A^2}{6}\left\{1 + \cos\left(\xi_a + \frac{2}{3}\pi\right)\right\}. \quad (129)$$

By comparing these two equations with Equations (126) and (127), we see that the effect of this change is equivalent to interchanging legs 2 and 3 in its effect on the outputs.

Next we consider the case where $\sin(2K_iL_i) = -1$ and $\sin(3K_oL_o) = +\frac{\sqrt{3}}{2}$. For the power from output 2, we substitute Equations (118) through (121) into Equation (112).

$$\frac{|a_2(L)|^2}{2} = \frac{A^2}{36}\{6 - 2\sin(\phi-\eta) - \sin(\phi-\eta) - 3\sqrt{3}\cos(\phi-\eta)\}$$
$$= \frac{A^2}{6}\left\{1 - \frac{1}{2}\sin(\phi-\eta) - \frac{\sqrt{3}}{2}\cos(\phi-\eta)\right\}$$
$$= \frac{A^2}{6}\left\{1 - \frac{1}{2}\cos(\xi_b) + \frac{\sqrt{3}}{2}\sin(\xi_b)\right\} \quad (130)$$
$$= \frac{A^2}{6}\left\{1 + \cos\left(\xi_b - \frac{2}{3}\pi\right)\right\}.$$

For the power from output 3, we substitute (118) through (121) into Equation (117).

$$\begin{aligned}
\frac{|a_3(L)|^2}{2} &= \frac{A^2}{36}\{7 - 1 - 3\sin(\phi-\eta) + 3\sqrt{3}\cos(\phi-\eta)\} \\
&= \frac{A^2}{6}\left\{1 - \frac{1}{2}\sin(\phi-\eta) + \frac{\sqrt{3}}{2}\cos(\phi-\eta)\right\} \\
&= \frac{A^2}{6}\left\{1 - \frac{1}{2}\cos(\xi_b) - \frac{\sqrt{3}}{2}\sin(\xi_b)\right\} \\
&= \frac{A^2}{6}\left\{1 + \cos\left(\xi_b + \frac{2}{3}\pi\right)\right\}.
\end{aligned} \tag{131}$$

By comparing these two equations with Equations (126) and (127), we see that the effect of this change is equivalent to interchanging legs 2 and 3 in its effect on the outputs. However, we had to redefine the phase origin (the point where phase is deemed to be zero). This should not disturb us, since the choice of origin is entirely arbitrary to begin with. A signal exhibiting periodic characteristics will take on every possible value of phase over time, so redefining the phase origin is akin to waiting a while before looking at a signal, and it does not affect the appearance of any of the signals.

By this time, it should be clear that the final condition, namely

$$\sin(2K_iL_i) = -1 \qquad \text{and} \qquad \sin(3K_oL_o) = -\frac{\sqrt{3}}{2} \tag{132}$$

will not change matters, but for completeness, we provide the equations anyway.

$$\begin{aligned}
\frac{|a_2(L)|^2}{2} &= \frac{A^2}{6}\left\{1 - \frac{1}{2}\cos(\xi_b) - \frac{\sqrt{3}}{2}\sin(\xi_b)\right\} \\
&= \frac{A^2}{6}\left\{1 + \cos\left(\xi_b + \frac{2}{3}\pi\right)\right\}.
\end{aligned} \tag{133}$$

$$\frac{|a_3(L)|^2}{2} = \frac{A^2}{6}\left\{1 - \frac{1}{2}\cos(\xi_b) + \frac{\sqrt{3}}{2}\sin(\xi_b)\right\} = \frac{A^2}{6}\left\{1 + \cos\left(\xi_b - \frac{2}{3}\pi\right)\right\}. \quad (134)$$

This exhaustive consideration of all possible conditions which meet the criteria for couplers with even split ratios shows that a reasonable model for the three outputs of the Mach-Zender optical fiber interferometer constructed with a 2×2 coupler at the input and a 3×3 coupler at the output can be given by the following equation. In this equation, the index k is an index to one of the three output legs. It can take on the values 1, 2, or 3.

$$\frac{|a_k(L)|^2}{2} = \frac{A^2}{6}\left\{1 + \cos\left[\xi - (k-1)\frac{2}{3}\pi\right]\right\}. \quad (135)$$

This equation represents the culmination of this very lengthy chapter of tedious mathematics. Even so, this model is not quite right. That is, it does not describe the actual behavior of a real optical fiber interferometric sensor precisely. Wherein lie the differences?

Firstly, this equation is based on the presumption that there are no losses in the couplers or fibers. Since there are losses in a real interferometer, the leading coefficient $\frac{A^2}{2}$ should be replaced by whatever amount of power does arrive at the output. We shall call this amount D. As stated in the Table of Symbols at the beginning of this dissertation, the units of D will vary, depending on the context. When we are speaking of optical power, D will be measured in watts. When the received optical power has been converted to a current by its action on a photodiode, D will be measured in amperes. When the current has been converted to a voltage through the action of a transimpedance amplifier, then D will be measured in volts. However, the *form* of the modified model we are developing here will not be altered.

A second reason for the inaccuracy of the model considered here is our failure to include a consideration of the polarization of the recombined light in our equations. We have assumed that the two combining beams can be fully parallel or fully anti-parallel, which implies that they both have the same amplitudes. (If the polarizations are anti-parallel, an additional phase shift of π radians occurs.) In practice, due to different degrees of attenuation in each leg of the interferometer, imperfections in the couplers, and rotation of the polarization of each beam, this will not be the case. The result of this is that the intensity of the interferometric output will not wander through the full range from 0 to D, but from somewhat above 0 to somewhat less than D. Put another way, the coefficient of the cosine in the above equation needs to be reduced from 1 to some lesser value. We shall define a new quantity, E, measured in the same units as D. This new quantity is defined implicitly by the following modified model.

$$\frac{|a_k(L)|^2}{2} = D\left\{1 + \frac{E}{D}\cos\left[\xi - (k-1)\frac{2}{3}\pi\right]\right\}. \tag{136}$$

We call the fraction E/D the *fringe depth*.[7] Multiplying this out gives

$$\frac{|a_k(L)|^2}{2} = D + E\cos\left[\xi - (k-1)\frac{2}{3}\pi\right]. \tag{137}$$

The three signals represented by this equation vary around a central value, D, by $\pm E$, at most. Whether or not they actually reach the two extrema at $D+E$ and $D-E$ depends on the signal ξ. If it has a very small amplitude, then the cosine will not vary much and so the extreme values will not, in general, be achieved. On the other hand, if ξ has a very large amplitude, more than $\pm\pi$ radians, in particular, then the signals are guaranteed to reach both extrema.

It is worth discussing the units of ξ at this point. As we tacitly assumed in the previous paragraph, ξ is measured in radians. It represents the amount of optical phase shift due to strain on the glass in the optical fiber interferometer. So the signal of interest, no matter what its natural units, produces differential stretching of the two legs

---

[7] Note that other authors may apply this terminology to different quantities.

of the interferometer. The number of wavelengths of differential stretching corresponds to the number of multiples of 2π radians of phase shift induced in the interferometric output.

In the equation as written, there are only two contributors to the phase shift. One is the signal of interest. The other is the choice of an output leg. However, as the earlier lengthy discussion of shifting the phase origin made plain, we are free to choose any origin we like, and only the difference in phase between the output of one leg and another is of importance.

There are other contributors to the phase. For example, changes in temperature and pressure may stretch the glass or permit it to relax, even if they are not the phenomena we want our sensor to detect. These additional factors usually vary slowly with time, although this is not necessarily so. If we lump them together into a single term $\phi(t)$, then we can write the equation which describes our complete model.

$$\frac{|\, a_k(L)\,|^2}{2} = D + E\cos\left[\xi(t) + \phi(t) - (k-1)\frac{2}{3}\pi\right]. \qquad (138)$$

This use of the symbol ϕ is not be confused with its earlier use to describe the shift in phase of the light in one of the two legs of the interferometer (the other was η).

One final observation about this model is in order. It is assumed that D and E are equal for any choice of output leg (1, 2, or 3). In practice, each output leg has its own value of D and E. Having noted this fact, we shall continue to use the approximation that they all are equal because of the simplicity this assumption entails, and the fact that it is a fairly good approximation.

C. SUMMARY

In this chapter we have applied Sheem's methods of analysis to the particular case where an optical fiber interferometric sensor has either a 2×2 coupler or a 3×3 coupler at the input and a 3×3 coupler at the output. We have derived a mathematical model which will allow us to design demodulators to recover the signal of interest. We have left numerous quantities in the equations as parameters so that further research might more readily ascertain their importance. For example, the degree to which the interferometric

outputs depart from a 120° phase difference from each other as the product of coupling coefficients and interaction length varies from the ideal. In the next chapter, we describe the construction of an optical fiber interferometric sensor suitable for providing inputs to experimental demodulators in the laboratory.

IV. CONSTRUCTION OF A 3×3 OPTICAL FIBER INTERFEROMETRIC SENSOR

In this chapter, we discuss the construction of an optical fiber interferometric sensor which we built in the laboratory for the purpose of providing signals with which to operate the three demodulators we investigated in our research.

Up to the time when we built this optical interferometer, we had been constrained to using simulations of interferometric outputs. One simulation was provided by a set of three Analog Interferometric Simulators. These were limited in the amount of peak phase shift they could deliver to around 2 rad, although the Analog Devices AD639 on which they depend permit ±500°. Exceeding about 2 rad led to increasingly apparent distortion in the waveforms delivered by the simulators. Since the newest class of interferometric sensors can easily generate optical phase shifts far in excess of this small value, these simulators were only suitable for the most rudimentary work.

A second simulation was provided by a Digital Quadrature Phase Shift Modulation Simulator. This simulation could easily achieve phase shifts of several hundreds of radians. Unfortunately, it was only able to produce square waves at its output. Thus the outputs were not very good replicas of the output of an optical interferometer, which can generate a continuous range of output amplitudes, not just two of them.[8]

A. APPLICABILITY OF THIS SENSOR

One of the chief purposes of building optical fiber interferometric sensors is to avoid the need to have electrical signals in inaccessible locations. Eliminating the need for electrical signals permits reductions in weight, cost, and susceptibility to electromagnetic interference (EMI). The sensor we have built for experimental purposes is a voltage sensor. Clearly there is no *avoidance* of the presence of electrical signals in a sensor which *detects* electrical signals! However, the benefit of great sensitivity is still

[8] For the Fringe Rate Demodulator, square waves were no limitation at all, since this demodulator makes interferometric outputs square before it processes them anyway.

present in our sensor: very small changes in the size of the piezoelectric cylinders create a noticeable optical phase shift in the sensor's interferometric output, so quite small voltages can be detected. When we discuss the performance of the Symmetric Analog Demodulator, for example, we shall see that it can detect voltages of 2.2 μV in a 1 Hz bandwidth and has a dynamic range of 115 dB (in the same bandwidth) at a frequency of 600 Hz. The most attractive feature of our sensor is its ease of operation. Voltage sources are easily controlled, so we can generate optical phase shift of controllable amounts with this sensor. It is an excellent tool for the kind of research we conducted into demodulation.

B. DETAILS OF CONSTRUCTION

Our interferometer was physically laid out as shown in the diagram in Figure 9. A single voltage signal is applied in opposite polarities to each of two Channel 5500 piezoelectric cylinders. This causes one cylinder to expand while the other contracts, and *vice versa*. The fibers are wrapped around each cylinder with constant tension. There are 9.099 m of 125 μm single-mode optical fiber in each leg, as measured from the 2×2 coupler's output to the 3×3 coupler's input. The actual length is not critical, so long as the two lengths are within a few centimeters of being the same. As one cylinder expands, it applies a strain to its fiber. At the same time, the other cylinder is contracting and its fiber is relaxing. The first fiber experiences an increase in its optical path length; the other fiber experiences a reduction in the optical path length.

Figure 10 shows the details of how the cylinder was clamped onto the mounting brackets in such a way that it could still respond to the applied voltage without undue mechanical interference from the mounting hardware.

To apply a constant tension to the fibers wrapped on each cylinder, we used the apparatus shown in Figure 11.[9] For our purposes, the amount of tension was not significant. Our desire was simply to ensure that the tension was a constant so that uniform expansion and contraction of the cylinders would produce uniform increases and

---

[9] The author would like to thank Dr. David Gardner for showing him this technique of ensuring constant tension in the fibers.

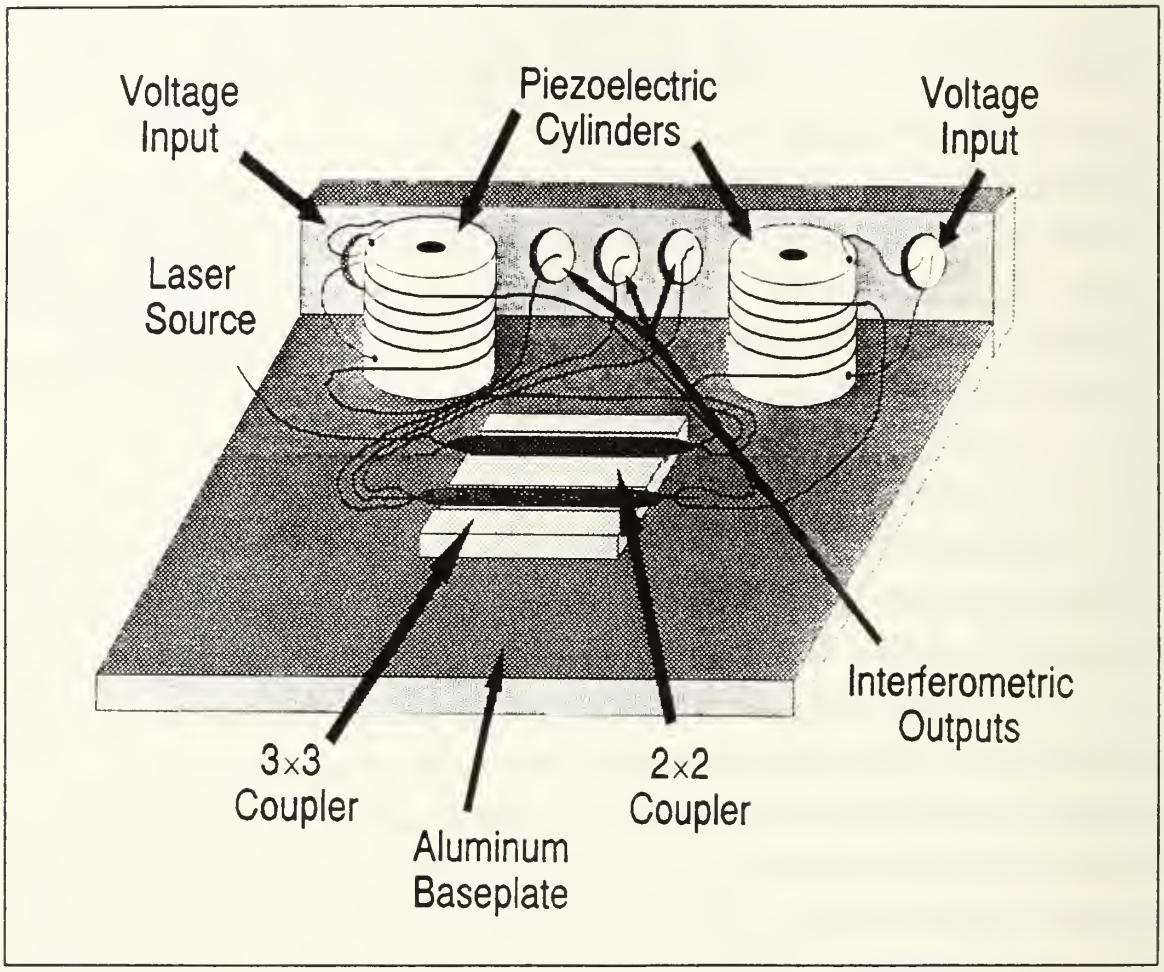

Figure 9 Physical layout of an optical fiber interferometric sensor of voltages.

decreases in the strain on the optical fiber wrapped around them.

The 2×2 optical fiber coupler we used was an Amphenol Model 945-122-1002. It is specified for a wavelength of 820 nm, although we operated it at 830 nm. As we said in Chapter III, the split ratio of the coupler is equal in both legs (measured by the manufacturer as 47%-53%), and the coupler is bidirectional. The excess loss is specified at below 1.0 dB (measured by the manufacturer as 0.59 dB).

The 3×3 coupler is a Sifam Model Special 33S 82C. It is specified for a wavelength of 830 nm. It also has equal splits in all three legs, if only one leg is used for input. Of course, in an interferometer this condition is not met, and so each output is different, as discussed in detail in Chapter III. The manufacturer measured the split ratio as shown in Table II. Our own measurements are shown in the same table. We made our

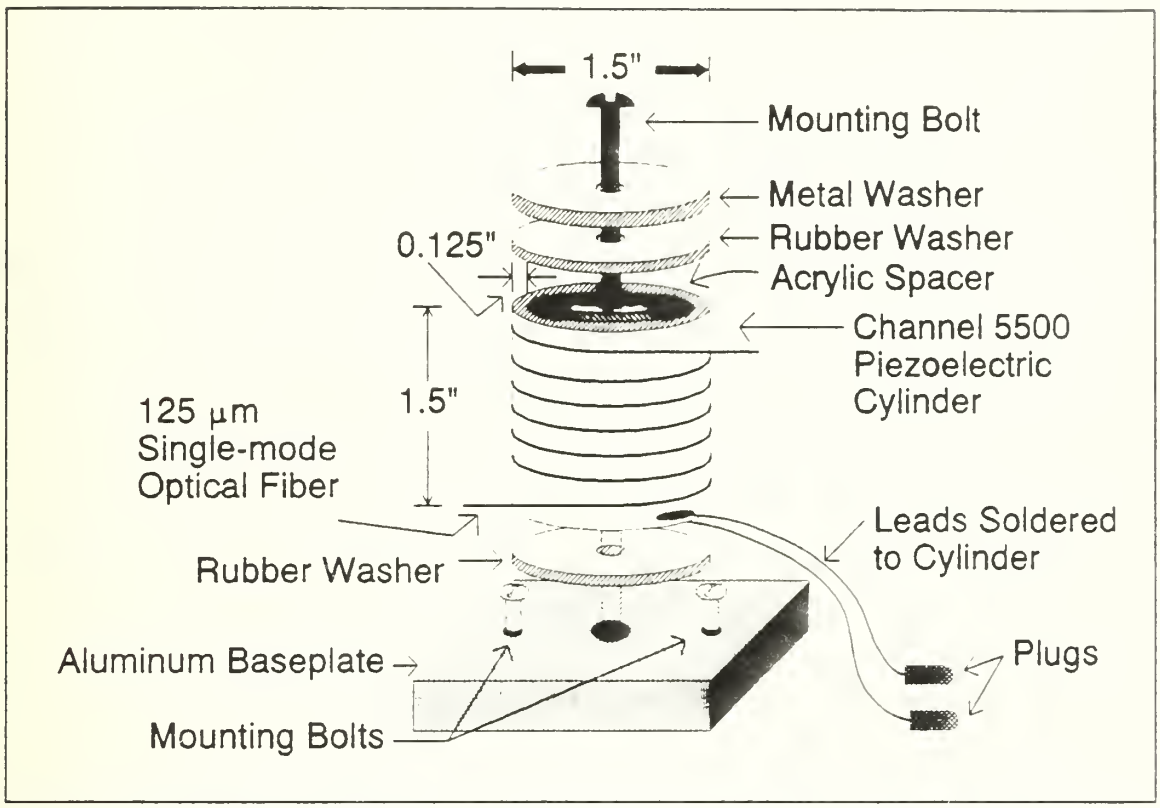

Figure 10 Detail of the assembly of the piezoelectric cylinders with fiber wrapped around them.

Table II Split-ratios of the Sifam Model Special 33S 82C 3×3 optical fiber coupler (S/N 01150).

Sifam's Measurements

Input \ Output	1	2	3
1	31%	34%	33%
2	35%	31%	34%
3	33%	34%	33%

Our Measurements

Input \ Output	1	2	3
1	27%	37%	36%
2	34%	27%	39%
3	33%	23%	44%

measurements by applying a known current to the laser diode, a Sharp LT-015 whose wavelength in a vacuum is 830 nm laser (560 nm in glass). This laser was repackaged by Seastar as a Model PT-450. To measure the power from each leg, we fused the laser

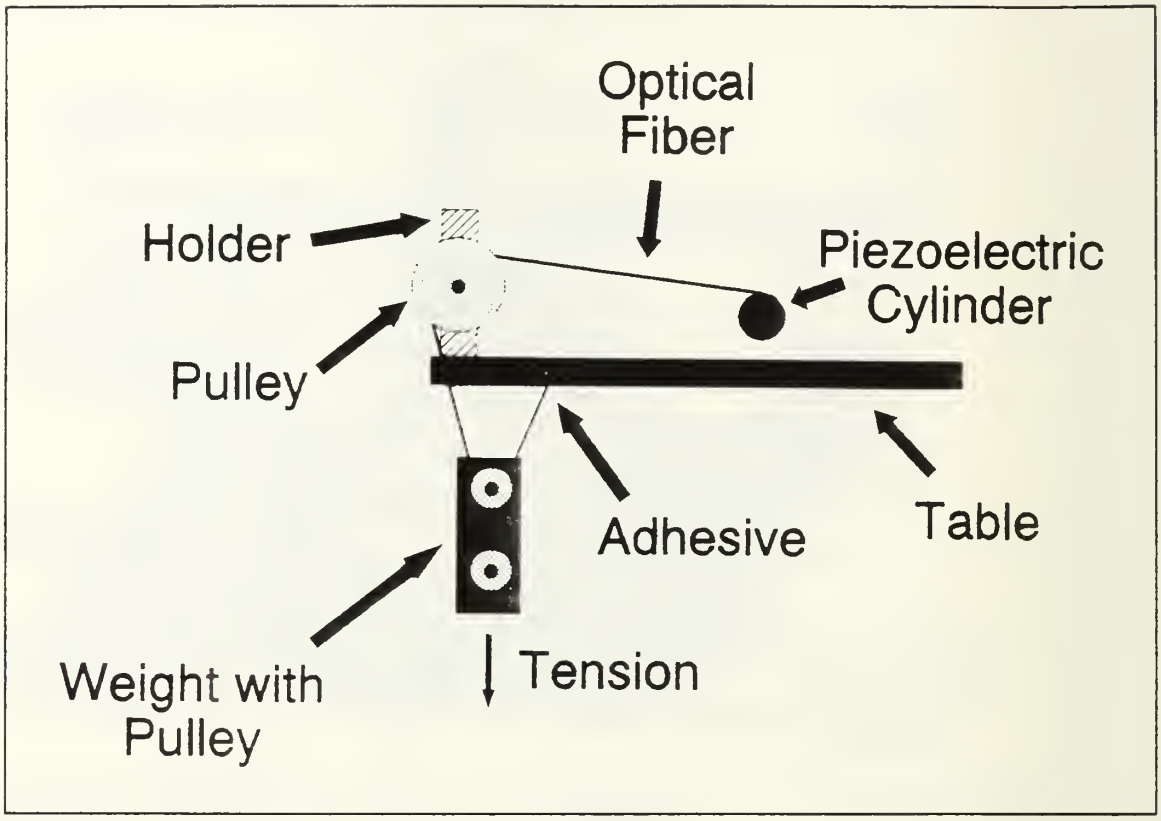

Figure 11 Apparatus used to obtain constant tension in the fiber wrapped on the cylinders. The fibers were wrapped by hand.

diode to each input leg in turn. For each input, we successively placed a different output leg into a slotted cylinder which we then inserted into a UDT Model 255 Photodiode with a barrel receptacle. A BNC connector on one end of the Photodiode was then mounted directly into the mating BNC connector on a UDT Model 550 Fiber Optics Power Meter. We did not calibrate the meter for operation at 830 nm. Since we were only interested in measuring the relative transmissivity of each leg, this omission is not a flaw in our technique. The chief elements of variability in this technique are:

1. The transmission of the fusion splice in each case is different, but since the total power is measured for each splice, this is not significant;

2. The insertion of an output into the slotted cylinder and its placement in the detector barrel is imprecise, but the UDT Model 550 is a large-area detector and hence does not require precise alignment.

The measurements at each of several laser diode currents were averaged together to yield the results shown in the left-hand half of the table. The agreement is only fair with the manufacturer's measurements. Hopefully the manufacturer's technique was somewhat less variable than was ours.

The 2×2 coupler had about 10 m of fiber attached on two leads; the other two leads had only about a meter of fiber attached. The 3×3 coupler had only about 1 m of fiber on each end of its three legs. We recommend obtaining them with as much fiber already attached to them as will be needed in the sensor where they will be used. This will permit the number of fusion splices to be reduced. Since each splice raises the possibility of more reflections, more transmissive loss, and more of a nuisance generally, this is a very useful reduction.

We used a Sumitomo Type 11X Fusion Splicer to splice our fibers together. It provides a microscope for precise positioning of the bared fiber prior to fusion by electric arc. This particular splicer does not permit a very large range of adjustment in the position of the fibers laterally and vertically, so if placement is not quite good in advance, it is very difficult to get it right without starting over again. As a consequence, splicing can consume a large amount of time (and did so).

A good way to check on the success of a splice is to shine light (we used laser light) through it before the fusion occurs. The far end of the receiving fiber can be connected to a photodetector and thence to either a power meter or an oscilloscope. By adjusting the position of both ends of the fiber to be fused, we can maximize the received power. We found that alternating between adjusting lateral position and vertical position enabled us to find the optimum position fairly quickly, if the optimum position could be reached at all by the adjustment controls on the fusion splicer. After fusion occurs, there should be more power received than before the fusion (by 0.5 to 1.0 dB). If this is not the case, then the fusion splice was poor. The fiber should be broken, the buffer should be stripped again, the ends should be cleaved once more, and the fusion splice should be repeated.

To make Mach-Zender interferometer with legs properly matched in length requires considerable care. Suppose enough fiber has been attached to the input coupler to form

the two legs of the interferometer. One of the two legs can be spliced to an input leg of the output coupler without too much trouble if we monitor the power transmitted through the leg both before and after splicing it to the output coupler. The connection of the remaining leg to the output coupler is considerably more difficult. Light passing through it also passes through the already-completed leg, since they are effectively connected together at the input coupler. When we bring the remaining leg close to the output coupler in order to splice it to the coupler, two coherent beams recombine, producing interference. No longer is there a constant power level from the coupler. This complicates the task of finding the optimal position of the remaining fiber prior to completing the second fusion splice. However, one can still search for the placement of the fibers which generates the maximal fringe depth.

A bigger problem occurs if this second fusion splice fails. In this case, the second leg will be shorter than the first. It generally is necessary to break the first leg again in order to ensure the lengths are equal (or nearly so). We recommend acquiring some practice and skill in performing fusion splices before tackling this tedious task.

Upon the completion of the construction of our interferometer, we placed the three output fibers of the terminating 3×3 optical fiber coupler into three slotted cylinders. Each of these was in turn inserted into a mounting barrel with a photodiode within it. We had two CLD42163 photodiodes and one CLD41461 photodiode available, and so we used them. Without calibrating the UDT Model 550 Fiber Optics Power Meter for operation at 830 nm, we measured the responsivity of these photodiodes as 370 mA/W for the two identical photodiodes and 362 mA/W for the odd one. Since we did not perform a calibration, these results are not likely to be accurate, but accuracy here was not crucial to our development of the demodulators. Our purpose was to develop an understanding of the factors which affected performance, not to optimize the performance. For fine tuning of the performance, however, the responsivity of the photodiodes is an important parameter of operation because it determines the amount of current delivered to the receiver stage.

C. SCALE FACTOR OF THE INTERFEROMETER

Our interferometer produces a very highly linear optical phase shift for an applied voltage. We used an HP6824A DC Power Amplifier to boost the output of an HP3314A Function Generator from an amplitude of 10 V maximum to an amplitude of 60 V maximum. For convenience, we adjusted the gain of the power amplifier to approximately 10. This amplified signal was then applied in opposite polarities to each of the piezoelectric cylinders in the interferometer. The upper photograph in Figure 12 shows the three outputs of our interferometer for a sinusoidal input with amplitude 2.79 rad. The lower trace shows the elliptical Lissajous figure which results when two of these are fed to the X and Y inputs of an oscilloscope.

The Lissajous figure closes on itself, retracing the same elliptical pattern, if an optical phase shift amplitude in excess of π radians is generated by the interferometer; otherwise it is open. We found that after closure had occurred, it was easy to see the ends of the traces and so count the number of closures as the applied voltage was increased. We noted the voltage for each such closure, which represented an additional π radians of optical phase shift. A summary of our observations is shown in Table III and Table IV.

If we apply a linear least-squares fit to these data, we find the relationship between nominal voltage displayed on the front panel of the HP3314A and the optical phase shift delivered by the interferometric sensor is given by the following equation:

$$A_{OUT} = \left(34.29 \pm 0.02 \ \frac{\text{rad}}{\text{V}}\right) V_{IN} + (-0.64 \pm 0.08 \ \text{mrad}). \tag{139}$$

We shall make extensive use of this highly linear relationship in further chapters in order to infer the output optical phase shift from a selected nominal input voltage.

D. SUMMARY

In this chapter, we described in detail the construction of an optical fiber interferometric sensor suitable for providing inputs to experimental demodulators. We found that this sensor generates output optical phase shifts dependent on an input voltage with a high degree of linearity. In the next chapter, we describe the design of the

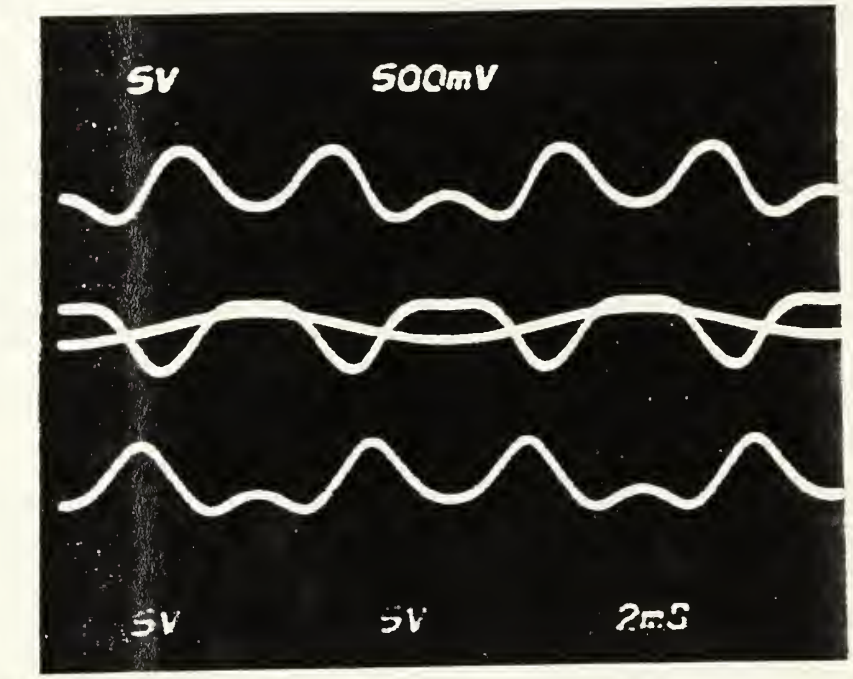

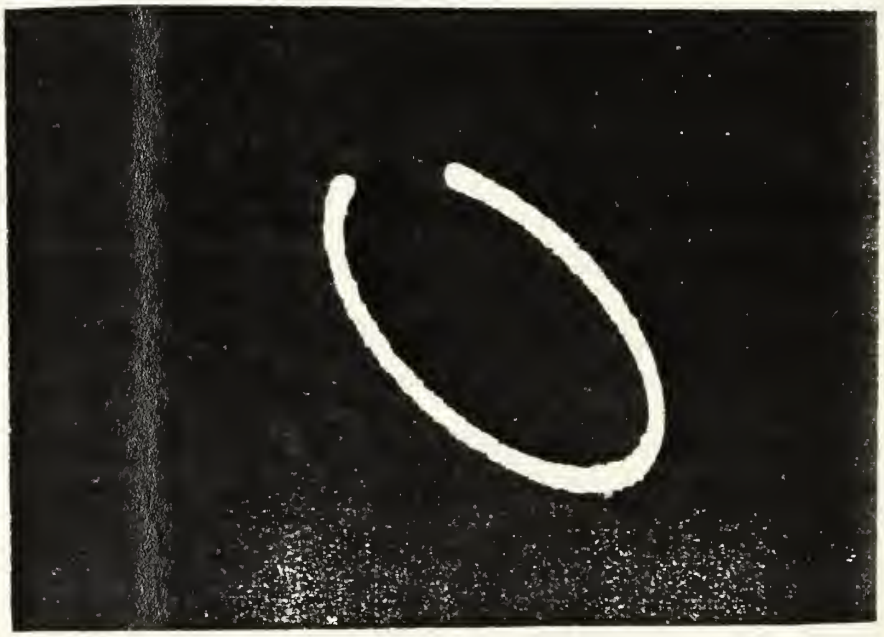

Figure 12 Upper trace: oscilloscope display of three interferometric outputs resulting from a sinusoidal stimulus (also shown) of amplitude 2.79 rad. Lower trace: two interferometric outputs on an XY plot generate a Lissajous figure.

Table III Measurements to determine the amount of optical phase shift output by the interferometer for a given voltage on the signal generator (one through 40 closures of the Lissajous pattern.)

Number of Closures of the Lissajous Figure	Nominal Input Voltage	Peak Output Voltage	Number of Closures of the Lissajous Figure	Nominal Input Voltage	Peak Output Voltage
1	91 mV	880 mV	21	1.95 V	18.65 V
2	182 mV	1.758 V	22	3.14 V	19.52 V
17	276 mV	2.667 V	23	2.14 V	20.48 V
14	368 mV	3.557 V	24	2.23 V	21.34 V
5	459 mV	4.439 V	25	2.32 V	22.25 V
6	552 mV	5.33 V	26	2.41 V	23.11 V
6	644 mV	6.22 V	27	2.50 V	23.97 V
8	734 mV	7.10 V	28	2.59 V	24.83 V
11	827 mV	8.00 V	29	2.68 V	26.66 V
10	920 mV	8.90 V	30	2.78 V	26.66 V
11	1.02 V	9.73 V	31	2.87 V	27.52 V
12	1.12 V	10.7 V	32	2.96 V	28.38 V
13	1.21 V	11.6 V	33	3.05 V	29.25 V
14	1.30 V	12.4 V	34	3.14 V	30.09 V
15	1.40 V	13.4 V	35	3.23 V	30.96 V
16	1.49 V	14.24 V	36	3.33 V	31.93 V
17	1.58 V	15.10 V	37	3.42 V	32.78 V
18	1.67 V	15.97 V	38	3.51 V	33.64 V
19	1.77 V	16.93 V	39	3.60 V	34.51 V
20	1.86 V	17.79 V	40	3.69 V	35.37 V

Table IV Measurements to determine the amount of optical phase shift output by the interferometer for a given voltage on the signal generator (41 through 79 closures of the Lissajous pattern).

Number of Closures of the Lissajous Figure	Nominal Input Voltage	Peak Output Voltage	Number of Closures of the Lissajous Figure	Nominal Input Voltage	Peak Output Voltage
41	3.78 V	36.23 V	61	5.61 V	53.6 V
42	3.87 V	37.09 V	62	5.70 V	54.4 V
43	3.97 V	38.06 V	63	5.79 V	55.3 V
44	4.06 V	38.92 V	64	5.89 V	56.3 V
47	4.15 V	39.77 V	65	5.97 V	57.1 V
46	4.24 V	40.63 V	66	6.06 V	58.0 V
47	4.33 V	41.49 V	67	6.16 V	58.8 V
48	4.42 V	42.36 V	68	6.25 V	59.7 V
49	4.51 V	43.22 V	69	6.33 V	60.5 V
50	4.60 V	44.08 V	70	6.42 V	61.4 V
51	4.69 V	44.99 V	71	6.51 V	62.2 V
52	4.78 V	45.85 V	72	6.61 V	63.2 V
53	4.88 V	46.7 V	77	6.69 V	63.9 V
54	4.97 V	47.5 V	7●	6.78 V	64.8 V
55	5.06 V	48.4 V	75	6.88 V	65.8 V
56	5.15 V	49.2 V	76	6.97 V	66.6 V
57	5.25 V	50.1 V	77	7.06 V	67.5 V
58	5.34 V	51.1 V	78	7.15 V	68.3 V
59	5.42 V	51.8 V	79	7.25 V	69.3 V
60	5.51 V	52.6 V			

first of three demodulators which we consider in detail in this dissertation, a fringe-rate demodulator.

V. DESIGN OF A FRINGE-RATE DEMODULATOR

A. INTRODUCTION

The method of fringe-rate demodulation was discussed at some length in Crooker [Ref. 10] and Crooker and Garrett [Ref. 11]. The fundamental idea is to take two of the outputs of an optical fiber interferometric sensor terminated by a 3×3 optical fiber coupler, convert them to two square waves, and measure the frequency of the modulation of the optical wave with a frequency-to-voltage converter. By integrating this result over time, we can recover the signal. An ambiguity results from the use of this scheme. We shall explain presently how this can be eliminated. A limitation inherent to the technique is that phase amplitudes of less than one half fringe ($\pm\pi$ rad) cannot be recovered successfully.

B. THEORY

When the signal of interest is strong, it induces a large peak phase shift in the light. At the moment that the signal peaks, however, the instantaneous frequency of the output is zero. Conversely, when the signal is zero, the output is changing most rapidly. This corresponds to a large instantaneous peak frequency of the interferometric output.

To see this, consider the mathematical form of the interferometric output $x(t)$ for a single input tone of frequency f. That is, if $\xi(t)$ represents a signal of interest

$$\xi(t) = A \sin(\omega t) = A \sin(2\pi f t), \tag{140}$$

then we may use Equation (5) of Chapter III to obtain

$$x(t) = D + E\cos[A\sin(2\pi ft) + \phi] \tag{141}$$

In this expression, the phase ϕ includes the phase terms due to choosing a particular output of the interferometer as well as all the extraneous influences on phase mentioned in Chapter III. Recall that D is the central value around which the output waveform varies, E is the peak departure of the interferometric output from D, A is the phase amplitude of the input, f is the frequency of the signal of interest, and t is the time. The instantaneous frequency of the output in hertz is defined as the derivative of the argument of the cosine function with respect to time, divided by 2π.

$$f_{INSTANTANEOUS} = \frac{1}{2\pi}\frac{d\xi(t)}{dt} = \frac{\dot{\xi}}{2\pi} = Af\cos(2\pi ft). \tag{142}$$

Here, we assume that the derivative of the phase term ϕ is small and can be neglected. Whenever the extraneous contributions to the phase shift are of a quasi-static nature, this is a reasonable assumption. The instantaneous frequency is maximal when the cosine in the derivative given by Equation (142) reaches a peak, that is, when

$$2\pi ft = n\pi \tag{143}$$

where n is an integer. This occurs when the sine in the interferometric output of Equation (141) is zero, since

$$\sin(n\pi) = 0, \tag{144}$$

that is, when the signal of interest passes through zero.

If we can convert the instantaneous frequency to a voltage, then we need only integrate it over time to recover the signal $\xi(t)$, in effect, reversing Equation (142). The chief difficulty in this scheme is not the conversion of frequency to voltage, since integrated circuits to perform this function are readily available. Rather, it is the fact that a high instantaneous frequency occurs both when $\xi(t)$ is rising and when it is falling. Yet frequency-to-voltage converters do not give different outputs for these two situations. We alluded to this problem in the introduction to this chapter.

We would like our converter to give, say, a rising output when the instantaneous frequency is high and when $\xi(t)$ is rising. With this choice, we would also like it to give a falling output when $\xi(t)$ is falling. Succinctly, we need to distinguish between two distinct situations, both of which give rise to high voltages from a frequency-to-voltage converter. If the voltage from the frequency-to-voltage converter can range from 0 V to, say, V_{MAX}, then we would like to invert this range on alternate cycles to 0 V to $-V_{MAX}$. Crooker's method calls for the use of an optional inverter to do this.

The use of a 3×3 coupler at the interferometer's output provides enough information to make it possible to distinguish between a high instantaneous frequency due to a *rising* signal of interest and a high instantaneous frequency due to a *falling* signal of interest. In its simplest form, the method uses two of the three available outputs and determines which one leads and which one lags the other. From Equation (5) in Chapter III, the 3×3 coupler generates three outputs of the form

$$x_k(t) = D + E\cos\left[\xi(t) - (k-1)\frac{2}{3}\pi\right] \tag{145}$$

where $\xi(t)$ is the signal of interest and k is a index which can be 1, 2, or 3. Here, we are ignoring the additional phase shifts due to extraneous influences such as pressure and temperature.

Figure 13 is a block diagram of a Fringe Rate Demodulator. Without any loss of generality, we can arbitrarily select two of the three outputs of the interferometer, say $x_1(t)$ and $x_2(t)$, as two channels of input to the Fringe Rate Demodulator. With this choice, Equation (145) implies that when $\xi(t)$ is increasing, $x_1(t)$ leads $x_2(t)$ by 120°. But when $\xi(t)$ is decreasing, $x_2(t)$ leads $x_1(t)$ by 120°. A comparable situation obtains no matter which pair of outputs we select.

We shall put both of these signals through comparators so that the result is either a logical 0 (0 volts) or a logical 1 (5 volts). One of these logical signals we now label I (for in-phase) and the other Q (for quadrature). This terminology is somewhat anachronistic, since the term "quadrature" generally refers to 90°, not 120°. Crooker [Ref. 10, p. 54] discovered that fringe-rate demodulation is largely insensitive to this fairly

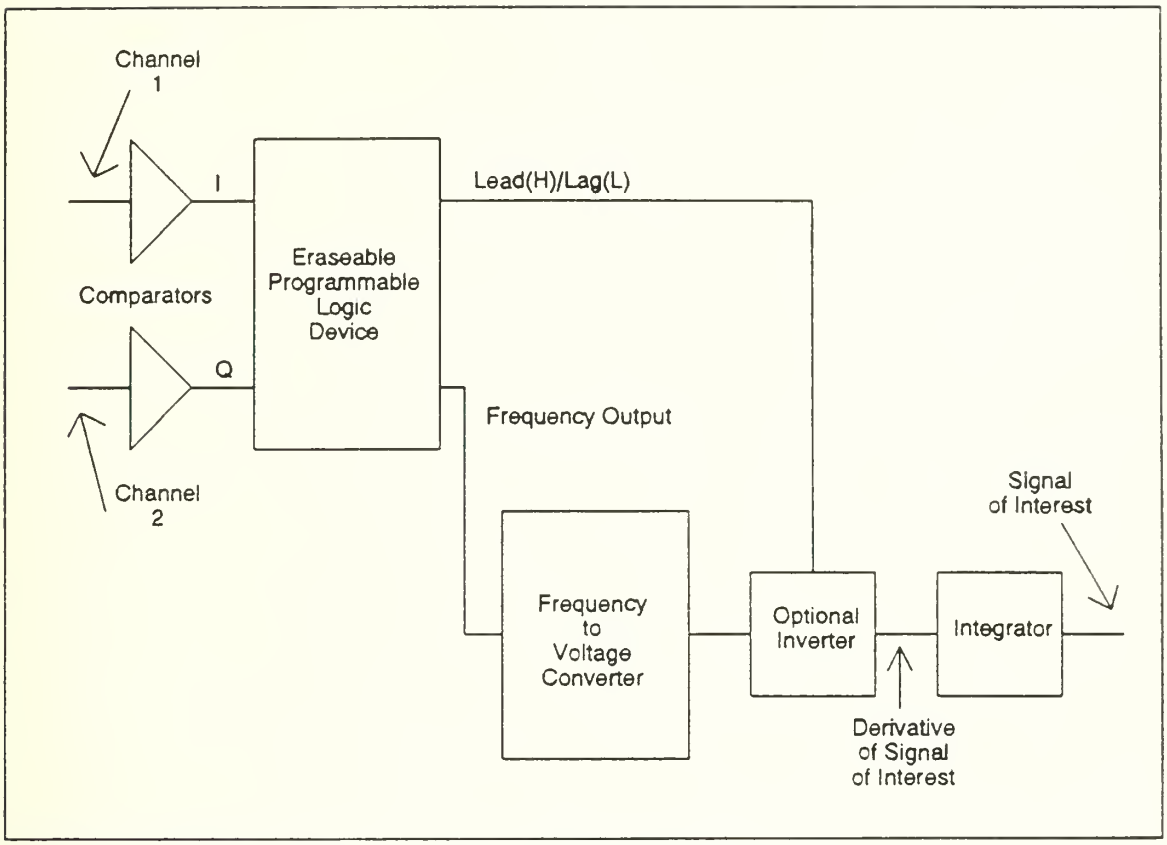

Figure 13 Block diagram of a Fringe Rate Demodulator.

large difference in phase angles. So although the fringe-rate method originally was conceived of as operating when a 90° phase difference were present, phase differences of 120° work perfectly adequately.

We now develop the Boolean logic which permits the determination of whether *I* leads *Q*, or *vice versa*. The resultant logic is different from that given in Crooker [Ref. 10] and Crooker and Garrett [Ref. 11]. Our purpose in altering her equations is to facilitate the programming of a programmable logic array (PLA) to contain all the logic, rather than using discrete logic integrated circuits. We made use of an Altera EP310 Erasable Programmable Logic Device (EPLD), a form of PLA which can be erased under ultraviolet light and reprogrammed. This characteristic is useful in the design of prototype systems.

We also modified Crooker's approach from one using synchronous, clocked logic to one using asynchronous logic. This permitted more rapid transitions of the outputs to

new states, which reduces the lag in recognizing that the signal which was leading before is now lagging, and *vice versa*.

We assume that I and Q cannot both make a transition simultaneously. That this is true is implied by Equation (145), for there is no angle ϕ such that

$$\cos(\phi) = \cos\left(\phi + \frac{2}{3}\pi\right) = 0. \tag{146}$$

The goal of the circuit is to produce a lead-lag decision signal LL which will take on the value 1 when I leads Q and the value 0 otherwise. The PLA will store the most recently computed value of LL in an internal flip-flop, present it as an output to the circuit, and use it to determine the next value of LL.

In addition to computing LL, the circuit must store the most recent values of I and Q internally, since these have a bearing on the determination of the next value of LL. These values we shall call I_{OLD} and Q_{OLD}. Like LL, they will be stored in flip-flops internal to the PLA. The EP310 requires that all computed values be presented as outputs to the circuit, so LL, I_{OLD}, and Q_{OLD} will be available as outputs.[10] Of course, we want LL as an output in any case so that it can provide the lead-lag decision to the optional inverter.

If we were using synchronous logic, LL, I_{OLD} and Q_{OLD} would only change when the clock signal permitted them to do so. Because we are using asynchronous logic, however, this is not the case. Instead, they swiftly take on new values in response to changes in the inputs. For the brief interval during which the old and new values differ, transitions must be taking place. Therefore we must take care that transitions in the outputs never give wrong results, even momentarily. In this case, there are two desired outputs. One is the signal LL (for lead-lag) which will be 1 if I leads Q and which will be 0 if Q leads I. The second output is a pulse train whose state changes whenever I or Q changes state. This pulse train provides the frequency input to a frequency-to-voltage converter. Since one cycle of I corresponds to the passing of one fringe (2π radians), and likewise for Q,

---

[10] We do not show I_{OLD} and Q_{OLD} in the block diagram of Figure 13.

we can generate two cycles of output for each fringe in this manner. This has the advantage of permitting slightly smaller phase shifts to be resolved by the fringe-rate demodulator. Theoretically, one can accept an interferometric output with as little as $\pm\pi/2$ radians of phase shift with this method. If the third output of the interferometer were incorporated in the logic, a more rapid pulse train could be generated, and this would lead to a minimum resolution of $\pm\pi/3$ radians of phase shift. In practice, these minima are not sufficient: one needs a number of fringes before reasonable fidelity in the reconstructed wave can be achieved.

Figure 14 contains a Karnaugh map of the digital logic necessary to generate LL. I_{OLD} is the value of the in-phase channel which was observed most recently. Q_{OLD} is the value of the quadrature channel which was observed most recently. I is the current (incoming) value of the in-phase channel. Q is the current (incoming) value of the quadrature channel. LL_{OLD} is the last computed value of the lead-lag signal which the circuit generated. The new value of the lead-lag signal, LL, is determined by looking up in the Karnaugh map that value which corresponds to the five inputs: LL_{OLD}, I_{OLD}, Q_{OLD}, I, and Q.

For example, suppose that the circuit's most recent output for LL was 0, which means that at the time when LL last was determined, the in-phase channel was lagging the quadrature channel.[11] If it so happened that $I_{OLD}=0$ and $Q_{OLD}=1$, then, since the in-phase channel was lagging before, we expect it to follow the quadrature channel to 1 very soon. If this happens, then $I=1$ and $Q=1$ after the transition occurs. As the table shows, this implies that the in-phase channel still lags the quadrature channel, so the new output LL should remain 0. But suppose, instead, that Q reverts to 0 without I ever having gone to 1. This means that the quadrature channel is now lagging the in-phase channel. Since the new values of the channels are $I=0$ and $Q=0$, the Karnaugh map shows that the next value of LL should be 1.

---

[11] This means that the in-phase channel changed after the quadrature channel changed.

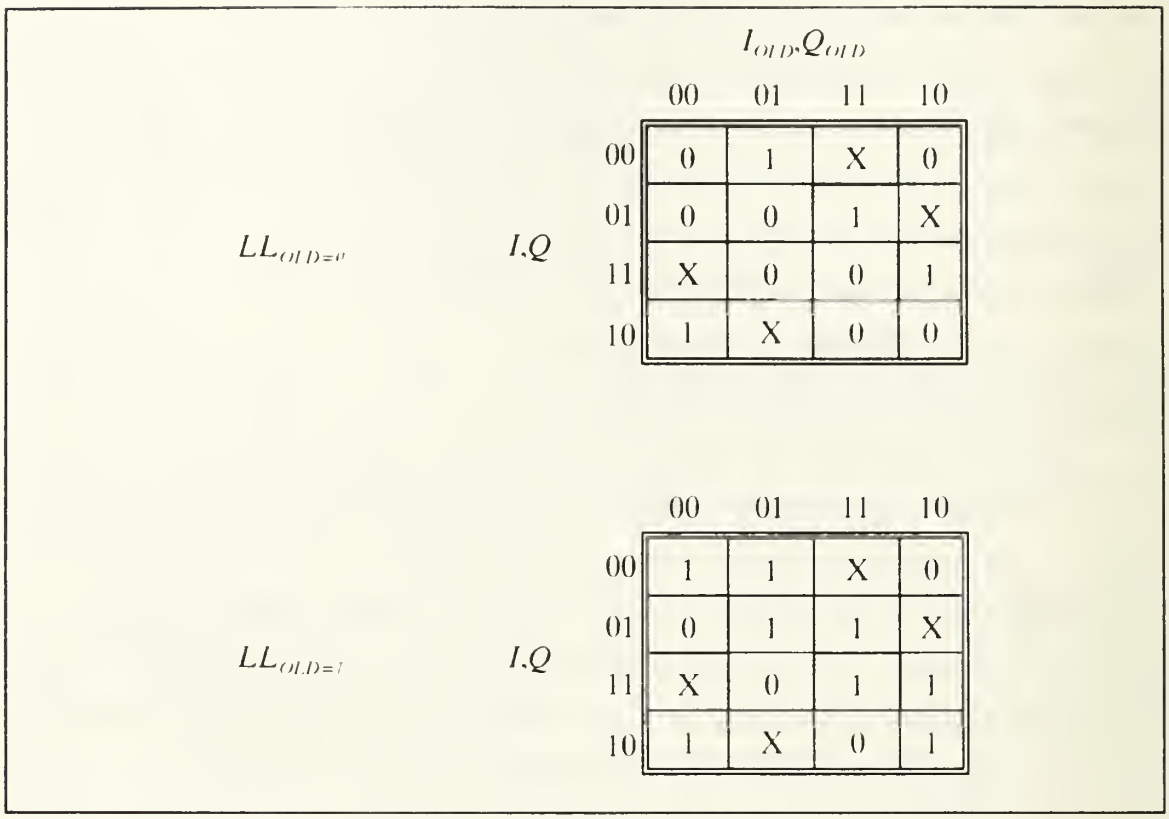

Figure 14 Karnaugh map of logic needed to generate *LL*.

All other entries in the Karnaugh map were filled out in a similar manner. The symbol X shows transitions which we do not expect ever to occur. The underlying supposition is that the in-phase and quadrature channels cannot both change at the same time, an assumption we have already discussed. The four logical equations of the EPLD are as follows.

$$\begin{aligned} LL = &\left(I \wedge \bar{I}_{OLD} \wedge \bar{Q}\right) \vee \left(I \wedge LL \wedge \bar{Q}_{OLD}\right) \\ &\vee \left(I \wedge Q \wedge \bar{Q}_{OLD}\right) \vee \left(\bar{I} \wedge LL \wedge Q_{OLD}\right) \\ &\vee \left(\bar{I} \wedge I_{OLD} \wedge Q\right) \vee \left(I_{OLD} \wedge LL \wedge Q\right) \\ &\vee \left(\bar{I}_{OLD} \wedge LL \wedge \bar{Q}\right) \vee \left(\bar{I} \wedge \bar{Q} \wedge Q_{OLD}\right), \end{aligned} \tag{147}$$

$$f_{OUT} = I \oplus Q, \tag{148}$$

$$I_{OLD} = I, \tag{149}$$

and

$$Q_{OLD} = Q. \tag{150}$$

The symbol $\wedge$ mean logical AND: the symbol $\vee$ means logical OR; and the symbol $\oplus$ means logical EXCLUSIVE-OR. These logical operations are defined more precisely in the Glossary.

C. DESIGN

We shall defer until Chapter IX the specifics of the design of a receiver to convert the interferometric outputs into voltage signals. For the time being, suffice it to say that these signals will be in the form of Equation (145), and that the units of D and E will be volts. The receiver will deliver signals in the range $D \pm E$, with $D = 0$ V and $E = 10$ V.

Figure 15 is a schematic of a comparator which we use to convert this bipolar signal to a unipolar (binary) signal. The LF311 comparator is made by National Semiconductor [Ref. 15, p. 5-194]. The databook uses the symbol for the open-collector output shown in Figure 15. The analysis of this circuit is given in Appendix A. The design equations derived there are repeated here. Provided that the conditions

$$V_S^- = -V_S^+, \tag{151}$$

$$R_1 \ll R_3, \tag{152}$$

$$R_2 \ll R_3, \tag{153}$$

and

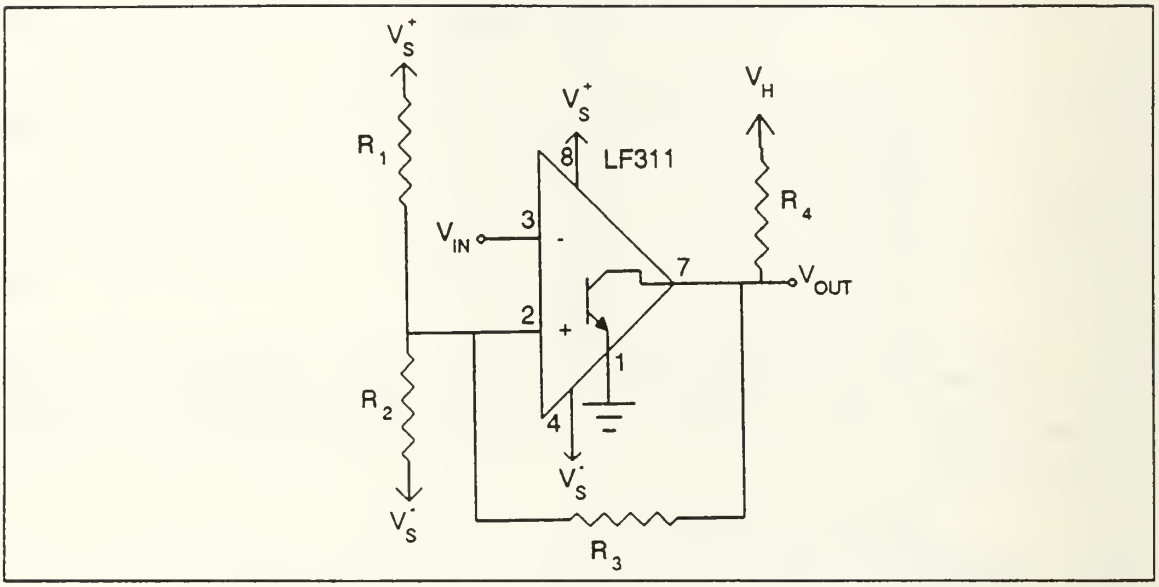

Figure 15 Comparator circuit used to convert bipolar interferometric outputs to binary levels of 0 or V_H.

$$R_1 \ll R_3. \tag{154}$$

are met, then the lower switching threshold of the comparator is given by

$$V_{THRESHOLD} \approx \frac{R_2 - R_1}{R_1 + R_2} V_S^- \tag{155}$$

and the upper threshold is higher than this by

$$V_{INCREMENTAL} \approx \frac{R_1 \| R_2}{R_3} V_H. \tag{156}$$

How much hysteresis we want is dependent on the amount of noise we expect to see. For our purposes, we chose to set $V_{THRESHOLD} = -50$ mV and $V_{INCREMENTAL} = +100$ mV. This means that switching of the output from high to low will only take place when the input goes below -50 mV, and switching from low to high will only take place when the input goes above $+50$ mV. We picked $R_1 = 1.00$ kΩ. Suppose that $R_2 = \alpha R_1$ for some number α. Then from Equation (155) we have

$$\frac{(\alpha-1)R_1}{(\alpha+1)R_1}V_S^+ = \frac{\alpha-1}{\alpha+1}V_S^+ = -50 \text{ mV}. \tag{157}$$

We shall select $V_S^+ = +15$V. Solving for α, we find

$$\begin{aligned}(\alpha-1)(15 \text{ V}) &= -(\alpha+1)50 \text{ mV} \\ \alpha(15 \text{ V}+50 \text{ mV}) &= 15 \text{ V}-50 \text{ mV} \\ \alpha &= \frac{14.95}{15.05} = 0.993.\end{aligned} \tag{158}$$

If we choose R_1 = 10.0 kΩ + 66.5 Ω (a series combination) and R_2 = 10.0 kΩ, then we find $V_{THRESHOLD}$ = −49.7 mV, which is reasonably close to the desired value, 50 mV.

Next we can apply Equation (156) to the desired amount of hysteresis, which is the difference between the upper and lower threshold levels, or 100 mV. The value of V_H is +5 V in our digital logic circuitry. So

$$\frac{R_1 \| R_2}{R_3}V_H = 100 \text{ mV} \tag{159}$$

$$\begin{aligned}R_3 &= \frac{R_1 \| R_2}{100 \text{ mV}}(5 \text{ V}) \\ &= \frac{5.017 \text{ k}\Omega}{100 \text{ mV}}(5 \text{ V}) \\ &= 251 \text{ k}\Omega.\end{aligned} \tag{160}$$

As it happens, standard 1% resistors do not come in values of 251 kΩ; the nearest value is 249 kΩ for R_3. Using the chosen resistor values, we expect to see lower and upper switch threshold levels of −48.7 mV and 49.6 mV, both of which are close enough to the desired values. To get smaller values would be difficult with 1% resistors without carefully choosing them for accuracy. Note that the 66.5 Ω resistor (which, with 10.0 kΩ, makes up R_1) is less than 1% of the 10.0 kΩ resistor as it is. This means that a resistor which has a nominal resistance of 10.0 kΩ might actually have as little as 9.9 kΩ and as

much as 10.1 kΩ. Adding 66.5 Ω to this does not guarantee that we get 10.0665 Ω. In the laboratory, we did not need to pick the 10.0 kΩ resistor specially, as it happened, but it could easily have been necessary. This is an unattractive feature of the design of this comparator which really arises because we want such a small level of hysteresis. If we relaxed this need, the inaccuracies of 1% components would cease to be a constraint.

Two of these comparators are used, one for each of the two interferometric outputs we choose to use in the Fringe Rate Demodulator. In Figure 16 we show the schematic of the rest of the Fringe Rate Demodulator. The unipolar outputs of the two comparators become the inputs to the *I* and *Q* inputs of the EP310 Erasable Programmable Logic Device (EPLD) described earlier in this chapter.

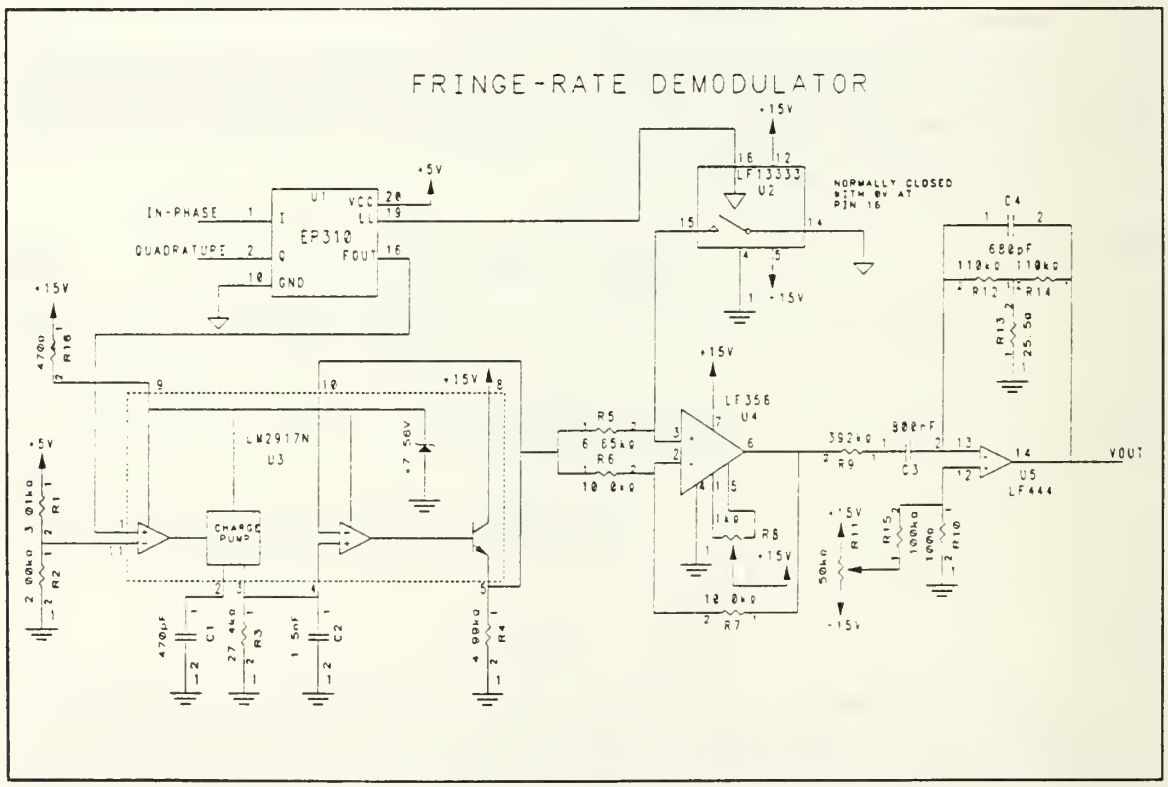

Figure 16 Schematic drawing of the Fringe Rate Demodulator. The receivers, transimpedance amplifiers, and comparators are omitted from this drawing.

The *LL* output of the EP310 causes the LF13333 Quad SPST JFET Analog Switch to alternate between connecting its D4 input at pin 15 to the ground at pin 14 and leaving D4 open. When D4 is grounded, the non-inverting input to the optional inverter

built around the LF356 Monolithic JFET-Input Operational Amplifier is grounded. This causes the LF356 to function as an inverting amplifier of gain 1. When D4 is left open, the voltage at the input to the LF356 is the same as that from the output of the LM2917N Frequency-to-Voltage Converter Because an operational amplifier with negative feedback tries to keep both its inputs at the same voltage level, there will be no current flowing through the feedback network, and so the output will not be inverted when D4 is left open.

The EP310 generates a frequency signal at its pin 16 which serves as the input to the LM2917N, which is often loosely referred to as a tachometer chip. This signal is formed from the exclusive-or of its two inputs, so the output frequency is roughly twice that of the input frequency. We cannot say it is precisely double, since the instantaneous frequency of a phase-modulated signal is not a constant. The voltage level provided to pin 11 of the LM2917N by a resistive divider comprising resistors R_1 and R_2 is around 2 V.

Our design differs in another respect from that in Crooker [Ref. 10, p. 53]. Crooker used a high-pass filter at the input to the frequency-to-voltage converter and a comparator threshold of zero. We used no filter, just a threshold about midway between the upper and lower voltage levels generated by the EP310. An advantage to avoiding the use of the filter is that, potentially, the absence of a capacitor could provide the ability to handle higher frequencies. Since the frequency input can be either 0 V or 5V, the input comparator of the LM2917N will not change unless the frequency input changes. Because this signal is derived from the interferometric outputs, its frequency is high when the phase in the interferometer is shifting most rapidly, and it is low when the phase shift reaches an extremum.

From the data sheet for the LM2917 [Ref. 15, p. 5-194], an equation describing the output voltage of the frequency-to-voltage converter is

$$V_{OUT} = V_{CC} f_{IN} C_1 R_3 K. \tag{161}$$

R_3 and C_1 are the external components attached to the charge pump within the converter. V_{CC} is 15 V, the voltage supplied to the output transistor within the converter. K is the

gain of the converter; it is roughly 1. The zener diode in the LM2917N limits the voltage from the operational amplifier which controls the transistor at its output to 7.56 V at most. We could include some gain in its feedback loop, but it is just as easy to apply the gain in the following stage, which is what we chose to do. We would like V_{OUT} to reach this maximum when the maximum input frequency occurs. What is this frequency?

For a signal of interest of the form

$$\xi(t) = A\sin(2\pi ft), \tag{162}$$

recall that the interferometric output is of the form

$$x(t) = D + E\cos[A\sin(2\pi ft)]. \tag{163}$$

We shall design the circuit to handle the case where $A = 100$ rad and $f = 200$ Hz. The peak instantaneous frequency in the interferometric output is roughly equal to the number of complete cycles in interferometric output in one second. In a quarter of a period of the signal of interest, $T/4$, there are $A/2\pi$ cycles of the interferometric output. So the frequency is roughly

$$\frac{\left(\frac{A}{2\pi}\right)}{\left(\frac{T}{4}\right)} = \frac{2A}{\pi T} = \frac{2Af}{\pi}. \tag{164}$$

However, the EP310 has logic which roughly doubles the frequency delivered to the LM2917N, so the actual frequency is therefore estimated as

$$f_{IN} = \frac{4Af}{\pi}. \tag{165}$$

Therefore we expect the EP310 to see a peak frequency of

$$f_{IN} = \frac{4(100\text{ rad})(200\text{ Hz})}{\pi} = 25.5\text{ kHz}. \tag{166}$$

Now from the specifications for the LM2917N [Ref. 15, p. 5-198], a restriction on the input frequency is

$$f_{IN} \leq \frac{I_1}{C_1 V_{CC}}. \tag{167}$$

In this expression, I_1 is the current delivered to the timing capacitor C_1, f_{IN} is the frequency delivered to the input of the LM2917N, and V_{CC} is the supply voltage. We can use this expression to determine the value of C_1 because I_1 is specified in the data book. We have chosen $V_{CC}=15$ V, and we have just found that $f_{IN}\approx 25.5$ kHz at most.

$$C_1 = \frac{I_1}{f_{IN} V_{CC}} = \left\{ \begin{array}{l} \dfrac{140\mu A}{(25.5\text{ kHz})(15\text{ V})} = 367\text{ pF for the minimum } I_1 = 140\mu A \\ \dfrac{240\mu A}{(25.5\text{ kHz})(15\text{ V})} = 630\text{ pf for the maximum } I_1 = 240\mu A \end{array} \right\}. \tag{168}$$

Unfortunately, the databook recommends keeping $C_1 > 500$ pF for accuracy. Whether or not we can handle the maximum frequency for this choice of C_1 depends on the current I_1, and this is dependent on the characteristics of the particular device we end up using.

We can calculate the peak frequency we can handle, however. We have

$$f_{IN} \leq \frac{I_1}{C_1 V_{CC}} = \left\{ \begin{array}{l} \dfrac{140\mu A}{(500\text{ pF})(15\text{ V})} = 18.7\text{ kHz if } I_1 = 140\mu A \\ \dfrac{240\mu A}{(500\text{ pF})(15\text{ V})} = 32.0\text{ kHz if } I_1 = 240\mu A \end{array} \right\}. \tag{169}$$

In the worst case, $I_1 = 140\ \mu A$ and $f_{IN} \leq 18.7$ kHz. If $f = 200$ Hz, then we must have

$$A \leq \frac{f_{IN}\pi}{4f} = \frac{(18.7\text{ kHz})\pi}{4(200\text{ Hz})} = 73.3\text{ rad.} \tag{170}$$

If we lower C_1 slightly to 470 pF, we can raise this to 78.0 rad. Although the accuracy of the output will suffer a little, we only need one capacitor to achieve this value, whereas it would take two to obtain 500 pF. The elimination of one component with a consequent increase in the permissible phase amplitude A is a satisfactory compensation for the sacrifice in accuracy.

By using the optional inverter, we create a bipolar output which is negative when I lags Q and positive otherwise. However, this signal is proportional to the derivative $\dot{\xi}(t)$ of the signal of interest, $\xi(t)$ in Equation (140). We must integrate this to recover $\xi(t)$ itself.

The LF444 Quad Low Power JFET Input Operational Amplifier performs the integration function. In Appendix A we derive equations to permit the design of this integrator. Equation (401) in the appendix shows that the output of our integrator circuit is

$$G(f) = \frac{V_{OUT}}{V_{IN}} = -\frac{1}{R_1 C_2}\frac{1}{j2\pi f} \tag{171}$$

provided that the input frequency f is much greater than the pole frequency f_p. There are actually two poles in this circuit. A design goal is to set them equal to each other. From Equation (397) in the appendix, we have

$$f_p = f_1 = \frac{1}{2\pi R_1 C_1} = f_2 = \frac{1}{2\pi R_2 C_2}. \tag{172}$$

We want to choose f_p so that the error in the phase is small in the frequency range of interest to us. We would like to have reasonable accuracy in both phase and gain when f>20 Hz (a design choice). From Equation (407) in the appendix, the error ϵ_P in the phase is given by

$$\epsilon_P = -2\tan^{-1}\left(\frac{f}{f_p}\right). \tag{173}$$

If we choose f_P=0.5 Hz, then this error will be only 3° for f=20 Hz; it will fall to 0.3° for f=200 Hz. From Equation (410) in the appendix, the error ϵ_M in the gain is given by

$$\epsilon_M = -\frac{1}{1+\left(\frac{f}{f_p}\right)^2}. \tag{174}$$

So for this same choice of f_p, the error in magnitude will be less than 0.06%, and it will be even less significant at higher frequencies.

Our choice of f_p=0.5 Hz determines the two products R_1C_1 and R_2C_2.

$$R_1C_1 = R_2C_2 = \frac{1}{2\pi f_p} = 318 \text{ ms}. \tag{175}$$

We also have to select the desired gain factor, $1/R_1C_2$. For an input to the interferometer of ±100 rad at f=200 Hz, the output of the frequency-to-voltage converter is measured as 3.8 V. To get an amplitude of 7.56 V out of the integrator under these conditions, the gain must be 7.56 V/3.8 V, or 2.0. So

$$\begin{aligned} \frac{1}{R_1C_2}\frac{1}{2\pi f} &= 2.0 \\ R_1C_2 &= \frac{1}{2\pi(200 \text{ Hz})(2.0)} = 398 \ \mu\text{s}. \end{aligned} \tag{176}$$

In the end, we increased the gain to about 3 by lowering R_1C_2 to around 265 μs.

By trial and error, we find combinations of R_1, R_2, C_1, and C_2 which meet these conditions and which are available or are easily produced from available components. A viable solution is

$$\begin{aligned} R_1 &= 392\text{k}\Omega, \qquad R_2 = 475 \text{ M}\Omega, \\ C_1 &= 800 \text{ nF}, \qquad C_2 = 680 \text{ pF}. \end{aligned} \tag{177}$$

The above discussion explains how the component values in the integrator in Figure 16 were chosen. To get the large resistance R_2 in the feedback network, we used a Tee-network. The values used in this network were obtained by applying Equations (416) and (418) of Appendix A. The form of the network illustrated there is repeated here in

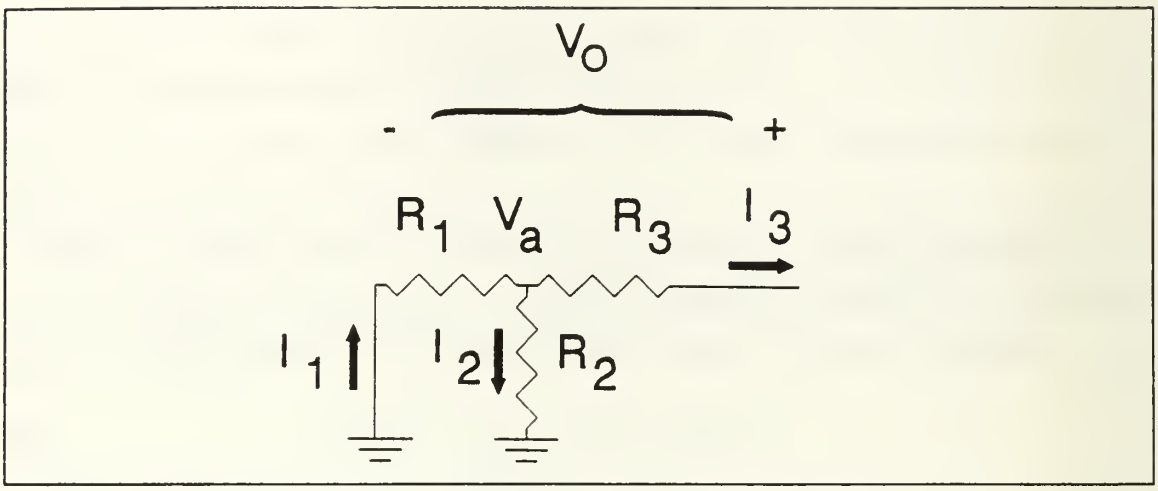

Figure 17 A Tee-network can be used to obtain large resistances.

Figure 17. Resistors R_1, R_2, and R_3 in Figure 17 on page 88 correspond to resistors R_{12}, R_{13}, and R_{14} in Figure 16 on page 82.

The effective resistance of our Tee is given by

$$R_{EFF} = \frac{R_{12}R_{14}}{R_{13}} = \frac{(110\ \text{k}\Omega)^2}{25.5\ \Omega} = 475\ \text{M}\Omega, \tag{178}$$

which is just the value of R_2 which we sought for the integrator.

There are two subsystems in the Fringe Rate Demodulator which could be modified to change its operating regime. The frequency-to-voltage converter is configured by the choice of R_3 and C_1 in Figure 16 to achieve its peak output voltage for a specified peak input frequency. This frequency is dependent on both the amplitude and the frequency of the signal of interest, and therefore changes in these two components could be made to accommodate a different set of signal parameters.

The integrator is the other subsystem which would need to be modified to accommodate such changes. The methods used in this chapter can be easily applied to make these changes, if needed.

D. SUMMARY

In this chapter we have considered a modification to a method proposed by Crooker [Ref. 10] and Crooker and Garrett [Ref. 11] which uses a frequency-to-voltage converter, an optional inverter, and suitable control logic to recover a signal of interest from the outputs of an optical fiber interferometric sensor terminated with a 3×3 optical fiber coupler. This method is very inexpensive, as we shall see in the next chapter, and takes up very little space physically. It is capable of operating with large phase amplitudes, provided that the bandwidth limitations of the converter are not exceeded. Its primary limitation is its inherent inability to recover signals of less than one half (or, if pushed, one third) of a fringe. For extremely sensitive optical fiber interferometric sensors, where large dynamic range can be achieved without dropping below this lower limit, this type of demodulator is excellent. In the next chapter, we consider the performance of the Fringe Rate Demodulator.

VI. PERFORMANCE OF THE FRINGE-RATE DEMODULATOR

A. OVERVIEW

In this chapter we examine the performance of a Fringe Rate Demodulator. The aspects of its performance which we consider are:

1. scale factor, which relates the phase amplitude in the modulated signal to the voltage amplitude in the demodulated signal;
2. small signal bandwidth;
3. maximum acceptable signal;
4. minimum detectable signal;
5. dynamic range;
6. complexity; and
7. approximate cost.

B. SCALE FACTOR

The scale factor is defined as the ratio of the demodulator's output voltage to the input phase. If the phase signal provided by the interferometric sensor is $\phi(t)$ and the output provided by the Fringe Rate Demodulator is $v(t)$, then we define the scale factor $F_{FRD}(t)$ of this demodulator by the equation

$$F_{FRD}(t) = \frac{\left(\frac{dv(t)}{dt}\right)}{\left(\frac{d\phi(t)}{dt}\right)} = \frac{dv(t)}{d\phi(t)}. \tag{179}$$

Ideally the scale factor would be constant. In practice, it is not. We shall call the multiplicative product Af of the phase shift A and the frequency f the *phase rate*, since the product is measured in radians per second. When the phase rate is too large, saturation of the frequency-to-voltage converter's output at the level of the high voltage power supply (or slightly below it) takes place.

The reason saturation occurs is clear if we consider the mathematical expressions for the output of the interferometer. Let a signal of interest $\xi(t)$ be applied to the interferometric sensor. If $\xi(t)$ is a sinusoid of amplitude A and frequency $\omega = 2\pi f$, then

$$\xi(t) = A\sin(\omega t). \tag{180}$$

After conversion of the interferometric output into its voltage analog, $\xi(t)$ is converted into the phase-modulated signal

$$\begin{aligned} x(t) &= D + E\cos[\xi(t) + \phi] \\ &= D + E\cos[A\sin(\omega t) + \phi]. \end{aligned} \tag{181}$$

The term ϕ represents an additional phase shift which accounts for the choice of one of the three outputs of the 3×3 coupler at the output of the interferometric sensor, as well as the effects of temperature, pressure, and other factors.

The instantaneous natural frequency of this interferometric output is given by the derivative of the argument of the cosine function. To get this in conventional frequency units (hertz), we divide by 2π. So the instantaneous frequency is given by
We assume that the derivative of ϕ is negligible, which is valid if ϕ is quasi-static.

Now the EP310 Erasable Programmable Logic Device (EPLD) generates a square wave as input to the LM2917N Voltage-to-Frequency Converter. This square wave has

$$
\begin{aligned}
f_{INSTANTANEOUS} &= \frac{1}{2\pi}\frac{d}{dt}(A\sin(\omega t)) \\
&= \frac{A\omega}{2\pi}\cos(\omega t) \\
&= Af\cos(\omega t).
\end{aligned}
\tag{182}
$$

twice the frequency $f_{INSTANTANEOUS}$ approximately. We have configured the LM2917N to provide a maximal output voltage for an instantaneous input frequency of 25.5 kHz. In Figure 18 is a graph showing the measured output of the LM2917N. The same data also are graphed in Figure 19, but each axis in that plot is logarithmic. A summary of the observations is given in Table V. The data were obtained by use of the instrumentation shown in Figure 20. We used an HP3314A Function Generator to create a square wave with a 50% duty cycle, ranging between 0 V and 5 V. The output of the LM2917N was averaged on an HP3456A Digital Voltmeter. A least-squares linear fit to the data gives the relationship

$$
V_{OUT} = \left(97.0\pm0.2\ \frac{\mu\text{V}}{\text{Hz}}\right) f + (14\pm4)\ \text{mV}, \tag{183}
$$

and the correlation coefficient in this linear fit is r=0.999976. The LM2917N is very linear, but the log-log plot shows the deviation from linearity at the low and high ends of the frequency scale: the output voltage reaches a floor of around 12.5 mV and a ceiling at around 5.30 V. The relatively large voltage offset of 12.5 mV limits the dynamic range of the device. We can calculate this ratio by the following method.

$$\text{Dynamic Range} = \frac{\text{Maximum output voltage}}{\text{Minimum output voltage}}$$

$$= \frac{5.29\ \text{V}}{12.5\ \text{mV}} \qquad (184)$$

$$= 423$$

$$\equiv 52.5\ \text{dB}.$$

This is a fairly poor dynamic range. It could be increased if we could lower the voltage offset, raise the voltage ceiling, or both. The voltage offset could be reduced by using a trim network with the output operational amplifier and transistor, though care would be required to avoid a high coefficient of change in the offset with temperature and time. The specification for the LM2917N states that the voltage offset typically is 3 mV, and is 10 mV at most. Since we measured more than 12 mV, a reduction in the offset should be easy to obtain. Getting the offset down to 3 mV would provide an increase in dynamic range of 12 dB.

The upper voltage limitation is due to the use of the LM2917N with its built-in zener diode. This diode limits the voltage to 7.56 V nominally; we measured the voltage as 7.47 V. The LM2907N could be substituted for the LM2917N. It has no zener diode built in. To obtain the same degree of stability, one could insert a discrete zener diode with a voltage higher than the 7.56 V of that in the LM2917N. With the 15 V power supplies we used, this would permit nearly double the dynamic range (an extra 6 dB).

The two changes that have been suggested here should provide an extra 18 dB of dynamic range without much effort. Replacing the frequency-to-voltage converter with one of greater inherent dynamic range is another approach to expanding the dynamic range.

Another way to view the dynamic range is not as the ratio of maximum to minimum output voltages but as the ratio of maximum to minimum input frequencies. This is not really suitable, however, since we could use as low an input frequency as we like. One could achieve as high a dynamic range as desired by this approach, but the resultant number would not be a helpful measure of performance.

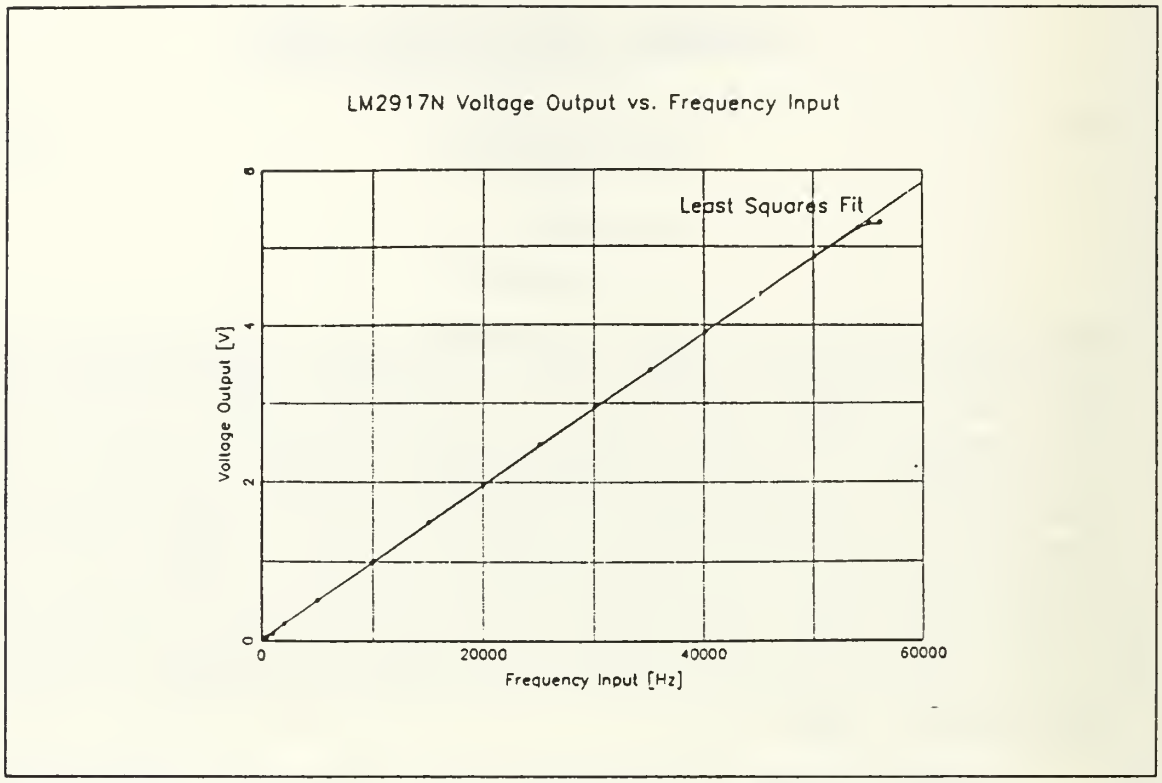

Figure 18 Graph of the output voltage of the LM2917N Frequency-to-Voltage Converter as a function of input frequency.

There is, however, a limit to the maximum input frequency of the LM2917N, and it was discussed in the last chapter. It is

$$f_{MAX} = \frac{I_2}{C_1 V_{CC}}. \tag{185}$$

Since I_2 may be as little as 140 μA, C_2 must be at least 500 pF (we have shaded this number a little, using only 470 pF) for accuracy. V_{CC} typically would be at least 5 V (but is 15 V in our demodulator), so the frequency input really should not exceed 19 kHz if we assume the "worst case" for I_2. That we obtained successful results up to 55 kHz must be regarded as due to having been lucky enough to obtain a superior sample of the LM2917N.

To measure the scale factor, we used the instrumentation illustrated in Figure 21. Our observations of input voltage, equivalent input phase, peak output voltage, and computed scale factor are shown in Table VI and Table VII. The equivalent phase

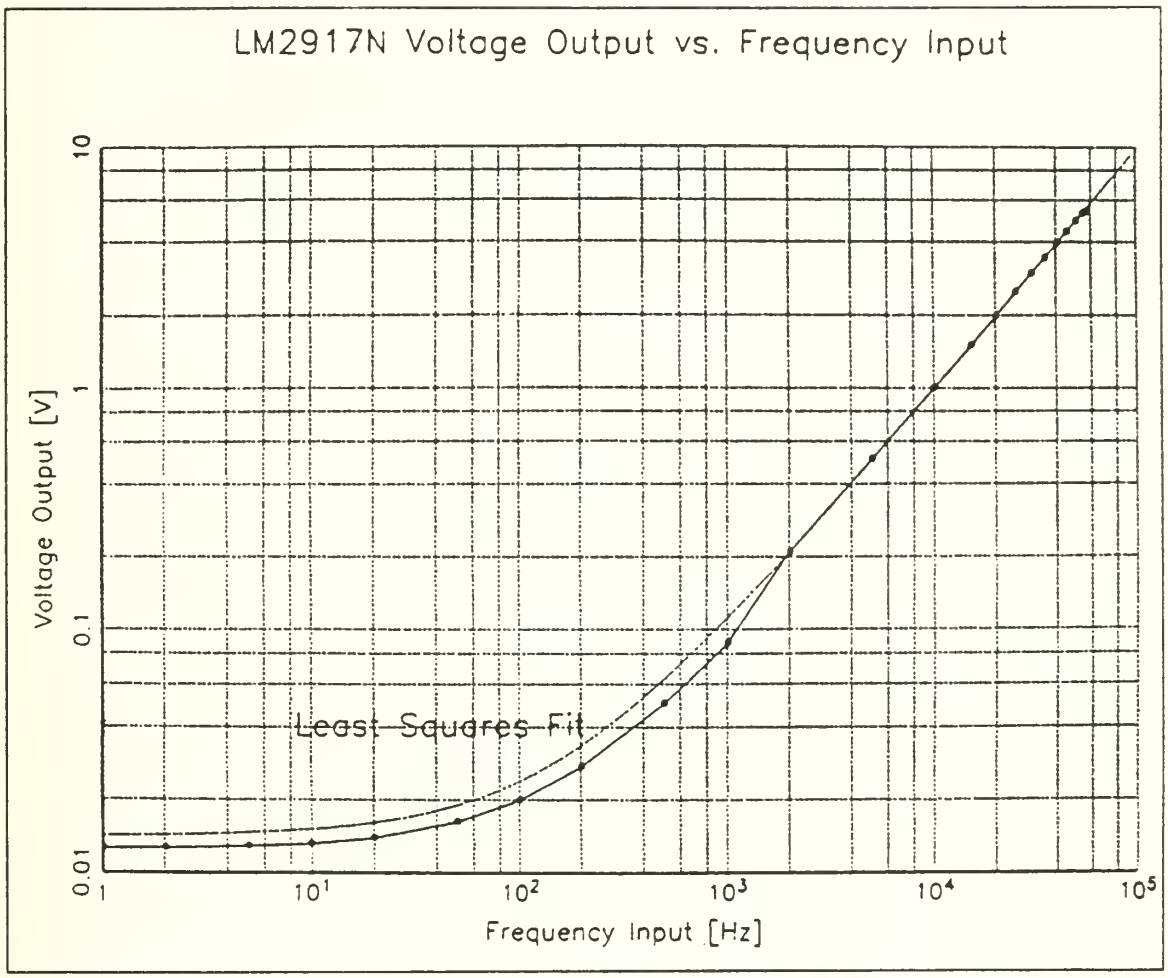

Figure 19 Graph of the output voltage of the LM2917N Frequency-to-Voltage Converter as a function on input frequency. This figure shows the same data as in Figure 18, but here it is plotted logarithmically on both axes.

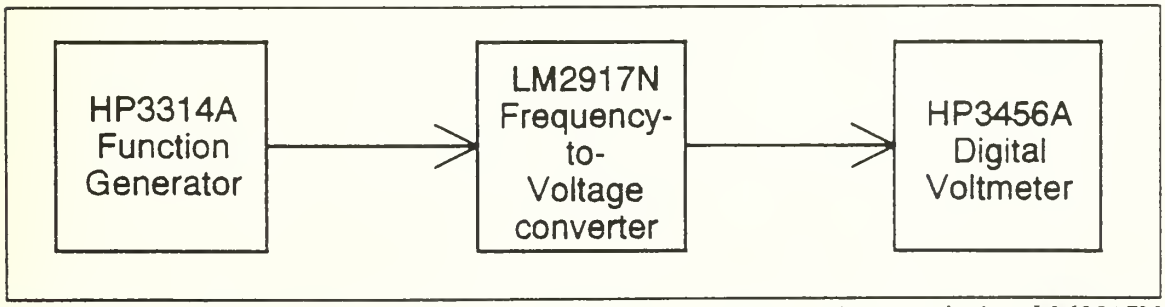

Figure 20 Instrumentation used to obtain the output voltage of the LM2917N Frequency-to-Voltage Converter as a function of input frequency.

amplitude shown in the tables was computed from the linear relationship found in Equation (139) on page 67 between voltage from the HP3314A Function Generator

Table V Summary of observations showing the output voltage of the LM2917N Voltage-to-Frequency Converter as a function of input frequency.

f_{IN}	V_{OUT} [V]
1 Hz	12.5±0.1
2 Hz	12.6±0.1 mV
5 Hz	12.80±0.10 mV
10 Hz	13.1±0.1 mV
20 Hz	13.9±0.1 mV
50 Hz	16.2±0.1 mV
100 Hz	19.9±0.1 mV
200 Hz	27.44±0.09 mV
500 Hz	49.9±0.1 mV
1 kHz	87.44±0.08 mV
2 kHz	208.89±0.02 mV
5 kHz	505.49±0.02 mV
10 kHz	997.33±0.03 mV
15 kHz	1.48674±0.00003 V
20 kHz	1.97469±0.00005 V
25 kHz	2.46907±0.00005 V
30 kHz	2.93716±0.00005 V
35 kHz	3.41414±0.00007 V
40 kHz	3.89596±0.00009 V
45 kHz	4.3769±0.0001 V
50 kHz	4.8569±0.0008 V
54 kHz	5.2288±0.0001 V
55 kHz	5.29019±0.00006 V
56 kHz	5.2955±0.0001 V

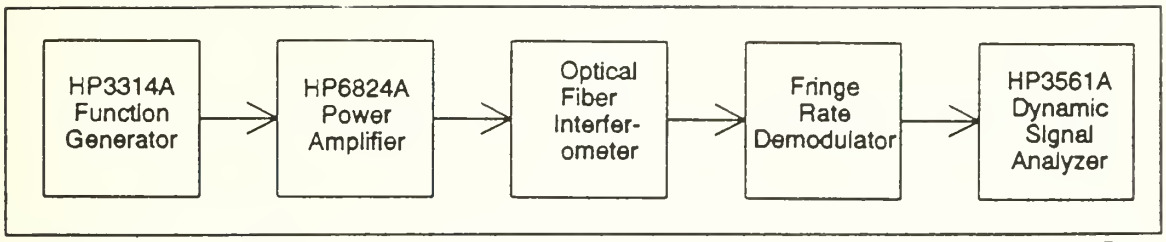

Figure 21 Instrumentation used to measure the scale factor of the Fringe Rate Demodulator.

when routed through the HP6824A Power Amplifier with gain 10. This relationship is repeated here:

$$A_{OUT} = \left(34.29 \pm 0.02 \ \frac{\text{rad}}{\text{V}}\right) + (-0.64 \pm 0.08 \text{ rad}). \tag{186}$$

No attempt has been made in these two tables to exclude some data from the averages. A cursory examination of these averages will reveal that the scale factor is between 105 and 120 mV/rad, and that it declines with increasing frequency as well as with increasing phase amplitude. As we have already discovered, increases in either of these quantities cause an increase in the instantaneous frequency of the input to the LM2917N Frequency-to-Voltage Converter. Thus the scale factor drops off with an increase in the phase rate, and this suggests that the slew rate limitation at the output of the LM2917N may be a factor. The slew rate of the LM2917N is not a published specification, however.

C. BANDWIDTH

The Fringe Rate Demodulator is inherently incapable of demodulating phase amplitudes of less than $\pi/2$ rad (or $\pi/3$ rad if all three outputs of the interferometer are used). This makes it impossible to define the bandwidth of the Fringe Rate Demodulator in the same manner that we shall use when we discuss the Symmetric Analog Demodulator. That is, we cannot speak of a small signal bandwidth: the demodulator does not

Table VI Measurements to obtain the scale factor of the Fringe-Rate Demodulator (f=50, 100, and 150 Hz).

f	V_{IN} (V, peak)	Equivalent Phase (rad)	V_{OUT} (V, peak)	Scale Factor (mV/rad)	Average Scale Factor (mV/rad)
50	1.00	33.7	4.2	125	120
	1.50	50.8	6.1	120	
	2.00	68.0	8.1	119	
	2.50	85.1	10.1	119	
	3.00	102	12.1	118	
100	1.00	33.7	4.0	119	118
	1.50	50.8	6.0	118	
	2.00	68.0	8.0	118	
	2.00	85.1	10.0	118	
	3.00	102	12.0	117	
150	1.00	33.7	4.03	120	117
	1.50	50.8	5.96	117	
	2.00	68.0	7.95	117	
	2.50	85.1	9.91	117	
	3.00	102	11.9	116	

respond to small signals. However, we can get an idea of the failure of the demodulator properly to respond at high frequencies if we consider the effect of increases in frequency on the scale factor, which we discussed in the previous section. If we fix the input phase amplitude, we can measure the scale factor over a range of frequencies. We find that eventually it drops to a level which is $1/\sqrt{2}$ times the size of the scale factor at low frequencies. This is the frequency which we will define as the upper limit on bandwidth. Of course, we expect it to be a function of the phase amplitude. The truth of the matter

Table VII Measurements to obtain the scale factor of the Fringe-Rate Demodulator (f=200, 250, and 300 Hz).

f (Hz)	V_{IN} (V,peak)	Equivalent Phase (rad)	V_{OUT} (V, peak)	Scale Factor (mV/rad)	Average Scale Factor (mV/rad)
200	1.00	33.7	4.00	116	116
	1.50	50.8	5.93	117	
	2.00	68.0	7.88	116	
	2.50	85.1	9.85	116	
	3.00	102	11.5	113	
250	1.00	33.7	3.92	116	111
	1.50	50.8	5.89	116	
	2.00	68.0	7.86	116	
	2.50	85.1	9.34	110	
	3.00	102	10.16	100	
300	1.00	33.7	3.90	116	106
	1.50	50.8	5.87	116	
	2.00	68.0	7.53	111	
	2.50	85.1	8.52	100	
	3.00	102	9.09	89	

is that it is the phase rate which is limited by various limitations on bandwidth within the Fringe Rate Demodulator, especially by that of the LM2917N Frequency-to-Voltage Converter. The frequency at which the scale factor dropped to this level and the scale factor itself are shown in Table VIII. The product of phase modulation amplitude and frequency, Af, is constant to within $\pm 5\%$, as one would expect from the characteristic limitation due to phase rate which is associated with this approach. The average value of 31 krad/s is consistent with the design goal of 25.5 kHz (see Equation (166)) and within the spread of typical device values for the LM2917N. The fact that it is greater

Table VIII These data show the bandwidth of the Fringe Rate Demodulator at various levels of input phase amplitude.

Input Voltage V_{IN} (V)	Equivalent Phase Amplitude (rad)	Output Voltage V_{OUT} (V)	Scale Factor F_{FRD} (mV/rad)	Band-width (Hz)	Af (krad/s)
1.00	33.7	3.02	89.61	850	28.6
1.50	50.8	4.34	85.43	610	30.9
2.00	67.9	5.70	83.95	460	31.2
2.50	85.1	7.20	84.61	360	30.6
3.00	102	8.52	83.53	320	32.6
				Average	30.8±1.4

than the design-value is not significant since the value depends on the choice of maximum acceptable distortion. When it is defined as the level giving 4% total harmonic distortion, the product Af is approximately 21 krad/s, as shown in Table IX.

D. MAXIMUM ACCEPTABLE SIGNAL

In Chapter XI we explain the performance of the Symmetric Analog Demodulator. There, we consider in detail how one can best assess the maximum phase amplitude that a demodulator can handle. For now, we shall simply state that our criterion for acceptability is that the total harmonic distortion induced in a sinusoidal signal be less than or equal to 4% after demodulation. On an oscilloscope, this level of distortion is barely perceptible. A series of graphs illustrating this assertion also are presented be presented in Figure 49 on page 186 in Chapter XI.

The harmonic distortion of the output of the Fringe Rate Demodulator is affected by several factors. The choice of an integrating capacitor in the LM2917N is one of the most significant. If it is too big, then the LM2917N cannot respond rapidly enough when its input frequency is high. Conversely, if the capacitor is too small, then the outputs are very noisy, and this is manifested in the harmonic distortion. The presence of a sizable

voltage offset at the output also leads to an abrupt change in the output of the optional inverter whenever the *LL* lead/lag signal changes state. This abrupt change is somewhat softened by the integrator which follows, but it still contributes some distortion. Also, because the Fringe Rate Demodulator is inherently unable successfully to demodulate excessively small phase amplitudes, we find that total harmonic distortion becomes very large for very small signals, too.

In Figure 22 we show a contour plot connecting combinations of input frequency and phase amplitude which result in equal levels of total harmonic distortion from the Fringe Rate Demodulator. The same data are plotted in Figure 23 in a surface plot, viewed in perspective. Both these plots were generated by computer programs which interpolated between data collected by a computer program operating our experimental apparatus on an IEEE-496 bus. In Table IX we show the results of interpolation on the same data to obtain the highest phase amplitude which will not cause the Fringe Rate Demodulator to exceed 4% total harmonic distortion. We do this calculation at all of the observed frequencies where interpolation was possible.

It is worth noting a few points about the data presented in Figure 22, Figure 23, and Table IX. The lowest distortion always occurs in the range between 100 Hz and 500 Hz. At both high and low frequencies, distortion goes up. This implies that it is not merely the phase rate which determines the level of distortion. If it were, we would expect the data to depend only on the product fA of frequency f and phase amplitude A, which it does not. The peak acceptable phase amplitude is roughly constant from 10 Hz to 100 Hz. It then begins to decline roughly in proportion to fA until the frequency reaches 1000 Hz. At higher frequencies, the distortion always exceeds the 4% level.

We can understand the behavior of the Fringe Rate Demodulator by considering what happens at the various extremes of input phase amplitude and frequency. When the product fA is low, then the frequency applied to the LM2917N Frequency-to-Voltage Converter is low. Under these conditions, the converter seldom outputs any charge from its charge pump. When it does, the charge is quickly drained from the integrating capacitor. The reason for this is that the charge pump only puts charge onto the capacitor in response to a transition of its frequency input from low to high or high to

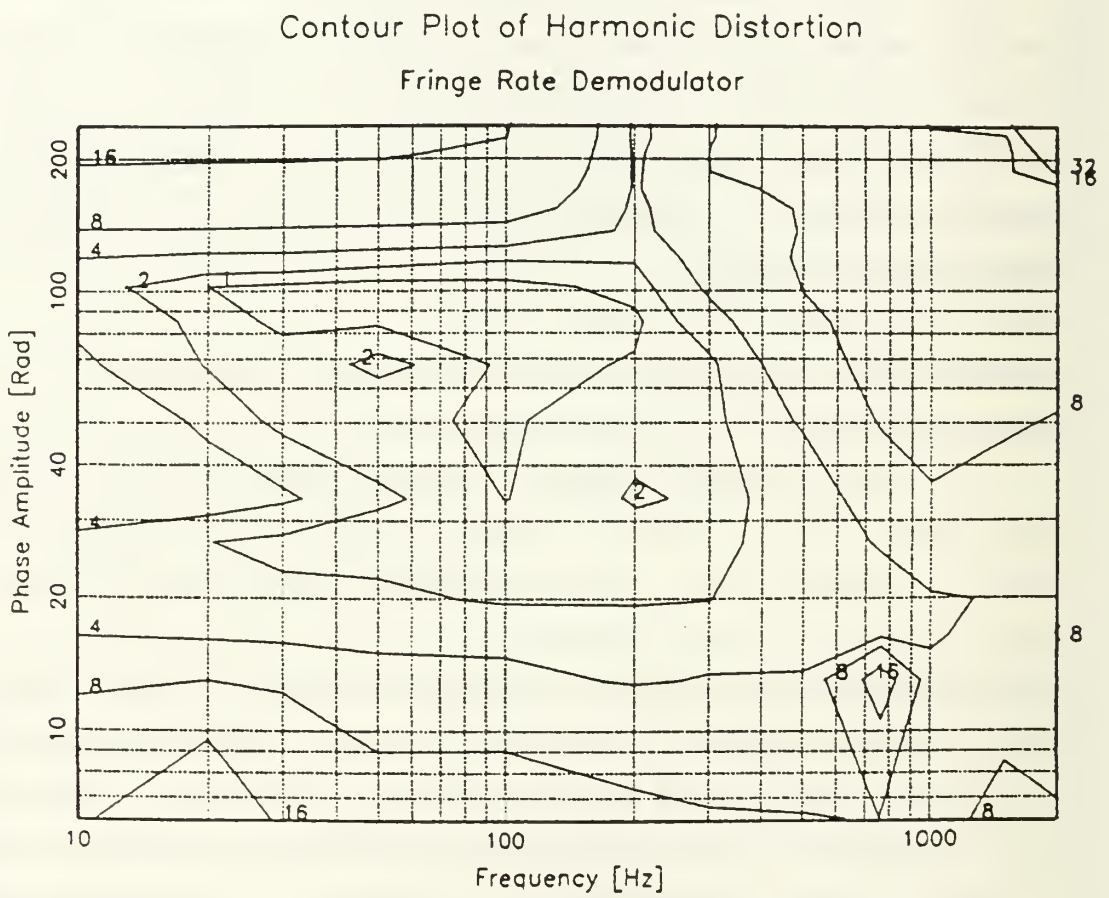

Figure 22 Contour plot of the total harmonic distortion in the Fringe Rate Demodulator as a function of frequency and phase amplitude.

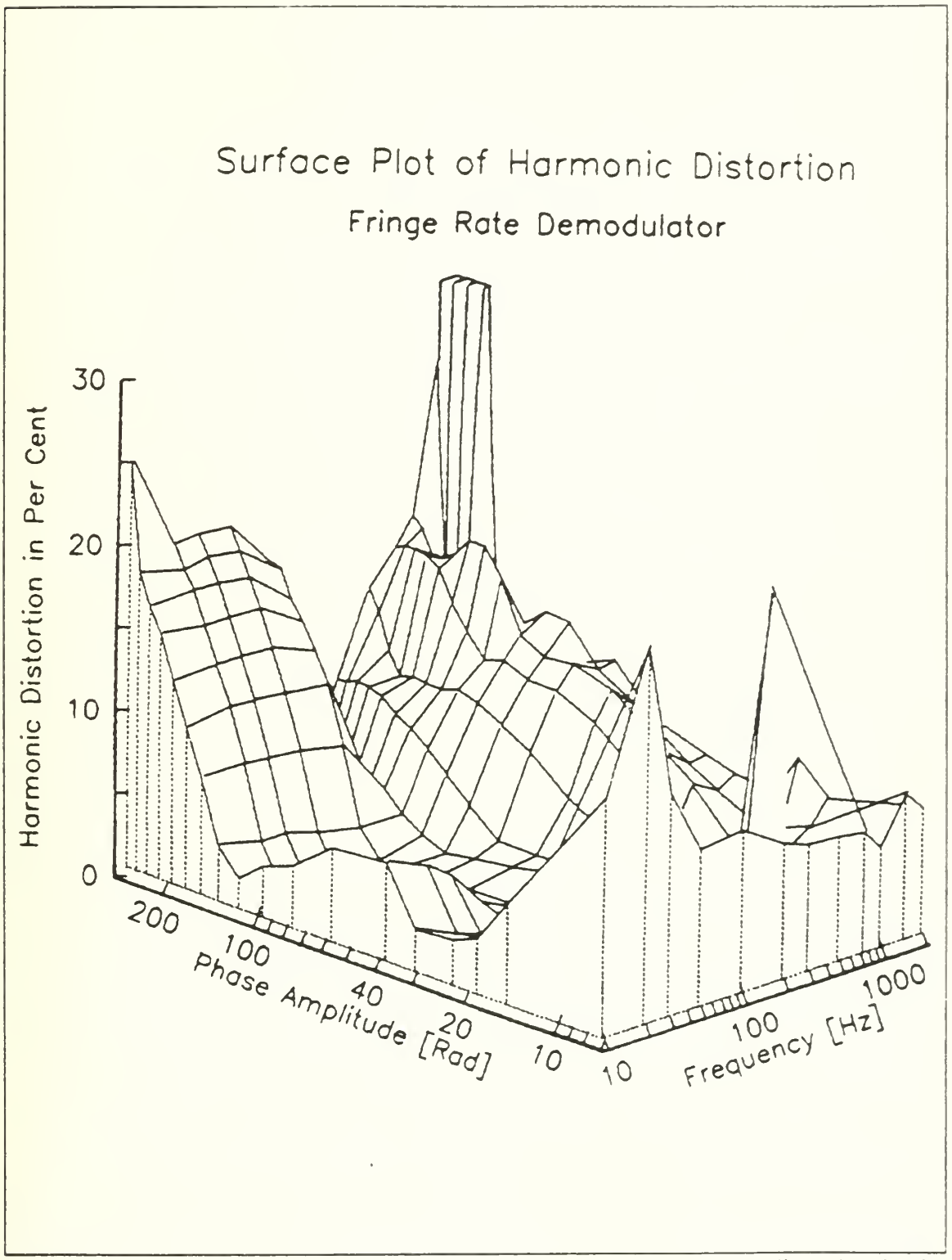

Figure 23 Perspective view of a surface plot of the total harmonic distortion in the Fringe Rate Demodulator as a function of frequency and phase amplitude.

Table IX Interpolation to determine the maximum phase amplitude resulting in 4% total harmonic distortion from the Fringe Rate Demodulator for several frequencies.

f (Hz)	Lower voltage (V)	Lower THD (%)	Upper voltage (V)	Upper THD (%)	Interpolated Voltage (V)	Equi-valent Phase (rad)	Af (krad/s)
10	3.5	3.9412	4.0	7.6147	3.508	120	1.2
20	3.5	3.3095	4.0	7.6276	3.580	122	2.4
30	3.5	3.317	4.0	7.4295	3.583	122	3.6
50	3.5	2.7395	4.0	7.2526	3.640	124	6.2
100	3.5	2.2206	4.0	6.7416	3.697	126	12.6
200	Total harmonic remained below 4% for all voltages applied (7 V max.)						
300	2.5	3.636	3.0	4.5001	2.711	92	27.6
500	1.0	2.4485	1.5	4.4076	1.396	47	23.5
750	0.6	2.9334	0.8	4.2590	0.7609	25	18.7
1000	0.6	3.7165	0.8	6.2645	0.6223	20.7	20.7
1500	Total harmonic distortion remained above 4% for all voltages applied.						
2000							

low. The charge is not added in anything like a continuous manner. Even if the product fA is high, if f is low, there will be relatively long periods during which no transitions of the converter's input occur. These take place whenever the phase amplitude reaches an extremum. During these periods, the pulsating nature of the converter's output again becomes evident, with an adverse effect on fidelity. It is little wonder, therefore, that one cannot simply increase the phase amplitude to compensate for a falling frequency. This pulsating current does not lend itself to a smoothly varying, distortionless output. A change in the frequency regime of the LM2917N (that is, a change in the value of the integrating capacitor and its resistive drain) would be required to reduce this effect. Even though the LM2917N shows a highly linear relationship between input frequency and output voltage, this is on an averaged basis. On an instantaneous basis, the noise-like

fluctuations in the current are significant. At high values of the product fA, the LM2917N saturates and distortion is the inevitable consequence. We find that the phase rate is 22.4 krad/s in the frequency band from 300 Hz to 1 kHz, based on a criterion of 4% total harmonic distortion.

E. MINIMUM DETECTABLE SIGNAL

For the Fringe Rate Demodulator to function requires transitions of its input from low to high and from high to low. Absent these transitions, there is no output. As the product Af of amplitude A and frequency f falls, the frequency input to the LM2917N becomes lower. As discussed in the previous section, this results in a pulsating current from the output of the LM2917N. The minimum detectable signal is one which just manages to create one transition, if only infrequently. Of course, faithful reproduction of this signal requires a much larger product Af. But provided that at least one transition occurs, the presence of the signal can be detected. Because the programmable logic generates two transitions for each complete cycle of the inputs, an output transition is guaranteed to occur if A is greater than $\pi/2$ rad. If this logic were modified to process all three interferometric outputs, the minimum detectable signal would drop to $\pi/3$ rad. Note that f does not enter into the determination of the detectability of the signal. It only affects the fidelity of the reconstruction of the signal of interest.

F. DYNAMIC RANGE

The dynamic range is the ratio between the maximum acceptable signal and the minimum detectable signal. The latter quantity is $\pi/2$ rad. The former is dependent on frequency, and was shown in Table IX on page 101. The ratio of these two as a function of frequency is tabulated in Table X.

By comparing the tabulated values of dynamic range to the maximum dynamic range of the LM2917N which is at the core of the Fringe Rate Demodulator, given in Table V, we can see that the demodulator fails to achieve this maximum. Why is this?

Table X Dynamic range of the Fringe Rate Demodulator.

f	Maximum Acceptable Signal	Minimum Detectable Signal	Dynamic Range	
			As a Fraction	In dB
10 Hz	120 rad	$\pi/2$	76.4	37.7
20 Hz	122 rad		77.7	37.8
30 Hz	122 rad		77.7	37.8
50 Hz	124 rad		70.9	38.0
100 Hz	126 rad		80.2	38.1
200 Hz	4% Total Harmonic Distortion was never reached, so maximum acceptable signal was undetermined.			
300 Hz	92 rad	$\pi/2$	58.6	35.4
500 Hz	47 rad		29.9	29.5
750 Hz	25 rad		15.9	24.0
1000 Hz	20.7 rad		13.2	22.4
1500 Hz	Total harmonic distortion remained above 4% so maximum acceptable signal was undetermined.			
2000 Hz				

It is because we used averaging of the pulsating output of the LM2917N in measuring its dynamic range, but we relied on a criterion of 4% total harmonic distortion in determining the maximum acceptable signal. It is not surprising, then, that the LM2917N appears to have a different dynamic range, since we assessed its performance in a different way. In Table VIII we found that the average phase rate was 30.8 krad/s; we would infer a peak amplitude of (30.8 krad/s)/(100 Hz)=308 rad when the frequency f=100 Hz. Using the criterion on which that table was based, the maximum dynamic range would be computed as (308 rad)/(π/2 rad)=46 dB.

An investigation into ways to reduce the total harmonic distortion from the Fringe Rate Demodulator should be undertaken to stretch its dynamic range. An examination

of different frequency-to-voltage converters or designs for converters built from discrete components may permit the dynamic range of the converter to be raised, too.

G. COMPLEXITY

The Fringe Rate Demodulator is easily the least complicated of the three demodulators evaluated in this dissertation. Apart from the receiver section, which each of the three schemes have in common, there are only seven integrated circuits in all, although the Altera EP310 Erasable Programmable Logic Device (EPLD) is admittedly a complicated one. However, the logic contained in it is quite simple.

H. APPROXIMATE COST

In Table XI we show the cost of the Fringe Rate Demodulator. In our implementation of the Fringe Rate Demodulator, we used an LF356 Operational Amplifier as the optional inverter and we used one of the four operational amplifiers within an LF444 Quad Operational Amplifier to perform the integration function. The only reason we did not use the LF444 for both functions is because we were using it for something else in another circuit. If one examines the receiver section (see Chapter IX), one discovers that the summing amplifier used in the receiver to remove D (the fixed offset of the interferometric output from 0 V) is one of the two operational amplifiers within an Analog Devices AD712. The LF444 could provide all three of the operational amplifiers needed in the Fringe Rate Demodulator, saving $4.56, or roughly 5% of the cost.

The EP310 and the three low-noise receiver amplifiers (OPA-111) together comprise around 80% of the whole cost of the demodulator. Therefore, finding less costly replacements is an attractive idea, since a low-noise receiver is not required to generate the requisite square waves. If we used combinational logic gates, two LF444 quad operational amplifiers, and a quad comparator would reduce the cost to less than $30.00.

Table XI Calculation of the cost of the integrated circuits used in the Fringe Rate Demodulator.

Part ID	Description	Quantity Required	Price	Source of Price	Total Cost of Part
EP310	Eraseable Programmable Logic Device (EPLD)	1	$44.70	Altera Corporation	$44.70
LM2917N	Frequency-to-Voltage Converter	1	$1.95	Digi-Key Corporation	$1.95
LF13333	Quad SPST JFET Analog Switch	1	$8.30	Marvac Electronics	$8.30
LM311 (similar to LF311)	Voltage Comparator	2	$0.32	Mouser Electronics	0.64
LF356	Monolithic JFET Input Operational Amplifier	1	$0.96	Digi-Key Corporation	$0.96
OPA-111	Low-noise Op Amp	3	$11.80	Burr-Brown	$35.40
AD712	General Purpose Op Amp	2	$3.60	Analog Devices	$7.20
LF444	Quad Low Power JFET Input Operational Amplifier	1	$1.65	Digi-Key Corporation	$1.65
TOTAL		15			$100.80

I. SUMMARY

In this chapter we have seen that the Fringe-Rate Demodulator is inexpensive, and is appropriate for sensors which generate large amounts of optical phase shift (more than $\pi/2$ rad in amplitude). We saw areas in which the performance might be improved. The inability of this sensor to handle signals below $\pi/2$ radians without gross distortion remains a serious drawback in some applications, however. In the next two chapters, we consider two other demodulation schemes that do not share this limitation.

VII. ASYMMETRIC DEMODULATION

In this chapter we describe a method of passive homodyne demodulation presented by Koo *et al.* [Ref. 16]. Koo's method requires the sine and the cosine of the signal of interest. These are obtainable from the output of an interferometer which uses a 3×3 coupler at its output, the kind in which we are interested. However, as is clear from Equation (5) on page (5), which is

$$\frac{|\,a_k(L)\,|^2}{2} = D + E\cos\left[\xi(t) + \phi(t) - (k-1)\frac{2}{3}\pi\right], \tag{187}$$

the outputs of this coupler are not the sine and the cosine: they are three cosines separated not by 90° but by 120°. We shall ignore the "static" phase shift ϕ (or, equivalently, consider it to be absorbed into the signal of interest, ξ.)

A. OBTAINING THE SINE OF THE SIGNAL OF INTEREST

To obtain the sine and cosine one could pick two of the three outputs arbitrarily, say outputs 1 and 2, and manipulate them as follows.

$$x_1 = D+E\cos(\xi). \tag{188}$$

$$\begin{aligned} x_2 &= D+E\cos\left[\xi-\frac{2}{3}\pi\right] \\ &= D-\frac{E}{2}\cos(\xi)+E\frac{\sqrt{3}}{2}\sin(\xi). \end{aligned} \tag{189}$$

We first subtract D from each term. How to compute D is not made clear by Koo, but we present a method in Chapter VIII.

Let

$$y_1 = x_1 - D = E\cos(\xi). \tag{190}$$

Subtracting D from x_2 removes the constant offset from zero:

$$x_2 - D = -\frac{E}{2}\cos(\xi) + E\frac{\sqrt{3}}{2}\sin(\xi). \tag{191}$$

If we add twice this quantity to the expression given by y_1, we obtain

$$(x_1 - D) + 2(x_2 - D) = E\sqrt{3}\sin(\xi). \tag{192}$$

By suitable rescaling, we can obtain the sine of the signal of interest. Let

$$y_2 = \left[\frac{(x_1 - D) + 2(x_2 - D)}{\sqrt{3}}\right] = E\sin(\xi). \tag{193}$$

We call this method of demodulation asymmetric because before the demodulation process can begin, we must take one output of the interferometer more or less as is, perform algebra on this and another output to get the sine, and totally disregard the third. In Chapter VIII we develop a new technique of passive homodyne demodulation which uses all three outputs in a similar manner, a symmetric manner, whence the name of both the chapter and the method.

B. THE ALGORITHM

In the asymmetric method of demodulation given by Koo, we first take the derivative of the sine and cosine.

$$\dot{y}_1 = \frac{dy_1}{dt} = -E\dot{\xi}\sin(\xi). \tag{194}$$

We multiply y_1 by the derivative of y_2 and we multiply y_2 by the derivative of y_1.

$$\dot{y}_2 = \frac{dy_2}{dt} = E\dot{\xi}\cos(\xi). \tag{195}$$

$$y_1\dot{y}_2 = E^2\dot{\xi}\cos^2(\xi). \tag{196}$$

$$y_2\dot{y}_1 = -E^2\dot{\xi}\sin^2(\xi). \tag{197}$$

$$\begin{aligned} y_1\dot{y}_2 - y_2\dot{y}_1 &= E^2\dot{\xi}[\cos^2(\xi)+\sin^2(\xi)] \\ &= E^2\dot{\xi}. \end{aligned} \tag{198}$$

We can integrate the result to get

$$\begin{aligned} \int[y_1\dot{y}_2 - y_2\dot{y}_1]dt &= \int E^2\dot{\xi}dt \\ &= E^2\int\frac{d\xi}{dt}dt \\ &= E^2\xi. \end{aligned} \tag{199}$$

This method produces a result which depends on the square of the number E. This number depends on the performance of the interferometer, reflecting the contrast between bright and dark fringes. It is desirable to eliminate this multiple. Again, Koo's paper does not address this detail of implementation; in fact, in his models, E and D both are tacitly treated as being 1. In Chapter VIII, we present a method for measuring E, too, which permits its removal from the result.

In discussing Koo's method, Giallorenzi points out that

> All real four quadrant analog [*sic*] multipliers have inaccuracies which will corrupt the detected signal and limit the minimum detectable signal $S(t)$. [Ref. 5, p. 658]

This is an egregious matter if large dynamic range is required but, at the same time, the peak phase shift which can be demodulated is on the order of 1 radian or so. When the peak rises to the level of thousands of radians, this becomes less problematic, for the lowest phase shifts which need to be demodulated are now higher, and so a higher noise floor can be tolerated.

C. SUMMARY

Recall that an interferometer terminated by a 3×3 coupler provides signals which are 120° out of phase from each other. The asymmetric demodulation algorithm described in this chapter requires two signals which are 90° out of phase from each other. To use this method of demodulation, we use one of the three outputs as is, regarding it as the cosine of the signal of interest. We must obtain the sine of the signal of interest in the manner described in this chapter. Obtaining the inverse sine or inverse cosine is ambiguous; with both the sine and the cosine available, the ambiguity vanishes. The ability to track the phase angle through more than just the four basic quadrants (−180° to +180°) is implicitly handled by the integration step.

Perhaps the least appealing feature of this algorithm is its asymmetry, that is, the discarding of a perfectly good output, and the different processing of the two remaining outputs. This objection is not a purely aesthetic one, for intuitively we suspect that a higher ratio of signal to noise could be achieved if no outputs were thrown away. However, there is another important drawback to the asymmetric demodulation algorithm: the output depends on the quantity E, which itself depends on the power in the output of the interferometer. This is a highly undesirable state of affairs because E varies, and we do not want the output of the demodulator to vary with it. In the next chapter, we develop a new method of passive homodyne demodulation which addresses both these deficiencies. We shall return to the asymmetric method of demodulation later when we describe a digital electronic implementation of it.

VIII. SYMMETRIC DEMODULATION

In Chapter VII we described the method of asymmetric demodulation, also called sine-cosine demodulation, which was presented by Koo *et al.* [Ref. 16]. In this chapter, we present a new method which uses all three outputs of the optical interferometer in a symmetric manner.[12] Figure 24 is a block diagram showing how symmetric demodulation is accomplished. The rest of this chapter is devoted to showing that this diagram correctly illustrates how to recover the signal $\xi(t)$ from the interferometric outputs.

A. THE INTERFEROMETRIC OUTPUTS WITH AND WITHOUT DISTORTION

From Equation (5) in Chapter III, we have

$$x_k = \frac{|\, a_k(L)\,|^2}{2} = D + E\cos\left[\xi(t) + \phi(t) - (k-1)\frac{2}{3}\pi\right]. \tag{200}$$

This gives the power from output k of the 3×3 coupler which terminates the optical fiber interferometric sensor, where k can be 1, 2, or 3. For the moment, we shall neglect the "static" phase shift $\phi(t)$, regarding it as part of the signal of interest $\xi(t)$, for example. The form of the three equations was given graphically in Figure 7 of Chapter III, which we repeat here in Figure 25. To make this plot, we used a sinusoidal stimulus

$$\xi(t) = A\sin(\omega t) = 5\pi\sin(2\pi f t). \tag{201}$$

All three interferometric outputs look similar, but they are shifted by 120° from each other. In the plot, the three outputs also are separated from each other vertically so that they can be seen individually, and the sinusoidal stimulus is superimposed on the plot (to a different scale) so that the relationship between the stimulus and the interferometric

---

[12] The author is indebted to Dr. Robert Keolian and Dr. Steven Garrett for discussions which led to the idea described in this chapter.

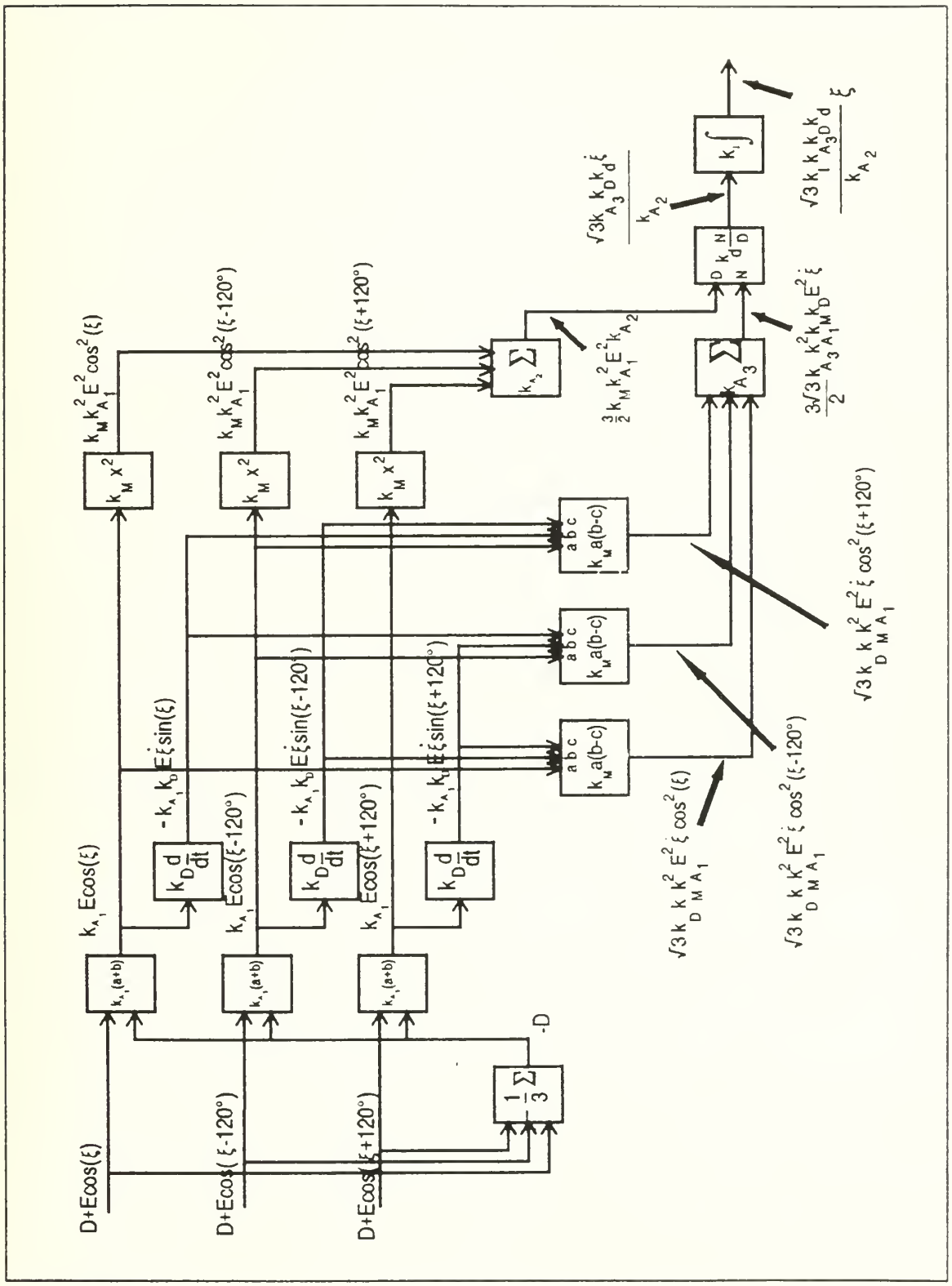

Figure 24 Block diagram of the symmetric demodulation algorithm.

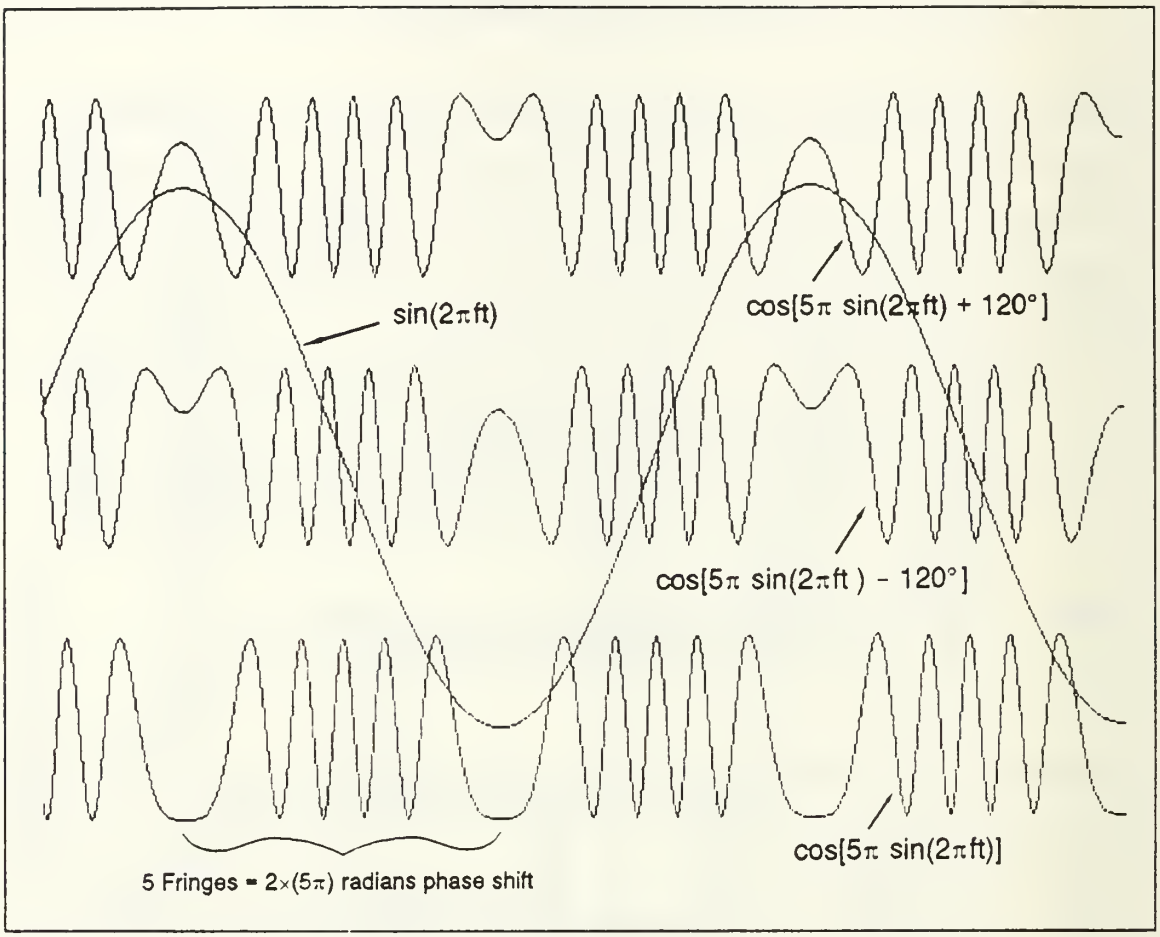

Figure 25 Simulation of an interferometric output with a peak phase amplitude of 5π radians.

outputs can be readily seen.

The simulated waveforms of Figure 25 are free of distortion. However, these images were drawn by computer on a video screen with only moderate resolution (dots per unit length), and so staircase-like jagged edges can be discerned in the curves.

In Figure 26, the upper traces show undistorted outputs of the interferometer we described in Chapter IV when stimulated by a sinusoidal waveform inducing an optical phase shift of π radians. The lower traces show distortion which we believe was due to reflections back into the laser, causing it to operate in an unstable manner. We were able to eliminate the distortion easily by adjusting the current through the laser. However, we believe that long-term stability will require either a temperature controller on the laser to prevent mode-hopping from occurring, or a optical fiber isolator to

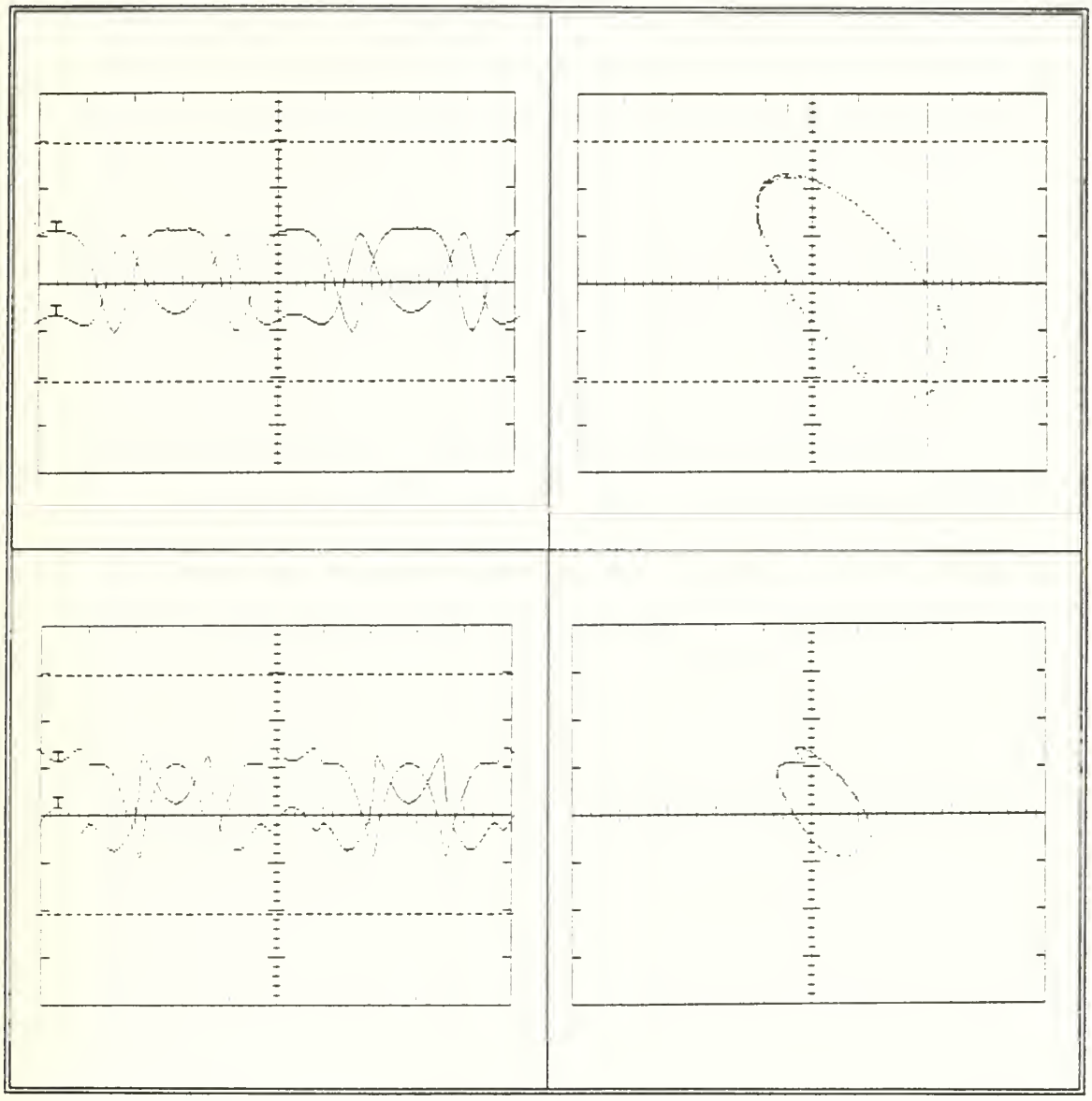

Figure 26 Interferometric outputs for $A = \pi$ rad. Upper traces: no distortion. Lower traces: distortion present. Left side: amplitude *v.* time. Right side: Lissajous figure.

prevent reflections by rotating their polarization. The left-hand side of the figure shows two of the three interferometric outputs plotted vertically against time on the lower axis. The right-hand side of the figure shows one of these outputs plotted against another to yield a Lissajous figure. Because we chose a phase-amplitude of π radians, the elliptical shape is just closed. With smaller phase amplitudes, the figure is not closed; with larger phase amplitudes, it remains closed and retraces the same path repeatedly.

B. MEASURING THE PHASE ANGLE BETWEEN INTERFEROMETRIC OUTPUTS

Before going on to explain how to recover the signal of interest, we shall digress at this point to explain a technique of measuring the actual phase difference between two outputs of the interferometer, using the Lissajous figure. At present, 3×3 optical fiber couplers are made by monitoring the ratio of power in each of the three outputs during fabrication to ensure the desired amount of power in each. This method is entirely suitable in the communications industry, but for interferometric applications, it would be preferable to monitor the phase difference between adjacent outputs and adjust it to be 120°.

In our technique of measuring the actual phase difference, we use a digital oscilloscope such as the Tektronix TEK2430. The plots in Figure 26 were displayed on and printed by a TEK2430. This oscilloscope has the useful feature of permitting measurements of the Lissajous figure's dimensions on the screen. Two separate measurements of the Lissajous figure permit us to compute the phase angle between any two interferometric outputs. We can show this by first considering the two waveforms. For generality, we need not assume that both waveforms have equal amplitudes, and so they take on the form

$$u_1(t) = E_1\cos(\xi(t)) \qquad \text{and} \qquad u_2(t) = E_2\cos(\xi(t)-\phi). \tag{202}$$

In these equations, the amplitudes are E_1 and E_2, $\xi(t)$ is the signal of interest, and ϕ is the phase angle between the two outputs. We first measure $u_1(t)$ at some time t_0 when $u_2(t)=0$. We can readily solve for the phase angle of $u_1(t)$ at this instant:

$$\xi(t) = \pm\cos^{-1}\left(\frac{u_1(t_0)}{E_1}\right)+n2\pi\ , \tag{203}$$

where n is an arbitrary integer. Knowing that $u_2(t)=0$ and that its phase must contain the same phase component $\xi(t)$, we can find the phase difference ϕ:

$$\xi(t)+\phi = \frac{\pi}{2}+m\pi$$

$$\phi = \frac{\pi}{2}+m\pi-\xi(t) \qquad (204)$$

$$\phi = \frac{\pi}{2}+m\pi-n2\pi\mp\cos^{-1}\left(\frac{u_1}{E_1}\right),$$

where m, like n, is an arbitrary integer.

Thus we only require two measurements to obtain the phase angle ϕ. We need the peak amplitude E_1 of the signal $u_1(t)$ and we need its amplitude at a time when the second signal $u_2(t)$ is zero. From their ratio and simple trigonometry, the phase angle can be obtained.

The oscilloscope we used makes it very easy to measure E_1. Actually, it is easier to measure $2E_1$, which is the greatest width of the elliptical Lissajous figure. We then measure the amplitude of the same signal along the axis where the second signal is zero. Actually, it is easier to measure the entire breadth of the Lissajous figure along this axis, which gives $2u_1(t)$ at time $t=t_0$. The ratio $(2u_1(t_0))/(2E_1)$ is, of course, the same as $u_1(t_0)/E_1$.

As an example of how to use this technique, we measured $2E_1=93.2$ mV and $2u_1(t_0)=74.0$ mV. For these values, the phase difference is

$$\phi = 90^\circ+\cos^{-1}\left(\frac{2u_1}{2E_1}\right) = 127^\circ. \qquad (205)$$

Notice that we have neglected the arbitrary integers m and n in this expression. This calculation give a phase difference which is 7° away from the 120° which we would have preferred the couplers to deliver. On the other hand, this difference is good empirical evidence for the robustness of the technique which we shall now describe, for we still managed to recover signals with excellent fidelity from this imperfect 3×3 coupler.

C. RECOVERING THE SIGNAL OF INTEREST

Our first goal in the processing of the three interferometric output signals is to eliminate the constant D from the three outputs by subtraction. An easy way to compute D in a circuit is to add up all three signals and divide by 3. A typical implementation of an adder has some gain factor k_1 associated with it. We will arrange matters so that $k_1 = -1/3$. If we add up the three signals, we get

$$\begin{aligned} S_1 &= k_1 \sum_{i=1}^{3} x_i = k_1 \sum_{i=1}^{3} \left\{ D + E\cos\left[\xi - (k-1)\frac{2}{3}\pi \right] \right\} \\ &= 3k_1 D + k_1 E \sum_{i=1}^{3} \cos\left[\xi - (k-1)\frac{2}{3}\pi \right]. \end{aligned} \tag{206}$$

On page 255 in Appendix A we prove the theorem given there as Equation (342), which is

$$\sum_{k=0}^{N-1} e^{j\left[\theta - k\frac{2\pi}{N}\right]} = \sum_{k=0}^{N-1} \left\{ \cos\left(\theta - k\frac{2\pi}{N} \right) + j\sin\left(\theta - k\frac{2\pi}{N} \right) \right\} = 0. \tag{207}$$

The real part of this expression can only be zero if

$$\sum_{k=0}^{N-1} \cos\left(\theta - k\frac{2\pi}{N} \right) = 0. \tag{208}$$

This is geometrically obvious since vectors comprising the sides of an equilateral, regular polygon must sum to zero because the polygon is closed. Applying this to Equation (206), we see that

$$S_1 = 3k_1 D = D. \tag{209}$$

Because we have a way of computing D (or, rather, its negative), we can subtract it from the interferometric outputs. This is akin to removing a constant offset from a signal by the use of lowpass filtering, except that using such a filter would preclude the correct processing of low frequency components in the signal of interest. What is worse, however, is that signals of interest with very small amplitude produce signals x_k which do

not vary much. This does not mean that they are always close to D, however; it only means that $\cos\left[\xi-(k-1)\frac{2}{3}\pi\right]$ is nearly constant. However, this constant multiplies E to produce different levels of signal in each of the three signal paths. Putting these signals through lowpass filters merely changes the constant offset, rather than eliminating it totally.

In Figure 24, three adders are used to perform the subtraction. Let their outputs be called x_{11}, x_{21}, and x_{31}. Because these adders have some gain, k_{A_1}, we have

$$x_{k1} = k_{A_1} E \cos\left[\xi-(k-1)\frac{2}{3}\pi\right]. \tag{210}$$

The next step is to differentiate each of the x_{k1}. The differentiators, too, have their own gain, k_D. The outputs of the three differentiators are

$$x_{k2} = k_D \dot{x}_{k1} = -k_D k_{A_1} E \dot{\xi} \sin\left[\xi-(k-1)\frac{2}{3}\pi\right]. \tag{211}$$

The three derivatives are simulated in the plots of Figure 27 for the same case as in Figure 25. Again, the sinusoidal stimulus is shown for reference, although still not to the same vertical scale as the derivatives. In the plots, we have dropped the second subscript, as if D were zero in x_k.

In the last chapter we described asymmetric demodulation and we went to some trouble to obtain the sine and cosine of the signal of interest from a set of three interferometric outputs, each 120° out of phase from the other. From the sine and cosine we obtained the derivative of each. It was an easy matter to cross-multiply, subtract, and integrate the result to obtain a scaled replica of the signal of interest. How can we extend this idea so that all three signals might be used? In discussions with the author, Dr. Robert Keolian had the insight to apply phasor techniques to this problem. Now phasors are a tool which only apply to linear systems: processing which entails multiplication is non-linear. One can *add* two phasors together and get another phasor. One cannot *multiply* two phasors together at all. When two sinusoids are multiplied

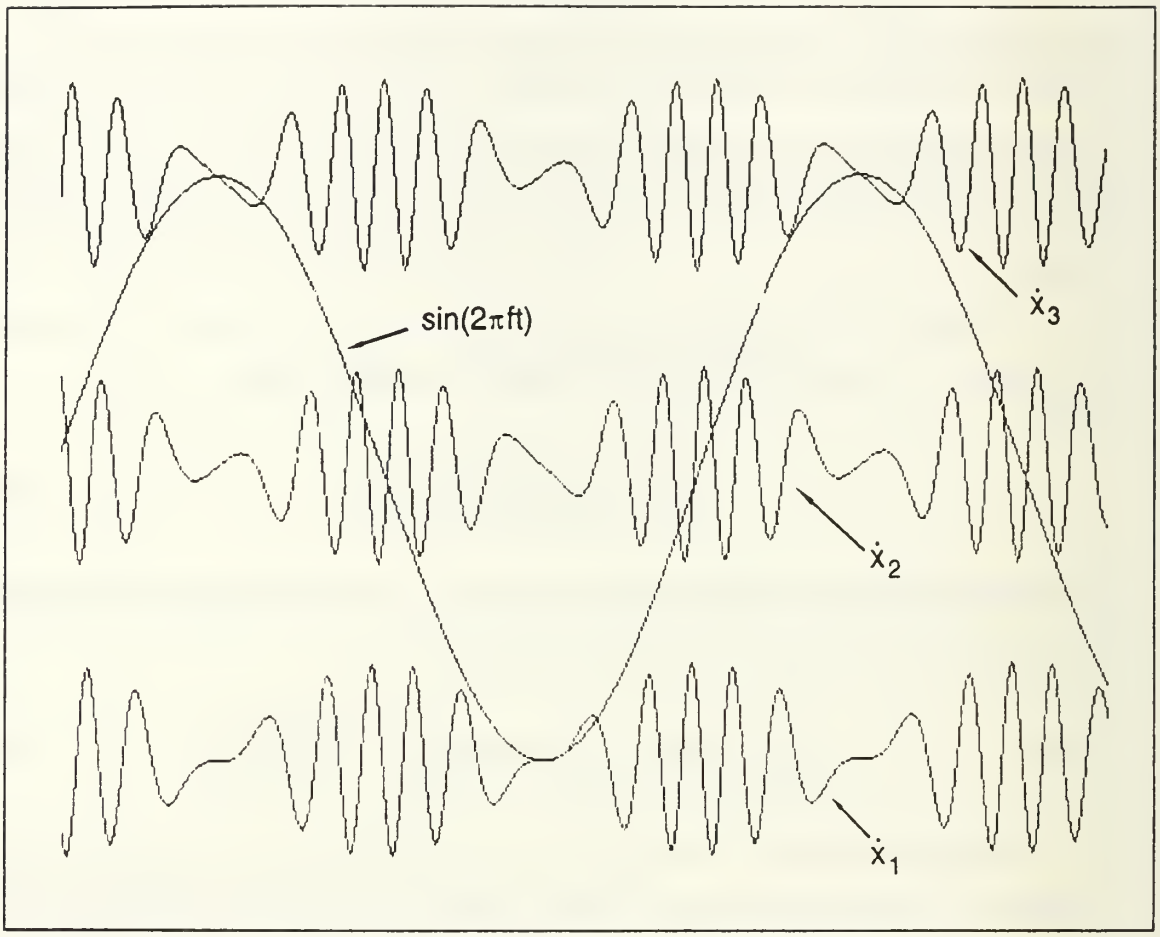

Figure 27 Simulations of the derivatives of the three interferometric outputs.

together, the result consists of the sum of two sinusoids. One of these has a frequency which is the sum of the input frequencies; the other has a frequency which is the difference between the input frequencies. If the two inputs have the same frequency, which is the case for two signals represented by two phasors, their product contains a term at twice the input frequency and a constant term. In what follows, we shall ignore the constant term and focus our attention on the sinusoidal term at twice the input frequency. The output at twice the input frequency could be represented as a phasor, too, but it would normally not be shown on the same phasor diagram because of the fact that its frequency is different.

We shall take the liberty of breaking the rule that phasors at different frequencies never be discussed in the same sentence or drawn on the same diagram. However, the

"phasor" representing the output signal at twice the frequency of the input signals is not a phasor in the conventional sense. Although in the figures which follow we show this output signal as an arrow in the complex plane, superimposed on a phasor diagram, the reader must be mindful that its frequency is different from that of the phasors in the diagram and the phase relationships between the various phasors and the output "phasor" are not constant. We shall be careful to use quotation marks around the word *phasor* whenever this output signal is being referred to. If the reader rebels at the heresy of using phasor techniques in non-linear signal processing, he may be somewhat mollified to know that without this highly unorthodox approach we would never have discovered the algorithm which we explain in this chapter.

In Figure 28 we show the phasor approach applied to asymmetric demodulation. The small, black arrows show the two signals, sine and cosine, that the asymmetric method uses. The cosine leads the sine, so it is the arrow labelled jE; the sine is labelled E. The derivatives are the intermediate-sized arrows with white interiors. The derivative of the E phasor is the $j\omega E$ phasor; the derivative of the jE phasor is the $-\omega E$ phasor. The large, diagonally-striped arrows shows the cross-product "phasors" which the asymmetric method produces. Both cross-products are the same. The product of E and the derivative of jE is $-\omega E^2$. The product of jE and the derivative of E also is equal to $-\omega E^2$.

At this point, the phasor approach collapses, for according to the asymmetric demodulation technique, the difference between these two cross-products is the derivative of the signal of interest. But the difference between these two "phasors" is zero; only their sum would yield a non-zero, real result. This problem evaporates if we stick to a trigonometric description of the signal processing; it only occurs because we have used the wrong tool, the phasor tool. Yet the geometric interpretation provided by the phasor methods made the discovery of the method a reality. Dr. Keolian's insight was to apply the method to the symmetric demodulation idea despite the obvious error in doing so.

Figure 29 uses phasors to depict the idea behind symmetric demodulation. As was the case in Figure 28 where we used phasors to explain asymmetric demodulation, the small, black arrows represent the outputs of the interferometer, but now there are three,

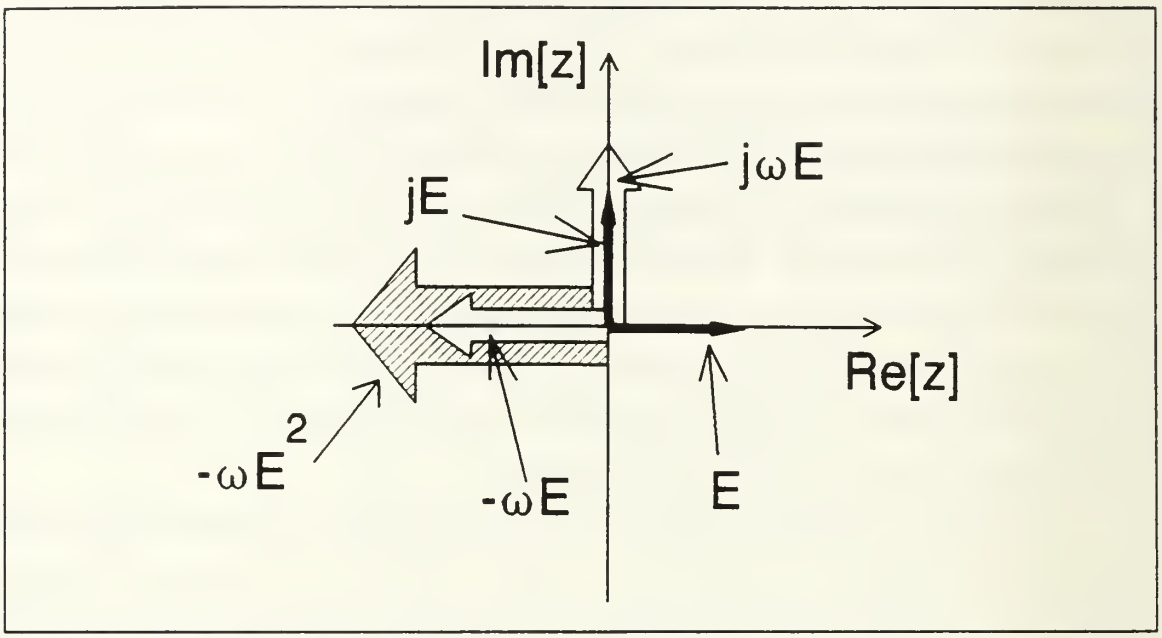

Figure 28 Phasor diagram depicting the operation of the asymmetric demodulation technique.

each separated by 120° from the other. (We use the notation $M\angle\theta$ to denote the complex number of magnitude M and phase angle θ.) The derivatives of these three signals are shown in the intermediate-sized, white arrows. In dotted outlines, we show the negatives of these three derivatives, too. Note how the derivative of one signal and the negative of the derivative of a second signal bracket the third signal in a symmetric manner. By taking the difference of the two derivatives, a phasor parallel to the third signal is formed.

In asymmetric demodulation, the effect of cross-multiplication of signals and derivatives was to create product "phasors" along the real axis. In symmetric demodulation, the product "phasors" line up along the 0°, 120°, and −120° axes, but because they contain E^2, their sum is not zero, as it would be if phasor addition of multiplied phasors were strictly correct, but the real constant 1.5. In fact, in general, one can divide 360° evenly into N pieces and add the squares of either the sines or the cosines to arrive at a total of $N/2$. Formally, we have the theorem

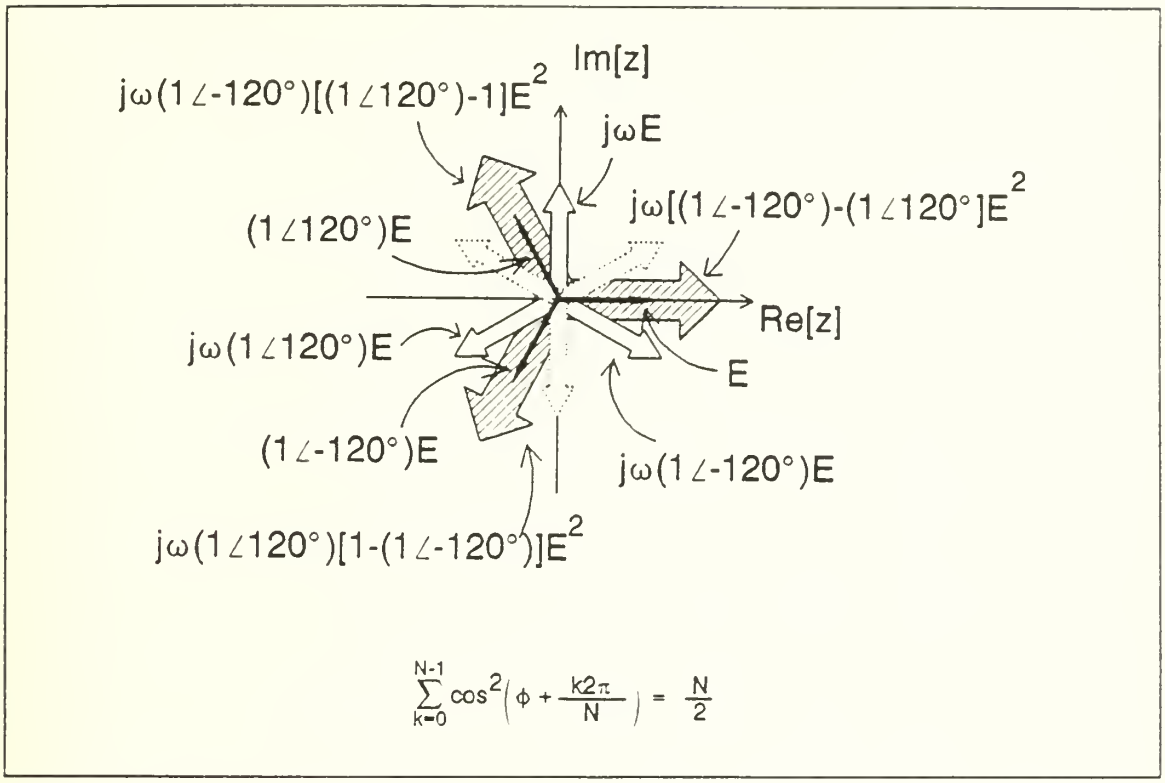

Figure 29 Phasor diagram depicting the operation of the symmetric demodulation technique.

$$\sum_{k=0}^{N-1} \cos^2\left(\phi + \frac{k2\pi}{N}\right) = \sum_{k=0}^{N-1} \sin^2\left(\phi + \frac{k2\pi}{N}\right) = \frac{N}{2} \tag{212}$$

from Equation (344) in Appendix A, where we also provide a proof.

Now that we have arrived through graphical ideas at the basic method of combining derivatives and signals in the method of symmetric demodulation, we can show in mathematical terms what is going on.

We start by combining signal x_{11} with the derivatives of x_{21} and x_{31}.

$$k_M x_{11}(\dot{x}_{21} - \dot{x}_{31}) = k_M k_{A_1} E \cos(\xi) \left[\begin{array}{l} -k_D k_{A_1} E \dot{\xi} \sin\left(\xi - \frac{2}{3}\pi\right) \\ \\ +k_D k_{A_1} E \dot{\xi} \sin\left(\xi + \frac{2}{3}\pi\right) \end{array} \right]. \tag{213}$$

This simplifies to

$$k_M x_{11}(\dot{x}_{21}-\dot{x}_{31}) = k_M k_{A_1}^2 k_D E^2 \dot{\xi}\cos(\xi)\left[-\sin\left(\xi-\frac{2}{3}\pi\right) + \sin\left(\xi+\frac{2}{3}\pi\right)\right]. \tag{214}$$

We can apply to this the trigonometric identity

$$\sin(A+B)-\sin(A-B) = 2\cos(A)\sin(B) \tag{215}$$

to obtain

$$\begin{aligned} k_M x_{11}(\dot{x}_{21}-\dot{x}_{31}) &= k_M k_{A_1}^2 k_D E^2 \dot{\xi}\cos(\xi)\left[2\cos(\xi)\sin\left(\frac{2}{3}\pi\right)\right] \\ &= \sqrt{3}k_M k_{A_1}^2 k_D E^2 \dot{\xi}\cos^2(\xi). \end{aligned} \tag{216}$$

Next we combine signal x_{21} with the derivatives of x_{31} and x_{11}.

$$k_M x_{21}(\dot{x}_{31}-\dot{x}_{11}) = k_M k_{A_1} E\cos\left(\xi-\frac{2}{3}\pi\right)\left[\begin{array}{r} -k_D k_{A_1} E\dot{\xi}\sin\left(\xi+\frac{2}{3}\pi\right) \\ +k_D k_{A_1} E\dot{\xi}\sin(\xi) \end{array}\right]. \tag{217}$$

This simplifies to

$$k_M x_{21}(\dot{x}_{31}-\dot{x}_{11}) = k_M k_{A_1}^2 k_D E^2 \dot{\xi}\cos\left(\xi-\frac{2}{3}\pi\right)\left[-\sin\left(\xi+\frac{2}{3}\pi\right) + \sin(\xi)\right]. \tag{218}$$

If we rewrite this as

$$k_M x_{21}(\dot{x}_{31}-\dot{x}_{11}) = k_M k_{A_1}^2 k_D E^2 \dot{\xi}\cos\left(\xi-\frac{2}{3}\pi\right)\left[\begin{array}{r} -\sin\left(\left[\xi-\frac{2}{3}\pi\right]-\frac{2}{3}\pi\right) \\ +\sin\left(\left[\xi-\frac{2}{3}\pi\right]+\frac{2}{3}\pi\right) \end{array}\right] \tag{219}$$

then we can apply the same trigonometric identity to get

$$k_M x_{21}(\dot{x}_{31}-\dot{x}_{11}) = k_M k_{A_1}^2 k_D E^2 \dot{\xi}\cos\left(\xi-\frac{2}{3}\pi\right)\left[2\cos\left(\xi-\frac{2}{3}\pi\right)\sin\left(\frac{2}{3}\pi\right)\right]$$
$$= \sqrt{3}k_M k_{A_1}^2 k_D E^2 \dot{\xi}\cos^2\left(\xi-\frac{2}{3}\pi\right). \tag{220}$$

Finally we combine signal x_{31} with the derivatives of x_{11} and x_{21}.

$$k_M x_{31}(\dot{x}_{11}-\dot{x}_{21}) = k_M k_{A_1} E\dot{\xi}\cos\left(\xi+\frac{2}{3}\pi\right)\left[\begin{array}{l} -k_D k_{A_1} E\dot{\xi}\sin(\xi) \\ \quad +k_D k_{A_1} E\dot{\xi}\sin\left(\xi-\frac{2}{3}\pi\right)\end{array}\right]. \tag{221}$$

This simplifies to

$$k_M x_{31}(\dot{x}_{11}-\dot{x}_{21}) = k_M k_{A_1}^2 k_D E^2 \dot{\xi}\cos\left(\xi+\frac{2}{3}\pi\right)\left[-\sin(\xi) - \sin\left(\xi-\frac{2}{3}\pi\right)\right]. \tag{222}$$

If we rewrite this as

$$k_M x_{31}(\dot{x}_{11}-\dot{x}_{21}) = k_M k_{A_1}^2 k_D E^2 \dot{\xi}\cos\left(\xi+\frac{2}{3}\pi\right)\left[\begin{array}{l} -\sin\left(\left[\xi+\frac{2}{3}\pi\right]-\frac{2}{3}\pi\right) \\ +\sin\left(\left[\xi+\frac{2}{3}\pi\right]+\frac{2}{3}\pi\right)\end{array}\right] \tag{223}$$

then we can once again apply the same trigonometric identity to get

$$k_M x_{31}(\dot{x}_{11}-\dot{x}_{21}) = k_M k_{A_1}^2 k_D E^2 \dot{\xi}\cos\left(\xi+\frac{2}{3}\pi\right)\left[2\cos\left(\xi-\frac{2}{3}\pi\right)\sin\left(\frac{2}{3}\pi\right)\right]$$
$$= \sqrt{3}k_m k_{A_1}^2 k_D E^2 \dot{\xi}\cos^2\left(\xi+\frac{2}{3}\pi\right). \tag{224}$$

Visualizing a plot corresponding to the manipulations which have been described here without using a computer is no easy feat. In fact, a plot of the difference between two derivatives is very similar to the plots of the derivatives themselves. Figure 30 shows a simulation of these differences in the derivatives for the case $A=5\pi$.

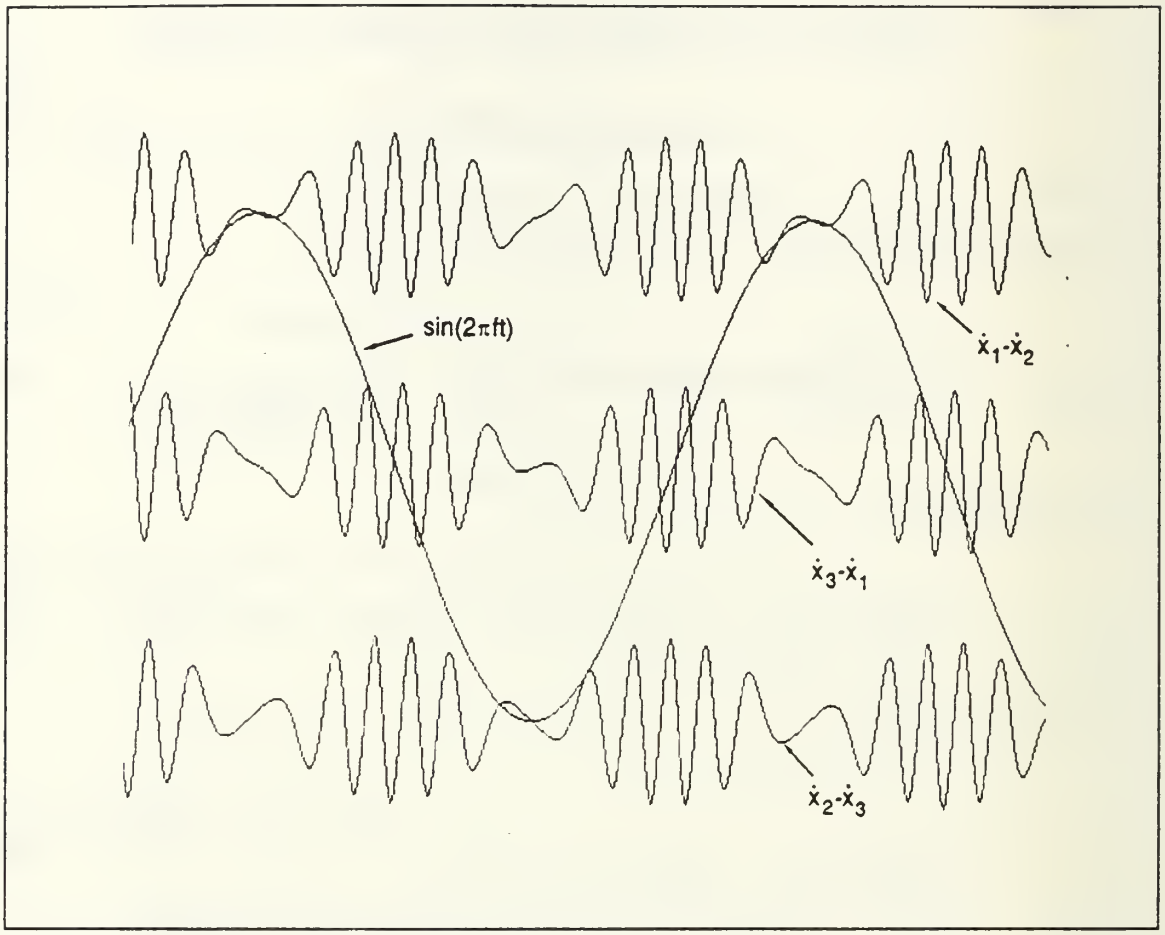

Figure 30 Simulations of the differences between the three possible pairings of derivatives of the interferometric outputs. The stimulus has amplitude $A=5\pi$ radians.

When we sum the three expressions of Equations (216), (220), and (224), using the gain constant k_{A_3}, we obtain

$$\sqrt{3}k_{A_3}k_M k_{A_1}^2 k_D E^2 \dot{\xi}\left[\cos^2(\xi)+\cos^2\left(\xi-\frac{2}{3}\pi\right)+\cos^2\left(\xi+\frac{2}{3}\pi\right)\right] \qquad (225)$$
$$= \frac{3}{2}\sqrt{3}k_{A_3}k_M k_{A_1}^2 k_D E^2 \dot{\xi}.$$

We have applied Equation (212) here.

The three plots in Figure 31 are simulations of the three formulas of Equation (225). Once again, we include the sinusoidal stimulus in order to make clear the relation of the complicated expressions of Equation (225) to the stimulus. Note that the

envelope of the three signals is itself now sinusoidal. How do we extract just the envelope?

If we wanted to, we could simply integrate the expressions in Equation (225) and get a fair replica of the original signal of interest, $\xi(t)$. However, there is a factor of E^2 in the expressions, which implies that the derivatives still depend on the contrast between the dark and light extrema of the interference pattern. Since this is a number which wanders due to changes in laser intensity (which itself depends on the temperature) and due to changes in the polarization angle of the light within the optical fiber interferometric sensor, it would be useful to eliminate this factor.

We can do this by squaring each of the signals x_{k1} and adding them up. The squaring operation can be performed with another multiplier of gain k_M and the addition can be performed with another adder of gain k_{A_2}. That is

$$k_{A_2}\sum_{k=1}^{3} k_M\left\{k_{A_1}E\cos\left[\xi-(k-1)\frac{2}{3}\pi\right]\right\}^2 = \frac{3}{2}k_{A_2}k_M k_{A_1}^2E^2. \qquad (226)$$

We have again applied Equation (212) in computing the sum.

In Figure 32 we illustrate the result of the summation for the example we have been using throughout this chapter in which the amplitude of the stimulus is $A=5\pi$ radians. It should be clear from the figure that the sum of products is indeed proportional to the derivative of the sinusoid displayed with it. In the figure, the amplitudes of each waveform have been scaled for convenience, and so they are not labelled.

Both Equations (225) and (226) include the factor E^2. We can eliminate this factor by dividing Equation (226) into Equation (225). Any practical divider has a gain which we shall call k_d (not to be confused with k_D, the gain of the differentiators discussed above). Division yields

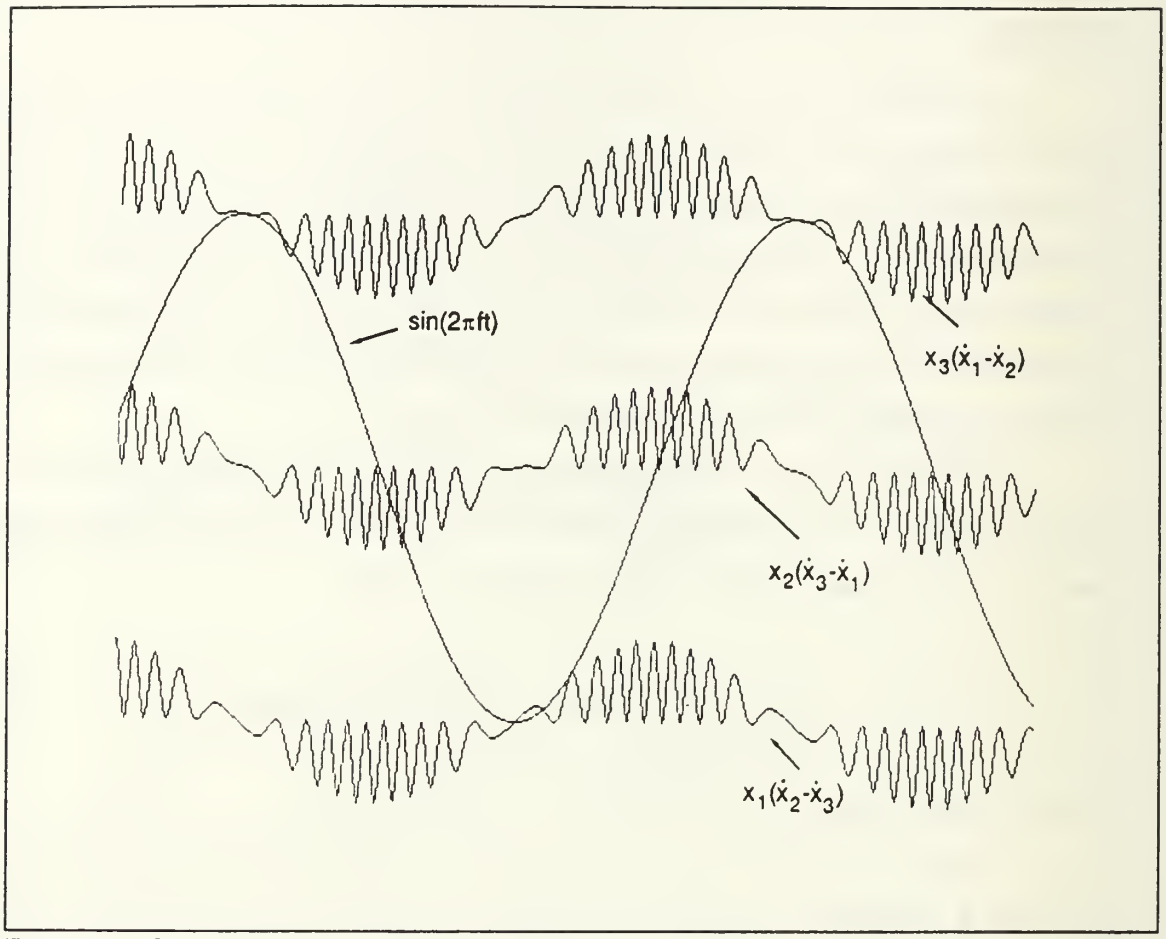

Figure 31 Plots of the products of one signal with the difference between the derivatives of the other two signals.

$$k_d \frac{\frac{3}{2}\sqrt{3}k_M k_{A_3} k_{A_1}^2 k_D E^2}{\frac{3}{2}k_{A_2} k_M k_{A_1}^2 E^2} \dot{\xi} = \frac{\sqrt{3}k_{A_3} k_D k_d}{k_{A_2}} \dot{\xi}. \tag{227}$$

We can integrate this with an integrator of gain k_I to get

$$k_I \int \frac{\sqrt{3}k_{A_3} k_D k_d}{k_{A_2}} \dot{\xi} dt = \frac{\sqrt{3}k_I k_{A_3} k_D k_d}{k_{A_2}} \xi. \tag{228}$$

Obtaining this expression has been the goal of this entire chapter. By the processing algorithm developed here, we have the ability to recover a scalar multiple of

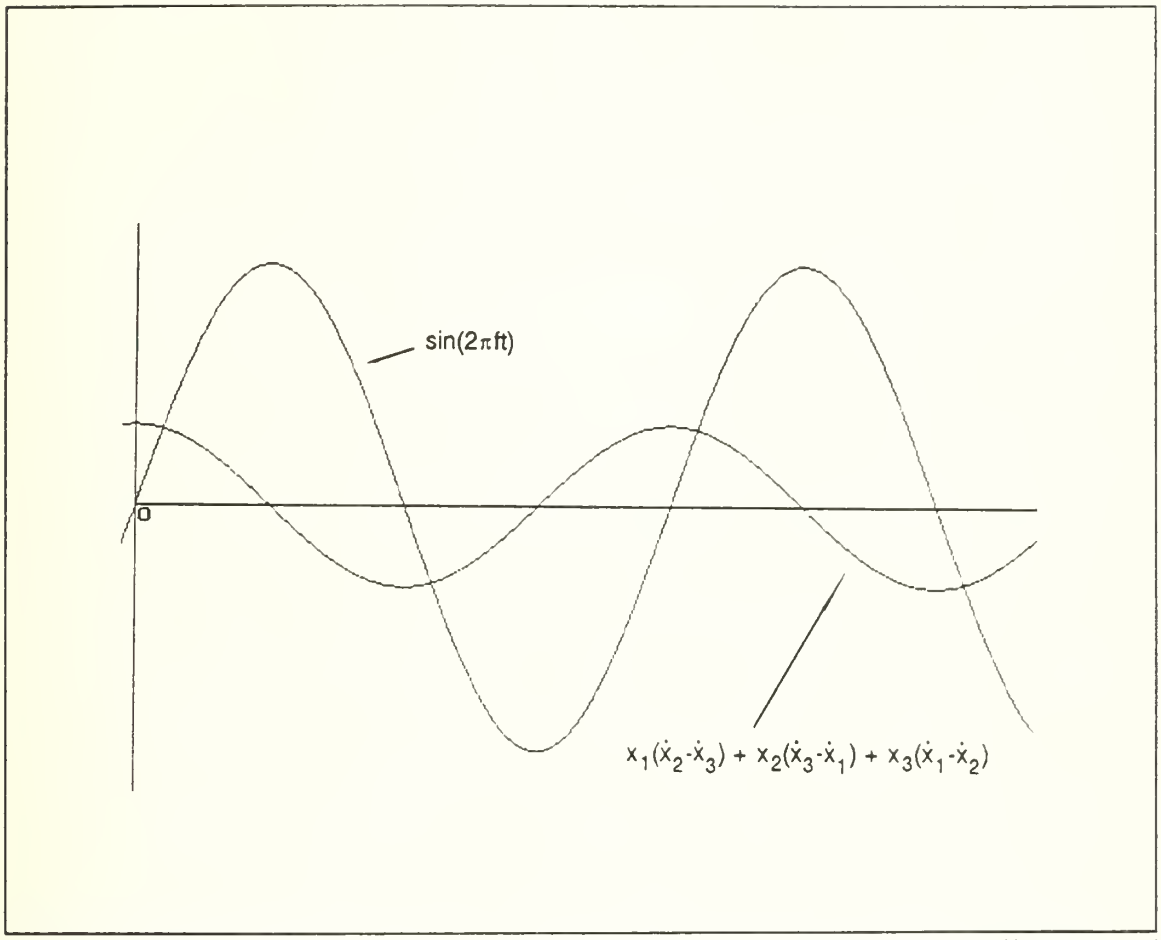

Figure 32 The result of adding up the three products of signals with differences of derivatives. Superimposed on it is the original stimulus of amplitude $A = 5\pi$ radians.

the signal of interest, $\xi(t)$. It is important to recognize that neither D nor E appear in this final expression. This means that the scale factor of the demodulator is independent of the average power in the laser, and it is also independent of the fringe depth.

The scalar multiple consists of factors which we can control in implementing the algorithm. They include the gains of two adders, the gain of three identical differentiators, and the gain of the final integrator. These factors can be chosen within certain constraints to provide $\xi(t)$ scaled to whatever level is desired. In an analog implementation of this scheme, clipping of signals constrains the selection of these parameters at the high-frequency limit, and the noise of the circuit constrains their selection at the low-frequency limit.

In the next chapter, we describe our implementation of this algorithm with analog electronics. In Chapter XI, we measure the performance of this implementation.

IX. DESIGN OF A SYMMETRIC ANALOG DEMODULATOR

In the last chapter we analyzed a new method of passive homodyne demodulation which we call symmetric demodulation, due to the fact that all three outputs of the optical fiber interferometric sensor are processed in the same (symmetric) manner. In this chapter we apply the analysis to the implementation of the technique in analog electronics.

Figure 33 is a schematic drawing of the circuit. The three inputs are shown at the left-hand side where three photodiodes convert the interferometric outputs into current signals. These currents are converted to voltage signals by three transimpedance amplifiers built around operational amplifiers U1, U2, and U3. The summation of the three voltage signals to compute D in Equation (200) in Chapter VIII is performed by the inverting scaling adders built around operational amplifier U4A. This sum is subtracted from the outputs of the transimpedance amplifiers by operational amplifiers U5A, U6A, and U7A.

The outputs of U5A, U6A, and U7A are described by Equation (210) in Chapter VIII. Their derivatives are computed in the differentiators built around operational amplifiers U5B, U6B, and U7B. The Analog Devices AD534 Multipliers U11, U12, and U13 have differential inputs. We apply one signal and a ground to one differential input in each. To the other, we apply the derivatives of the other two signals according to Equations (216), (220), and (224) in Chapter VIII. Each signal is multiplied internally by the difference between the two derivatives of the other two signals. These three outputs are added in the inverting scaling adder built around operational amplifier U14A to yield the result modelled in Equation (225) in Chapter VIII. In order to remove the factor of E^2 in that result, another expression with E^2 in it is computed by the inverting adder built around operational amplifier U4B, which gets its own input from three more AD534 Multipliers, U8, U9, and U10. These multipliers are configured to square their inputs, which are the interferometric outputs stripped of D. The sum of

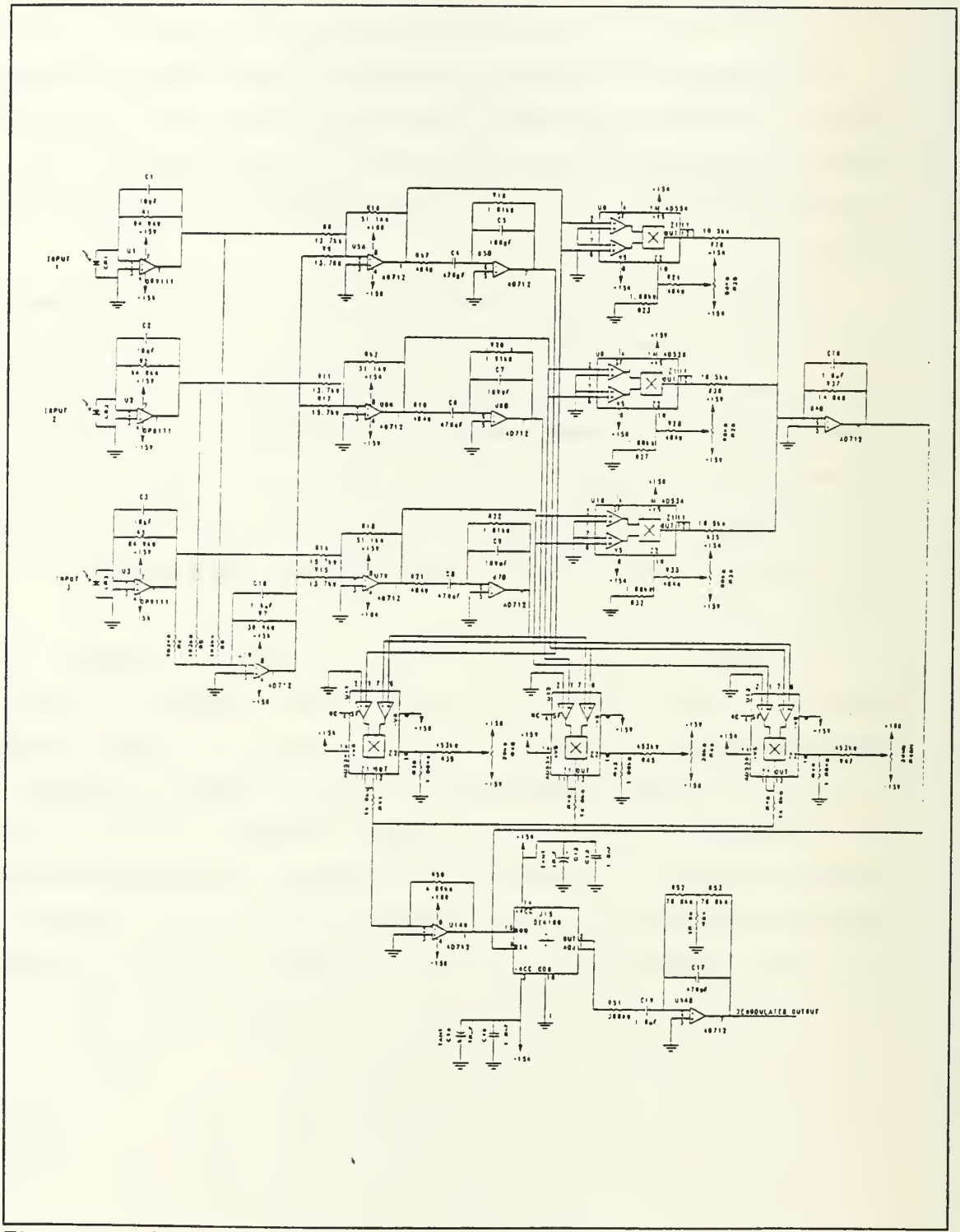

Figure 33 Schematic diagram of an implementation of the symmetric analog demodulation technique in analog electronics. Power-supply bypass capacitors are omitted in this diagram.

these squares is of the form given in Equation (226) of Chapter VIII. The Burr-Brown DIV100 Divider U15 takes the ratio of the output of U14A and that of U4B. This result is proportional to the derivative of the signal of interest, but without dependence on D or E, as shown in Equation (227) in Chapter VIII. The final step in the circuit is to reconstruct from this the signal of interest as shown in Equation (228) of Chapter VIII. The integration is performed by the integrator built around operational amplifier U14B.

We now turn to a detailed discussion of each of the several stages in the Symmetric Analog Demodulator.

A. THE RECEIVERS

The receivers comprise the three photodetectors CR1, CR2, and CR3 together with the three transimpedance amplifiers built around operational amplifiers U1, U2, and U3. These three amplifiers are Burr-Brown OPA111s. They feature very low bias currents of, at most, 2 pA, which contribute only 130 nV to the output offset voltage when passed through the 64.9 kΩ feedback resistors R1, R2, and R3.[13] The input voltage offset is less than 500 μV. This offset voltage appears with gain 1 at the output of the transimpedance amplifier. The maximum drift in input offset current is 5 μV/K; over 50 K of temperature drift, this amounts to no more than a 250 μV drift in the 500 μV figure previously mentioned for a total of no more than 750 μV. Although this amount is far larger than that due to the bias current, it is nonetheless very small. The unity gain bandwidth of the OPA111 is 2 MHz.

The OPA111 also provides very low voltage noise, no more than 40 nV/$\sqrt{\text{Hz}}$ at a frequency of 100 Hz, and typically only 15 nV/$\sqrt{\text{Hz}}$. Since this is the input stage of the entire circuit, we wish to minimize the contribution of the receiver to the overall noise, so the OPA111 makes a good choice.

---

[13] As is the case in nearly all the work described in this dissertation, we used resistors with 1% tolerance. This was largely for convenience, because they were available. In many cases, resistors of lower tolerance could have been used. The main exceptions to this statement are the active sub-circuits such as integrators and differentiators.

When the laser's monitor current was 58.2 μA (indicating that the laser diode was emitting 7.1 mW optical power), the three photodiodes produced measured voltages D=26.3 mV, 25.9 mV, and 29.0 mV across transimpedance amplifiers with 500 Ω in the feedback path. The fluctuation in these voltages was E=9 mV, 10 mV, and 10 mV. We increased the resistances to 64.9 kΩ in order to raise the peak voltages to around 5 V under these conditions. The value 5 V was about half-way through the range in which we desired to work, −10 V to +10 V. This allowed room for fluctuations of the laser power to higher levels without saturating the transimpedance amplifiers. These changes altered the voltages from the transimpedance amplifiers to

$$D \approx (150\ \mu\text{W})\left(370\ \frac{\text{mA}}{\text{W}}\right)(64.9\ \text{k}\Omega) \qquad (229)$$
$$= 3.6\ \text{V}.$$

and

$$E \approx (55\ \mu\text{W})\left(370\ \frac{\text{mA}}{\text{W}}\right)(64.9\ \text{k}\Omega) \qquad (230)$$
$$= 1.3\ \text{V}.$$

In the laboratory, we used fairly lengthy (≈1 m long) coaxial leads to transmit the currents from the photodiodes to the transimpedance amplifiers. The capacitance presented by these leads was sufficient to act as a differentiator of the interferometric signals, enhancing their high frequencies. We compensated for this empirically by placing 10 pF capacitors C1, C2, and C3 across the feedback. We believe these could be reduced or eliminated if more attention were paid to lead capacitances by placing the photodiodes in close proximity to the amplifiers.

The choice of operational amplifiers throughout the rest of the circuit was not as critical. We selected Analog Devices AD712 dual precision operational amplifiers. These have a higher unity-gain bandwidth than the OPA111s, 4 MHz. Their voltage noise is typically 45 nV/√Hz at 100 Hz, higher than the typical value of 15 nV/√Hz for the

OPA111, but still respectably small. Their input offset voltage is at most 3 mV. Their input bias current has a maximum of 75 pA. These are good, general-purpose operational amplifiers.

In Chapter VIII, Equation (209) implied that the averaging circuit implemented around operational amplifier U4A needs to have gain $k_f = -1/3$. We can achieve this by picking 102 kΩ input resistors R4, R5, and R6 and a 34.0 kΩ feedback resistor R7. The design of summing amplifiers is explained in numerous books on operational amplifiers (for example, see Sedra and Smith [Ref. 17]) and so will not be further discussed here, except to say that we also added a 1 μF feedback capacitor C18 in parallel with the 34.0 kΩ resistor R7 to eliminate the ripple in the output. The ripple was due to the fact that although each interferometric output is assumed to have equal central values D and peak deviations E from this value; in fact these values are not all equal to one another. Furthermore, the phase differences between different legs are not exactly 120°. As a result, the sum is not a constant. The capacitor masks the variation in the result. Although it only produces an approximation of the theoretical constant D, we found that the amount of constant offset left after the subsequent addition stage in U5A, U6A, and U7A was not so severe as to render the technique of symmetric demodulation useless.

The summing circuits U5A, U6A, and U7A are designed to provide the summing gain k_{A_1} of Equation (210) in Chapter VIII. Again we want to let these amplifiers have peak outputs of 5 V to permit fluctuations in laser power without causing saturation of the amplifiers. Since these summers remove D from the signal, the amplitudes coming out of them is dependent on E and the gain of the summers. From Equation (230) we know that $E = 1.3$ V. So we should pick the gain to be

$$k_{A_1} = \frac{5\ \text{V}}{1.3\ \text{V}} = 3.8. \tag{231}$$

We can achieve roughly this level of gain (precision is not important here because the signal levels are so highly variable) by selecting 13.7 kΩ input resistors and 51.1 kΩ feedback resistors. For this choice, we actually achieve

$$k_{A_1} = \frac{51.1\ \text{k}\Omega}{13.7\ \text{k}\Omega} = 3.73. \tag{232}$$

The next step in the demodulation technique is to differentiate the outputs of the summing amplifiers U5A, U6A, and U7A. Operational amplifiers U5B, U6B, and U7B are configured to do this. Figure 70 in Appendix A shows a generalized circuit to perform differentiation. We present a detailed analysis of the circuit in that appendix. The key results are given in Equations (399), (405), and (407). The first of these equations gives the transfer function $G(f)$ of the differentiating circuit if the two pole frequencies are equal to one another and if the operating frequency is well below this.

$$G(f) = \frac{V_{OUT}}{V_{IN}} \approx -R_2 C_1 j2\pi f = k_D. \tag{233}$$

The second of these equations gives the relative error in the magnitude of the gain, which depends on how far away from the pole frequency f_p we elect to operate.

$$\epsilon_M = -\frac{1}{1+\left(\frac{f_p}{f}\right)^2}. \tag{234}$$

The third of these equations gives the error in the phase of the gain, which, likewise, depends on how far away from the pole frequency we elect to operate.

$$\epsilon_P = -2\tan^{-1}\left(\frac{f}{f_p}\right). \tag{235}$$

We designed the circuit to handle peak phase shifts of 100 radians when the signal of interest had a frequency of 200 Hz. The time for the signal of interest to change from zero to its peak amplitude is a quarter of a cycle, or $\pi/2$ radians. So if the peak phase shift is A, there are

$$\frac{A}{\left(\frac{\pi}{2}\right)} \tag{236}$$

cycles of the interferometric output in a quarter cycle of the signal of interest. The period of a cycle is T, so a rough approximation of the peak frequency present in the signal of interest is

$$\frac{A}{\left(T\frac{\pi}{2}\right)} = \frac{2Af}{\pi}. \tag{237}$$

Thus we expect frequencies up to

$$\frac{2(100 \text{ rad})(200 \text{ Hz})}{\pi} = 12.7 \text{ kHz}. \tag{238}$$

We can use this value, along with our desire to keep the phase error less than 2° at this peak frequency, to choose the pole frequency.

$$\begin{aligned} \epsilon_p &= -2\tan^{-1}\left(\frac{f}{f_p}\right) \\ 2^\circ &< \left|-2\tan^{-1}\left(\frac{12.7 \text{ kHz}}{f_p}\right)\right|. \end{aligned} \tag{239}$$

From this, we conclude that we must pick $f_p = 728$ kHz. This means that

$$R_1C_1 = R_2C_2 = \frac{1}{f_p} = 219 \text{ ns}, \tag{240}$$

which we get by applying Equation (397) in Appendix A.

In picking the gain of the differentiator, we have a conflict between what we would like the gain to be and what the AD712 can deliver. We still want a 5 V margin between the expected peak signal and the upper limit of 10 V we want to impose. For a simple, sinusoidal signal of interest of the form

$$\xi = A\sin(2\pi ft), \tag{241}$$

the derivative of the interferometric outputs (after passing through the summers) is

$$\begin{aligned}\dot{\xi} &= k_D \frac{d}{dt} k_{A_1} E\cos[A\sin(2\pi ft)] \\ &= -2\pi f k_D k_{A_1} AE\cos(2\pi ft)\sin[A\sin(2\pi ft)].\end{aligned} \tag{242}$$

To ensure that, when $f=200$ Hz and $A=100$ rad, we still do not get more than 5 V from the circuit, we set

$$\begin{aligned}5\ \text{V} &= 2\pi f k_D k_{A_1} AE = 2\pi f R_2 C_1 k_{A_1} AE \\ R_2 C_1 &= \frac{5\text{V}}{2\pi f k_{A_1} AE}\ .\end{aligned} \tag{243}$$

We sought a peak output of 5 V from the adders U5A, U6A, and U7A, so we will treat

$$\frac{5\ \text{V}}{k_{A_1} E} \approx 5\ \text{V}. \tag{244}$$

Hence

$$\begin{aligned}R_2 C_1 &= \frac{1}{2\pi Af} \\ &= \frac{1}{2\pi(100\text{rad})(200\text{Hz})} \\ &= 7.96\ \mu\text{s}.\end{aligned} \tag{245}$$

But at high frequencies, the AD712 will is not guaranteed to sustain more than a 3 MHz gain-bandwidth product. That is

$$\begin{aligned} \text{Gain} \times \text{Bandwidth} &= 3\ \text{MHz} \\ (2\pi R_2 C_1 f) \times \text{Bandwidth} &= 3\ \text{MHz} \\ \text{Bandwidth} &= \frac{3\ \text{MHz}}{(2\pi R_2 C_1 f)}. \end{aligned} \tag{246}$$

The maximum permissible bandwidth is dictated by the maximum frequency f in this equation. Setting the bandwidth equal to the maximum frequency, we get

$$\begin{aligned} f &= \sqrt{\frac{3\ \text{MHz}}{2\pi R_2 C_1}} \\ &= \sqrt{\frac{3\ \text{MHz}}{2\pi(7.96\ \mu\text{s})}} \\ &= 245\ \text{kHz}. \end{aligned} \tag{247}$$

But earlier we decided we needed 728 kHz for the pole frequency. Figure 34 is a Bode plot of the gain of the AD712 and of the differentiator gain characteristic we want to achieve. As long as we demand less gain than the operational amplifier can provide, the feedback control loop is closed, and our desired gain is the actual gain of the circuit. But if the gain we want gets too big, the operational amplifier no longer has enough excess loop gain to keep control: the amplifier's own transfer characteristic becomes dominant. As the figure makes clear, we must compromise by lowering the gain of the differentiator until its characteristic peaks at the pole frequency, 728 kHz, where it intersects the gain characteristic of the operational amplifier. The new value of the gain is

$$\begin{aligned} R_2 C_1 &= \frac{3\ \text{MHz}}{2\pi f^2} \\ &= \frac{3\ \text{MHz}}{[2\pi(728\text{kHz})^2]} \\ &= 901\ \text{ns}. \end{aligned} \tag{248}$$

By trial and error, we find combinations of R_1, R_2, C_1, and C_2 which correspond to

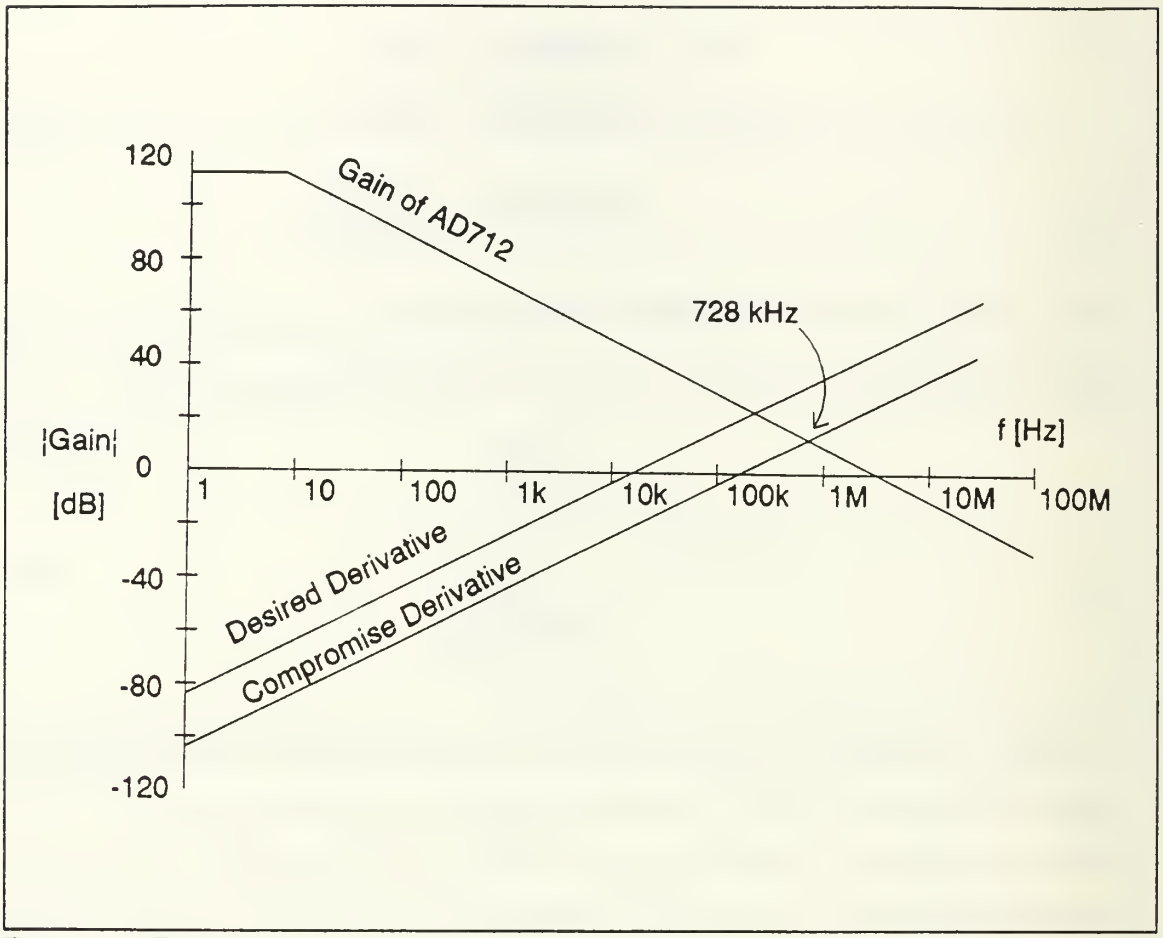

Figure 34 Design of a Differentiator. A compromise is necessary in setting the gain of the differentiator to avoid exceeding the gain-bandwidth product of the amplifier, an AD712 in this case.

available values of the components and which meet the conditions we have derived in Equations (240) and (248). A suitable combination is

$$\begin{aligned} R_1 &= 464\ \Omega & C_1 &= 470\ \text{pF} \\ R_2 &= 1.91\ \text{k}\Omega & C_2 &= 100\ \text{pF} \end{aligned} \tag{249}$$

and these are the values in the schematic in Figure 33 on page 133. The gain constant for the differentiator thus is

$$k_D = -R_2C = -901 \text{ ns.} \tag{250}$$

The multipliers U11, U12, U13, U8, U9, and U10 in the schematic are very easy to use. Three of them are used to compute the cross-product of interferometric signals with the difference in the derivatives of the other two signals. These are the multipliers U11, U12, and U13.

One differential pair of inputs is one interferometric output (with D subtracted off) and ground (zero). The other pair consists of the outputs of two differentiators. Their difference is computed internally to these AD534 multipliers and the product is produced at the output.

The squares of the interferometric outputs (with D subtracted off) are computed by U8, U9, and U10. Later on in the circuit, the denominator input to the DIV100 (U15) must be positive. To guarantee this, we connected these three multipliers to produce negative squares. So the inputs were provided to a non-inverting terminal of one of the differential inputs and to an inverting terminal on the other differential input. The remaining input terminals were connected to ground.

The AD534 has a built-in multiplicative scale factor of 0.1 V^{-1}. Thus two full scale inputs (10 V is full scale) will produce an output of (0.1 V^{-1})(10 V)(10 V) = 10 V.[14] Since we have been assuming that peak signal levels of 5 V are present at the outputs of all stages, we expect to see (0.1 V^{-1})(5 V)(5 V) = 2.5 V. The small signal bandwidth of the AD534 is 1 MHz. Its noise spectral density is large compared to that associated with good operational amplifiers: 800 nV/$\sqrt{}$Hz at 10 kHz; it is larger at 100 Hz, about 900 nV/$\sqrt{}$Hz.

The adder in U14A is very similar to that in U4A described earlier. To compute the required gain, we make use of Equation (225) in Chapter VIII. It gives the output of this adder as

---

[14] The scale factor can be adjusted, but we have not used this feature. Analog Devices has a new multiplier, the AD734, which has a scale factor which can vary dynamically. By varying the scale factor in a suitable manner, division is made possible, in addition to multiplication.

$$\frac{3}{2}\sqrt{3}k_{A_3}k_M k_{A_1}^2 k_D E^2 \dot{\xi}. \tag{251}$$

We want this to peak at 5 V when $A = 100$ rad and $f = 200$ Hz. So

$$\begin{aligned} \frac{3}{2}\sqrt{3}k_{A_3}k_M k_{A_1}^2 k_D E^2 \dot{\xi} &= -\frac{3}{2}\sqrt{3}k_{A_3}k_M k_{A_1}^2 k_D E^2 A 2\pi f \sin[A\sin(2\pi f t)] \\ 5\ \text{V} &> \frac{3}{2}\sqrt{3}k_{A_3}(0.1\ \text{V}^{-1})(3.8)^2(901\ \text{ns})(1.3\ \text{V})^2 A 2\pi f \\ k_{A_3} &= \frac{2(5\ \text{V})}{3\sqrt{3}(0.1\ \text{V}^{-1})(3.8)^2(901\ \text{ns})(1.3\ \text{V})^2(100\ \text{rad})2\pi(200\ \text{Hz})} \\ &= 7.0. \end{aligned} \tag{252}$$

We later decided to lower this value in order to accommodate input phase shifts of 239 rad, more than the 100 rad used in this calculation, so our final choice for input resistors to U14A was 14.0 kΩ with a 4.99 kΩ feedback resistor, giving

$$k_{A_3} = \frac{4.99\ \text{k}\Omega}{14.0\ \text{k}\Omega} = 0.356. \tag{253}$$

We now turn to the summer U4B which adds together the squares of the interferometric outputs (with D subtracted off) which are produced by U8, U9, and U10.

From Equation (226) in Chapter VIII,

$$\begin{aligned} \frac{3}{2}k_{A_2}k_M k_{A_1}^2 E^2 &\le 5\ \text{V} \\ k_{A_2} &\le \frac{2(5\ \text{V})}{3k_M k_{A_1}^2 E^2} \\ &= \frac{2(5\ \text{V})}{3(0.1\ \text{V}^{-1})(3.8)^2(1.3\ \text{V})^2} \\ &= 1.37. \end{aligned} \tag{254}$$

We selected input resistor R26, R30, and R35 to be 10.5 kΩ and the feedback resistor R37 to be 14.0 kΩ, giving an actual value of

$$k_{A_2} = 1.33. \tag{255}$$

The outputs of the two adders U14A and U4B form the numerator and denominator inputs respectively to the Burr-Brown DIV100 (U15). The DIV100 has a small signal bandwidth of 350 kHz. The denominator needs to be greater than 250 mV for reasonable accuracy, and it must be positive. As mentioned above, this was easily arranged by causing the multipliers U8, U9, and U10 to generate negative squares. Subsequently U4B inverted the sum, so this constraint was met.

The DIV100 has a scale factor

$$k_d = 10 \text{ V}. \tag{256}$$

In the range 10 Hz to 10 kHz, the DIV100 generates voltage noise between 370 μV/$\sqrt{\text{Hz}}$ and 1 mV/$\sqrt{\text{Hz}}$. This is greater than the noise of the AD534 multipliers, and it is vastly bigger than the noise of the operational amplifiers we have used so far. We will examine the consequences of this fact in Appendix F.

We use the DIV100 to remove the effects of E from the demodulated signal. Recall that E is affected by laser power and the fringe depth of the interference pattern, which varies as the polarization of the light within the interferometer wanders.

The output of the divider is given by Equation (227) in Chapter VIII, which is

$$\frac{\sqrt{3}k_{A_3}k_D k_d}{k_{A_2}}\xi. \tag{257}$$

Upon integration by U14B, Equation (228) of Chapter VIII shows that the demodulator's output is

$$\frac{\sqrt{3}k_f k_{A_3}k_D k_d}{k_{A_2}}\xi. \tag{258}$$

The final gain constant is that of the integrator:

$$k_1 = -\frac{1}{R_{51}C_{17}} = 6.89\times10^3 \text{ s}^{-1}. \quad (259)$$

We can now substitute all the constants into Equation (258):

$$\frac{\sqrt{3}(6.89\times10^3 \text{ s}^{-1})(0.356)(901 \text{ ns})(10 \text{ V})}{1.33} = 29 \frac{\text{mV}}{\text{rad}}, \quad (260)$$

which is very close to the value 31 mV/rad measured in Chapter XI.

B. WAVEFORMS

In the last chapter we showed computer simulations of the waveforms which would exist at various stages of the symmetric demodulation process if the signal of interest were a sinusoid. In this section we present photographs of an oscilloscope display of the waveforms actually present in the Symmetric Analogue Demodulator for sinusoidal inputs.

Figure 35 shows two photographs of the interference patterns generated by the interferometer we built. Both patterns were generated by a 100 Hz stimulus. In the upper photograph, the phase amplitude $A=33.7$ rad; in the lower trace, $A=67.9$ rad. Note that the amplitude of the interference pattern is the same in each photograph, and the points of minimum frequency in the interference pattern always correspond to the extrema of the stimulus.

Figure 36 shows the outputs of the differentiators U5B, U6B, and U7B. The frequency of the stimulus is 100 Hz as before, and the upper and lower traces still correspond to phase amplitudes of 33.7 and 67.9 rad, respectively. Note how high-frequency noise is very evident in the photographs. Noise was completely absent in the computer simulations. The differentiators amplify the high frequencies, so any noise which is already present in the interferometric outputs is enhanced. This also explains why the amplitude of the derivatives is largest in the region where the interferometric outputs are oscillating most rapidly.

In the last chapter, we were able to show computer simulations of the differences between each of the two derivatives. We cannot show photographs of the differences because the differences are computed inside the AD534 differential-input analog

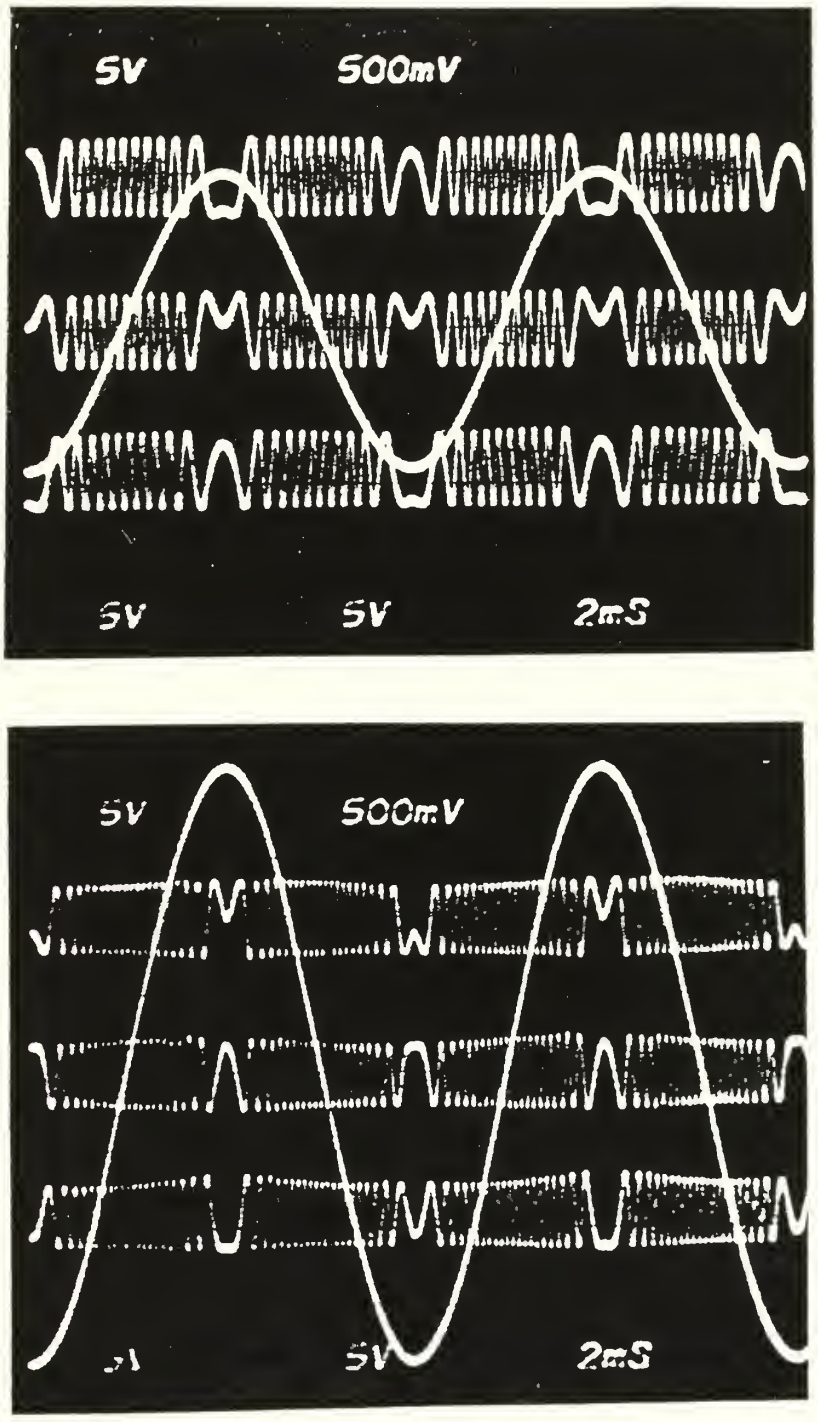

Figure 35 Three outputs of the optical fiber interferometric sensor with the 100 Hz sinusoidal stimulus superimposed. Upper photograph: $A = 33.7$ rad. Lower photograph: $A = 67.9$ rad.

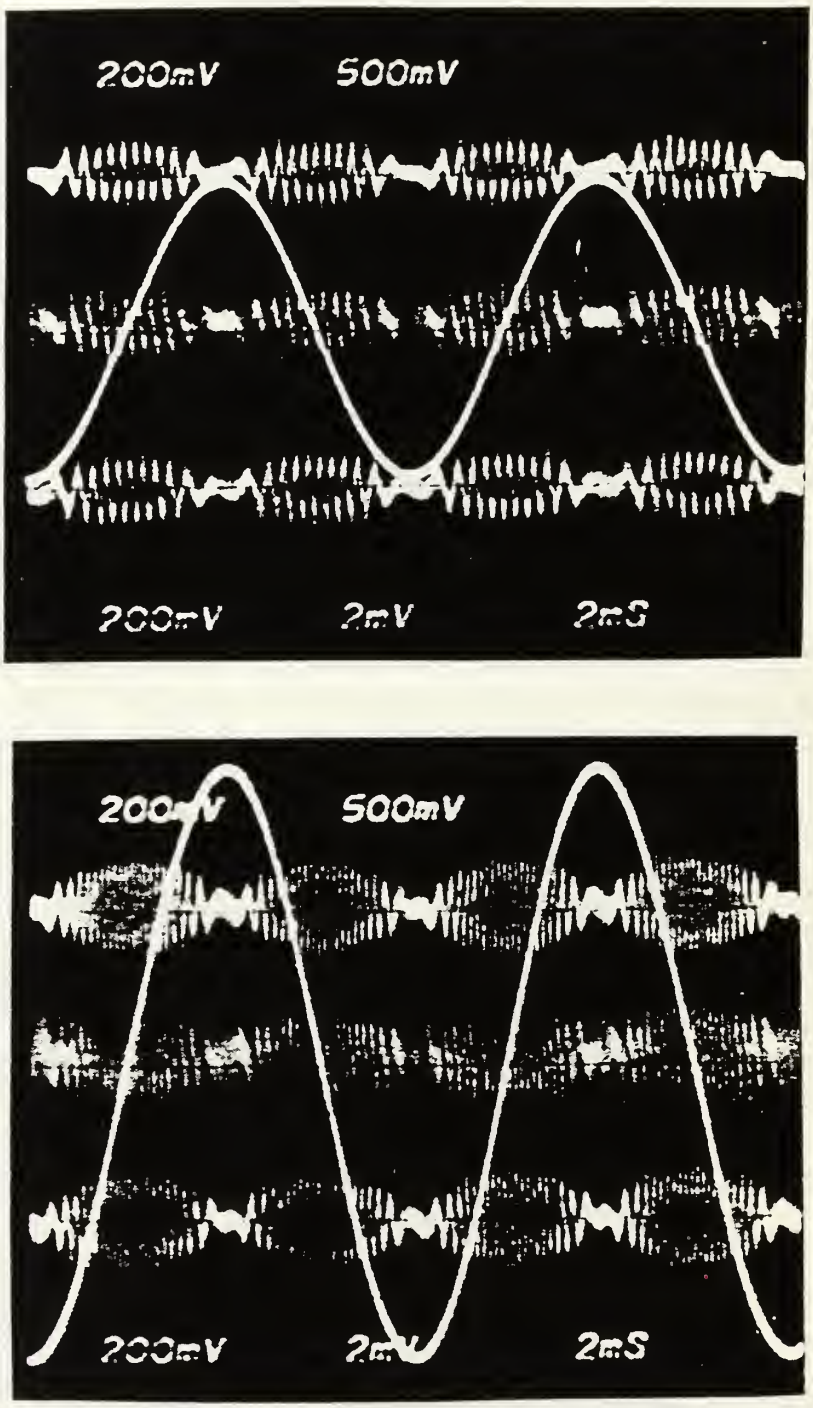

Figure 36 Derivatives of three outputs of the optical fiber interferometric sensor with the 100 Hz sinusoidal stimulus superimposed. Upper photograph: $A = 33.7$ rad. Lower photograph: $A = 67.9$ rad.

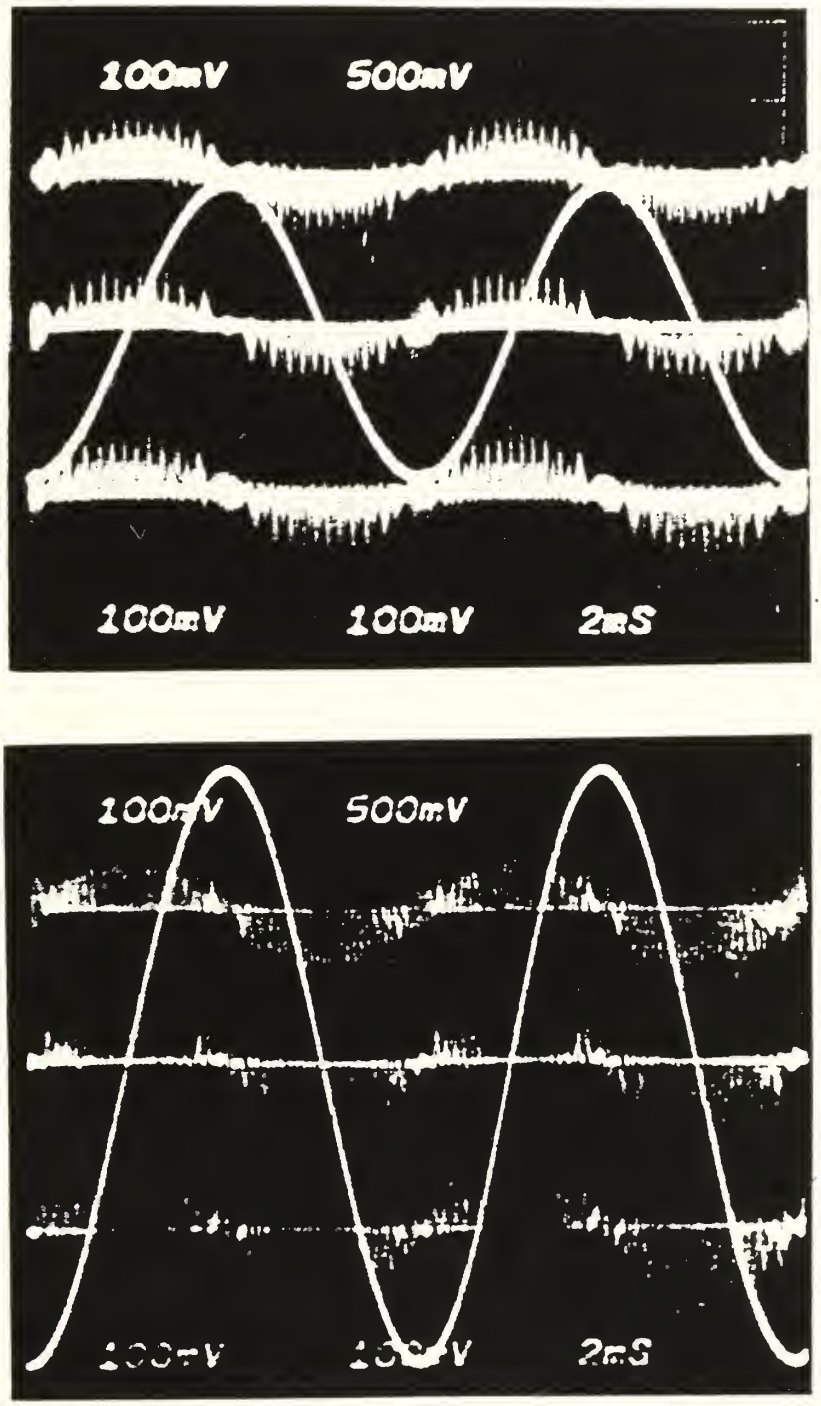

Figure 37 Products of each output with the difference between the derivatives of the other two; the 100 Hz sinusoidal stimulus is superimposed. Upper photograph: $A = 33.7$ rad. Lower photograph: $A = 67.9$ rad.

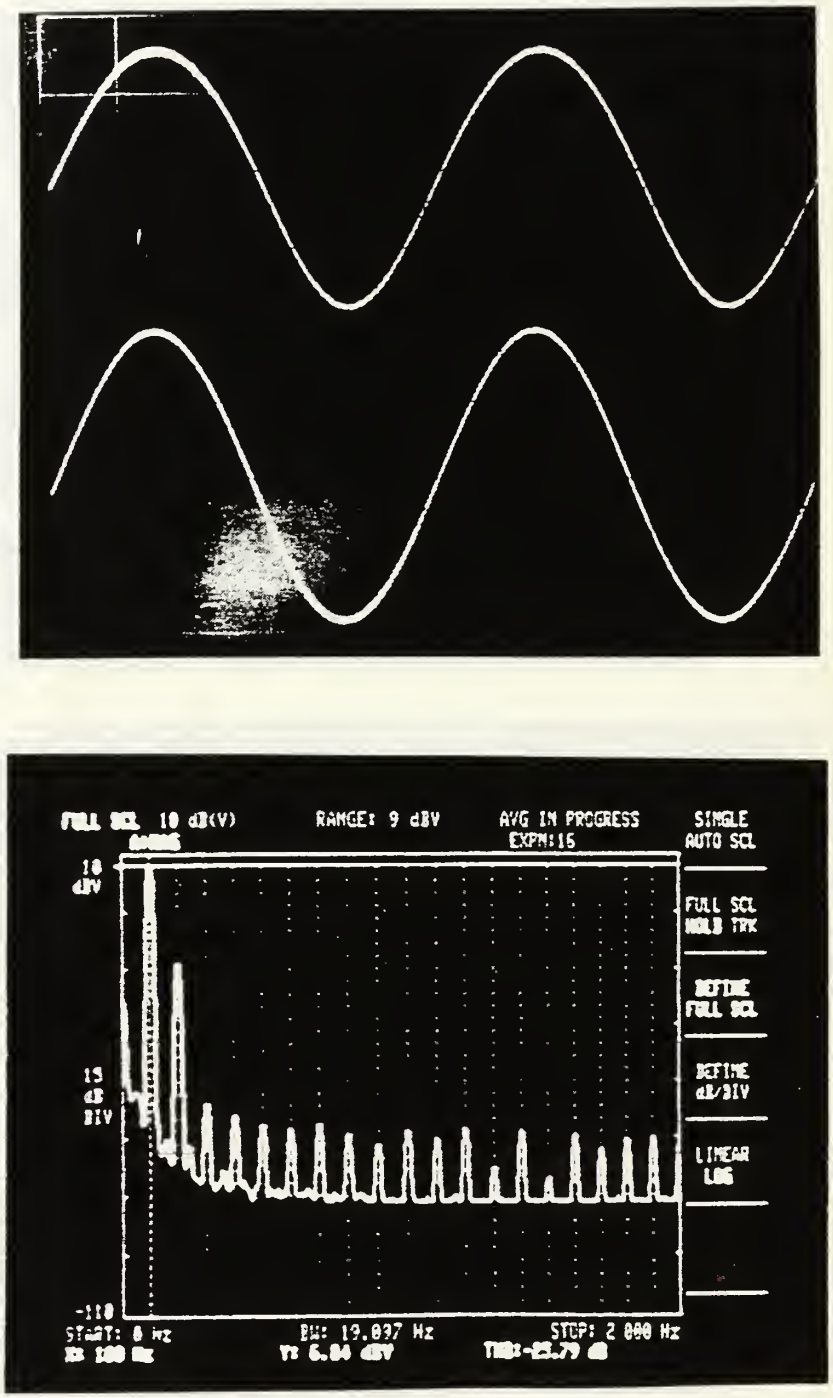

Figure 38 Symmetric Analogue Demodulator output, $f = 100$ Hz. $A = 137$ rad. Upper photograph, upper trace: undistorted input; lower trace, demodulator output. Lower photograph: FFT of demodulator output with 5% THD present.

multipliers. The results of the multiplication, however, are shown in Figure 37. The frequency of the stimulus and the phase amplitudes are the same as before. The envelope of the traces now is a sinusoid with the same frequency as the stimulus, but shifted in phase by 90°. Noise is still rather severe in these photographs, and one begins to wonder if a faithful replica of the stimulus can be reconstructed.

Figure 38 shows that after summing the three products and integrating them, we do indeed get a good replica of the stimulus. The upper trace in the upper photograph is the undistorted sinusoid generated by the HP3314A Function Generator. The lower trace in the upper photograph is the output of the demodulator. In the lower photograph is a Fast Fourier Transform (FFT) of the demodulator's output. The photographs in Figure 38 correspond to a stimulus of frequency 100 Hz and the phase amplitude $A=136.5$ rad. At this high phase amplitude, the distortion has reached the 5% level (-25.79 dB), but this is hard to discern from the oscilloscope trace alone.

We have also used triangular waves to excite the sensor; the demodulator outputs a triangle wave, just as it should.

C. SUMMARY

This chapter and the previous one have described the most innovative aspect of the work described in this dissertation. We developed a new algorithm for demodulating the outputs of an optical fiber interferometric sensor terminated by a 3×3 optical fiber coupler. Unlike the asymmetric demodulation method described in Chapter VII, the symmetric demodulation method processes all outputs of the interferometer in a similar fashion. None is discarded. The algorithm was arrived at in a semi-intuitive manner by the entirely unorthodox application of phasor techniques to a non-linear process. Its correctness could not be demonstrated, however, by such ill-chosen (but intuitively helpful) methods. We had to rely on the use of trigonometry (or the equivalent use of complex exponentials and their complex conjugates).

The symmetric demodulation method has an additional advantage (apart from symmetry) over the asymmetric method. The dependence of the output of the demodulator on the central value D of the output of the interferometer and on the

amplitude E of the fluctuations around D is absent from the final result. The asymmetric demodulation method achieves independence from D, but not from E.

In the next chapter we digress briefly to discuss the measurement of noise. Upon the completion of this digression, we shall be in a position to measure the performance of our implementation of the symmetric demodulation algorithm in the presence of noise.

X. MEASURING NOISE

In this chapter we present the methods we have used to measure noise and the results of measurements of the noise of our instruments. The purpose of doing this is to be sure that when we measure the noise of the Symmetric Analog Demodulator and the Asymmetric Digital Demodulator we do not inadvertently measure the noise of instruments. If the noise introduced by the instruments is less than that observed from the demodulators, then it is reasonable to infer that this inadverteney has not occurred. All measurements were taken at 590 Hz. This value was chosen slightly offset from 600 Hz in order to avoid contamination by the abundant sources of 60 Hz harmonics which existed in our laboratory.

A. HOW TO MEASURE NOISE

We generally used two independent techniques to measure noise. The easiest entailed the use of an HP3561A Dynamic Signal Analyzer. This device has 400 frequency bins which it uses in performing a Fast Fourier Transform on the input wave form. The bandwidth of each bin is dependent on the user's choice of frequency span (the lowest and highest frequencies of interest). It also depends on the user's choice of "window" function. The instrument offers a selectable option to present the root-mean-squared voltage in each bin divided by the square root of the bandwidth. Thus, the units of measure become $V/\sqrt{Hz}$ rather than V. This instrument is attractive because it is so easy to use.

B. HP3561A DYNAMIC SIGNAL ANALYZER

The HP3561A measured its own noise floor. The instrument has a 1 MΩ input impedance, and we placed a matched 50 Ω load across its two inputs. The inputs were AC coupled by a selection on the front panel of the instrument. The HP3561A displayed its own measurement of the noise as 56.2 $nV/\sqrt{Hz}$ (−145 $dBV/\sqrt{Hz}$). This cannot be due

to the presence of the 50 Ω load, whose noise spectral density $e_R^{\dagger}$ can be computed from the expression

$$e_R^{\dagger} = \sqrt{4kTR} \tag{261}$$

where $k = 1.381 \times 10^{-23}$ J/K is Boltzmann's constant, T is the temperature, and R is the resistance. If we take the temperature as 300 K (room temperature) and use 50 Ω for R, then the load would only generate 910 pV/√Hz (−181 dbV/√Hz), considerably less than that measured for the HP3561A. Our measurement of the noise compares well with the value specified for the HP3561A, at most −141 dBV/√Hz.

C. EG&G PRINCETON APPLIED RESEARCH MODEL 5210 LOCK-IN AMPLIFIER

This device, like the HP3561A Dynamic Signal Analyzer, can measure its own noise floor. Like the HP3561A, it has a 1 MΩ input impedance. It is calibrated only for source impedances much smaller than this. We simply shorted the differential inputs together. We set the lock-in amplifier's sensitivity scale factor set to 10^8, time constant τ to 1 s, and the filter skirts to decline at −12 dB per decade of increase of frequency. The output of the lock-in amplifier was averaged on an HP3456A Digital Voltmeter, and was $V_{OUT} = 0.53 \pm 0.19$ V. We can convert this to a voltage noise spectral density $e_{5210}^{\dagger}$ referred to the input from the formula

$$e_{5210}^{\dagger} = \frac{V_{OUT}}{S\frac{1}{\sqrt{8\tau}}} = 15 \ \frac{\text{nV}}{\sqrt{\text{Hz}}} \qquad \left(-157 \ \frac{\text{dBV}}{\sqrt{\text{Hz}}}\right). \tag{262}$$

This compares well with the noise floor specified for the Model 5210, 5 nV/√Hz (−166 dBV/√Hz) at 1 kHz (we measured the noise floor at 590 Hz).

D. ANALOG INTERFEROMETRIC SIMULATORS

We made two measurements of the noise of each of the Analog Interferometric Simulators, one with open inputs, the other with shorted inputs. These results were within a standard deviation of each other, as shown in Table XII. The standard deviations were divided by the sensitivity setting of the lock-in amplifier (10^7) and by

Table XII Measurements of the noise of the Analog Interferometric Simulators, taken on the Model 5210 Lock-In Amplifier.

Simulator	Inputs	Output Voltage (V_{RMS}) ± Standard Deviation	Noise Spectral Density	
			nV/√Hz	dBV/√Hz
1	Open	3.4±1.9	960	−121
2		3.3±1.7	920	−120
3		2.5±1.3	700	−123
1	Shorted	3.6±1.7	1000	−120
2		2.7±1.4	780	−122
3		3.0±1.7	860	−121

$1/\sqrt{(8\tau)}$, the square root of the equivalent noise bandwidth, with a time constant τ=1 s. These values are almost two orders of magnitude larger than the noise floor of the lock-in amplifier itself, so we can be fairly confident that they are not an artifact of the instrumentation.

E. AN INVERTING AMPLIFIER

As a final check on the correctness both of our measuring techniques and our ability theoretically to predict the noise of an electronic circuit, we consider a simple inverting amplifier built around the same operational amplifier, the OPA-111, that we use in the optical receivers of each of the three demodulators considered in this research. The circuit we shall consider is diagrammed in Figure 39.

There are five spectral noise sources shown in the figure. The noise from the preceding stage is $e_s^{\dagger}$. The two resistors R_1 and R_2 have voltage noise spectral densities $e_{R1}^{\dagger}$ and $e_{R2}^{\dagger}$. The operational amplifier provides noise modelled by the voltage noise spectral density $e_n^{\dagger}$ and the current noise spectral density $i_n^{\dagger}$ at the inputs. We will regard the operational amplifier as ideal (having infinite gain), so with all noise sources suppressed, the voltage at both the inverting and non-inverting inputs of the operational amplifier must be zero. We consider the effects of each noise source separately: the

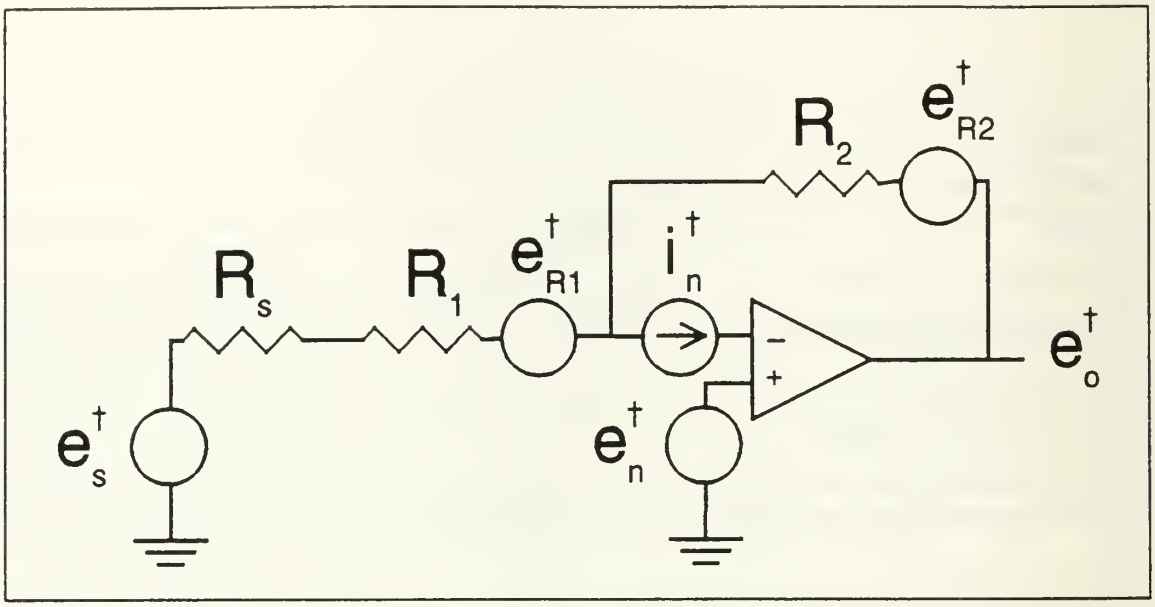

Figure 39 Noise sources in an inverting amplifier.

Pythagorean sum of each of them gives the total output noise voltage spectral density $e_o^{\dagger}$. We shall assume that each noise source is uncorrelated to any other. This implies that the Pythagorean sum, by which we specifically mean the square root of the sum of the squares of the effects due to each noise source individually, is an appropriate method for combining the various contributions of the noise together.

1. Noise sources $e_s^{\dagger}$ and $e_{R1}^{\dagger}$

We can lump these two noise sources together. Both are operated upon by the inverting amplification characteristic of the amplifier, just as any ordinary voltage input would be. If we assume that the source resistance is negligible, then each noise source is simply multiplied by the factor $-R_2/R_1$. The two contributions to the noise then are

$$-\frac{R_2}{R_1}e_s^{\dagger} \quad \text{and} \quad -\frac{R_2}{R_1}e_{R1}^{\dagger} = -\frac{R_2}{R_1}\sqrt{4kTR_1}. \tag{263}$$

The negative sign is unimportant in the final analysis because noises add as the square root of the sum of the squares of the contributions to the noise.

2. Noise source $e_{R_2}^{\dagger}$

When noise sources $e_s^{\dagger}$ and $e_{r1}^{\dagger}$ are suppressed, there can be no currents flowing through the system. Thus the voltage source

$$e_{R_2}^{\dagger} = \sqrt{4kTR_2} \tag{264}$$

contributes to the output noise voltage spectral density with gain one.

3. Noise source $e_n^{\dagger}$

Inputs to the non-inverting terminal of the operational amplifier are amplified by gain $1+R_2/R_1$, and this is the case with this noise source, too. The contribution to the noise from this source then is

$$\left(1+\frac{R_2}{R_1}\right)e_n^{\dagger}. \tag{265}$$

4. Noise source $i_n^{\dagger}$

If any of the noise from this source were to flow through resistor R_1, then there would be a non-zero voltage at the inverting terminal of the operational amplifier. An ideal operational amplifier maintains the inverting terminal and the non-inverting terminal at equal potentials, namely zero, so the current flowing through R_1 must be zero. All the current must flow through resistor R_2 and so this source's contribution to the noise is

$$i_n^{\dagger}R_2. \tag{266}$$

5. Total noise

The sum of all these contributions to the noise can be expressed as

$$e_o^{\dagger} = \sqrt{\left(\frac{R_2}{R_1}e_s^{\dagger}\right)^2 + \left(\frac{R_2}{R_1}\right)^2 4kTR_1 + 4kTR_2 + \left[\left(1+\frac{R_2}{R_1}\right)e_n^{\dagger}\right]^2 + \left(i_n^{\dagger}R_2\right)^2}. \qquad (267)$$

A comparison of the predicted noise and the measured noise for this circuit is shown in Table XIII. The entries with zero noise from the source were made with no source connected, that is, with the input resistor R_1 grounded. The last column shows a measurement taken with the input resistor connected to the output of one of the Analog Interferometric Simulators. Notice the excellent agreement between the predicted and the observed values. More than any other measurement cited so far, this consistency between theory and observation gives us confidence both in our ability theoretically to analyze noise and practically to observe it.

Now that we have briefly discussed the instruments with which we can measure noise and have performed a detailed analysis on a particular circuit, we are ready to incorporate these techniques in measuring the performance of the Symmetric Analog Demodulator so that we can determine its minimum detectable signal.

Table XIII Comparison of predicted and observed noise levels from an inverting amplifier.

R_1		10 kΩ				49.9 kΩ
R_2		2.00 MΩ	1.00 MΩ	100 kΩ	10.0 kΩ	64.9 kΩ
Noise source and its effect at the output	e_{R2}†	0 V/√Hz (short circuit to ground)				1.23 μV/√Hz
	e_{R1}†	2.57 μV/√Hz	1.29 μV/√Hz	129 nV/√Hz	12.9 nV/√Hz	37.4 nV/√Hz
	e_{R2}†	182 nV/√Hz	129 nV/√Hz	40.7 nV/√Hz	12.9 nV/√Hz	32.8 nV/√Hz
Burr-Brown OPA-111	e_n† 15 nV/√Hz	3.02 μV/√Hz	1.52 μV/√Hz	165 nV/√Hz	30.0 nV/√Hz	34.5 nV/√Hz
	i_n† 500 aA/√Hz	1.00 nV/√Hz	500 pV/√Hz	50.0 pV/√Hz	5.00 fV/√Hz	32.5 pV/√Hz
Predicted Output Noise Spectral Density	e_o†	4.0 μV/√Hz	2.0 μV/√Hz	210 nV/√Hz	35 nV/√Hz	1.2 μV/√Hz
Parameters of the Lock-in Amplifier	Sensitivity	10^6		33.3×10^6	10^8	10^7
	Time constant	1 s				
	Filter skirts	-12 dB per decade				
Output voltage ± Standard Deviation		1.5±0.7 V	1.0±0.5 V	2.2±1.2 V	1.2±0.6 V	4.4±2.3 V
Output noise spectral density		4.2 μV/√Hz	2.8 μV/√Hz	190 nV/√Hz	33 nV/√Hz	1.2 μV/√Hz

XI. PERFORMANCE OF THE SYMMETRIC ANALOG DEMODULATOR

A. OVERVIEW

In this chapter we examine the performance of the Symmetric Analog Demodulator. The aspects of its performance which we consider are:

1. scale factor, which relates the phase amplitude in the modulated signal to the voltage amplitude in the demodulated signal;
2. small signal bandwidth;
3. maximum acceptable signal;
4. noise floor;
5. dynamic range;
6. complexity; and
7. approximate cost.

These are the same characteristics we examined in assessing the performance of the Fringe Rate Demodulator, plus one new one: the noise floor. This did not arise in the case of the Fringe Rate Demodulator because its principle of operation made it incapable of demodulating signals with less than half a fringe (an optical phase shift of $\pi/2$ radians) and so the useful signals were always very much stronger than the noise anyway. The Symmetric Analog Demodulator is capable of demodulating signals both above and below the one-half fringe level. In fact, at the lower end it is only the noise that prevents it from recovering arbitrarily small signals.

B. SCALE FACTOR

As with the Fringe Rate Demodulator, the scale factor is defined as the ratio of the demodulator's output voltage to the input phase. If the phase signal provided by the interferometric sensor is $\phi(t)$ and the output provided by the Symmetric Analog Demodulator is $v(t)$, then we define the scale factor $F_{SAD}(t)$ of the demodulator by the equation

$$F_{SAD}(t) = \frac{\left(\frac{dv(t)}{dt}\right)}{\left(\frac{d\phi(t)}{dt}\right)} = \frac{dv(t)}{d\phi(t)}. \tag{268}$$

Ideally the scale factor would be constant. In practice, it is not. We shall call the multiplicative product of the phase shift A and the frequency f the *phase rate*, since the product is measured in radians per second. When the phase rate is too large, saturation of the electronics at the level of the power supplies (or slightly below them) takes place. The reason saturation occurs is clear if we consider the mathematical expressions for the output of the interferometer and its derivative. Let a signal of interest $\xi(t)$ be applied to the interferometric sensor. If $\xi(t)$ is a sinusoid of amplitude A and frequency $\omega=2\pi f$, then

$$\xi(t) = A\sin(\omega t). \tag{269}$$

After conversion of the interferometric output into its voltage analog, $\xi(t)$ is converted into the phase-modulated signal

$$x(t) = D + E\cos[\xi(t)+\phi] = D + E\cos[A\sin(\omega t)+\phi]. \quad (270)$$

The term ϕ represents an additional phase shift which accounts for the choice of one of the three outputs of the 3×3 coupler at the output of the interferometric sensor, as well as the effects of temperature, pressure, and other factors.

The derivative of $x(t)$ with respect time is

$$\dot{x} = \frac{dx(t)}{dt} = -AE\omega\cos(\omega t)\sin[A\sin(\omega t)+\phi]. \quad (271)$$

Since the product $AE\omega$ is a voltage limited to the level of the supply voltage (or possibly a little less), this product must not exceed some specific value or saturation results.[15]

On the other hand, when this product is very low, the noise produced by the differentiators in the demodulator dominates the product $AE\omega$ and so the outputs no longer adequately approximate the derivatives of the inputs.

In either of these limits, the scale factor of the demodulator deviates from the constant level desired. It drops off sharply in the former case, since further increases in the value of the amplitude A of the signal of interest cannot increase the outputs of the differentiators past their limit. In the latter case, the scale factor rises as A get smaller. This occurs because the outputs of the differentiators, which are now noisy and very small, are multiplied by one of the undifferentiated signals. While this signal continues to decline, its product with the ostensible derivative does not decline as rapidly as it should. In other words, the circuit provides too much output for the input it receives.

In the intermediate range, where the scale factor is roughly constant, the combination of optical fiber interferometer and Symmetric Analog Demodulator is

---

[15] In general, the product $AE\omega$ will also be multiplied by one or more other multiplicative constants k_i which depend on the specific choices of components in the design. It is the complete product of all the k_i and $AE\omega$ which is limited. However, in the design there is some latitude available in picking these various constants to achieve the performance desired.

essentially linear in operation. This means that the output frequency is that of the input to the sensor, namely ω, and the output amplitude is proportional to the amplitude of the input to the sensor.

Two other reasons for the departure of the scale factor from a constant are the limited bandwidth and the limited slew rate of the components of the Symmetric Analog Demodulator. These create distortion of the waveforms, and the distortion becomes more severe when high frequencies are significant.

To measure the scale factor in the region where it is a constant, we used an HP3314A Function Generator to generate a sinusoidal test signal. To create the phase-modulated signals used by the Symmetric Analog Demodulator, we can apply this test signal either to the optical interferometer described in Chapter IV or to the Analog Interferometric Simulators described in Appendix C. Because the use of the optical interferometer introduces the added complications of laser phase noise and wandering of the direction of polarization of the optical waves in the interferometer, we chose Analog Interferometric Simulators for performing our measurements of scale factor.

We discovered that to rely on the HP3314A to provide outputs of the same amplitude as the setting on the front panel is unwise when the amplitudes are very small: the outputs are inaccurate. The data on which we based this conclusion are shown in Table XIV. V_{IN} is the voltage selected on the front panel of the HP3314A Function Generator. V_{OUT} is the voltage observed on the HP3561A Dynamic Signal Analyzer, expressed in root-mean-squared logarithmic form (dBV).[16] Because it is a root-mean-squared measurement, we can multiply it by $\sqrt{2}$ to get the equivalent peak amplitude of the observed output, and we can then take the ratio $\sqrt{2}V_{OUT}/V_{IN}$. This ratio should equal the constant 1, which would be the case if the actual output were always equal to the observed output. The ratios shown in Table XIV are graphed against input voltage V_{IN} in Figure 40. Clearly, the ratios deviate more and more from 1 when $V_{IN} \leq 1$ mV.

---

[16] One decibel is defined as 10 times the logarithm of the power in a signal. Since voltage squared divided by resistance equals power through the resistance, a decibel also is 20 times the logarithm of the voltage across the resistance, if the resistance is taken as 1 Ω. This is the conventional definition of 1 dBV, even if the resistance is *not* equal to 1 Ω.

To compensate for this deficiency, we kept the output voltage of the HP3314A Function Generator above this level but interposed a Gertsch Model 480 Ratio Standard between the HP3314A and the inputs to the Analog Interferometric Simulators. The output of the HP3314A could then be kept close to the value selected on its front panel by keeping it higher than 1 mV. The ratio selected on the front panel of the Model 480 was then used to attenuate the output of the HP3314A to the low level needed for noise measurements. While the data we consider here are above the noise, we generally used the Model 480 Ratio Standard anyway, once we had found that the amplitude of the output of the HP3314A was not reliable at small signal levels.

That the use of the Model 480 Ratio Standard provides accurately reduced signal levels, down to the level of 1 μV is clear from the data in Table XV. To obtain these data, we used the instrumentation shown in Figure 41. The outputs of the HP3314A Function Generator had an amplitude of 10.00 mV, were attenuated by the Gertsch Model 480 Ratio Standard, and were measured in two ways. The HP3561A Dynamic Signal Analyzer provided one measurement. The combination of the EG&G Princeton Applied Research Model 5210 Lock-In Amplifier and HP3456A Digital Voltmeter provided a second measurement.

The HP3561A normally provides measurements in RMS form. However, this time we used the arithmetic capability of the device to multiply this value by $\sqrt{2}$ and so convert the readings into peak amplitudes. The Model 5210 Lock-In Amplifier likewise provides its measurements in RMS form. After first averaging the outputs of the Model 5210 on the HP3456A, we provided the $\sqrt{2}$ factor ourselves.

In Table XV, f is the frequency of the signal applied by the HP3314A; *Ratio* is the reduction ratio selected on the front panel of the Model 480; V_{EFF} is the effective output of the Model 480, computed by taking the product $V_{IN} \times Ratio$, where V_{IN}=10.00 mV; V_{FFT} is the effective peak output of the Model 480 measured on the HP3561A Dynamic Signal Analyzer; S is the scale factor of the Model 5210 Lock-In Amplifier in volts/volt; N is the number of samples averaged by the HP3456A; V_{DV} is the average ± the standard deviation of the output of the Model 480 Ratio Standard as measured with the HP3456A Digital Voltmeter; and V_{LI} is the average ± the standard deviation of the voltage

Table XIV Inaccuracies in the output of the HP3314A Function Generator when small amplitudes are specified.

V_{IN}	V_{OUT}	$\sqrt{2}\ V_{OUT}\ V_{IN}$
6.00 V	12.52 dBV	0.996
3.00 V	6.49 dBV	0.995
2.00 V	2.95 dBV	0.993
1.00 V	-2.96 dBV	1.01
600 mV	-7.40 dBV	1.01
300 mV	-13.44 dBV	1.00
200 mV	-16.98 dBV	1.00
100 mV	-22.98 dBV	1.00
60.0 mV	-27.42 dBV	1.00
30.0 mV	-33.46 dBV	1.00
20.0 mV	-37.00 dBV	0.999
10.0 mV	-43.01 dBV	1.00
6.00 mV	-47.42 dBV	1.00
3.00 mV	-53.46 dBV	1.00
3.00 mV	-57.00 dBV	0.999
1.00 mV	-63.09 dBV	0.991
600 µV	-67.49 dBV	0.995
300 µV	-73.62 dBV	0.983
200 µV	-77.27 dBV	0.968
100 µV	-83.65 dBV	0.929
60.0 µV	-88.89 dBV	0.847
30.0 µV	-95.30 dBV	0.810
20.0 µV	-100.2 dBV	0.691
10.0 µV	-113.0 dBV	0.317

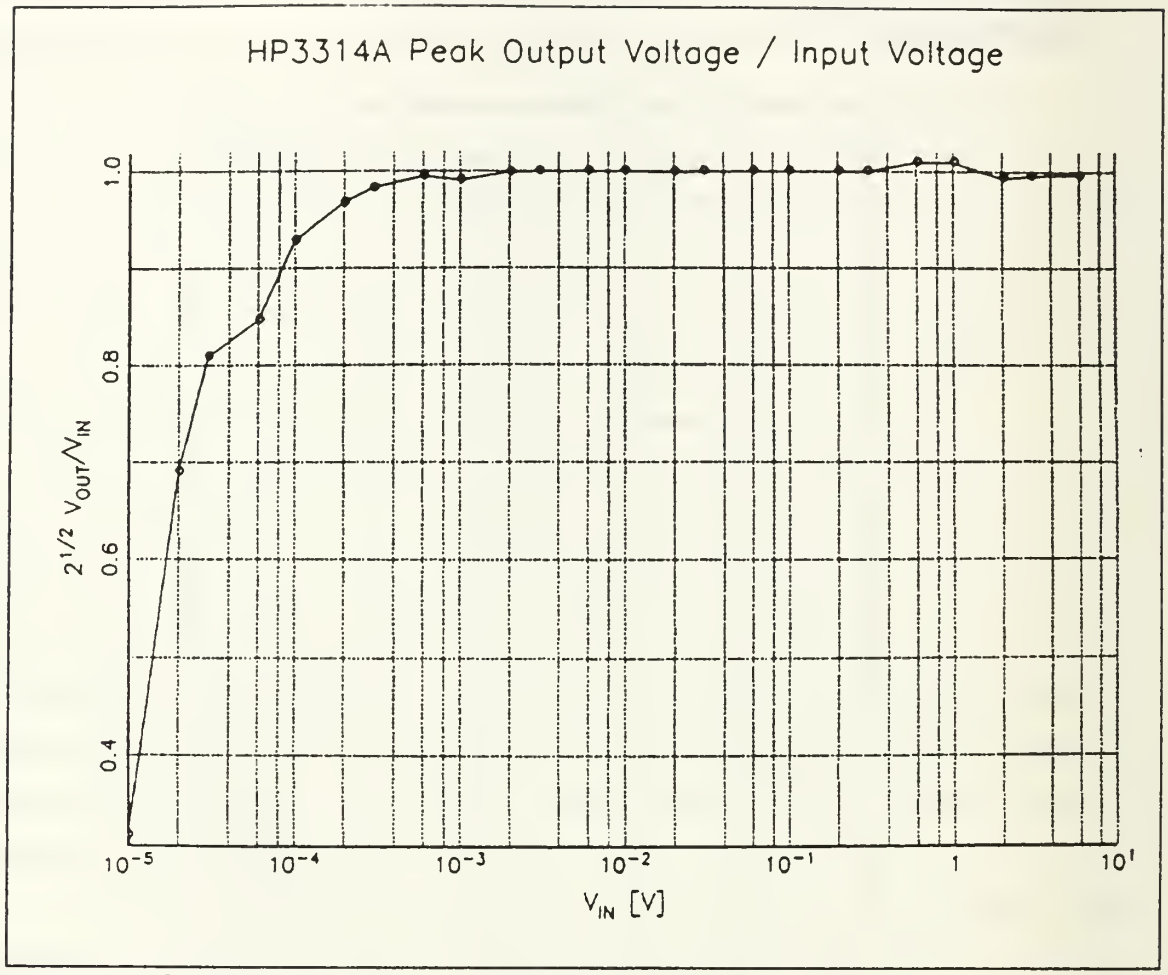

Figure 40 Graph of the ratio V_{OUT}/V_{IN} shown in Table XIV.

detected by the Model 5210 Lock-in Amplifier, computed as

$$V_{LIA} = \frac{\sqrt{2}V_{DV}}{S} \tag{272}$$

to express the output of the Model 480 Ratio Standard in terms of peak amplitude rather than RMS amplitude.

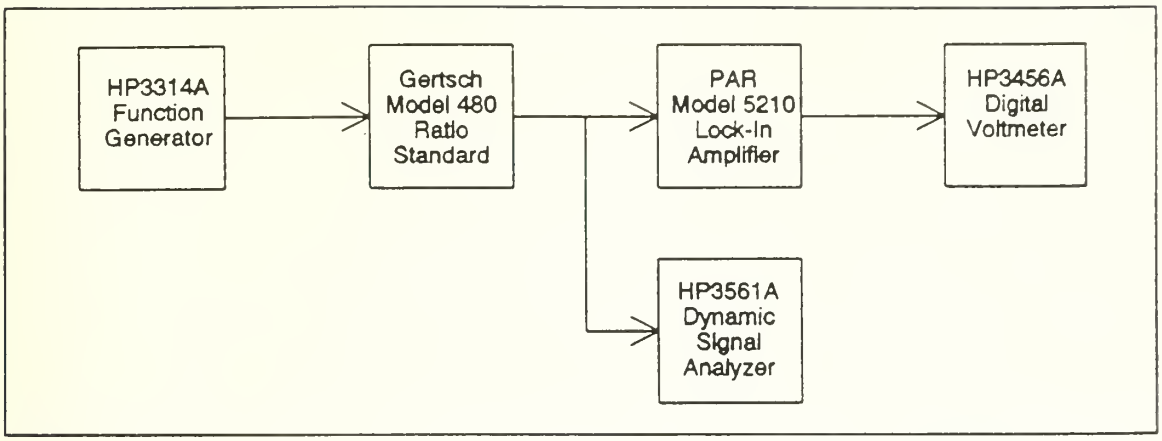

Figure 41 This instrumentation was used to verify that the Gertsch Model 480 Ratio Standard could provide accurately scaled replicas of the signals from the HP3314A Function Generator.

We used the HP3561A Dynamic Signal Analyzer in a mode which averages successive readings with 16 exponentially decaying weights.[17] Where the average fluctuated to an excessive degree, a dash is shown in Table XV. The exponential averaging mode would not give results of less than 121.6 nV during our observations, although smaller numbers were observable if RMS averaging were used instead. However, the RMS values at higher levels did not appear to be much different from those obtained with exponential averaging.

We operated the Model 5210 Lock-In Amplifier with a time constant τ = 1 s and a filter skirt which dropped off at 12 dB per octave of frequency. We selected a mode which provides both the magnitude and the phase of its input.

The magnitude output of the Model 5210 Lock-In Amplifier was provided as an input to an HP3456A Digital Voltmeter. This device was set to average N samples. Each sample was performed by integrating the input over 10 power line cycles, or 167 ms. The error shown in Table XV for V_{DV} is the square root of the sample variance provided

---

[17] The HP3561A Dynamic Signal Analyzer permits one to specify the number of such weights, but no control over the size of the weights is provided. In this mode, the averaging gives greatest emphasis to the most recent data. Therefore, the HP3561A can follow a mean which is a function of time, provided the mean does not wander too rapidly.

Table XV These data show that the Gertsch Model 480 Ratio Standard can accurately scale an input voltage of 10 mV to as little as 1 μV.

f	*Ratio*	V_{LH}	V_{HH}	S	N	V_{DC}	V_{LL}
20	1.000000	10.00 mV	10.01 mV	10^3	128	7.16464 ± 0.00060 V	10.13233 ± 0.00085 mV
	0.100000	1.000 mV	1.000 mV	10^4		7.1447 ± 0.0022 V	1.01041 ± 0.00031 mV
	0.010000	100.0 µV	100.1 µV	10^5		7.1314 ± 0.0048 V	100.853 ± 0.068 µV
	0.001000	10.00 µV	10.01 µV	10^6		7.1307 ± 0.0026 V	10.0843 ± 0.0037 µV
	0.000100	1.000 µV	1.020 µV	10^7		7.130 ± 0.028 V	1.0084 ± 0.0039 µV
	0.000010	100.0 nV	125.2 nV	10^8		7.16 ± 0.18 V	101.2 ± 2.6 nV
	0.000001	10.00 nV	121.6 nV	10^8		1.80 ± 0.17 V	25.5 ± 2.4 nV
100	1.000000	10.00 mV	10.01 mV	10^3	256	7.12552 ± 0.00085 V	10.0770 ± 0.0012 mV
	0.100000	1.000 mV	1.001 mV	10^4		7.1189 ± 0.0012 V	1.00677 ± 00017 mV
	0.010000	100.0 µV	100.2 µV	10^5		7.0760 ± 0.0085 V	100.07 ± 0.12 µV
	0.001000	10.00 µV	10.03 µV	10^6		7.1001 ± 0.0092 V	10.041 ± 0.013 µV
	0.000100	1.000 µV	1.002 µV	10^7		7.16 ± 0.21V	1.012 ± 0.030 µV
	0.000010	100.0 nV	124.7 nV	10^8		7.4 ± 1.8 V	104 ± 26 nV
	0.000001	10.00 nV	121.6 nV	10^8		2.62 ± 0.85V	37 ± 12 nV
1000	1.000000	10.00 mV	10.02 mV	10^3		7.18008 ± 0.00030 V	10.15416 ± 0.00043 mV
	0.100000	1.000 mV	1.002 mV	10^4		7.1743 ± 0.00018 V	1.01460 ± 0.00025 mV
	0.010000	100.0 µV	100.3 µV	10^5		7.1458 ± 0.00029 V	101.056 ± 0.041 µV
	0.001000	10.00 µV	10.05 µV	10^6		7.0813 ± 0.0029 V	10.0144 ± 0.0041 µV
	0.000100	1.000 µV		10^7		7.076 ± 0.022 V	1.0007 ± 0.0031 µV
	0.000010	100.0 nV	121.6 nV	10^8		6.87 ± 0.17 V	97.2 ± 2.4 nV
	0.000001	10.00 nV	121.6 nV	10^8		0.86 ± 0.21V	12.2 ± 2.9 nV

by the HP3456A Digital Voltmeter.

To measure the scale factor F_D of the demodulator, we applied the outputs of the Model 480 Ratio Standard to the inputs of three Analog Interferometric Simulators as shown in Figure 42. This setup is very similar to that in Figure 41. The difference is the presence of the simulators and the demodulator, and the absence of the HP3561A Dynamic Signal Analyzer. The outputs of the simulators were provided to the Symmetric

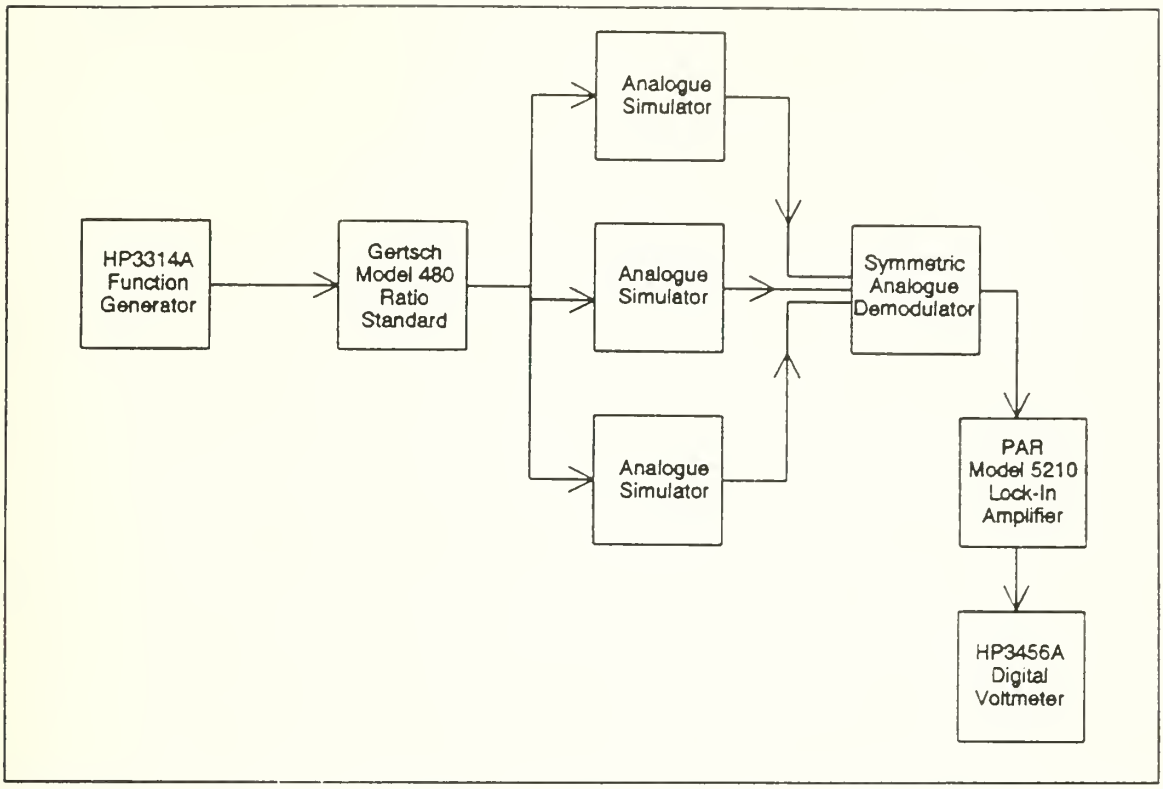

Figure 42 Setup used to measure the scale factor f_D of the Symmetric Analog Demodulator.

Analog Demodulator.

The output of the HP3314A Function Generator was set to have an amplitude of 1.00 V. This is a value well within the ability of the HP3314A to output an accurate amplitude, as established by the data in Table XIV. The smallest ratio set on the Gertsch Model 480 Ratio Standard was 0.000500. This resulted in a signal amplitude of 500 μV, well above the minimum reliable signal level of about 1 μV established by the data in Table XV.

We again used an EG&G Princeton Applied Research Model 5210 Lock-In Amplifier to make measurements of the outputs of the demodulator. The filter time constant set on the front panel of the lock-in amplifier was 1 s. The filter had a roll-off of 12 dB per octave increase in frequency. The equivalent noise bandwidth B of the lock-in can be computed from the formula

$$B = \frac{1}{8\tau} \tag{273}$$

where τ is the filter time constant. This formula is derived in Appendix A.

We fed the output of the lock-in amplifier to an HP3456A Digital Voltmeter, which averaged 768 samples of the lock-in amplifier's output. Each such sample is actually itself an average of the input, conducted over an integral number of cycles of the power lines. We chose 10 cycles for this integration process. This resulted in averaging for a little over two minutes. The output scale factor F_D of the demodulator is computed from the formula

$$F_D = \frac{\sqrt{2}V_{OUT}}{S\phi_{EFF}} \tag{274}$$

where S is the sensitivity of the lock-in amplifier in volts/volt, V_{OUT} is the average voltage from the lock-in amplifier as calculated by the HP3456A Digital Voltmeter, and ϕ_{EFF} is the phase from the analog simulators. The quantity ϕ_{EFF} is computed from the formula

$$\phi_{EFF} = V_{IN}\ Ratio\ F_{S_{EFF}}. \tag{275}$$

In this expression, *Ratio* is the ratio set on the Gertsch Model 480 Ratio Standard, V_{IN} is the output level of the HP3314A Function Generator, and $F_{S,EFF}$ is the average scale factor for the Analog Interferometric Simulators. As shown in Chapter IV, this is 918±4 mrad/V.

The observations are summarized in Table XVI. As was mentioned earlier, the scale factor is not constant for all possible inputs. When the multiplicative product of signal amplitude and frequency is too small, the outputs of the differentiators cease to be proportional to that product, and so the scale factor rises. Conversely, when the product of the two is too big, saturation of the outputs of various components within the demodulator occurs, and so the scale factor drops. Both these trends are evident in the data of Table XVI. In between the two extremes, however, we must conclude that the scale factor F_D is approximately 31 mV/rad.

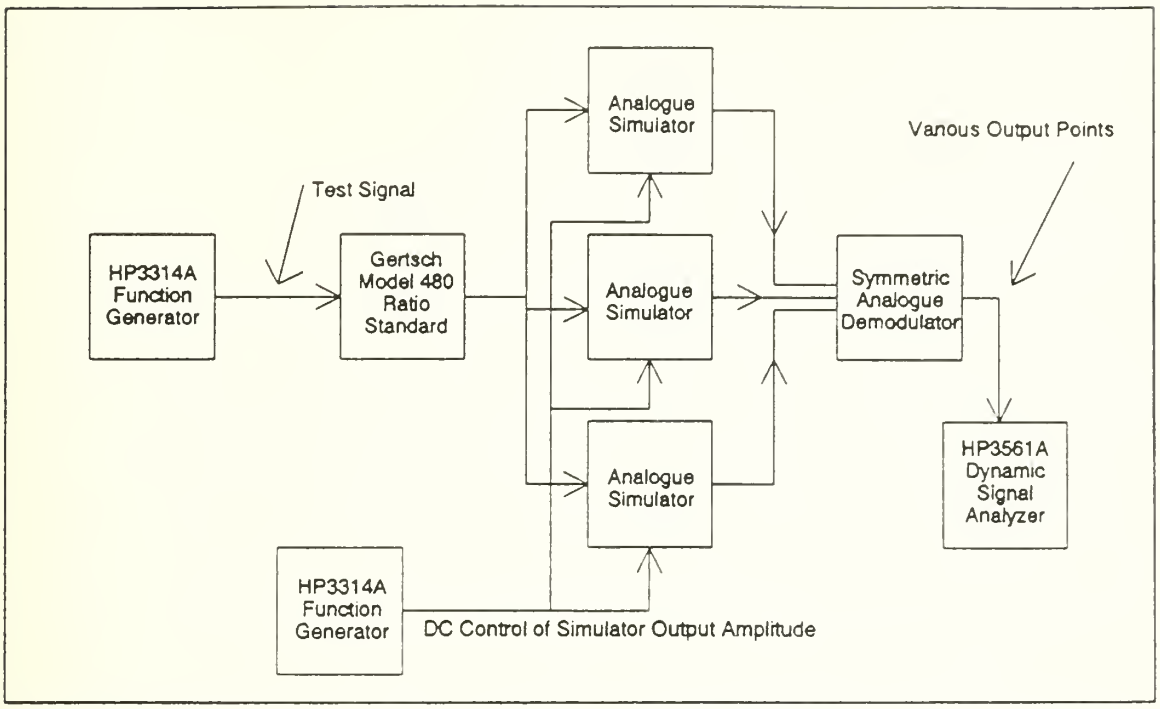

Figure 43 Instrumentation for an experiment to test whether the increase in scale factor at low combinations of amplitude and frequency could be due to a failure of the DIV100's divider input to stay within acceptable limits.

The increase in scale factor for low combinations of amplitude and frequency led us to hypothesize, at first, that the denominator voltage input into the Burr-Brown DIV100 divider integrated circuit was becoming dominated by noise, so that it stopped decreasing as the numerator input decreased. We devised an experiment to test this theory, and concluded that it is untenable. Figure 43 shows the instrumentation we used to test this hypothesis. We used one HP3314A Function Generator to create a sine wave. This was attenuated by a Gertsch Model 480 Ratio Standard and then applied to the three main inputs of the Analog Electronic Simulators. This created a simulated interferometric sensor output. The amplitude of the output could be adjusted by setting a DC offset on a second HP3314A and applying this to the AM input of the simulators. In mathematical terms, the output of simulator k was

$$x_k(t) = E\cos[A\sin(\omega t)-(k-1)\frac{2}{3}\pi]. \quad (276)$$

In this expression, A and ω are controlled by the first HP3314A whereas E is controlled by the second one.

The results of our measurements are given in Table XVII and in Table XVIII. The primary signal generator provided a frequency f=100 Hz and a peak voltage output V_{GEN}=10.00 V. This signal was scaled down by a factor of 0.500000 by the Gertsch Model 402 Ratio Standard to create an effective output voltage of 5.00 V. The DC signal applied to the AM input of the Analog Interferometric Simulator is V_{AM} in Table XVII. E is the peak amplitude of the output of the simulator. $V_{CONTROL}$ is the voltage supplied to the denominator of the DIV100 divider in the Symmetric Analog Demodulator as a control. $V_{OUT,RMS}$ is the RMS voltage provided by the Symmetric Analog Demodulator.

As the value of E increases, the control voltage continues to climb at just the right rate to hold the output constant. However, when E surpasses 1.74 V, the control voltage is saturated and so the output voltage begins to grow due to the absence of any control. So from Table XVII we see that the maximum amplitude E from the simulators that can still be accepted by the Symmetric Analog Demodulator is around 1.74 V peak and that control is maintained as long as $V_{CONTROL}$ does not saturate, *i.e.*, remains below about 13.77 V.

To obtain the data in Table XVIII, we applied a 1 kHz sine wave with a peak amplitude of 3.00 V to the ratio standard. We then lowered the output of the ratio standard to apply progressively weaker signals to the inputs of the Analog Interferometric Simulators. The DC signal applied to the AM input of the simulators was held constant at 897 mV to keep the peak voltage out of the simulator to a nominal 1.50 V, the level which was set to be present when the AM input was left open. The actual amplitude from the simulator was measured as 1.49 V. The data show that the drop in phase shift from the simulators did not have any effect on $V_{CONTROL}$, the control voltage, but of course the demodulator's output continued to drop as the input peak phase shift dropped. In view of the data in Table XVII, we must infer that the change in scale

Table XVI Measurements to obtain the scale factor of the Symmetric Analog Demodulator.

f [Hz]	*Ratio*	V_{LH}	ϕ_{LH}	S [V/V]	V_{LL}	k_D [mV/rad]
23	0.100000	100 mV	918 mrad	10^3	2.01 ± 0.055 V	31.0
	0.050000	50.0 mV	459 mrad		1.00 ± 0.076 V	30.7
	0.025000	25.0 mV	918 mrad		0.51 ± 0.066 V	31.4
	0.012500	12.5 mV	11.5 mrad		0.261 ± 0.055 V	47.8
35	1.000000	1.00 V	918 mrad	10^2	2.3340 ± 0.0041 V	36.0
	0.100000	100 mV	918 mrad	10^3	2.801 ± 0.033 V	45.4
	0.010000	10.0 mV	9.18 mrad	10^4	2.91 ± 0.42 V	44.8
	0.005000	5.00 mV	4.59 mrad		1.55 ± 0.40 V	47.8
65	1.000000	1.00 V	918 mrad	333.3	7.8236 ± 0.0079 V	43.0
	0.100000	100 mV	918 mrad	3.33×10^3	9.293 ± 0.072 V	43.0
	0.010000	10.0 mV	9.18 mrad		983 ± 71 mV	45.4
	0.005000	10.0 mV	4.59 mrad		512 ± 80 mV	43.0
110	1.000000	1.00 V	918 mrad	333.3	7.0990 ± 0.0047 V	32.8
	0.100000	100 mV	918 mrad		794.1 ± 3.4 mV	36.7
	0.010000	10.0 mV	9.18 mrad		37.2 ± 3.7 mV	36.1
	0.005000	10.0 mV	9.18 mrad		37.2 ± 3.7 mV	34.4
200	1.000000	1.00 V	918 mrad	333.3	6.7219 ± 0.0027 V	36.1
	0.100000	100 mV	918 mrad		717.6 ± 2.6 mV	33.2
	0.010000	10.0 mV	9.18 mrad		69.4 ± 1.9 mV	32.1
	0.005000	5.0 mV	4.59 mrad		33.8 ± 2.3 mV	36.1
300	1.000000	1.00 V	918 mrad	3.33×10^3	6.7219 ± 0.0027 V	43.0
	0.100000	100 mV	9.18 mrad		7.186 ± 0.026 V	33.2
	0.010000	10.0 mV	9.18 mrad	33.3×10^3	2.91 ± 0.42 V	33.8
	0.001000	1.00 mV	918 µrad	10^5	2.84 ± 0.69 V	43.8
590	1.000000	1.00 V	918 mrad	333.3	6.5138 ± 0.0012 V	30.1
	0.100000	100 mV	918 mrad	3.33×10^3	6.7976 ± 0.0067 V	31.4
	0.010000	10.0 mV	9.18 mrad	33.3×10^3	6.811 ± 0.069 V	31.5
	0.001000	1.00 mV	918 µrad	10^5	2.09 ± 0.21 V	32.2
1000	1.000000	1.00 V	918 mrad	333.3	6.4731 ± 0.0021 V	29.9
	0.100000	100 Mv	918 mrAD	3.33×10^3	6.7374 ± 0.0035 V	31.1
	0.010000	10.0 mV	9.18 mrad	33.3×10^3	6.760 ± 0.045 V	31.3
	0.001000	1.00 mV	918 µrad	10^5	2.05 ± 0.13 V	31.6

Table XVII These data show some examples of combinations of frequency and amplitude which cause the divisor input to the DIV100 to saturate, resulting in a loss of control of the output amplitude.

V_{AM}	E	$V_{CONTROL}$	$V_{OUT,RMS}$
2.00 V	1.19 V	6.29 V	97.33 mV
1.50 V	1.33 V	7.94 V	97.72 mV
1.00 V	1.47 V	9.79 V	97.72 mV
897 mV	1.49 V	9.84 V	97.78 mV
500 mV	1.61 V	11.83 V	97.72 mV
60 mV	1.74 V	13.77 V	98.12 mV
0 V	1.75 V	13.78 V	100.0 mV
−500 mV	1.90 V	13.78 V	117.2 mV
−1.000 V	2.03 V	13.77 V	135.8 mV
−1.500 V	2.17 V	13. 77 V	155.8 mV

factor for small input phase shifts cannot be due to a loss of control. Note that in Table XVIII, a decrease in the input phase shift of a factor of 10 is matched by a similar decrease in the output of the demodulator.

It is likely that the output of 65.24 mV_{RMS} when the nominal output of the simulators was 2.75 rad peak phase shift was due to the fact that the AD639 is increasingly inaccurate as the input gets larger than about 2 radians.

It must be emphasized that there is considerable latitude in choosing the scale factor during the design process. Gains can be set at various stages of the Symmetric Analog Demodulator to achieve the overall, desired scale factor. Specifically, the gains of the differentiators, the two summing amplifiers which sum the outputs of the two sets of six multipliers, and the integrator in the output of the demodulator all can be varied from the values we chose.

The gains chosen for the differentiators and the integrators are perhaps the most influential, since their effects are a function of frequency. By a judicious choice of these gains, not only can the scale factor be varied, but so can the envelope of the dynamic

Table XVIII These data rule out the hypothesis that the rise in scale factor with small combinations of amplitude and frequency can be due to a failure of the denominator input of the DIV100 to stay within range.

Ratio	V_{LEF}	ϕ_{LEF}	$V_{CONTROL}$	V_{OUTRMS}
1.000000	3.00 V	2.75 rad	10.42 V	65.24 mV
0.100000	300 mV	275 mrad	10.46 V	7.129 mV
0.010000	30 mV	27.5 mrad	10.49 V	715 μV
0.001000	3 mV	2.75 mrad	10.49 V	71 μV
0.000100	300 μV	275 μrad	10.49 V	——

range.

A comparison between the measured scale factor (31 mV/rad) and the predicted scale factor (29 mV/rad) is good evidence that the theoretical models provide a good description of the real system.

C. BANDWIDTH

The bandwidth of a system is the range of frequencies in which input signals can lie and still be processed usefully. In the case of linear systems, the frequency into the system is the same as the frequency out of the system. Therefore it is sensible to speak of the gain of the system at that frequency. In such systems, some frequency f_{PEAK} will have the highest gain through the system. At some higher frequency f_{UPPER}, the gain in power will only be one half that at f_{PEAK}.[18] If $f_{PEAK} \neq 0$, then there may also be a lower frequency f_{LOWER} with only half the gain in power. If there is no such frequency, then we specify $f_{LOWER}=0$ Hz. If $f_{PEAK}=0$, then we define the bandwidth B by

[18] The frequency f_{UPPER} is often called f_{3dB}, since the power is 3 dB lower at this frequency than at f_{PEAK}. If a signal's level is measured in volts or amperes, the power is half its maximum when the voltage or current is down by a factor of $1/\sqrt{2} \approx 0.7071$.

$$B = f_{UPPER}. \tag{277}$$

If $f_{PEAK} \neq 0$, then we define B by

$$B = f_{UPPER} - f_{LOWER}. \tag{278}$$

Unfortunately, interferometric sensors are not linear systems, inasmuch as they can generate many frequencies[19] for each input frequency. Likewise, interferometric demodulators are not linear systems, inasmuch as they can generate one output frequency for many input frequencies. The straightforward definitions of bandwidth just given for linear systems do not apply in an obvious way for these non-linear systems. How does one characterize the bandwidth of such a system?

As we have seen in earlier chapters, the interferometric output from output k can be modelled as

$$x_k(t) = D + E \cos\left[A \sin(\omega t) + \phi(t) - (k-1)\frac{2}{3}\pi\right]. \tag{279}$$

Here, E is the amplitude of the interference fringes and D is their central value. It is convenient for our present purposes to lump the two additional contributors to the phase together as one term ϕ. We shall treat this as a quasi-static term, neglecting its variation over time. In this case, we get the simplified expression

$$x(t) = D + E \cos[A \sin(\omega t) + \phi] \tag{280}$$

for the form of an unspecified output of the interferometer. This can be expanded using a well-known trigonometric identity.

---

[19] A countably infinite number of harmonics of the input frequency is generated, although most of the higher frequencies are completely negligible.

$$x(t) = D + E\cos(\phi)\cos[A\sin(\omega t)] - E\sin(\phi)\sin[A\sin(\omega t)]. \tag{281}$$

This has a Fourier expansion, given by Abramowitz [Ref. 18, p. 361]

$$x(t) = D + \cos(\phi)\left\{ J_0(A) + 2\sum_{k=1}^{\infty} J_{2k}(A)\cos[2k\omega t]\right\} - \sin(\phi)\left\{ 2\sum_{k=0}^{\infty} J_{2k+1}(A)\cos[(2k+1)\omega t]\right\}. \tag{282}$$

The function $J_k(A)$ is the Bessel function of order k. The dependence of the Bessel function on k and A is illustrated graphically in Appendix E.

If we examine Equation (282), we see that there are two sources of constants. One of these is D and the other is $J_0(A)$ attenuated by the factor $\cos(\phi)$. There also are even harmonics attenuated by the same factor, $\cos(\phi)$, and odd harmonics attenuated by a different factor, $\sin(\phi)$.

In this equation, we see clearly the manner in which the interferometer generates a multiplicity of output frequencies for a single input frequency. Notice, however, the dependence of the amplitude of the kth harmonic on $J_k(A)$. As A varies, so does the strength of this harmonic. When A is smaller than 1, $J_1(A)$ is bigger than $J_k(A)$ for all $k>1$. So in this small-signal regime, the system is not too unlike a linear system in that the fundamental frequency is dominant. The smaller A becomes, the more accurate this statement becomes.

In the small-signal regime, therefore, the bandwidth both of the interferometer and the demodulator can be defined in a manner similar to that in which it is defined for simple linear systems. Experimentally, we find that there is a maximum frequency f_{UPPER} where the gain in power is half that at f_{PEAK}. This frequency increases as A declines, but eventually reaches a limit at which it stops increasing. The interferometer is a lowpass system, so there is no lower frequency of half the gain in power. Therefore we will define the small signal bandwidth B as

$$B = f_{UPPER}. \tag{283}$$

Now the Symmetric Analog Demodulator was designed to have a low-frequency roll-off in gain, so it is actually a bandpass system. However, as we shall see, the high-frequency cutoff f_{UPPER} is so much higher than the low-frequency cutoff f_{LOWER} that the difference

$$B = f_{UPPER} - f_{LOWER} \approx f_{UPPER}. \tag{284}$$

The situation is different in the large-signal regime. When $A>>1$, the graphs in Appendix E show that the dominant frequencies are near fA. If too many of these dominant frequencies are attenuated by the system, it is impossible for the demodulator correctly to reproduce a signal of the form given in Equation ?. A better way to characterize the system in this regime is by the total harmonic distortion in the output. This is an indirect measure of the extent to which these high-frequency components are disproportionately altered by the system.

To measure the bandwidth of the Symmetric Analog Demodulator in the small-signal regime, we want only the fundamental at frequency $f=\omega_0/2\pi=f_0$ to be present. Equation (282) implies that, unless we control ϕ, we cannot guarantee that the fundamental will be present at all, nor can we be sure that the second harmonic at $f=2f_0$ will be suppressed. To arrange this, we want

$$\phi = \frac{\pi}{2} + k\pi \tag{285}$$

where k is an integer, so that

$$\sin(\phi) = 1 \tag{286}$$

and

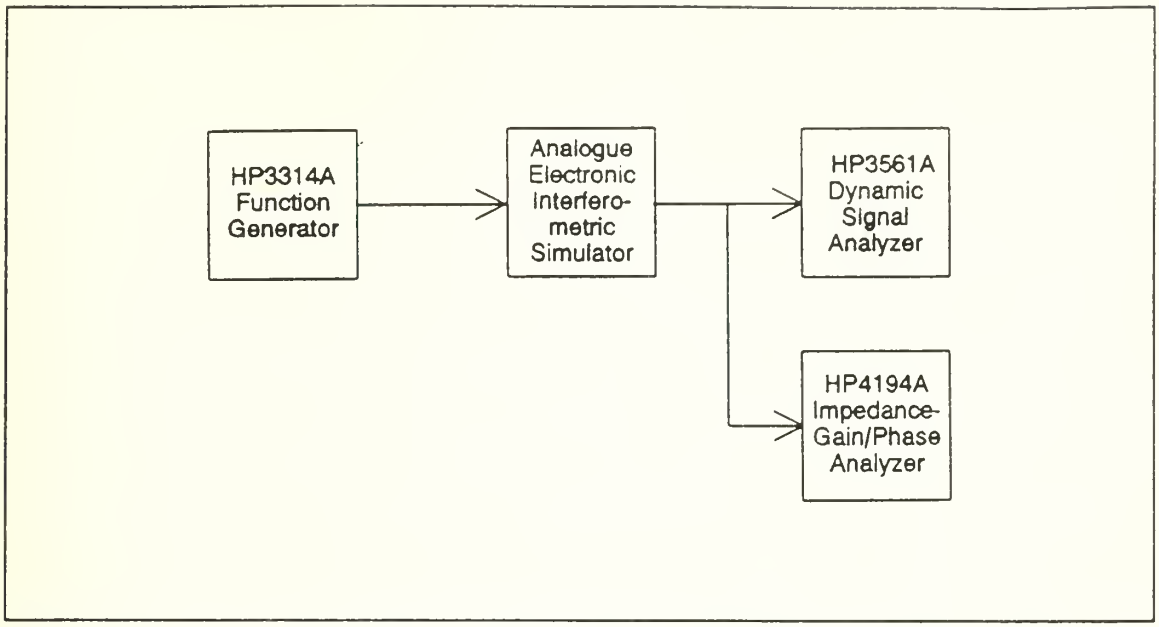

Figure 44 Instrumentation used to measure the small-signal bandwidth of the Analog Electronic Simulators.

$$\cos(\phi) = 0. \tag{287}$$

Now if we keep A small, then no odd harmonics above the fundamental will be present in strength, and likewise for all the even harmonics.

These conditions guided our selection of the analog electronic simulators rather than the optical interferometer to provide test inputs to the demodulator. They have a separate input to which a voltage dictating the "static" phase ϕ can be provided, in addition to the usual input to which a voltage dictating A can be given. This is the input labelled "PZT". The value of D can be set to zero by adjustment of the DC offset at the output through a control labelled "STATIC" on the front panel of the simulator. The effect of these settings, provided A is small enough, is to change the interferometric signal to this much simpler form:

$$x(t) \approx -2E\, J_1(A)\, \cos(\omega t). \tag{288}$$

We can now vary ω and so determine the small-signal bandwidth by finding the frequency f_{UPPER} where the scale factor decreases by $1/\sqrt{2}$. Before measuring the small-signal

bandwidth of the Symmetric Analog Demodulator itself, however, we first measured the small-signal bandwidth of the Analog Electronic Simulators. Figure 44 shows the instrumentation we used to measure the small-signal bandwidth of the analog electronic simulators. The HP3561A Dynamic Signal Analyzer was used to establish what DC level needed to be applied to the PZT input in order to eliminate the even harmonics, *i.e.*, the level needed to set $\cos(\phi)=0$ in Equation (282) and so generate the simple interferometric signal of Equation (288). We found that a DC voltage of 954 mV, corresponding to a phase shift of 876 mrad, was suitable. We set the output of the simulator to have no static offset, *i.e.*, $D=0$ in Equation (279). The elimination of the even harmonics by proper adjustment of ϕ also made the static offset $\cos(\phi)J_0(A)=0$. The harmonic distortion from the simulator was measured at only -65 dB or 0.06% total harmonic distortion when the input to the simulators was $V_{IN}=100$ mV. Converting this to the equivalent phase shift produced by the simulators, A was set to

$$\begin{aligned} A &= V_{IN}\, f_{S,EFF} \\ &= (100\ \text{mV})\left(918\ \frac{\text{mrad}}{\text{V}}\right) \\ &= 91.8\ \text{mrad}. \end{aligned} \tag{289}$$

This distortion rose to 1% for $V_{IN}=500$ mV, which we took as an acceptable level for the experiment.

Figure 45 shows a graph of the bandwidth of the Analog Interferometric Simulators. This plot was generated by the HP4194A Impedance-Gain/Phase Analyzer, set to cover a frequency span of 5 MHz. The measured bandwidth of the simulators is 1 MHz. Knowing the bandwidth of the simulators permits us to consider the bandwidth of the Symmetric Analog Demodulator. If its bandwidth is less than 1 MHz, then we can be sure that we shall have measured the bandwidth of the demodulator itself, and not that of the simulators.

Figure 46 shows the instrumentation we used to measure the bandwidth of the Symmetric Analog Demodulator. It is only slightly modified from that used to measure the bandwidth of the Analog Interferometric Simulators, shown in Figure 45. We have

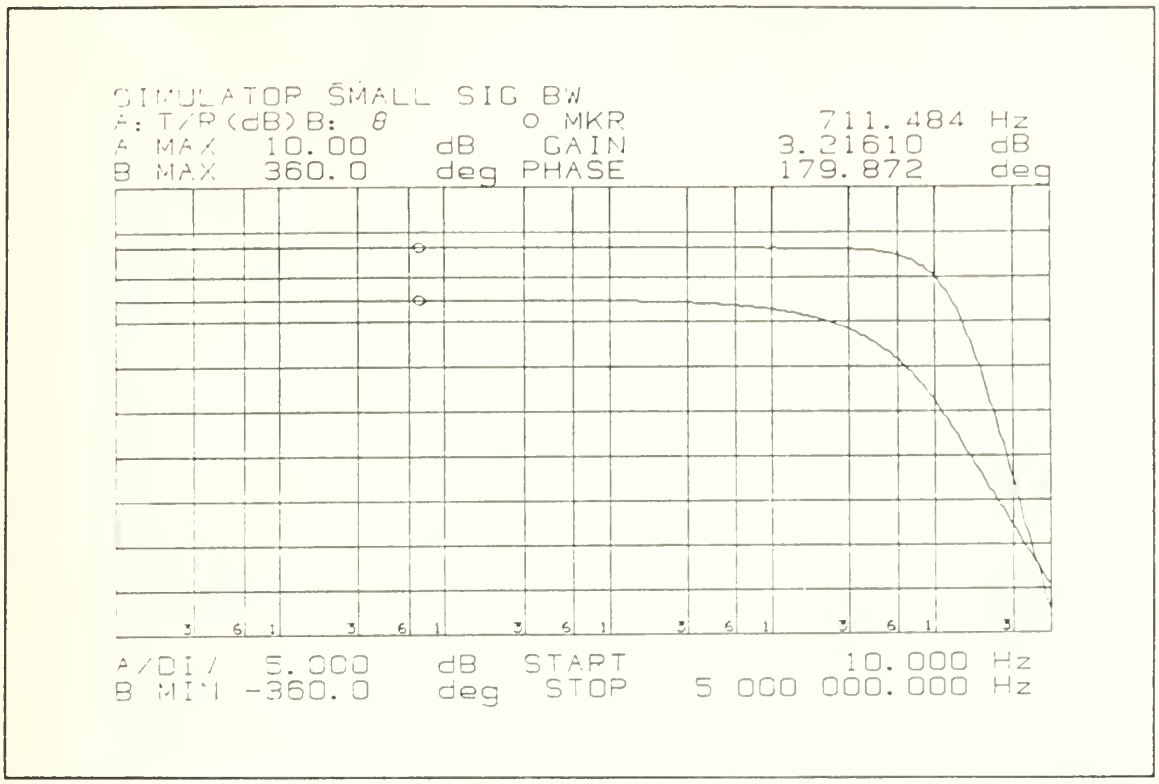

Figure 45 Small-signal bandwidth of the Analog Interferometric Simulators. The upper trace is the magnitude of the gain; the lower trace is its phase. The gain is down by 3dB at f = 1 MHz.

provided two additional simulators in order to provide simulations of the remaining two outputs of an optical fiber interferometer with a 3×3 output coupler.

We also performed measurements of the bandwidth of the Symmetric Analog Demodulator with larger inputs to the simulators. To get larger inputs still, we replaced the simulators with the combination of the HP6824A Power Amplifier and optical fiber interferometric sensor. In Figure 47 are plots of the magnitude of the gain of the combination of simulator (or interferometer) with demodulator. The five traces shown here indicate decreasing bandwidths when larger signals are provided to the simulators or interferometer. The four highest bandwidths are with the Analog Interferometric Simulators as inputs; the lowest is with the power amplifier and interferometer instead of the simulators. In decreasing order of bandwidth, the inputs had peak phase shifts of 219 mrad, 690 mrad, 2.17 rad, 5.54 rad, and 9.28 rad. We found that the small signal bandwidth was 113 kHz.

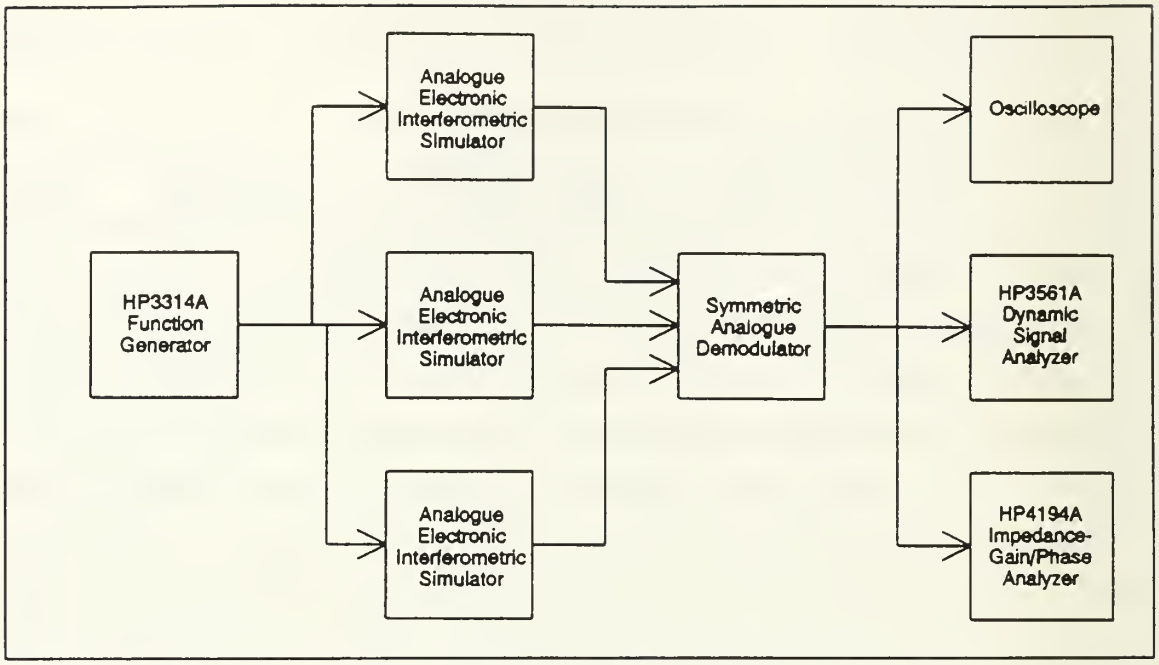

Figure 46 Block diagram of instrumentation for determining the small-signal bandwidth of the Symmetric Analog Demodulator.

The higher the input phase, the less accurate is Equation (288), so the usefulness of these plots is more open to question. In the next section, we shall characterize the performance of the Symmetric Analog Demodulator for large phase shifts at the input by considering the resultant total harmonic distortion. However, the plots make it clear that bandwidth and signal amplitude are inversely proportional. The small signal bandwidth of the Symmetric Analog Demodulator is 113 kHz. This is well below the 1 MHz bandwidth of the Analog Interferometric Simulators, so we can be sure we really are measuring the effect of the demodulator, not the simulators.

D. MAXIMUM ACCEPTABLE SIGNAL

We considered the small-signal bandwidth in the previous section. When the interferometer is subjected to signals with large phase amplitudes, this is no longer an effective measure of the performance of the demodulator. The reason, as we have seen, is that there is a multiplicity of frequencies present in the output of the interferometer and they all are important to the reconstruction of the input signal, modelled in Equation ?.

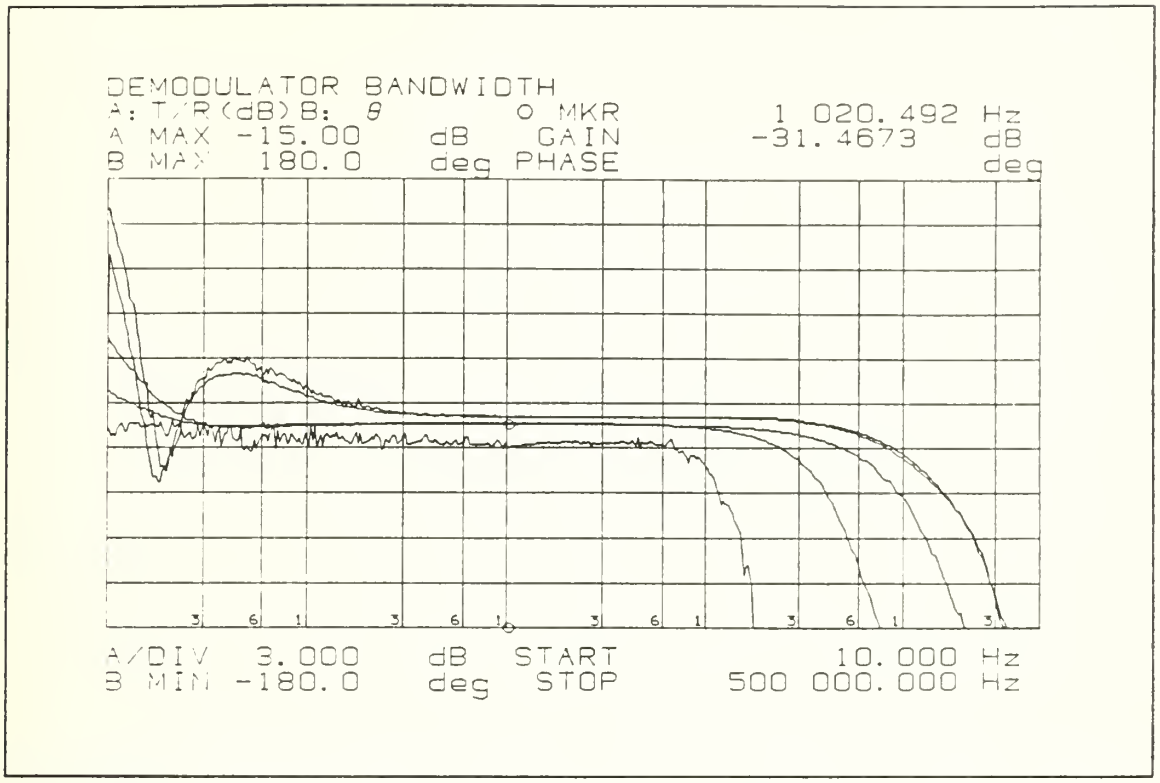

Figure 47 Measured bandwidth of the Symmetric Analog Demodulator (113 kHz for small signals). In descending order of bandwidth, the phase inputs to the demodulator were 219 mrad, 690 mrad, 2.17 rad, 5.54 rad, and 9.28 rad.

There is no precise amplitude of the signal of interest beyond which the demodulator fails to perform properly. The degradation in the quality of the output is gradual. What is more, both the amplitude and the frequency of the signal of interest have a bearing on this degradation.

The amplitude A of the signal of interest is what determines the amount of phase shift delivered to the demodulator by the interferometric sensor. If the signal of interest has frequency f and creates a peak phase shift of A radians, then in one period $T = 1/f$ of the signal of interest, the interferometric output undergoes $A/(2\pi)$ cycles (fringes). Thus, in one second, the interferometric output undergoes up to $(Af)/(2\pi)$ transitions. It is obvious from this reasoning, therefore, that the interferometric output has frequency components at higher frequencies than f, and this is true even if A is less than 2π.

The Fourier series of Equation (282) gives this statement a more precise meaning inasmuch as it quantifies the relative strengths of the various harmonic components. The

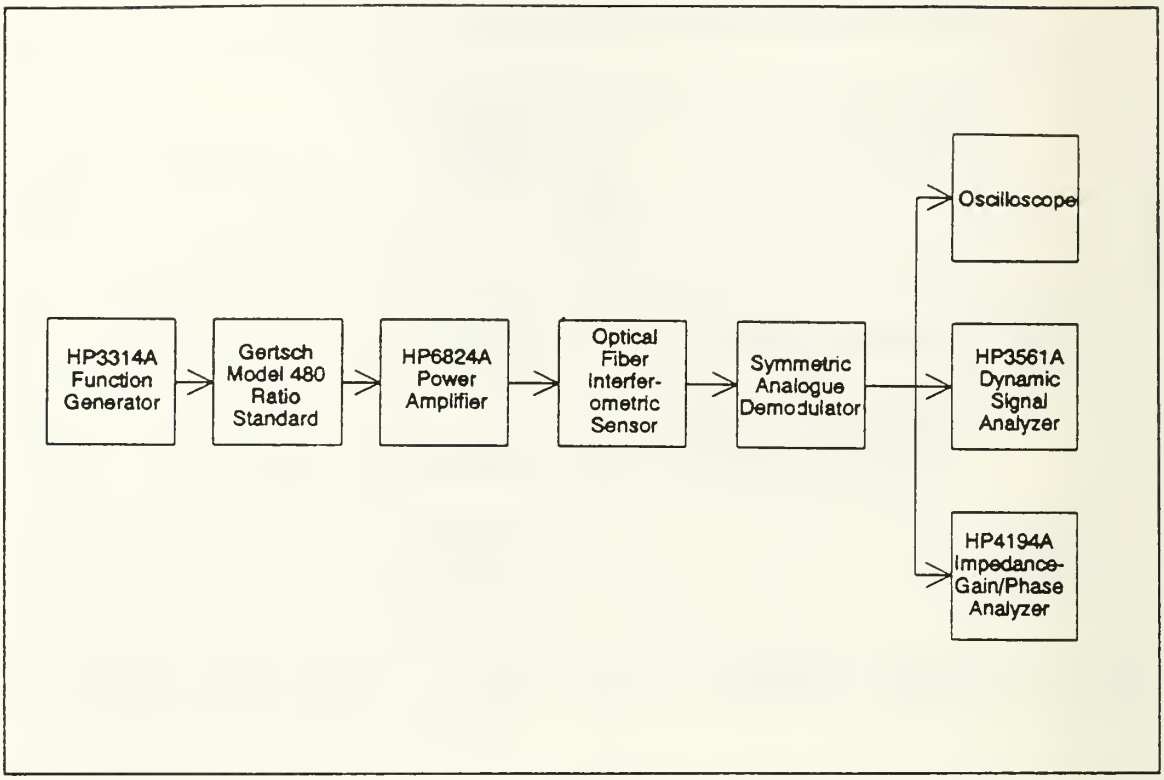

Figure 48 Block diagram of instrumentation for measuring the bandwidth of the Symmetric Analog Demodulator when the input is from the combination of power supply and optical fiber interferometer.

bandwidth of the demodulator is limited, and the frequency content of the interferometric output is affected by this limit. So there is a relationship between the bandwidth of the demodulator and the amplitude and frequency of the signal of interest. The limited bandwidth of the demodulator which we examined in the previous section has the effect of distorting its output because it attenuates higher frequency components more than lower frequency components. This is not the only distorting influence, however.

We have called the multiplicative product of phase shift and frequency the *phase rate*, since the product is measured in radians per second. When the received signal is differentiated, a signal results whose magnitude is proportional to the phase rate. A second mechanism for creating distortion is saturation of any of the demodulator's

internal amplifiers.[20] Saturation occurs when the amplifier receives excessively large inputs. So an excessively large phase rate can cause saturation. At the onset of saturation at any internal amplifier, distortion of the output begins to grow. As the degree of saturation intensifies, so does the consequent distortion.

To quantify the gradual loss of output quality due to limited bandwidth and limited phase rate, we can measure the total harmonic distortion present at the output of the demodulator when a single-frequency test signal is applied. When the signal of interest applied to the interferometer has frequency f, its harmonic overtones have frequencies kf for $k>2$. The output of the Symmetric Analog Demodulator will also contain these overtones. If the RMS amplitude at frequency kf is A_k, then the total harmonic distortion is defined as

$$\text{THD} = \frac{\sqrt{\sum_{k=2}^{\infty} A_k^2}}{|A_1|}. \tag{290}$$

For our purposes, we are not very concerned with how one might determine an acceptable level of total harmonic distortion. For audio applications, figures as low as 0.01% total harmonic distortion often are bandied about for amplifiers, although the linearity of speakers and the ability of the human ear to detect distortion below 1% is questionable. If one's objective is simply to determine that a particular frequency is present, considerably more distortion than this is permissible.

We have found experimentally that for distortion to be easily seen when a sinusoid is displayed on an oscilloscope, the level of total harmonic distortion must be between 4% and 10% or higher. Because of this fact, we have made measurements of the peak phase shift required to exceed 4% total harmonic distortion, and we have done so over a range of frequencies. We illustrate the fact that distortion of less than 1% is barely perceptible visually in the series of oscilloscope traces shown in Figure 49.

---

[20] An amplifier is saturated when its output is at the limit dictated by the power supplies or when it is slew-rate limited.

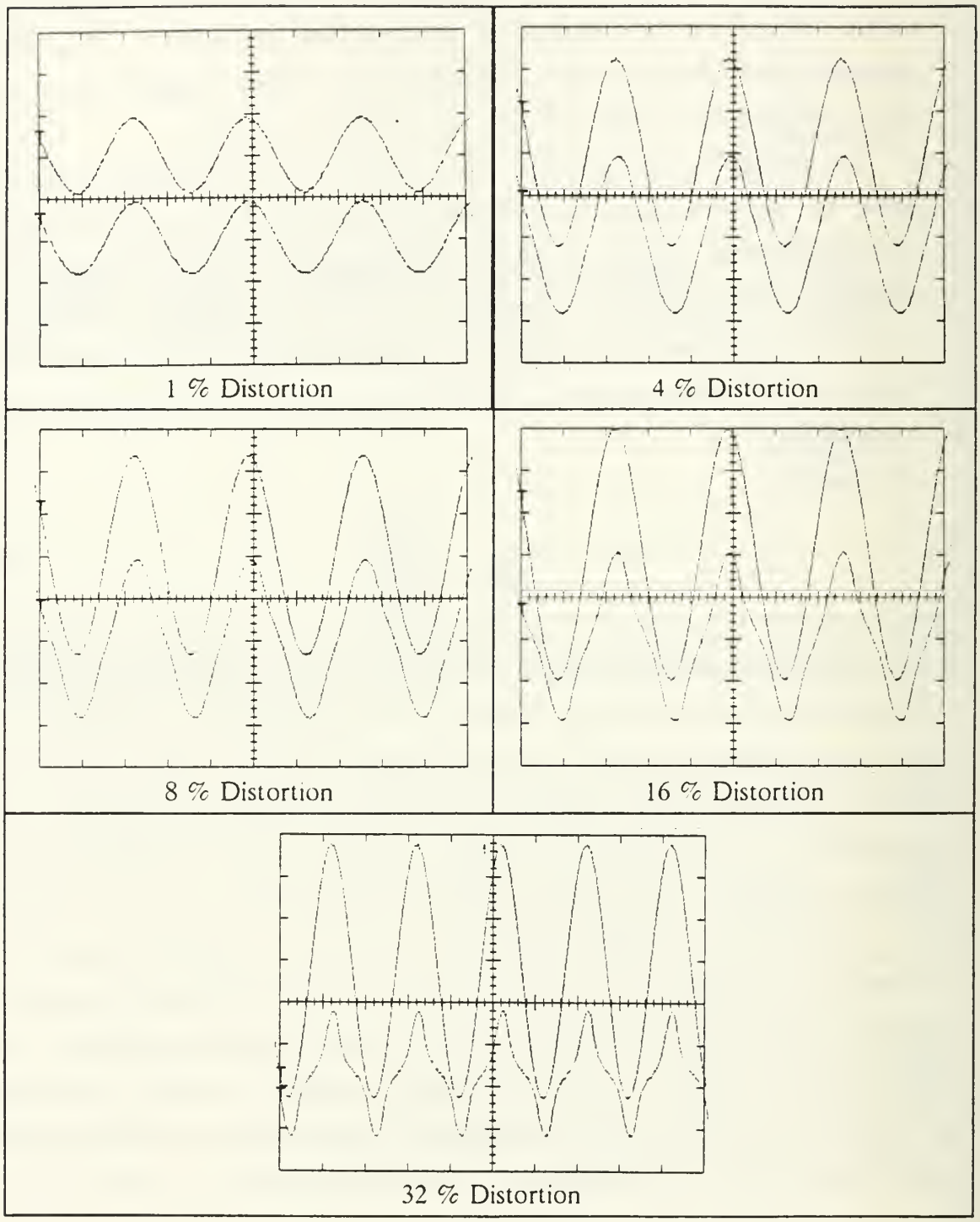

Figure 49 Five oscilloscope traces of increasingly distorted sinusoidal waveforms (lower traces) with an undistorted waveform for comparison (upper traces).

To measure the total harmonic distortion, we used the instrumentation depicted in Figure 50. The HP3561A Dynamic Signal Analyzer permits the user to designate the fundamental frequency and up to 20 harmonics. It automatically computes the harmonic distortion that these overtones represent.

The data are shown in Table XIX and graphed in Figure 51. In the table, V_{IN} is the voltage from the HP3314A Function Generator. The HP467A Power Amplifier was adjusted to give a gain of approximately 10 V/V. With this combination, the relationship between the phase generated by the interferometer and the voltage shown on the front panel of the HP3314A was found in Chapter IV by a least-squares fit to be

$$A = \left(34.29 \pm 0.02 \ \frac{\text{rad}}{\text{V}}\right) V_{IN} + (-0.64 \pm 0.08 \text{ rad}) \tag{291}$$

Table XIX These are the peak input phase shifts required to force the Symmetric Analog Demodulator output to exceed 4% total harmonic distortion.

f_{IN}	V_{IN}	A_{IN} (rad)	$f_{IN} A_{IN}$ (krad/s)
10 Hz	5.8 V	200	1.3
20 Hz	5.1 V	170	3.5
30 Hz	6.1 V	210	6.3
60 Hz	5.6 V	190	12
100 Hz	6.6 V	230	23
200 Hz	6.7 V	230	46
300 Hz	6.4 V	220	66
600 Hz	4.2 V	140	86
1 kHz	1.7 V	58	58
2 kHz	1.1 V	37	74
3kHz	700 mV	23	70
6kHz	360 mV	12	70
10 kHz	177 mV	5.4	54

and this is the equation used to compute A_{IN} in Table XIX. The product $f_{IN}A_{IN}$ also is shown in the table. The voltage selection on the front panel of the HP3314A was varied until the HP3561A indicated that the total distortion was 4%.

Gradual drift of the direction of polarization of the light in the interferometer alters

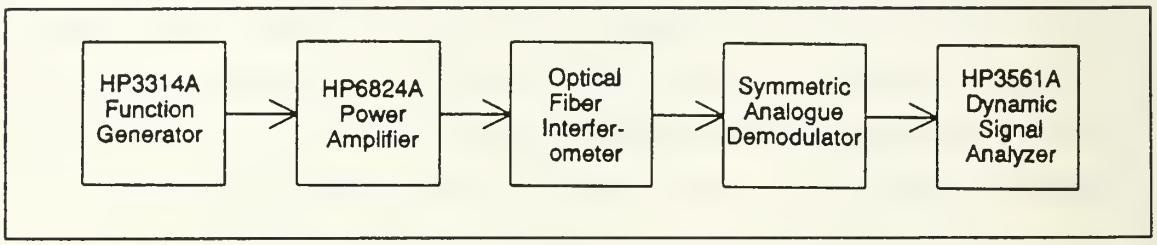

Figure 50 This instrumentation was used to measure the phase shift required to exceed 4% total harmonic distortion in the output of the Symmetric Analog Demodulator.

the fringe visibility and appears related to increases in laser noise which we observed to occur whenever fringe visibility declined markedly. These problems both can easily be corrected as necessary by varying the laser current, and we made these corrections in the course of this experiment in order to ensure that the demodulator had an undistorted interferometric waveform on which to operate. Consequently, the values of D and E in Equation (279) could not be held constant during this experiment. Undoubtedly this affected our measurements of the peak phase shift needed to exceed 4% total harmonic distortion. To obtain improved measurements would require the use of an interferometer with a reduced propensity to generate such noise, or a feedback controller to regulate the temperature of the laser and so keep it away from combinations of current, temperature, and back-reflection which cause such noise. (An alternative way to eliminate back-reflections would be to incorporate an optical isolator.) It is comforting to know, however, that even in the presence of this noise, the demodulator was generally able to recover the signal, albeit in a degraded manner. Of course, it was designed to counter the effects of changes in D and E in the model of Equation (279).

There are two distinct regions to the graph in Figure 51. For frequencies of up to about 300 Hz, the graph is horizontal. This reflects a limitation on the peak optical phase shift we could achieve through the use of the HP6824A Power Amplifier, which

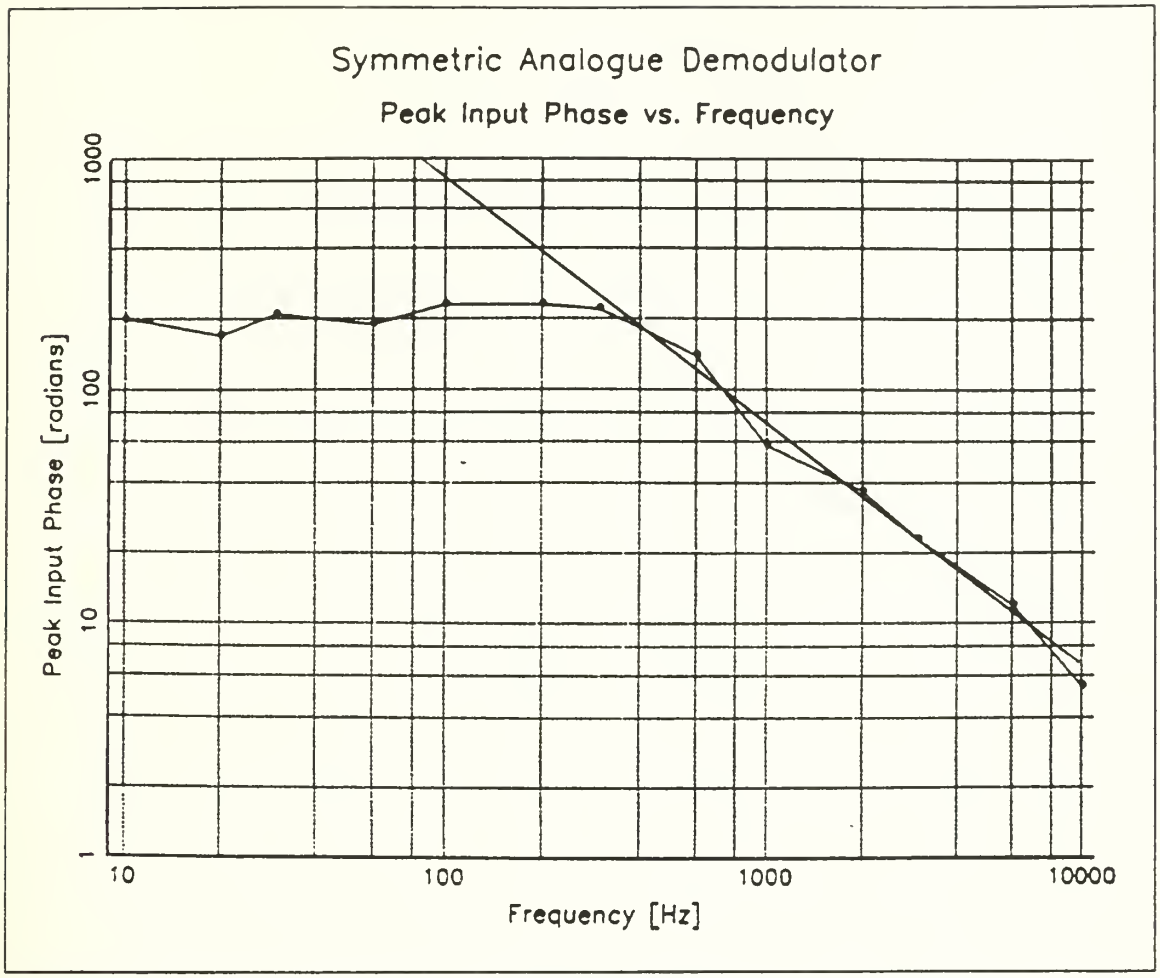

Figure 51 Peak phase shift into the Symmetric Analog Demodulator necessary to exceed 4% total harmonic distortion. The straight line extrapolates the region of constant phase rate to low frequencies.

saturated at around 60 V. The phase is so linear with voltage up to this limit that there is no reason to suppose that higher voltages applied to the piezoelectric cylinders in the optical interferometer would not continue to generate greater phase shifts. However, this was the most powerful amplifier we had available and so we could neither verify this supposition, nor obtain phase shifts in excess of about 250 radians.

For frequencies above about 300 Hz the graph begins to fall at roughly 20 dB per decade of frequency.[21] We have seen that it is the product of phase shift and frequency, the phase rate, which is crucial to the correct operation of the Symmetric Analog Demodulator. This product cannot exceed a value which is approximately constant over the range in which the demodulator operates with constant scale factor. For the demodulator, we have Af on the order of 65 krad/s. Recall that in the design, we sought voltage levels of 5 V at the output of each internal amplifier when the peak input phase A was 100 radians and the frequency of the signal of interest was 200 Hz. If the actual saturation voltage is 13.5 V, then we would expect a maximum phase rate of

$$\frac{V_{SAT}}{V_{DESIGN}} \phi_{MAX} f_{MAX} = \frac{13.5}{5}(100 \text{ rad})(200 \text{ Hz}) = 54 \frac{\text{krad}}{\text{s}} \tag{292}$$

which is close to what we achieved.

Further insight into the performance of the Symmetric Analog Demodulator can be gleaned from two further plots of harmonic distortion. Figure 52 shows a contour plot of the harmonic distortion as a function of the frequency and the phase amplitude of the signal of interest. The contour lines join points with equal harmonic distortion. The data were taken by a computer operating our apparatus on an IEEE-496 bus. The contour plot represents interpolation between the points where measurements were taken.

The same data are displayed in a different form in Figure 53, which is a perspective view of a three-dimensional plot of the total harmonic distortion above the plane of frequency and phase amplitude of the signal of interest.

From these two plots, we can see that there is a large region in the center of the plots where distortion is quite low. Not surprisingly, distortion becomes severe where the phase rate (the product of phase amplitude and frequency) is high, for under these circumstances, high frequencies are present in the interferometric output, and they are

---

[21] This appears to be a linear decline on a log-log plot and is a rectangular hyperbola on a linear-linear plot.

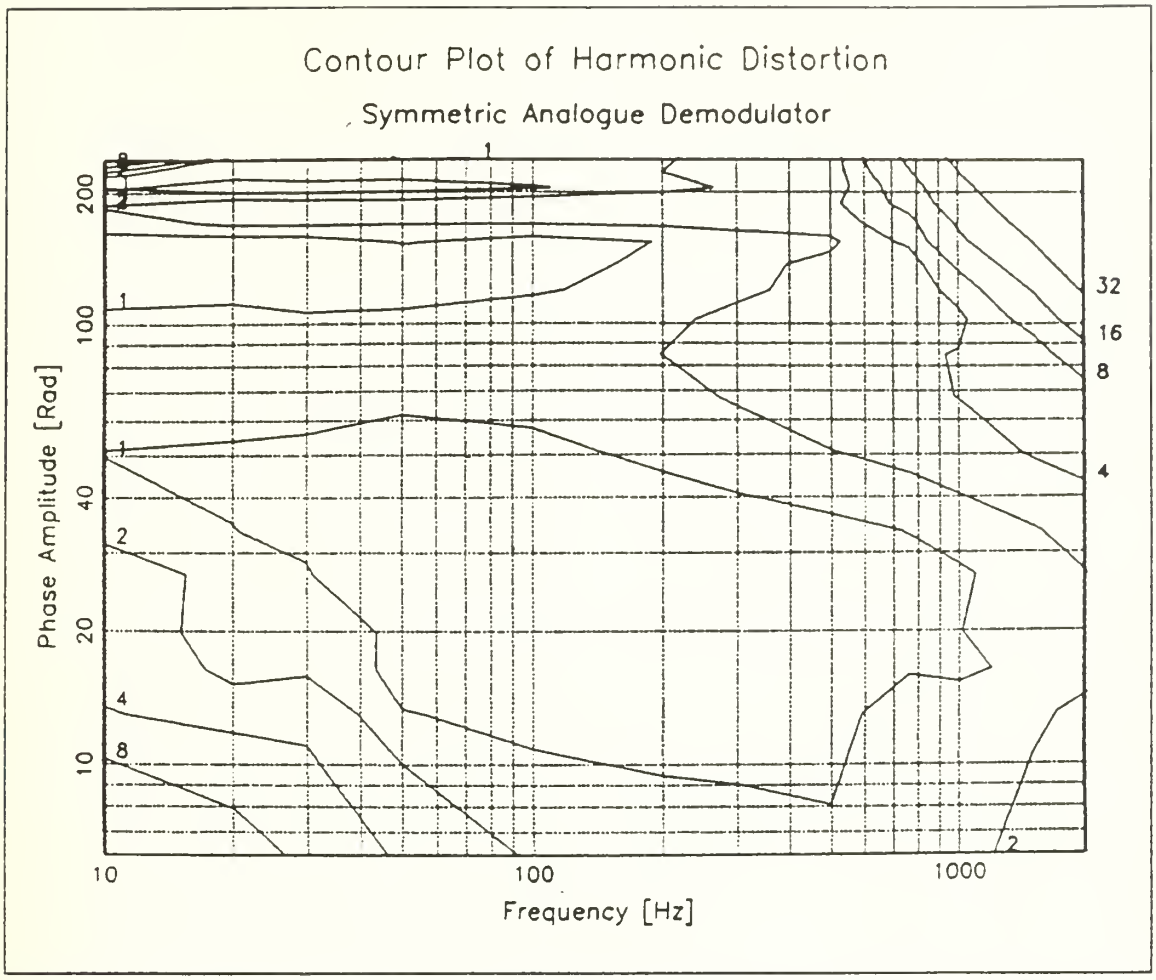

Figure 52 Contour plot of the Harmonic Distortion in the output of the Symmetric Analog Demodulator as a function of frequency and amplitude of the signal of interest.

adversely affected by the limited bandwidth of the demodulator.

In the opposite corner, distortion due to noise from the differentiators is evident. The other two corners also show increased total harmonic distortion, although for high frequencies and low phase amplitudes, it still is below 4%. For low frequencies and large phase amplitudes, the low-frequency roll-off of the integrators distorts the output.

To modify our design to set a different maximum acceptable signal, it is necessary to ensure that the gains within the demodulator are altered so that when this phase rate is present, no amplifier reaches saturation. It is also necessary that no amplifier be expected to change its outputs faster than its specified slew rate (measured in volts per second). Some increase in the maximum permissible phase rate can be achieved by

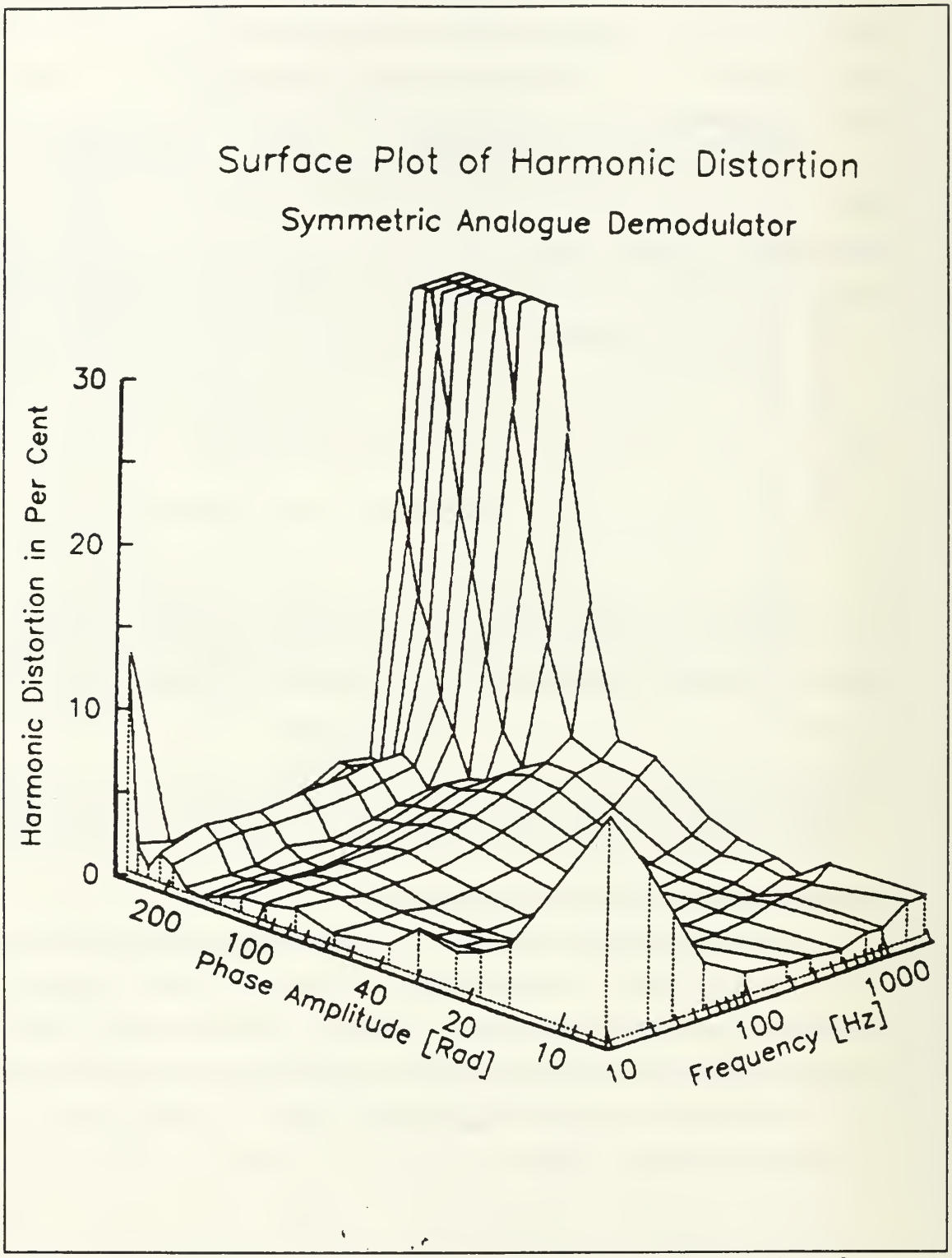

Figure 53 Surface plot of the Harmonic Distortion in the output of the Symmetric Analog Demodulator as a function of frequency and amplitude of the signal of interest.

limiting the outputs of the internal amplifiers to small enough levels. However, this measure has an adverse effect on dynamic range since the ratio of peak signal-to-noise declines if the peak output signal must be smaller but the noise is fixed in magnitude.

E. NOISE FLOOR

We have now seen that in the small-signal regime, the demodulator has a bandwidth of around 113 kHz. We have also examined the peak phase shifts (as a function of frequency) which can be demodulated with less than 4% total harmonic distortion. Let us now turn to the performance when only very small phase shifts are present.

To measure the noise floor, we used the same instrumentation shown earlier in Figure 42. At that time, we were interested in measuring the scale factor of the Symmetric Analog Demodulator. Here, we use the same measuring technique, but because the inputs are small, we are actually measuring the noise. We measure the mean voltage delivered by the demodulator and its standard deviation. The ratio of the mean to the standard deviation is defined as the ratio of signal to noise, S/N. To obtain the noise floor, we simply measure S/N while gradually decreasing S. When $S/N=1$ (0 dB), the signal and the noise are of equal strengths. The only difficulty is that as the signal vanishes, the lock-in amplifier becomes progressively less able to detect anything. So we shall try to extrapolate to the noise floor without actually reducing S all the way to it.

We set the HP3456A Digital Voltmeter to perform 10 integrations per cycle of the power line, and to take 768 such samples. The effect of this was to give over two minutes of averaging. The HP3314A Function Generator was set to provide a peak output voltage of 1.00 V. This signal was reduced by the Gertsch Model 480 Ratio Standard to maintain a precise peak. We applied the effective scale factor for the Analog Interferometric Simulators which is shown in Appendix C to be is $F_{S,EFF}$ = 918±4 mrad/V to calculate the effective peak phase A from the simulators. The EG&G Princeton Applied Research Model 5210 Lock-In Amplifier was operated with a time constant $\tau=1$ s and with a filter roll-off of 12 dB per octave. The equivalent noise bandwidth resulting from these settings can be computed from the formula

Table XX Measurements to obtain the noise floor of the Symmetric Analog Demodulator (23-110 Hz). Data marked with an asterisk (*) were not included in the least-squares fit.

f	Ratio	V_{EFF}	A_{EFF}	S	$V_{OUT,RMS}$	S/N
23 Hz	0.100000	100 mV	91.8 mrad	10^3	2.01±0.055 V	31 dB
	0.050000	50.0 mV	45.9 mrad		1.00±0.076 V	22 dB
	0.025000	25.0 mV	23.0 mrad		0.51±0.066 V	18 dB
	0.012500	12.5 mV	11.5 mrad		0.261±0.055 V	13 dB
	0.006250	6.25 mV	5.74 mrad		0.147±0.048 V	10 dB *
35 Hz	1.000000	1.00 V	918 mrad	10^2	2.3340±0.0041 V	55 dB
	0.100000	100 mV	91.8 mrad	10^3	2.801±0.033 V	38 dB
	0.010000	10.0 mV	9.18 mrad	10^4	2.91±0.42 V	17 dB
	0.005000	5.00 mV	45.9 mrad		1.55±0.40 V	12 dB
	0.002500	2.50 mV	2.30 mrad		1.02±0.34 V	10 dB *
65 Hz	1.000000	1.00 V	918 mrad	333.3	7.8236±0.0079 V	60 dB
	0.100000	100 mV	91.8 mrad	3.3×10^3	9.293±0.072 V	42 dB
	0.010000	10.0 mV	9.18 mrad		983±71 mV	23 dB
	0.005000	5.00 mV	11.5 mrad		512±80 mV	16 dB
	0.002500	2.50 mV	2.29 mrad		289±58 mV	14 dB *
110 Hz	1.000000	1.00 V	918 mrad	333.3	7.0990±0.0047 V	64 dB
	0.100000	100 mV	9.18 mrad		794.1±3.4 mV	47 dB
	0.010000	10.0 mV	9.18 mrad		78.2±4.6 mV	25 dB
	0.005000	5.00 mV	4.59 mrad		37.2±3.7 mV	20 dB
	0.002500	2.50 mV	2.29 mrad		19.9±3.5 mV	15 dB

$$B_{EQN} = \frac{1}{8\tau} = 125 \text{ mHz}. \tag{293}$$

The experimental observations are shown in Table XX and Table XXI. It will be noticed that when signal levels are strong, the signal-to-noise ratio drops roughly 6 dB for every halving of the effective voltage V_{III}, as it should. This is somewhat inaccurate, which is not too surprising inasmuch as the standard deviation of each set of measurements is not always the same at a single value of the frequency f. It also becomes grossly inaccurate for the lowest signal levels, 5.74 mrad and 2.30 mrad, at 23 Hz and 35 Hz respectively. These data show that the standard deviation does not change too much at these low levels, and if the standard deviation truly measures the noise, this is to be expected. However, the mean fails to decline by one half at these low levels. Doubtless this is due to the fact that the mean and the noise are now of comparable values.

To extrapolate the declining ratio of signal to noise to the level where signal and noise are equal, *i.e.*, where the signal-to-noise ratio is 1 (0 dB), all the data except those marked with an asterisk (*) in Table XX and Table XXI were subjected to a least squares linear curve fit. The signal-to-noise ratio in dB was regarded as the independent variable and the logarithm to the base 10 of the effective peak input phase shift was regarded as the dependent variable. Table XXII shows the linear equations which result from this procedure. To find the noise floor, it is only necessary to let S/N be 0 in each equation. This gives the logarithm of the phase shift A which would produce an output voltage equal to the noise. Thus, by this procedure, we can regard *all* of the output noise as due to phase noise at the input.

The great utility of the lock-in amplifier is its ability synchronously to detect less and less signal if it examines a narrower and narrower bandwidth. In order to isolate the performance of the Symmetric Analog Demodulator from that of the lock-in amplifier, we should normalize the noise floor found by this extrapolation process by dividing it by

Table XXI Measurements to obtain the noise floor of the Symmetric Analog Demodulator (200 Hz - 1.00 kHz).

f	Ratio	V_{LH}	A_{EFF}	S	$V_{OUT\,RMS}$	S/N
200 Hz	1.000000	1.00 V	918 mrad	333.3	6.7219±0.0027 V	68 dB
	0.100000	100 mV	91.8 mrad		717.6±2.6 mV	49 dB
	0.010000	10.0 mV	9.18 mrad		69.4±1.9 mV	31 dB
	0.005000	5.0 mV	4.59 mrad		33.8±2.3 mV	31 dB
	0.002500	2.5 mV	2.29 mrad		16.9±2.3 mV	17 dB
300 Hz	1.000000	1.00 V	918 mrad		6.7175±0.0024 V	69 dB
	0.100000	100 mV	91.8 mrad	3.33×10^3	7.186±0.026 V	49 dB
	0.010000	10.0 mV	9.18 mrad	33.3×10^3	7.31±0.20 V	31 dB
	0.001000	5.00 mV	4.59 mrad	10^5	2.84±0.69 V	12 dB
	0.000500	500 µV	2.29 mrad		1.37±0.62 V	6.9 dB
590 Hz	1.000000	1.00 V	918 mrad	333.3	6.5138±0.0012 V	24 dB
	0.100000	100 mV	91.8 mrad	3.33×10^3	6.7976±0.0067 V	60 dB
	0.010000	10.0 mV	9.18 mrad	33.3×10^3	6.811±0.069 V	40 dB
	0.001000	1.00 mV	4.59 mrad	10^5	2.09±0.21 V	20 dB
	0.000500	500 µV	2.29 mrad		1.07±0.21V	14 dB
1.0 kHz	1.000000	1.00 V	918 mrad	333.3	6.4731±0.0021 V	70 dB
	0.100000	100 mV	91.8 mrad	3.33×10^3	6.7374±0.0035 V	66 dB
	0.010000	10.0 mV	9.18 mrad	33.3×10^3	6.760±0.045 V	44 dB
	0.001000	1.00 mV	4.59 mrad	10^5	2.05±0.13V	24 dB
	0.000500	500 µV	2.29 mrad		1.03±0.14 V	18 dB

Table XXII Least squares fit of the logarithm of phase input to the Symmetric Analog Demodulator to achieve a given ratio S/N of signal to noise.

Frequency	Least-squares fit
$23Hz$	$\log\left(\frac{A_{EFF}}{1rad}\right) = [(50\pm7)\times10^{-3}]\frac{S}{N}_{dB} + (-2.6\pm0.1)$ with r=0.983
$35Hz$	$\log\left(\frac{A_{EFF}}{1rad}\right) = [(53\pm2)\times10^{-3}]\frac{S}{N}_{dB} + (-2.96\pm0.06)$ with r=0.9989
$65Hz$	$\log\left(\frac{A_{EFF}}{1rad}\right) = [(53\pm1)\times10^{-3}]\frac{S}{N}_{dB} + (-3.22\pm0.05)$ with r=0.9994
$110Hz$	$\log\left(\frac{A_{EFF}}{1rad}\right) = [(52\pm2)\times10^{-3}]\frac{S}{N}_{dB} + (-3.39\pm0.06)$ with r=0.9986
$200Hz$	$\log\left(\frac{A_{EFF}}{1rad}\right) = [(51\pm1)\times10^{-3}]\frac{S}{N}_{dB} + (-3.55\pm0.06)$ with r=0.9990
$300Hz$	$\log\left(\frac{A_{EFF}}{1rad}\right) = [(53.3\pm0.6)\times10^{-3}]\frac{S}{N}_{dB} + (-3.69\pm0.02)$ with r=0.9998
$590Hz$	$\log\left(\frac{A_{EFF}}{1rad}\right) = [(53\pm2)\times10^{-3}]\frac{S}{N}_{dB} + (-4.12\pm0.08)$ with r=0.998
$1kHz$	$\log\left(\frac{A_{EFF}}{1rad}\right) = [(57\pm7)\times10^{-3}]\frac{S}{N}_{db} + (-4.4\pm0.3)$ with r=0.979

Table XXIII Computation of the phase noise spectral density for the Symmetric Analog Demodulator.

Frequency f	Logarithm of Phase Floor $\log_{10}(A\ IV)$	Phase A	Bandwidth B	Phase Spectral Density $A^{\dagger}$
23 Hz	−2.55	2.88 mrad	125 mHz	8.0 mrad/√Hz
35 Hz	−2.962	1.09 mrad		3.09 mrad/√Hz
65 Hz	−3.218	606 μrad		1.71 mrad/√Hz
110 Hz	−3.386	410 μrad		1.16 mrad/√Hz
200 Hz	−3.547	284 μrad		803 μrad/√Hz
300 Hz	−3.686	210 μrad		583 μrad/√Hz
590 Hz	−4.117	92 μrad		220 μrad/√Hz
1 kHz	−4.41	72 μrad		110 μrad/√Hz

the square root of the bandwidth.[22] The bandwidth of the lock-in amplifier can be computed from Equation (293).

Table XXIII shows the computation of the phase noise spectral density from the equations of Table XXII. It is important to note that the generation of a linear curve-fit from logarithmic data is not as reliable as doing so from linear data. While the data shown in Table XXII show the standard deviation of the error in both the mean and the variance of the logarithmic data, taking the corresponding linear data to the same number of decimal places is inappropriate. In Table XXIII we have contented ourselves with quoting the resulting phase noise spectral density $A^{\dagger}$ to two or three decimal places.

Figure 54 presents the data of Table XXIII in graphical form. Note that the spectral density is not constant with frequency, as it would be if the noise were white. Instead, it declines at the rate of about 20 dB per decade of increase in frequency, *i.e.*, the noise voltage spectral density is proportional to the reciprocal of the frequency, $1/f$.

---

[22] If we were considering the power spectral density, we could simply divide by the bandwidth in hertz. Since the phase shift (or, for that matter, the voltage) are proportional to the square root of the power, we divide either of them by the square root of the bandwidth. The resultant units are rad/√Hz or V/√Hz.

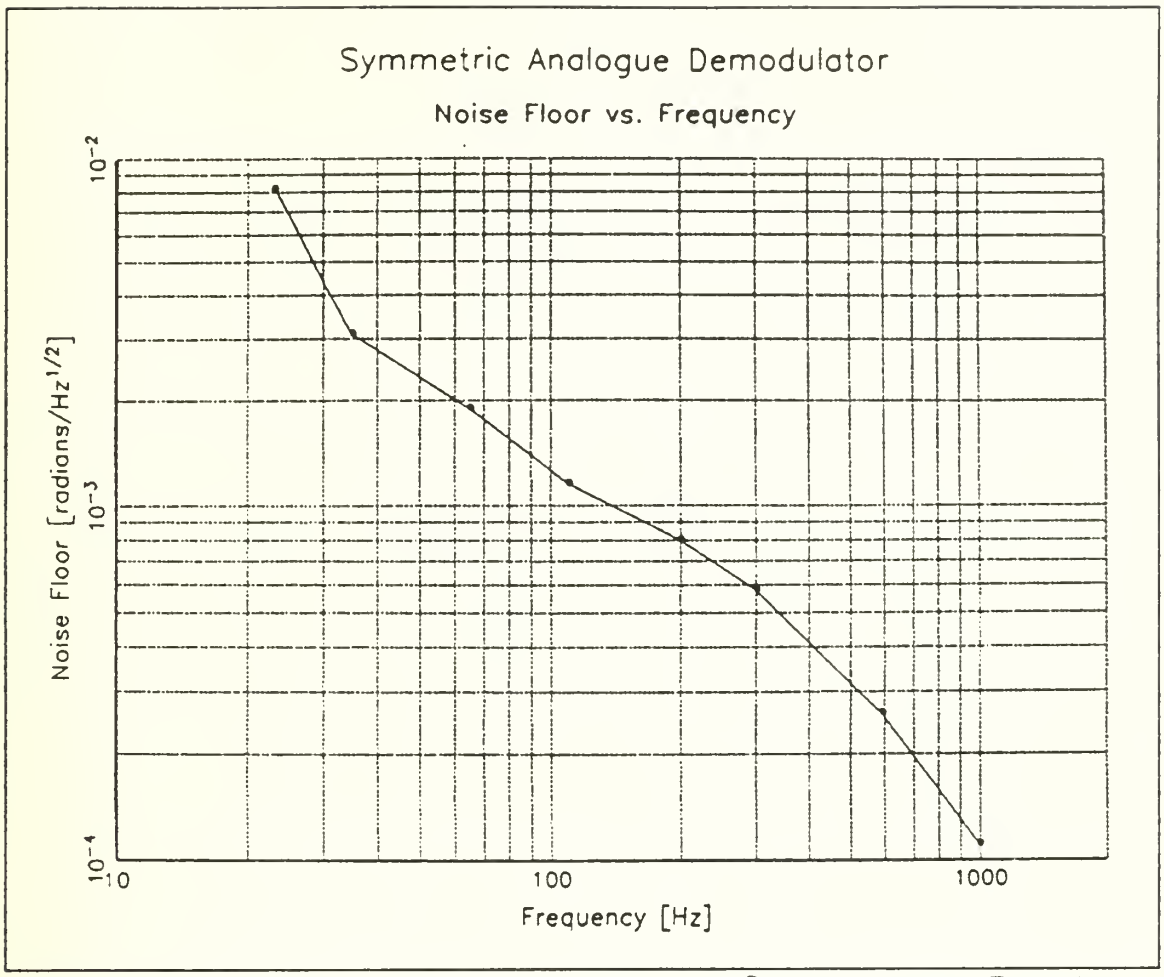

Figure 54 Plot of the phase noise spectral density of the Symmetric Analog Demodulator as a function of frequency of the signal of interest. The spectral density indicates the minimum discernible signal in a one hertz bandwidth.

Consequently, its noise power spectral density declines at a rate proportional to $1/f^2$. This is a form of "pink" noise, for the lower frequencies are noisier. It is not to be confused with that variety of noise usually called pink or $1/f$ noise and whose *power* declines at the rate $1/f$. The voltage spectral density of that kind of noise declines at the rate of $1/\sqrt{f}$. [23]

Pink noise is what one would expect from the Symmetric Analog Demodulator since its output stage is an integrator. An integrator has a $1/f$ voltage gain characteristic. If white noise were present at its input, pink noise should be present at the output, at least

[23] The term "pink" is applied by analogy with visible light, in which the lowest frequencies are red and the highest frequencies are blue.

until the intrinsic noise of the output stage itself becomes significant. Generally speaking, operational amplifiers can be modelled as generating white noise at their outputs when the frequency is above about 100 Hz. If the input noise is greater, however, then this noise is not noticeable until very high frequencies are reached, for only then does the gain characteristic of the amplifier attenuate the input noise sufficiently for it to be less than the amplifiers own noise. We show in the detailed noise analysis in Appendix F that the demodulator's output noise is indeed due to the effect of integration of white noise from the analog divider.

Now the input to the Symmetric Analog Demodulator as a whole may be white, but the differentiation that takes place early in the demodulation process would convert this white noise to "blue" noise, *i.e.*, noise with more high frequency content than low frequency content. Yet this noise is largely dwarfed by the noise inherent to the Analog Devices AD534 multipliers. This, in turn, is swamped by the white noise output of the Burr-Brown DIV100. When the white noise reaches the integrator, a characteristic decline in power proportional to $1/f^2$ results.

F. DYNAMIC RANGE

The dynamic range of the Symmetric Analog Demodulator is the difference between the smallest and the largest phase shift it can successfully demodulate. As we have seen, we can characterize the largest phase shift as that which produces the most harmonic distortion that we can tolerate. We can characterize the lowest phase shift as that which is equal to the noise of the demodulator. The upper limit is essentially fixed in character. The lower limit, however, is a function of the bandwidth under consideration, for we have expressed the noise floor in phase noise spectral density.

We shall choose this spectral density as the lower limit. Implicit in using this as the lower end of the dynamic range is the assumption that we are looking in a 1 Hz bandwidth. We can increase the dynamic range of the Symmetric Analog Demodulator by narrowing the bandwidth in which we view the output. Likewise, if we widen the bandwidth, diminished dynamic range is the consequence.

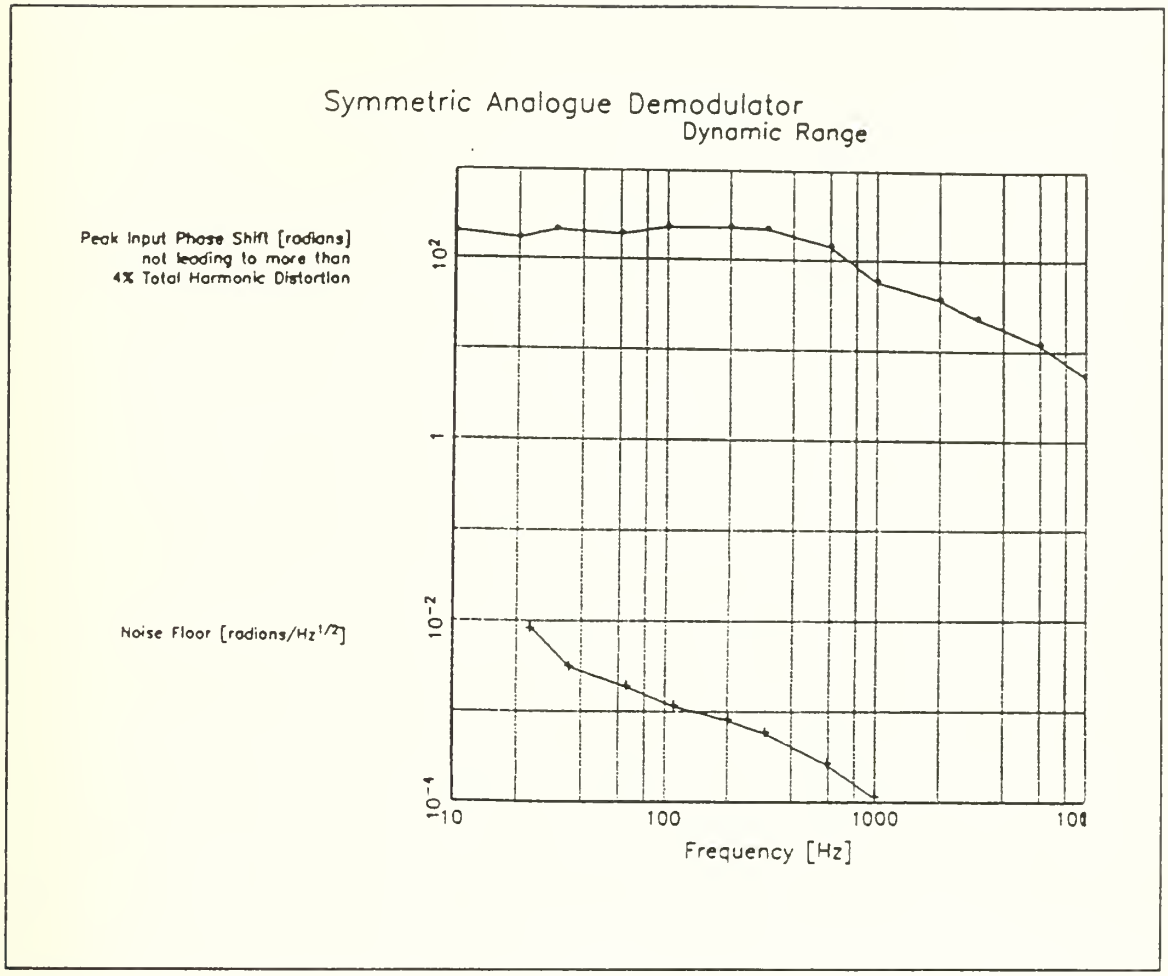

Figure 55 The dynamic range of the Symmetric Analog Demodulator when the output is viewed in a 1 Hz bandwidth.

Of course, changing the bandwidth in the frequency domain is tantamount to varying the duration of observation in the time domain. To achieve a narrower bandwidth, we observe the output of the demodulator for a longer period of time. Conversely, to widen the bandwidth, we shorten the period of observation.

In Figure 55, we show plots of the maximum acceptable signal (that which induces 4% total harmonic distortion) and the phase noise in a 1 Hz bandwidth. These data were shown separately when we considered these two characteristics of the performance of the Symmetric Analog Demodulator previously. Here they are superimposed on the same scale. The dynamic range is the ratio of the upper limit at a frequency to the lower limit.

Since this plot is logarithmic, the dynamic range in a 1 Hz bandwidth can be obtained by subtracting the lower limit from the upper limit in decibels.

For example, at a frequency f=590 Hz, the dynamic range of the Symmetric Analog Demodulator in a 1 Hz bandwidth is

$$\frac{\text{Maximum acceptable phase (4\% THD)}}{\text{Phase noise in a 1 Hz bandwidth}} = \frac{140 \text{ rad}}{260\ \mu rad} = 5.38\times10^{5} \equiv 115 \text{ dB}. \quad (294)$$

G. COMPLEXITY

The Symmetric Analog Demodulator is of only moderate complexity. The chief difficulty is understanding the principles of its operation. This is essentially just an exercise in mathematics. Of course, the beauty of the mathematical models is not entirely matched by that of the real signals. They are noisy; those of the models have no noise. More significantly, the models we have used, those on which the algorithm are based, assume that all three outputs of the 3×3 coupler have the same constant offset D, the same amplitude E (see Equation (279) on page 176), and precisely 120° phase shift between each output and any other output. In reality, these assumptions are more or less wrong. Despite this fact, the demodulator works quite well.

As far as the circuit itself is concerned, it does not consist of very many parts. It could be integrated onto a single (or possibly a very few) application-specific integrated circuits (ASIC) for some reduction in the amount of space, weight, and power required. As it is, it could fit onto a single printed circuit board without much difficulty.

H. APPROXIMATE COST

Table XXIV provides a calculation of the cost of the integrated circuits in the Symmetric Analog Demodulator. The parts are identified by their part numbers. The quantity of each part required is listed, along with prices from recent price lists. (The

Table XXIV Calculation of the cost of the integrated circuits used in the Symmetric Analog Demodulator.

Part ID	Description	Quantity Required	Price	Source of Price	Total Cost of Part
AD534	Analog Multiplier	6	$29.95	Analog Devices	$179.70
DIV100	Analog Divider	1	$36.60	Burr-Brown	$36.60
OPA-111	Low-noise Op Amp	3	$11.80	Burr-Brown	$35.40
AD712	General Purpose Op Amp	5	$3.60	Analog Devices	$18.00
TOTAL		15			$269.70

source of the price is provided.) The total price of under $269.70 is very modest for a demodulator with more than 110 dB dynamic range, extending from hundreds of microradians to hundreds of whole radians. A practical demodulator would include some additional items, such as the printed circuit board, passive components, connectors, packaging, and the like. Also, any commercially available demodulator would have some level of profit built into the price, too.

Subsequent to the construction of this demodulator, Analog Devices released the AD734 integrated circuit multiplier. At $14.77 for a single chip, it is cheaper than the AD534 at $29.95 by a factor of 2. Its bandwidth is 10 MHz, versus 1 Mhz for the AD534. Finally, its scale factor is programmable, whereas on the AD534 it is essentially fixed. This change lets the new chip perform division as well as multiplication. If it were used, the DIV100 chip used in our demodulator could be replaced by this new device.

I. SUMMARY

In this chapter we have considered the performance of a passive homodyne demodulator which employs a new algorithm for demodulation, namely, symmetric demodulation. We have seen that the dynamic range achieved is 115 dB, and this was without pushing the design to handle low levels of signal. The phase rate is 65 krad/s,

and this, too, could be improved. This demodulator permits handling of signals both below and above the level of π rad of optical phase shift, which gives it a very decided advantage over fringe-rate demodulators. Its cost is low, less than $270, and we mentioned that the cost and performance both could be improved by the use of a new integrated circuit multiplier whose bandwidth is greater than that of the AD534 by a factor of 10 and whose cost is a factor of two lower.

In the next chapter, we return to the asymmetric demodulation algorithm, describing its implementation in digital, rather than analog, electronics.

XII. DESIGN OF AN ASYMMETRIC DIGITAL DEMODULATOR

A. BACKGROUND

In this chapter we consider the design of a digital circuit to implement the asymmetric demodulation scheme discussed in Chapter VII. The purpose is to prove that a digital implementation is feasible. Many techniques of sophisticated signal processing are more easily done with digital electronics, and so a system which recovers the signals in a digital form and furnishes them to following circuits in the same form is useful in some applications.

Any digital technique requires that an incoming analog signal first be sampled and digitized. Since the optical fiber interferometric sensors which we consider in this dissertation have three outputs, one for each output fiber of the interferometer, there are three analog signals available. The symmetric method described in Chapter VIII uses all three, but the asymmetric method can discard one of these,[24] and this is how we implemented it. We can use an analog-to-digital converter (A/D) to convert the analog signals to two binary numbers representing their values.

Of course, one could provide a digital output to following circuits from the output of an analog demodulator. However, we chose to attempt to demonstrate the feasibility of doing the whole demodulation in digital circuitry. For the purpose of showing that the scheme works, we terminate it with a conversion from digital back to analog. This would not typically be required in an application. However, it makes it quite easy to see the wave form output by the demodulator on an ordinary oscilloscope.

It is desirable that the range of voltages across which the A/D can operate match the range of voltages across which the signal ranges. This takes full advantage of the resolution which the A/D possesses. This is especially important when the number of bits

---

[24] It is possible to use all three interferometric outputs in fabricating the in-phase and quadrature components required by the asymmetric demodulation method, but there is no clear advantage to doing so. There is a drawback, in that more circuitry is needed to do so.

in the digital representation is small, for there are fewer numbers available for representing all possible voltages. It is wasteful to use, say, only one third of the full range of an A/D.

Matching the range of the signals to that of the A/D is not easy. It is particularly difficult with the signals output by an optical fiber interferometric sensor because they are modelled by the equation

$$x_k(t) = D + E\cos\left[\xi(t) + \phi(t) - (k-1)\frac{2}{3}\pi\right]. \qquad (295)$$

Recall that in this equation, D is a central value around which the outputs vary; E is the peak variation of the signals from this value; $\xi(t)$ is the signal of interest, a reconstruction of which we want the demodulator to provide; $\phi(t)$ is an additional phase shift due to extraneous factors; and the final multiple of $2\pi/3$ is due to the particular choice of output from the interferometer. Now D and E both vary in an uncontrollable way. Changes in laser power and changes in polarization both have an effect on these parameters. So the A/D must be able to handle signals in the range $D \pm E$, and since this range is variable, it must be able to handle the greatest possible range that this can have. On average, we do not expect the signals to have this maximal range, and so some mismatch between the range of the signals and the range of the A/Ds is inescapable.

The earliest point where digitization can be performed is just after the receiver section, where the signals have been converted for the first time to voltage signals described by Equation (295). However, we shall postpone the digitization until after D has been subtracted from each of the two signals in analog circuitry. This is not strictly necessary since some A/Ds can handle a voltage range which is not centered around 0 V (we say its range is offset from zero). Many of them, however, and in particular the ones we used, require that the offset voltage be known. To measure it entails adding all three outputs together, as shown in the discussion of symmetric demodulation in Chapter VIII. This means that we must have a receiver for each of the three outputs, even though in the asymmetric method only two are needed for the algorithm. Since it takes little extra effort to perform the subtraction of D in analog circuitry, we elected to do this.

Ideally, one would be able to eliminate the effects of variability of E, the peak deviation of the signal from D. In the symmetric demodulation scheme, this is done by a ratiometric technique. There unfortunately is no way to measure E prior to digitization of the signals without fairly elaborate analog processing, in which case the question must arise, why not use an analog demodulator? If a digital signal is needed for later processing, then the analog demodulator's output could be digitized. Only one A/D would be required, and strict control over the output amplitude would be available for a given phase amplitude. One could measure E in digital circuitry, but this would have to occur after the digitization, and so the benefit of being able to match the range of the analog to digital conversion to the peak values of the signal would not be available. So we shall live with the wastefulness of resolution inherent in not being able to control E, and shall digitize the signals once the average value has been subtracted off. This must be seen as a major flaw in the use of a digital demodulator.

There are several approaches we could have taken in implementing an asymmetric digital demodulator. An obvious one would have been to use either a microprocessor or a dedicated Digital Signal Processor (DSP) integrated circuit to perform the calculations required by the algorithm. We considered this, but found that the number of instructions needed to complete all the processing necessary on each pair of samples of data would take longer to process than the 2.5 μs required by the A/D we chose to use, the Analog Devices AD7769. To take full advantage of the speed of the A/D, we would have needed two DSPs in parallel. This is feasible, but we elected a different course.

We decided to implement the algorithm with a purely hardware circuit. We used dedicated multipliers, adders, subtractors, and registers. The registers permit the use of a pipe-lined architecture in which different samples of data are being processed simultaneously at various stages of the circuit. The result of this approach is a complicated circuit (especially on a breadboard), but the processing is so fast that the A/Ds remain the limiting factor on speed, which was what we had in mind.

B. DETAILED DESIGN

The schematic diagrams for the Asymmetric Digital Demodulator are given in Figure 56 through Figure 59. The majority of the integrated circuits in the demodulator operate on a single +5 V power supply. However, the A/D and the D/A have special requirements. The A/D requires a +12 V power supply. Its absolute peak supply voltage is +15 V, but we felt that to push the operation to this limit was unwise, even though we were already using +15 V commonly for analog circuits, and despite the need for an additional power supply. The D/A requires a −5 V power supply for its negative analog output reference. Unlike the AD7769 A/D, it can handle up to ±17 V for its main power supplies, so running it on the standard ±15 V was not a problem.

As we mentioned earlier, the AD7769 has an input to specify the offset voltage, the voltage around which the inputs fluctuate. This value is restricted to staying between +2 V and +6.8 V. Because +5 V is already available, and is within this range, we shall use it for the V_{BIAS} input to the AD7769. For greater accuracy, one should use a precision voltage reference at this input, a precaution we have ignored.

The variation from this offset is specified as a voltage at the V_{SWING} input of the AD7769. It can be between +2.0 V and +3.0 V. We shall specify it to be +3.0 V; a voltage divider composed of 10.0 kΩ and 30.1 kΩ resistors divides the +12 V power supply down to +3.0 V to provide this reference. Strictly speaking, this voltage, too, should be provided with a precision reference, but again, we have ignored this.

Our interferometric signals have had D removed from them. The offset voltage specified at the V_{BIAS} input requires that we add +5 V back in to the signal. Also, the deviation E of the signals from the central value must be scaled so that it never exceeds V_{SWING} in magnitude.

The AD7769 requires a clock signal which can have a frequency of up to 400 kHz, thus providing a conversion period of 2.5 μs. The clock signal must be a square wave from 0 to +5 V. We generated this using an HP3314A Function Generator. This signal functions as a strobe to cause conversion to begin. There actually is an internal clock, too. However, the external clock is the one which we use to synchronize the entire

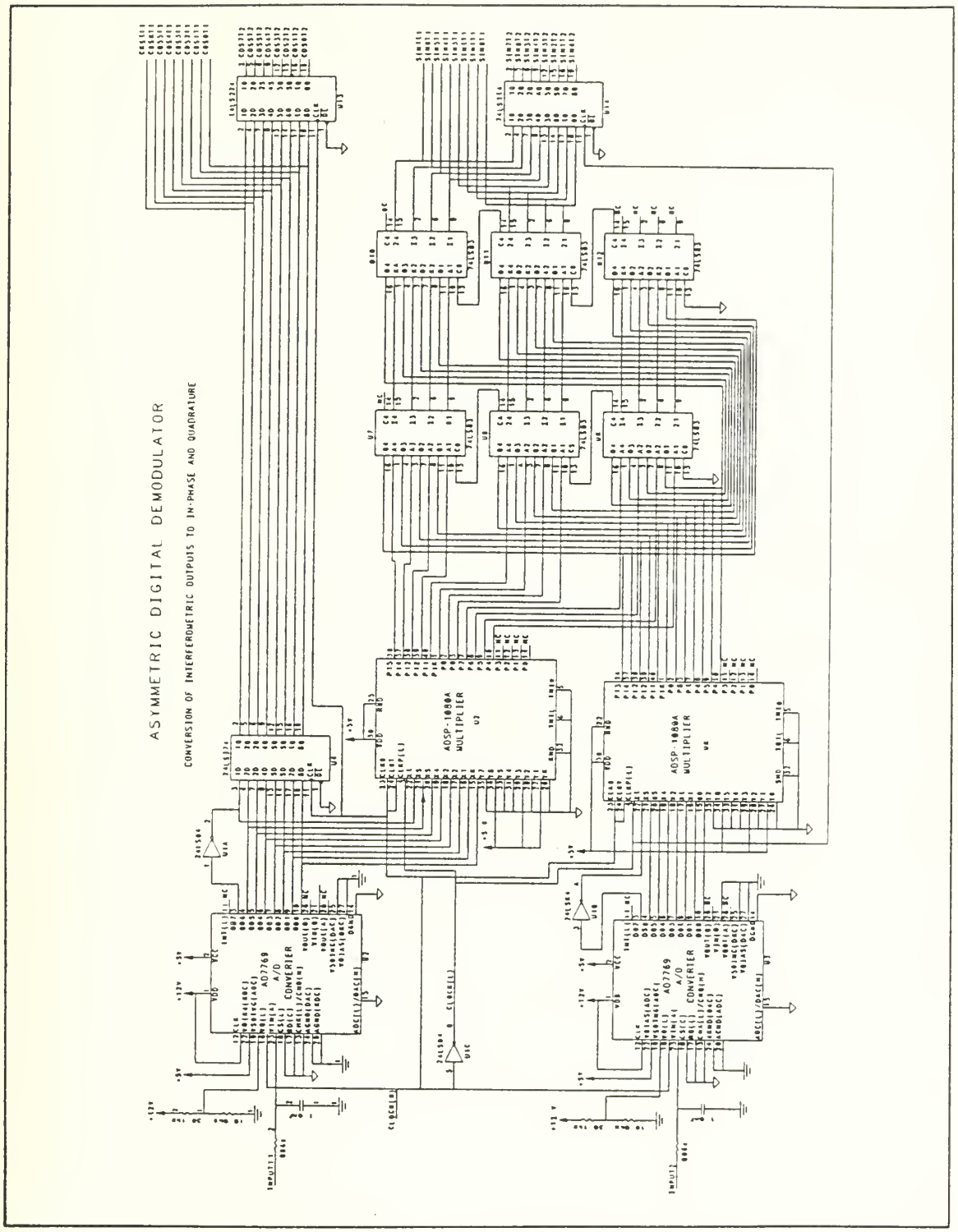

Figure 56 Schematic of the Asymmetric Digital Demodulator. This section converts two of the interferometric outputs to digital form and creates an in-phase and a quadrature signal from them.

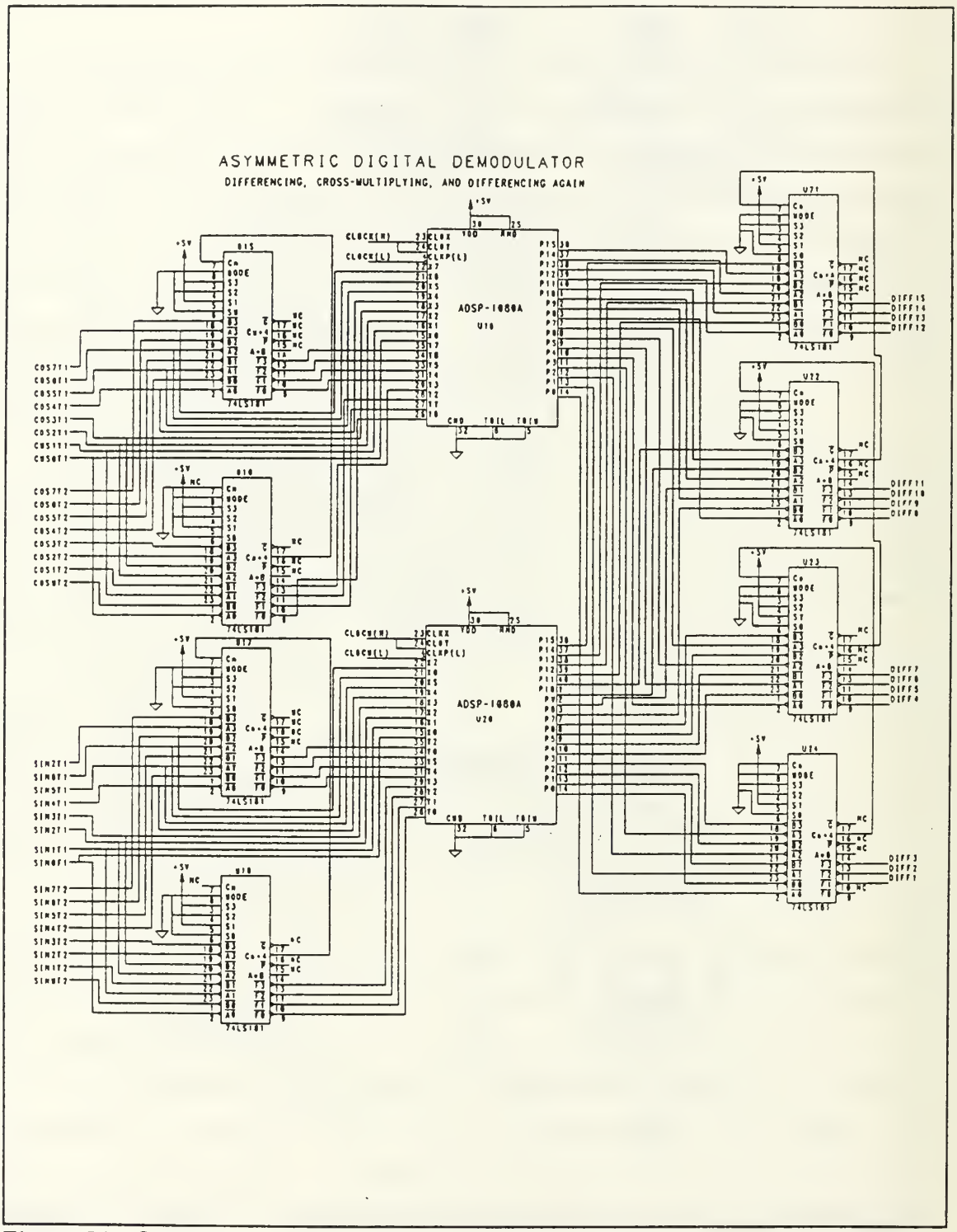

Figure 57 Schematic of the Asymmetric Digital Demodulator. This section finds differences between consecutive samples, cross-multiplies one signal with the difference from the other signal, and subtracts one from the other.

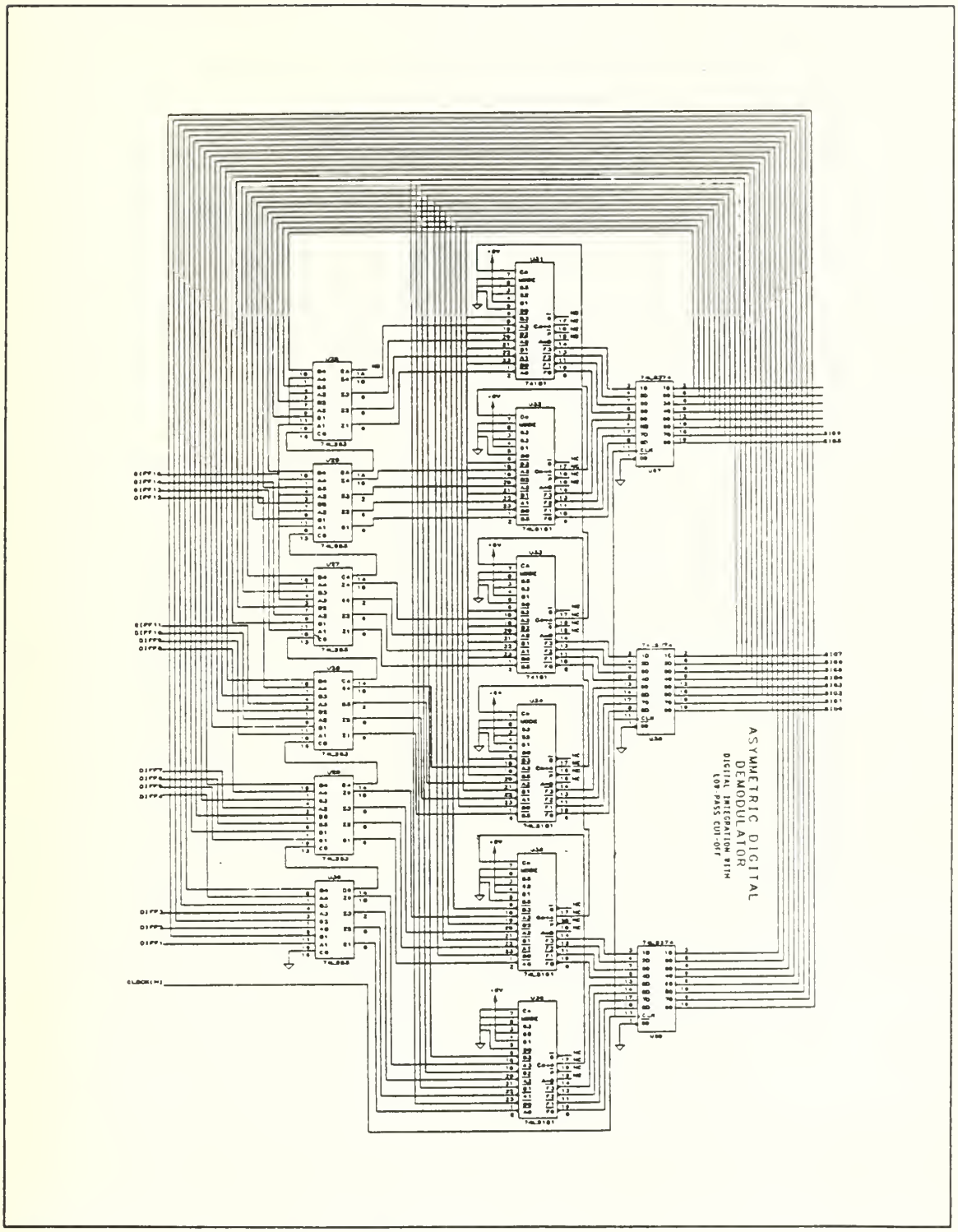

Figure 58 Schematic of the Asymmetric Digital Demodulator. This section performs an integration of the derivative of the signal of interest which was created in the preceding section.

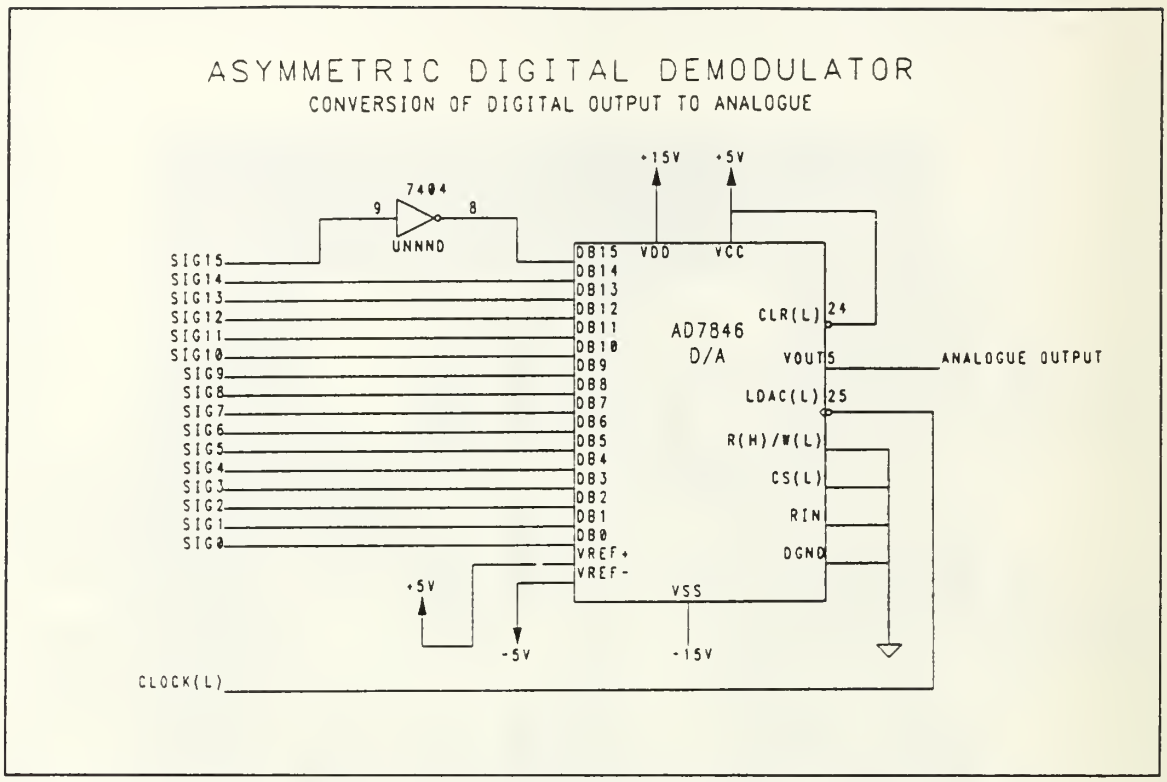

Figure 59 Schematic drawing of the Asymmetric Digital Demodulator. This section is the digital-to-analog converter which creates an analog reconstruction of the output of the digital circuitry.

pipeline processor.

At the end of the conversion, an unsigned 8-bit binary quantity appears on the data lines. To facilitate subsequent arithmetic, this is converted to a signed quantity by logical inversion of its high-order bit 7. Before conversion, the bits can be regarded as having the following weights:

Bit	7	6	5	4	3	2	1	0
Weight	2^{-1}	2^{-2}	2^{-3}	2^{-4}	2^{-5}	2^{-6}	2^{-7}	2^{-8}

After conversion, the bits should be re-interpreted to mean

Bit	7	6	5	4	3	2	1	0
Weight	-2^0	2^{-1}	2^{-2}	2^{-3}	2^{-4}	2^{-5}	2^{-6}	2^{-7}

The effect of this is to devote the first bit to the function of carrying the sign of the value held in the other 7 bits. These bits can give values between 0 and $1-2^{-7}=0.9922$. The result of using all 8 bits then is a signed number in the range -1 to 0.9922. The conversion then has created an unscaled cosine function, but, if the value of the input has a variation of less than V_{SIGNAL}, then the output is scaled by a factor less than one.

The inversion of the high-order bit is performed by U1A, a 76LS04 hex-inverter. We can regard one of the two outputs as the cosine. From it and the other input (with its 120° phase shift) we want to construct the sine. This is equivalent to saying that a 120° phase shift is not correct: we want it to be 90°.

How can we accomplish this? The two digitized signals now have the form

$$x_1(t) = \cos(\xi) \qquad \text{and} \qquad x_2(t) = \cos\left(\xi - \frac{2}{3}\pi\right). \tag{296}$$

We can make use of the trigonometric identity

$$\cos(A-B) = \cos(A)\cos(B)+\sin(A)\sin(B) \tag{297}$$

to rewrite $x_2(t)$ as

$$x_2(t) = \cos(\xi)\cos\left(\frac{2}{3}\pi\right)+\sin(\xi)\sin\left(\frac{2}{3}\pi\right) = -\frac{1}{2}\cos(\xi)-\frac{\sqrt{3}}{2}\sin(\xi). \tag{298}$$

From this we can obtain $\sin(\xi)$ by the linear combination

$$\frac{2}{\sqrt{3}}x_2(t)-\frac{1}{\sqrt{3}}x_1(t) = \frac{2}{\sqrt{3}}\left(-\frac{1}{2}\cos(\xi)+\frac{\sqrt{3}}{2}\sin(\xi)\right)+\frac{1}{\sqrt{3}}\cos(\xi) = \sin(\xi). \tag{299}$$

In digital electronics, as in analog, we must take care that quantities remain within specific limits. In our case, the interpretation we have placed on the bits of an 8-bit word is such that quantities must remain within the range -1 to 0.9922. Does the computation

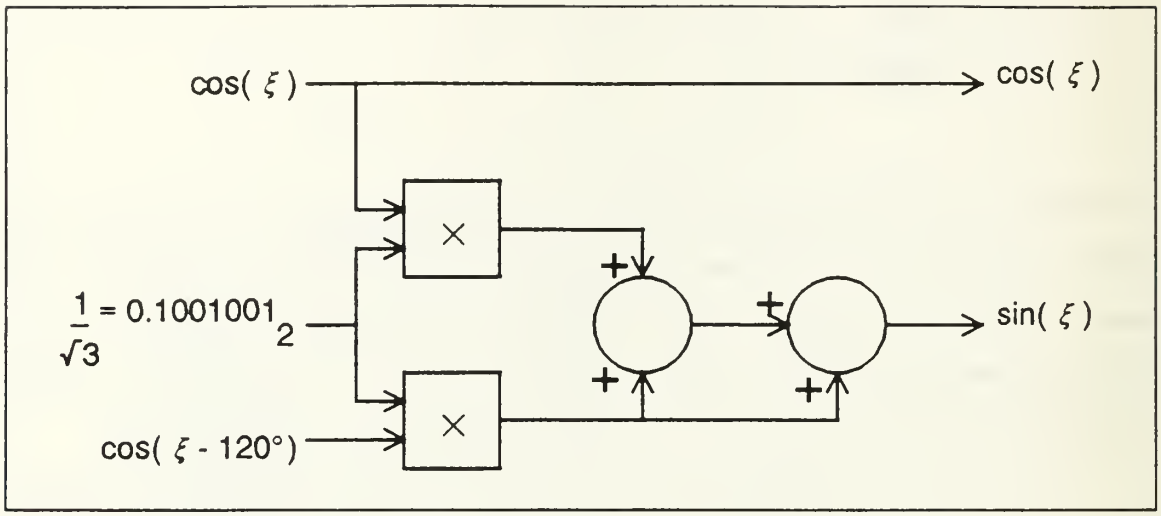

Figure 60 Block diagram showing how to obtain the in-phase and quadrature wave forms without overflow.

shown in Equation (299) cause any intermediate results to be outside this range? That depends on the specific manner in which we implement the equation. The obvious way to integrate it is with two multipliers to do the scaling and one adder to perform the summation. However, the scale factor $2/\sqrt{3} \approx 1.155 > 1$, so this method can indeed cause an overflow. If we perform the scaling in two steps, however, as illustrated in the block diagram in Figure 60, then overflow cannot occur.

To see that this method avoids overflow, we can rewrite Equation (299) as

$$\left(\frac{1}{\sqrt{3}}x_2(t)+\frac{1}{\sqrt{3}}x_1(t)\right)+\frac{1}{\sqrt{3}}x_2(t). \tag{300}$$

We have already shown that this sum yields $\sin(\xi)$. We now digress briefly in order to see how to rewrite the first term in a manner that makes its magnitude clear.

In general, the expression $A\cos(\psi)+B\sin(\psi)$ can be rewritten as

$$A\cos(\psi)+B\sin(\psi) \;=\; D\cos(\psi+\phi) \tag{301}$$

where D and ϕ are values which we would like to determine. To do so, we use the trigonometric identity

$$\cos(A+B) = \cos(A)\cos(B)-\sin(A)\sin(B) \tag{302}$$

to give

$$D\cos(\psi+\phi) = D\cos(\phi)\cos(\psi)-D\sin(\phi)\sin(\psi). \tag{303}$$

We can equate the coefficients of the sine and cosine to yield

$$A = D\cos(\phi) \quad \text{and} \quad B = D\sin(\phi). \tag{304}$$

From the trigonometric identity

$$\sin^2(\phi)+\cos^2(\phi) = 1 \tag{305}$$

we have

$$A^2+B^2 = D^2\cos^2(\phi)+D^2\sin^2(\phi) = D^2\left[\cos^2(\phi)+\sin^2(\phi)\right] = D^2. \tag{306}$$

Hence

$$D = \sqrt{A^2+B^2}. \tag{307}$$

We can solve for the angle ϕ by taking the ratio of the two coefficients:

$$\frac{B}{A} = \frac{D\sin(\phi)}{D\cos(\phi)} = \tan(\phi). \tag{308}$$

So

$$\phi = \tan^{-1}\left(\frac{B}{A}\right). \tag{309}$$

Applying Equation (301) to Equation (300) gives

$$\begin{aligned}\frac{x_2(t)}{\sqrt{3}}+\frac{x_1(t)}{\sqrt{3}} &= -\frac{1}{2\sqrt{3}}\cos(\xi)+\frac{1}{2}\sin(\xi)+\frac{1}{\sqrt{3}}\cos(\xi)\\ &= \frac{1}{2\sqrt{3}}\cos(\xi)+\frac{1}{2}\sin(\xi) \qquad (310)\\ &= \frac{1}{\sqrt{3}}\cos\left[\xi+\tan^{-1}\sqrt{3}\right].\end{aligned}$$

From this, we see that by breaking up the method into two parts, as in Equation (300), we avoid overflow, since $1/\sqrt{3}<1$.

We implemented the scaling with two Analog Devices ADSP-1080A 8-Bit Multipliers, labelled U5 and U6 in the schematic of Figure 57 on page 208. They generate a 16-bit result; at this point, however, we retain only the most significant 8 bits and ascribe to them the same meaning as before. The signed 8-bit numbers are in the range -1 to 0.9922.

The inputs to the multipliers arrive one conversion time after the clock signal arrives at the AD7769 A/D Converters. Since the multipliers use the same clock, they start multiplying the previous cycle's words at this point; the new words must wait for another cycle. To keep the word in the cosine path synchronized with this process, we have inserted a 74LS374 Octal Latch (U4) which delays the word in the cosine path by one cycle, too. The outputs of the multipliers are released on the opposite cycle of the clock. This means that the multiplier takes a full half-cycle before it releases its output. Latch U4 has no such delay; its outputs arrive at latch U13 quite soon after the normal clock occurs. The word released by the multipliers, in contrast, takes a more tortuous path through two stages of three 74LS83 4-bit adders, which perform the two additions of Figure 60 on page 214. They are quite fast, however, compared to the 1.25 μs for half of a clock cycle, so their outputs have no trouble catching up at latch U14 with the corresponding word at U13. At this point, U13 holds an 8-bit cosine of the signal of interest and U14 holds an 8-bit sine of it.

Figure 61 is a block diagram of the asymmetric demodulation algorithm. Note that the data are not continuous either in time or in magnitude. They are equally spaced

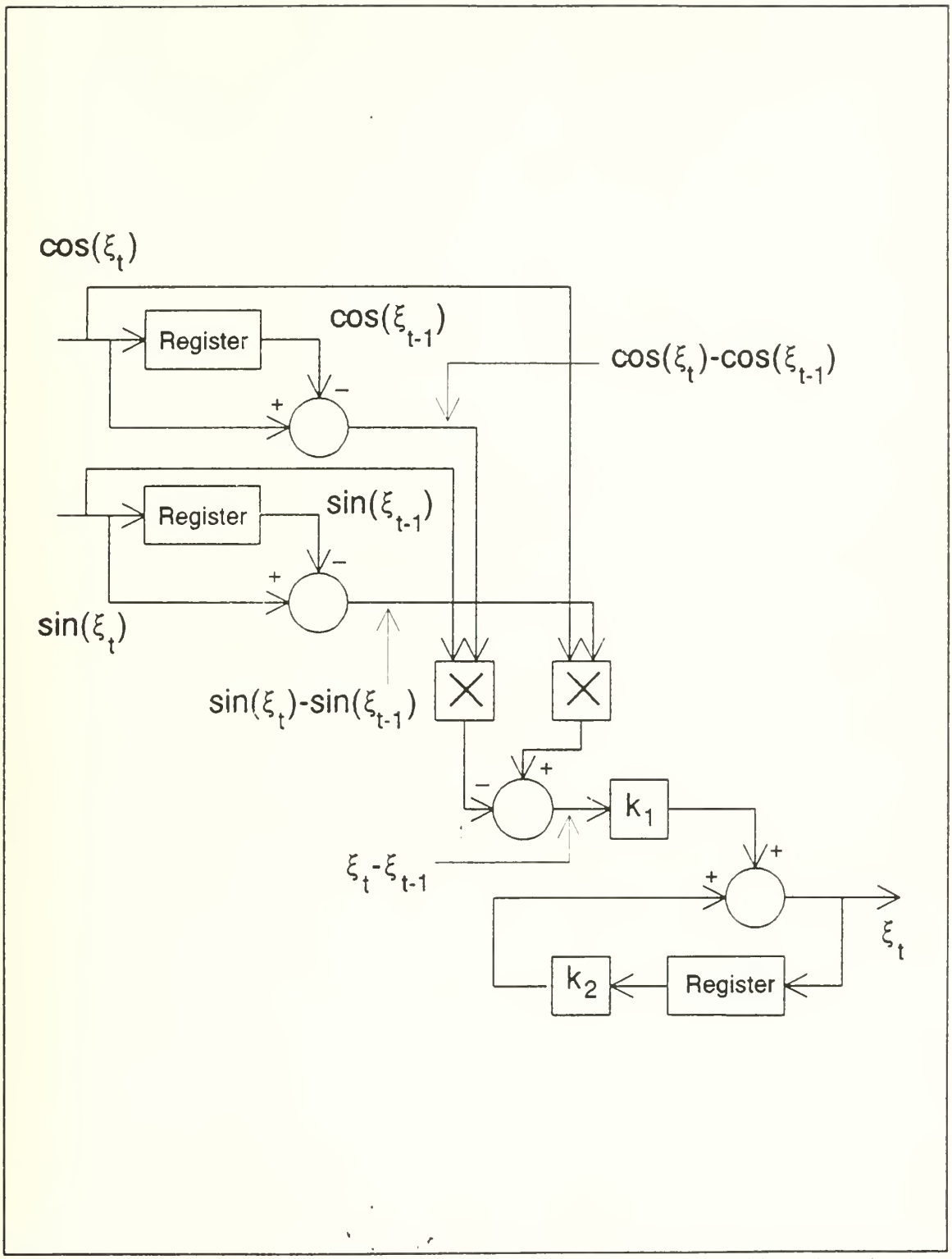

Figure 61 Block diagram showing the asymmetric demodulation algorithm when the data are digital words taken at successive sampling instants *t-1*, *t*, *t+1*, *etc.*

digital words corresponding to sample times $t-1$, t, $t+1$, *etc*. The difference between two successive words is computed by saving the current word in a register and subtracting it from the next word to come along. A digital multiplier finds the product between the current sample word and the difference between the current sample word in the other signal path and its previous value. When the difference between these products is taken, we obtain

$$\begin{aligned} &\cos(\xi_t)\left[\sin(\xi_t) - \sin(\xi_{t-1})\right] - \sin(\xi_t)\left[\cos(\xi_t) - \cos(\xi_{t-1})\right] \\ &\quad = \sin(\xi_t)\cos(\xi_{t-1}) - \cos(\xi_t)\sin(\xi_{t-1}) \\ &\quad = \sin\left[\xi_t - \xi_{t-1}\right]. \end{aligned} \tag{311}$$

If the sample interval is sufficiently small (*i.e.*, if the sample frequency is sufficiently high), then the argument of the sine in Equation (311) is very small. In this case, we can use the small-angle approximation. The output of the subtractor is

$$\sin\left[\xi_t - \xi_{t-1}\right] \approx \xi_t - \xi_{t-1}. \tag{312}$$

We can integrate this first-order difference to recover a sequence corresponding to the signal of interest, ξ.

The integration amounts to weighting these differences by the multiple k_1 and adding them into a running sum. The running sum, however, is also added in on itself. It would swiftly grow without bound if k_2 were not less than one. We shall explain how to pick these two constants presently.

From the schematics of Figure 57 and Figure 58, it can be seen that two successive words in each data path are subtracted by the 74LS181 4-Bit Arithmetic Logic Units (ALUs) U15 and U16 (for the cosine path) and U17 and U18 (for the sine path) to yield first-order differences. These differences are analogous to the derivatives of the continuous-time algorithm. The current data words and the differences are cross-multiplied by two more ADSP-1080A multipliers U19 and U20. As with U5 and U6, these accept data on the normal clock and release the products on the inverted clock. Shortly after the inverted clock triggers this release, the difference between the two cross-

products is produced by four more 74LS181 ALUs. These ALUs comprise a 16-bit subtractor circuit; all 16 output bits of each multiplier are used. The outputs of U21 through U24 are digital words representing the first difference (analogous to the derivative) of the signal of interest.

The 16-bit difference is then processed by a digital integrator in order to recover the signal of interest. Of course, a true integrator would have infinite gain at frequency 0, so what we really want is a low-pass filter which approximates an integrator at high frequencies. An analog filter which has a low-pass characteristic and a cut-off[25] frequency $f=f_0$ has a Laplace transform

$$H(s) = \frac{1}{s+2\pi f_0}. \tag{313}$$

If we let the complex variable s be purely imaginary, then

$$s = j\omega = j2\pi f. \tag{314}$$

If $f \gg f_0$, then this transfer function becomes

$$H(j2\pi f) = \frac{1}{j2\pi f+2\pi f_0} \approx \frac{1}{j2\pi f}, \tag{315}$$

which is the transfer characteristic of an integrator.

The impulse response $h(t)$ of the system is given by the inverse Laplace transform of the transfer function.

$$h(t) = \mathcal{L}^{-1}[H(s)] = e^{-2\pi f_0 t} \tag{316}$$

---

[25] The cut-off frequency is the frequency at which the magnitude of the gain has declined by 3 dB from the peak.

Taking the right-sided Z-transform[26] of this, we get

$$\begin{aligned} Z[h(nT)] &= Z\left[e^{-2\pi f_0 nT}\right] \\ &= \sum_{n=0}^{\infty} e^{-2\pi f_0 nT} z^{-n} \\ &= \sum_{n=0}^{\infty} \left(e^{-2\pi f_0 T} z^{-1}\right)^n \\ &= \frac{1}{1-e^{-2\pi f_0 T} z^{-1}} \qquad \text{Sum of a geometric series} \end{aligned} \tag{317}$$

The advantage to having obtained this equation is that the necessary filter coefficients for a digital filter to implement this function can be read right from the equation. Strum and Kirk [Ref. 19, pp. 350-351] show that a difference equation

$$y(n) = \sum_{k=1}^{N} a_k y(n-k) + \sum_{i=0}^{L} b_k x(n-k) \tag{318}$$

has a Z-transform

---

[26] The right-sided Z-transform is useful in converting difference equations into algebraic equations. Since a sampled-data system uses finite differences rather than infinitesimal differences, the Z-transform can be used with sampled systems just as the Laplace transform can be used with continuous-time systems. The definition of the right-sided Z-transform is

$$Z[x(nT)] = \sum_{n=0}^{\infty} x(nT) z^{-n}$$

where T is the time between successive (regularly spaced) samples.

$$H(z) = \frac{Y(z)}{X(z)} = \frac{Z[y(n)]}{Z[x(n)]} = \frac{\sum_{k=0}^{L} b_k z^{-k}}{1 - \sum_{k=1}^{N} a_k z^{-k}}. \tag{319}$$

We want to implement a difference equation corresponding to the Z-transform function in Equation (317). Noting that the coefficients $b_0 = 1$, $a_0 = e^{-2\pi f_0 T}$, and all the other a_k and b_k are zero, the required difference equation is

$$y_n = e^{-2\pi f_0 T} y_{n-1} + x_n. \tag{320}$$

We chose to set the cutoff frequency $f_0 = 10$ Hz, and the sampling interval $T = 2.5$ μs is the maximum which the AD7769 A/D converters can sustain. Thus the difference equation becomes

$$y_n = 0.9998429 y_{n-1} + x_n. \tag{321}$$

We now check for the gain of the transfer function at a frequency $f = 200$ Hz. We would like the gain to be 1 at this frequency, that is, we would like a signal of amplitude 1 to create an output of the same magnitude at this frequency. To find the gain, we must first find the digital frequency corresponding to the real frequency $f = 200$ Hz. The digital frequency can take on values from 0 to 2π and is given by

$$\theta = 2\pi \frac{f}{f_s} \tag{322}$$

where $f_s = 400$ kHz is the sampling frequency. So with $f = 200$ Hz, the frequency response is

$$H(\theta) = \frac{b_0}{1 - a_0 e^{j\theta}} = \frac{1}{1 - 0.9998429 e^{j2\pi \frac{200 \text{ Hz}}{400 \text{ kHz}}}} = 318 \angle 88°. \tag{323}$$

To reduce the gain to 1, we divide b_0 by 318, yielding 0.00314. The difference equation now takes the form

$$y_n = 0.9998429y_{n-1} + 0.00314x_n. \tag{324}$$

The coefficients in this equation are inconvenient in our hardware implementation. So we will round the gain down to the next lowest power of two. The coefficient 0.9998429 can be rewritten as $1 - 1.570673 \times 10^{-4}$. By doing this, we can build the integrator by adding in the value y_{n-1} accumulated so far, and subtracting off a small fraction of it. When we round off (in binary) we obtain $a_0 = 1 - 2^{-13}$ and $b_0 = 2^{-9}$. Using these values to check the frequency response when f=200 Hz, we find it is $0.621\angle 88°$. Since the magnitude of the gain is below 1, this integrator should be stable.

We shall implement the difference equation

$$y_n = y_{n-1} + (2^{-9})x_n - (2^{-13})y_{n-1} \tag{325}$$

which is quite easy to do in digital hardware. However, because we are using 16-bit numbers x_n, we need a large number of bits in the accumulator.

The schematic in Figure 58 on page 208 shows the most significant 15 bits of x_n entering the accumulator shifted down by nine bit positions. However, as we are dealing with signed binary numbers, the high-order bit must be provided to all high bit locations to avoid the loss of this sign information. The most significant 16 bits y_{n-1} of the output registers U37, U38, and U39 are added in with the scaled-down multiple of x_n in adders U25 through U30. The sums are then reduced by $2^{-13}y_{n-1}$ in the Arithmetic Logic Units (subtractors) U31 through U36. The difference represents the next output of the demodulator.

At this point, one could simply pass the digital output to any succeeding circuits that required it. We used an Analog Devices AD7846 Digital-to-Analog Converter in order to display the resultant wave form on an oscilloscope and to permit measurements on the performance of the system.

The AD7846 requires ±15 V and +5 V power. In order to provide bipolar outputs of ±10 V, it also needs ±5 V reference voltages. As before, we ignored the precaution of using precision voltage references here, but better performance would result if we did so.

Unfortunately, the design of the digital integrator proved to be easier than its implementation. After repeated checks to see that the analysis and the wiring both were right, we finally abandoned the attempt to make it work and substituted an analog integrator in its place. In view of the fact that the main thrust of the research was into demodulation, not digital integration, this expedient seemed reasonable, albeit somewhat embarrassing. We took the inputs to the digital integrator as inputs to the AD7846 Digital-to-Analog Converter instead and puts the analog output from the AD7846 into an analog integrator. The performance measurements in the next chapter therefore do not reflect a fully-digital implementation of the asymmetric demodulation scheme. This deficiency needs to be investigated and corrected in follow-on research. Extensive simulation has confirmed that the design is valid, and so the error must be in the wiring of the integrator.

C. SUMMARY

In this chapter we described an implementation of the asymmetric demodulation algorithm in digital hardware. The complexity of this circuit is very high. This is partly due to the use of hardware multipliers and adders, as opposed to a microprocessor or a digital signal processing (DSP) integrated circuit, and partly due to the use of multiple four-bit and eight-bit integrated circuits in places where more bits were required (up to 24 at the end).

The use of 8-bit analog-to-digital converters at the input and a 16-bit digital-to-analog converter at the output is quite unusual in digital circuitry. At the input, the dynamic range of the signal of interest is contained not in the amplitude of the interferometric outputs, but in their phase, so we can get away with using an 8-bit converter without sacrificing dynamic range. The demodulation process converts the phase modulation into fluctuations in amplitude. Along the way, the 8-bit quantities are multiplied together to generate 16 bits, making the use of a 16-bit digital-to-analog converter at the output an appropriate and worthwhile expense. Of course, if succeeding circuitry did not require an analog replica of the signal of interest, the digital-to-analog converter could be omitted altogether.

In the next chapter, we consider the performance of the Asymmetric Digital Demodulator we have just described.

XIII. PERFORMANCE OF THE ASYMMETRIC DIGITAL DEMODULATOR

A. OVERVIEW

In this chapter we examine the performance of the Asymmetric Digital Demodulator. The aspects of its performance which we consider are:

1. scale factor, which relates the phase amplitude in the modulated signal to the voltage amplitude in the demodulated signal;
2. small signal bandwidth;
3. maximum acceptable signal;
4. noise floor;
5. dynamic range;
6. complexity; and
7. approximate cost.

These are the same characteristics we examined in assessing the performance of the Fringe Rate Demodulator and the Symmetric Analog Demodulator.[27] The Asymmetric Digital Demodulator is capable of demodulating signals both above and below the one-half fringe level.

The techniques used to measure the performance of the Asymmetric Digital Demodulator were essentially the same as those described in Chapter XI, where we presented the results of measurements of the performance of the Symmetric Analog Demodulator. Rather than repeat the information here, we will simply present the

---

[27] In the case of the Fringe Rate Demodulator, measurement of the noise did not arise because its principle of operation made it incapable of demodulating signals of less than half a fringe ($\pm\pi/2$ radians) and so the useful signals were always very much stronger than the noise anyway.

results. In the description of the Symmetric Analog Demodulator's performance, simply substitute the Asymmetric Digital Demodulator in its place.

B. SCALE FACTOR

Table XXV, Table XXVI, and Table XXVII contain summaries of our measurements of the scale factor of the Asymmetric Digital Demodulator. To assist in the understanding of these data, Figure 62 is a graph of the scale factor for frequency 200 Hz. It is clear from the data that the scale factor is not a constant, as we would prefer. However, in the horizontal region of the graph it is approximately 35 mV/rad. At low levels of optical phase shift (phase amplitude) the scale factor begins to climb. This is due to the increasing significance of noise in the output; this has the effect of providing a steady average signal output even though the phase amplitude continues to drop. Since the scale factor is calculated as the ratio of output to input, it appears to rise. If we narrowed the bandwidth, the noise would be less severe and so the apparent rise in scale factor would occur at a lower phase amplitude. A similar effect was observed when we measured the scale factor of the Symmetric Analog Demodulator.

It should be noted that implicit in quoting the scale factor in volts per radian is the fact that the output of the Asymmetric Digital Demodulator has been converted to a voltage. So we are, in effect, quoting a combination of the results of the digital demodulation as well as the scale factor of the analog output stage. A more suitable way to quote the scale factor would be as a magnitude of a binary number per radian of optical phase shift. Because we took the output of the Asymmetric Digital Demodulator before the final integration required by the asymmetric demodulation algorithm had been performed, we cannot quote this value. It would, however, be a function of the gain of the digital integrator, just as in our case it is a function of the gain of the analog integrator.

C. BANDWIDTH

When we measured the bandwidth of the Symmetric Analog Demodulator, we applied very small signals from the Analog Interferometric Simulators. This permitted us

Table XXV Determination of the scale factor of the Asymmetric Digital Demodulator for frequencies of 50 Hz and 100 Hz.

Frequency [Hz]	Input Voltage (peak)	Input Phase [rad]	Output Voltage (peak)	Scale Factor [mV/rad]
50	3.00 V	102	1.84 V	18.0
	2.50 V	85.1	1.52 V	17.9
	2.00 V	67.9	1.24 V	18.3
	1.50 V	50.8	970 mV	19.1
	1.00 V	33.7	650 mV	27.9
	500 mV	16.5	300 mV	18.2
	400 mV	13.1	270 mV	29.4
	300 mV	9.6	190 mV	19.7
	200 mV	6.2	140 mV	22.5
	100 mV	2.8	70 mV	25.1
	50 mV	1.1	80 mV	74.5
100	3.00 V	102	2.80 V	27.4
	2.50 V	85.1	2.40 V	28.2
	2.00 V	67.9	16.5	29.4
	1.50 V	50.8	1.31 V	25.8
	1.00 V	33.7	940 mV	27.9
	500 mV	16.5	500 mV	30.3
	400 mV	13.1	410 mV	31.4
	300 mV	9.6	290 mV	30.1
	200 mV	6.2	195 mV	31.4
	100 mV	2.8	100 mV	35.9
	50 mV	1.1	90 mV	83.8

to obtain the small-signal bandwidth of the demodulators very easily. The Asymmetric Digital Demodulator output such distorted wave forms for the small phase shifts generated by the simulators that we could not effectively measure its small-signal bandwidth. Any phase amplitude below 2 rad created more than 4% total harmonic

Table XXVI Determination of the scale factor of the Asymmetric Digital Demodulator for frequencies of 150 Hz and 200 Hz.

Frequency [Hz]	Input Voltage (peak)	Input Phase [rad]	Output Voltage (peak)	Scale Factor [mV/rad]
150	3.00 V	102	3.11 V	30.4
	2.50 V	85.1	2.66 V	41.3
	2.00 V	67.9	2.21 V	32.5
	1.50 V	42	1.70 V	33.5
	1.00 V	33.7	1.15 V	34.2
	500 mV	16.5	600 mV	36.4
	400 mV	13.1	490 mV	37.5
	300 mV	9.6	380 mV	39.4
	200 mV	9.6	230 mV	37.0
	100 mV	2.8	115 mV	41.3
	50 mV	1.1	65 mV	60.5
200	3.00 V	102	3.24 V	41.3
	2.50 V	85.1	2.86 V	33.6
	2.00 V	67.9	2.29 V	33.7
	1.50 V	50.8	1.73 V	33.7
	1.00 V	33.7	1.20 V	35.7
	500 mV	16.5	607 mV	36.8
	400 mV	13.1	470 mV	35.9
	300 mV	9.6	380 mV	39.4
	200 mV	6.2	250 mV	40.2
	100 mV	2.8	115 mV	41.3
	50 mV	1.1	60 mV	55.9

distortion at all frequencies. We suspect that the situation could be improved with a less conservative design. We set the digitization reference levels high enough to preclude an input signal from ever exceeding them, an unhappy situation which would have damaged the analog-to-digital converters. Had we included voltage-protection circuitry, we could

Table XXVII Determination of the scale factor of the Asymmetric Digital Demodulator for frequencies of 250 Hz and 300 Hz.

Frequency [Hz]	Input Voltage (peak)	Input Phase [rad]	Output Voltage (peak)	Scale Factor [mV/rad]
250	3.00 V	1.1	3.60 V	35.2
	2.50 V	85.1	3.10 V	36.4
	2.00 V	67.9	2.50 V	36.8
	1.50 V	50.8	1.90 V	37.4
	1.00 V	33.7	1.16 V	34.5
	500 mV	16.5	560 mV	33.9
	400 mV	13.1	500 mV	38.2
	300 mV	9.6	370 mV	38.4
	200 mV	6.2	250 mV	40.2
	100 mV	2.8	70 mV	25.1
	50 mV	1.1	30 mV	27.9
300	3.00 V	102	2.33 V	22.8
	2.50 V	85.1	1.94 V	22.8
	2.00 V	2.8	1.60 V	23.6
	1.50 V	50.8	1.20 V	23.6
	1.00 V	2.8	780 mV	23.2
	500 mV	16.5	400 mV	24.2
	400 mV	13.1	340 mV	26.0
	300 mV	9.6	250 mV	25.9
	200 mV	6.2	170 mV	27.3
	100 mV	2.8	90 mV	32.3
	50 mV	1.1	35 mV	32.6

have decreased the reference levels, effectively using more of the dynamic range of the digitizers, and this would very likely have permitted the bandwidth measurements we were unable to obtain with the present design. This is an area for more investigation in the future.

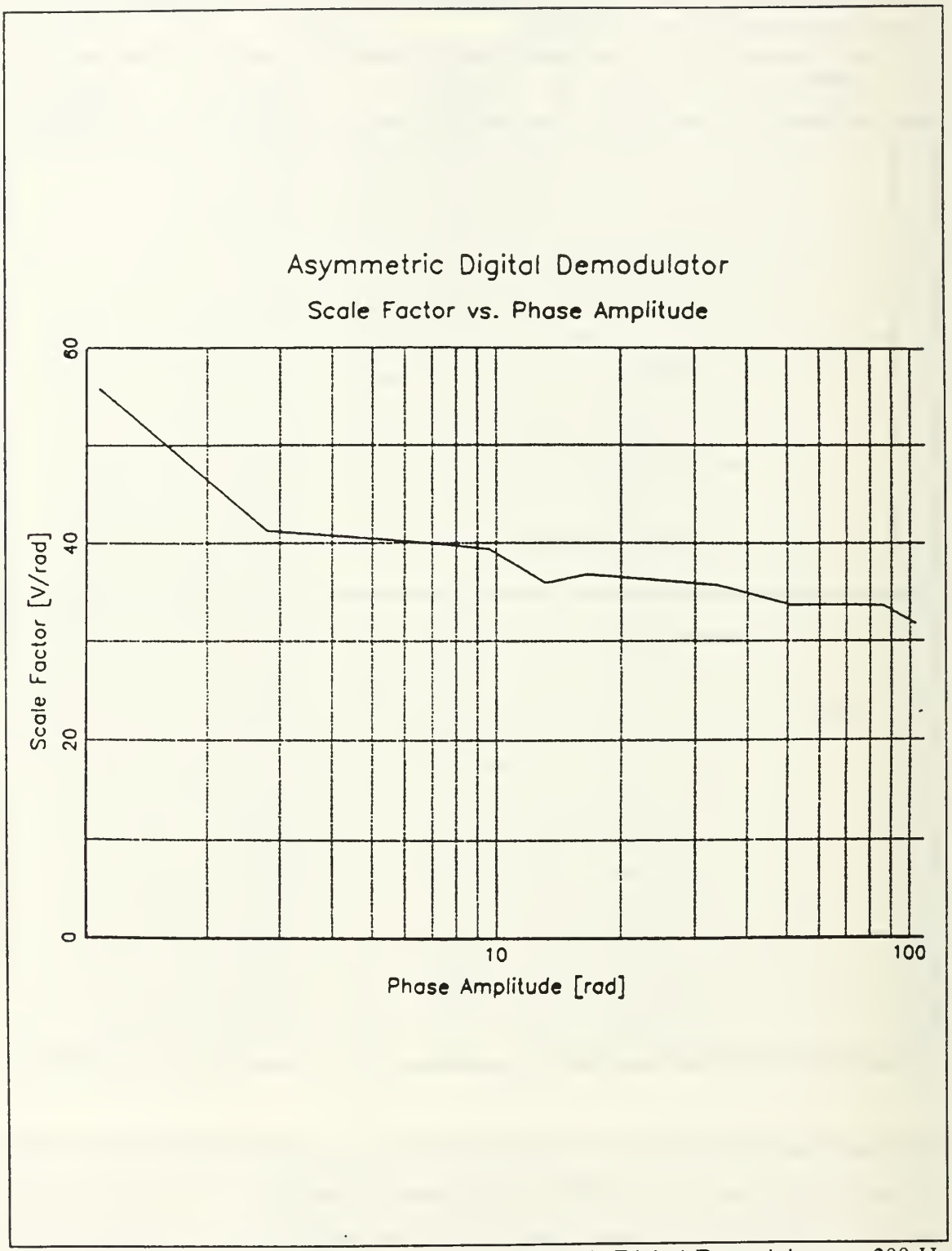

Figure 62 Graph of the scale factor of the Asymmetric Digital Demodulator at 200 Hz as a function of input phase amplitude.

D. MAXIMUM ACCEPTABLE SIGNAL

As in our assessment of the performance both of the Fringe Rate Demodulator and the Symmetric Analog Demodulator, we shall regard the maximum acceptable signal as the highest signal amplitude which creates no more than 4% total harmonic distortion. Observations of the total harmonic distortion (in %) for various combinations of input optical phase amplitude and frequency are presented in Table XXVIII, Table XXIX, and Table XXX. We have shown the phase amplitude in radians. The odd values are due to our having actually used round numbers for the voltage amplitude from the HP3314A Function Generator. The phase amplitudes were computed from the command voltage by the linear least squares fit

$$\text{Phase amplitude} = \left(34.29\ \frac{\text{rad}}{\text{V}}\right) V_{IN} - 0.64\ \text{mrad}. \tag{326}$$

A contour plot derived from these data is given in Figure 63. The contours join combinations of input optical phase shift and frequency which yield equal levels of total harmonic distortion. An alternative view of the same data is provided in the surface plot of Figure 64.

By studying the two plots and the data from which they were derived, we can draw a number of useful conclusions. When the phase rate (the product of phase shift and amplitude of the signal of interest) is high, distortion becomes extremely severe. It is fairly large at each of the other three corners in the plots, too. Where both frequency and phase shift are low, the adverse effects of quantization noise are responsible for the harmonic distortion. In one of the other two corners of the plots, frequency is low but phase amplitude is high. In the other, phase amplitude is low but frequency is high. At low frequencies, quantization noise is significant at the extrema of the signal of interest. This is true even if the phase amplitude is high, because the instantaneous frequency gets so low at these points. Conversely, at high frequencies, if the phase amplitude A is not very big, very few quantization levels are used, and distortion again ensues. In the central area of the plots, where the surface plot shows deep, crinkly valleys, the harmonic

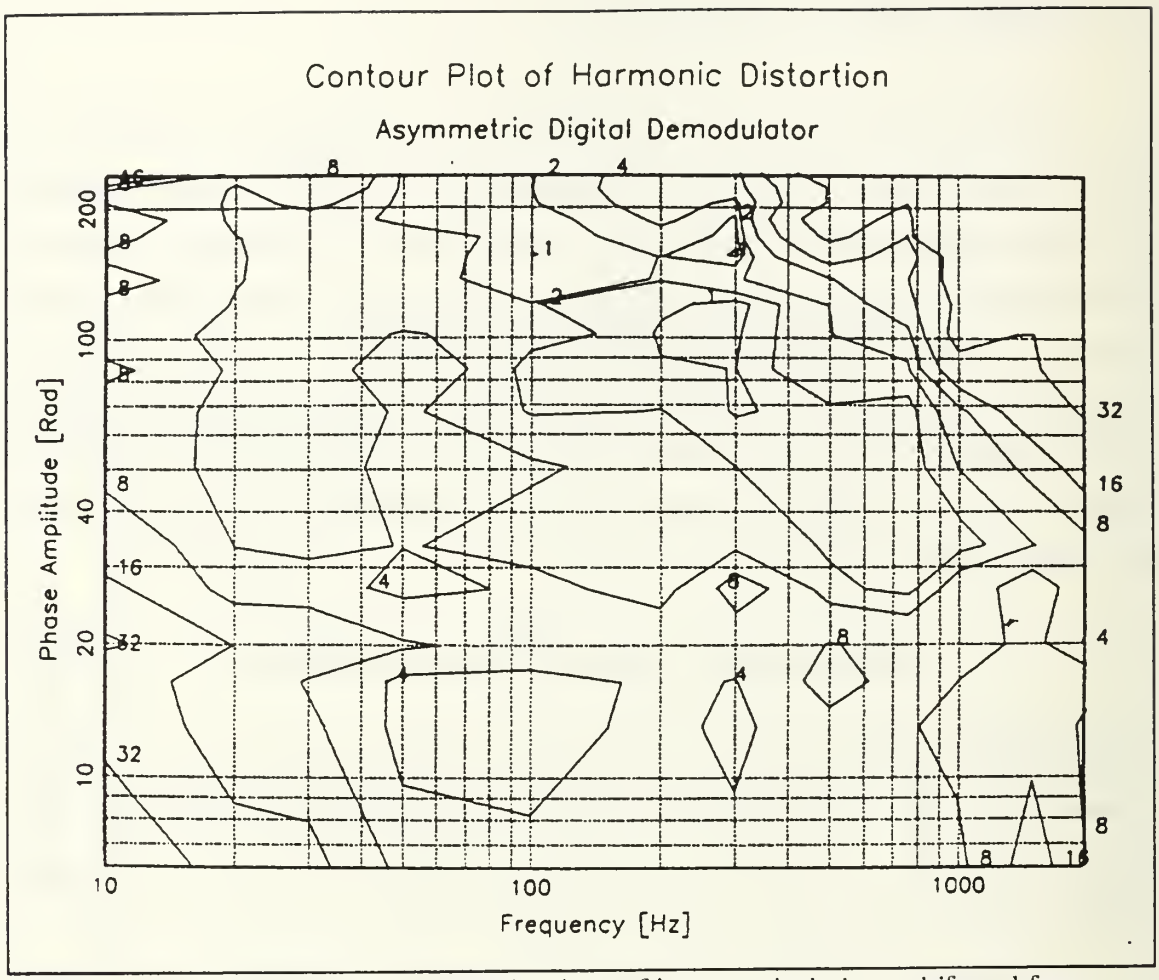

Figure 63 Contour plot showing combinations of input optical phase shift and frequency which yield the same amount of total harmonic distortion in the Asymmetric Digital Demodulator.

distortion is low, but not very even. In this regime, the Asymmetric Digital Demodulator provides a useful output.

We used linear interpolation between the observations in Table XXVIII, Table XXIX, and Table XXX to obtain the maximum acceptable phase amplitude as a function of frequency. The results are shown in Table XXXI in tabular form and they are plotted in Figure 65. At frequencies above 300 Hz, the maximum acceptable frequency drops off at roughly 20 dB per decade of frequency increase. This is to be expected when the phase rate limit is the dominant effect on harmonic distortion.

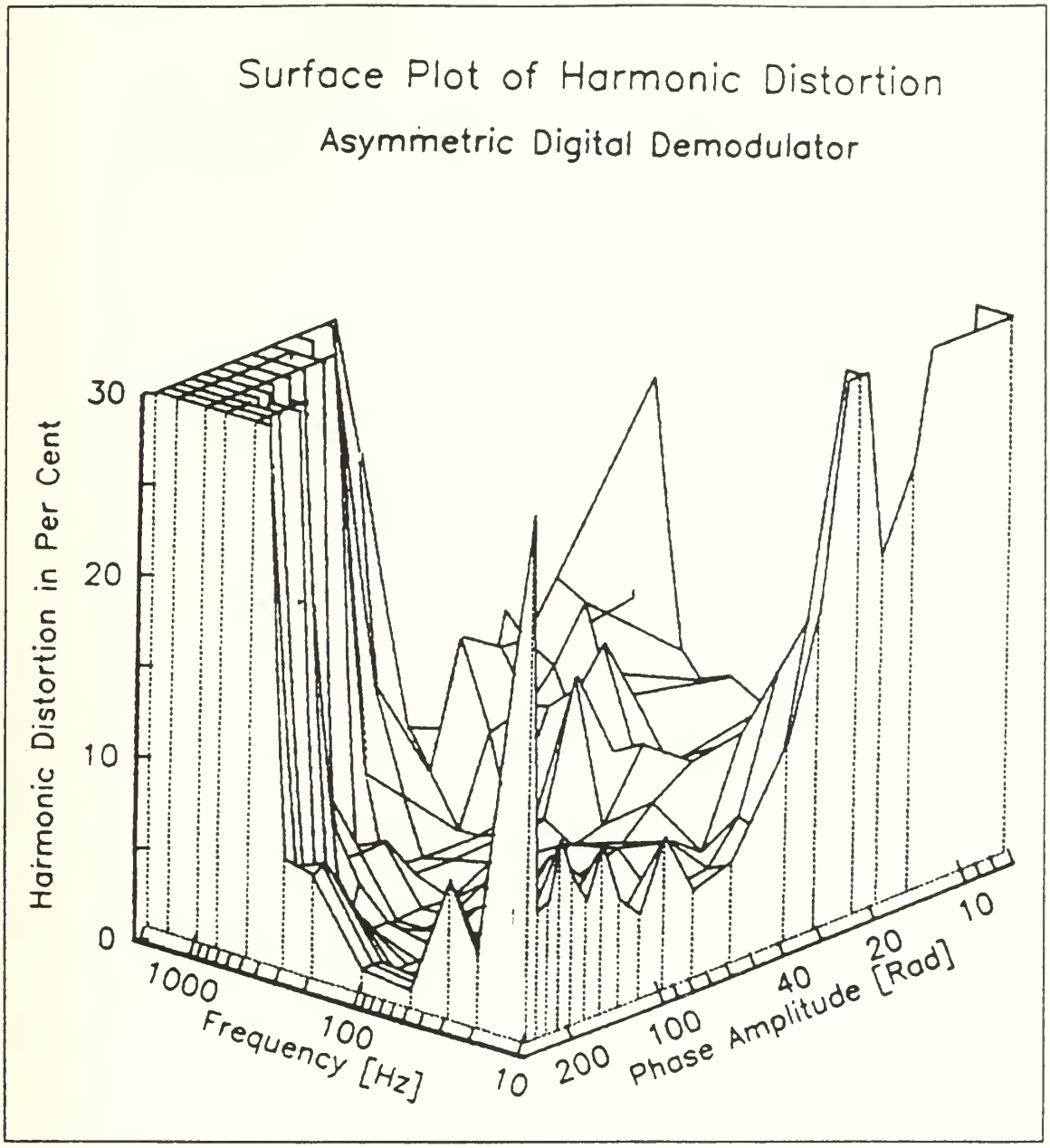

Figure 64 Surface plot showing the total harmonic distortion in the Asymmetric Digital Demodulator as a function of various combinations of input optical phase shift and frequency .

There is an anomaly in the data at 200 Hz. For large phase amplitudes, the harmonic distortion at 200 Hz is higher than that at the next lowest frequency (100 Hz) *and* at the next highest frequency (500 Hz). This is true around the level of 4% total harmonic distortion, but at even higher phase amplitudes, it no longer is the case. In any

Table XXVIII Total harmonic distortion (in %) of the Asymmetric Digital Demodulator as a function of input optical phase shift and frequency (phase shift from 6.22 rad to 33.7 rad).

		Optical Phase Shift [rad]					
		6.22	13.1	16.5	19.9	26.8	33.7
Frequency [Hz]	10	48.9	23.8	19.8	34.4	17.8	11.4
	20	19.8	9.3	11.0	15.8	4.66	3.96
	30	18.3	8.85	7.58	12.6	5.42	3.29
	50	5.41	2.58	2.94	8.52	2.87	4.10
	100	4.26	3.36	2.92	6.17	4.75	3.24
	200	4.07	4.60	4.65	6.25	2.72	2.20
	300	4.48	3.40	3.85	5.39	10.3	3.23
	500	5.54	6.66	10.1	8.18	2.38	1.74
	750	4.89	7.32	5.35	6.67	1.40	1.14
	1000	6.23	10.8	8.03	6.43	5.80	1.15
	1500	20.7	11.7	8.97	9.13	10.5	3.89
	2000	8.16	7.19	10.2	3.61	5.21	5.86

event, this fact, combined with the absence of points exceeding 4% total harmonic distortion at 50 Hz and 100 Hz makes it impossible to determine whether the maximum acceptable signal continues to increase at 20 dB per decade as the frequency drops lower. The most phase shift our interferometer could generate was around 250 rad. and so an investigation of higher phase shifts at low frequencies was not feasible.

E. NOISE FLOOR

We performed noise measurements on the Asymmetric Digital Demodulator using the same technique as we used with the Symmetric Analog Demodulator. The observations are summarized in the data of Table XXXII and Table XXXIII. Recall that

Table XXIX Total harmonic distortion (in %) of the Asymmetric Digital Demodulator as a function of input optical phase shift and frequency (phase shift from 50.8 rad to 137 rad).

		Optical Phase Shift [rad]					
		50.8	67.9	85.1	102	119	137
Frequency [Hz]	10	6.13	5.45	8.97	5.29	6.51	9.90
	20	2.66	3.17	3.26	3.16	3.81	4.14
	30	2.86	2.77	2.65	3.10	2.84	2.73
	50	4.96	4.30	6.01	4.19	2.50	2.32
	100	4.32	1.80	1.18	2.83	2.03	1.44
	200	2.83	2.05	1.08	.833	1.25	2.07
	300	2.00	.856	.986	.853	.596	3.70
	500	1.54	1.63	4.00	3.91	4.01	7.65
	750	1.14	1.34	3.25	6.40	12.9	15.7
	1000	4.09	6.15	24.5	39.7	35.7	40.7
	1500	9.58	24.7	19.9	29.6	190	105
	2000	22.2	33.4	103	108	117	65.1

when we discussed the performance of the Symmetric Analog Demodulator, a clear trend was evident that allowed us to extrapolate to the point where the ratio of signal to noise reached 0 dB. This is much more difficult in the case of the Asymmetric Digital Demodulator, especially at the lower frequencies. We have halved the input optical phase shift for each successive observation, yet we do not always see a 6 dB decline in the ratio of signal to noise, as we expect. In some cases, the decline is nowhere near 6 dB. We may, however, follow the extrapolative procedure for the data when the frequency is 195 Hz and up.

In Table XXXIV we show the results of a linear curve fit on some of the data given in Table XXXIII. We have excluded some of the data points, as indicated, because they do not appear to be consistent with the hypothesis of a 6 dB decline in the ratio of

Table XXX Total harmonic distortion (in %) of the Asymmetric Digital Demodulator as a function of input optical phase shift and frequency (phase shift from 154 rad to 239 rad).

		Optical Phase Shift [rad]					
		154	171	188	205	222	239
Frequency [Hz]	10	7.21	8.82	11.1	8.02	7.68	29.4
	20	4.20	4.09	3.02	3.26	3.58	4.70
	30	2.65	2.61	2.81	4.67	6.82	8.32
	50	2.70	2.88	1.55	1.45	1.58	1.56
	100	0.971	1.17	1.14	1.85	1.96	1.90
	200	2.06	3.08	4.58	5.79	6.66	6.27
	300	0.816	1.36	1.72	2.91	6.03	6.65
	500	20.6	36.4	48.6	33.5	33.3	49.9
	750	10.4	15.5	19.3	32.3	96.0	228
	1000	42.6	185	183	428	133	127
	1500	112	97.0	105	152	95.2	51.1
	2000	72.1	56.4	73.8	45.8	76.3	85.5

signal-to-noise with every halving of the phase amplitude. We also have omitted doing a curve fit for the data in Table XXXII because no clear trend of this sort is evident upon inspection.

We can easily evaluate these expressions for the case where the ratio of signal to noise $S/N = 0\ dB$. Converting these intercepts to a phase amplitude in radians gives the values shown in Table XXXV. The observations were made with the time constant of the lock-in amplifier set to 1 s, and the amplifier's filter skirts had a 12 dB/decade roll-off. The resultant bandwidth is 125 mHz. Dividing the floor in radians by the square root of the bandwidth gives the phase noise spectral density in the last column of Table XXXV. These values are also plotted in Figure 66.

Table XXXI Maximum phase amplitude acceptable to the Asymmetric Digital Demodulator, given as a function of input frequency, based on accepting 4% total harmonic distortion.

Frequency [Hz]	Maximum Acceptable Phase Amplitude [rad]	Af (krad/s)
10	Total harmonic distortion remained above 4% for all phase amplitudes.	
20	129	2.5
30	199	5.9
50	Total harmonic distortion never exceeded 4% for high phase amplitudes.	
100		
200	181	36.2
300	211	63.3
500	117	58.5
750	89	66.7
1000	50	50.0
1500	34	51.0
2000	22	44.0

Note that the decline in the noise floor that is evident from 195 Hz to 1 kHz seems to reverse somewhat at 2 kHz. The reason for this is not clear. Further investigation may permit this anomaly to be cleared up. In the meantime, however, we must emphasize that the method of extrapolation we have used here is somewhat rough.

F. DYNAMIC RANGE

The dynamic range is the ratio of the maximum acceptable signal to the noise floor. We have combined the results of the last two sections in the plot of Figure 67. At a frequency of 500 Hz, the dynamic range is 86 dB. This compares very favorably with the

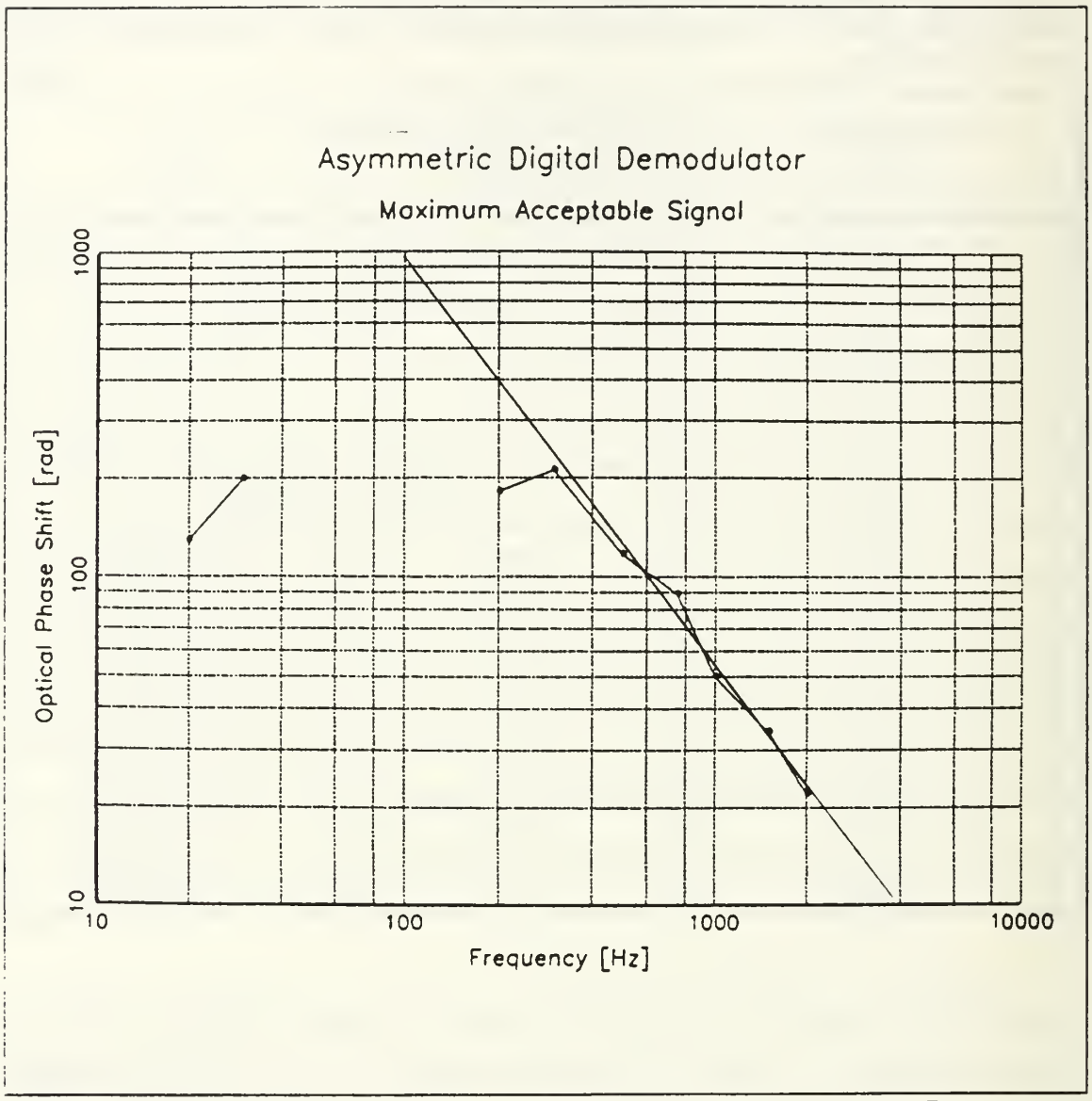

Figure 65 Maximum phase amplitude acceptable to the Asymmetric Digital Demodulator as a function of input frequency. The straight line extrapolates the region of constant phase rate to low frequencies.

30 dB dynamic range of the Fringe Rate Demodulator at this frequency, but it is considerably less than the 115 dB of the Symmetric Analog Demodulator at 590 Hz, which is not too far removed in frequency. On the other hand, the most dynamic range one could achieve with a 16-bit digital-to-analog converter is 96 dB, so 86 dB does not seem too bad, compared to that. Considering the problems discussed earlier in

Table XXXII Measurements of the noise floor of the Asymmetric Digital Demodulator for frequencies from 19 Hz to 97 Hz.

Frequency [Hz]	Ratio	Phase Amplitude	Output Voltage [V_{RMS}]	Signal-to-Noise Ratio [dB]
19	1.000000	4.59 rad	1.15±0.22	14
	0.500000	2.30 rad	1.121±0.031	31
	0.250000	1.15 rad	2.24±0.52	13
	0.125000	574 mrad	1.93±0.13	24
	0.050000	230 mrad	1.07±0.12	19
	0.025000	115 mrad	1.19±0.60	6
28	1.000000	4.59 rad	1.046±0.091	21
	0.500000	2.30 rad	0.725±0.025	21
	0.250000	1.15 rad	0.5685±0.0076	38
	0.125000	574 mrad	1.233±0.017	37
	0.050000	230 mrad	0.36±0.22	4.1
	0.025000	115 mrad	0.52±0.50	0.2
49	1.000000	4.59 rad	1.076±0.037	29
	0.500000	2.30 rad	0.7623±0.0089	39
	0.250000	1.15 rad	0.478±0.012	32
	0.125000	574 mrad	1.124±0.025	33
	0.050000	230 mrad	0.158±0.015	20
	0.025000	115 mrad	0.478±0.095	19
97	1.000000	4.59 rad	0.7974±0.0098	38
	0.500000	2.30 rad	0.712±0.084	19
	0.250000	1.15 rad	0.3041±0.0027	41
	0.125000	574 mrad	0.1915±0.0023	38
	0.050000	230 mrad	0.2066±0.0055	32
	0.025000	115 mrad	0.2528±0.004	36

Table XXXIII Measurements of the noise floor of the Asymmetric Digital Demodulator for frequencies from 195 Hz to 2 kHz.

Frequency [Hz]	Ratio	Phase Amplitude	Output Voltage [V_{RMS}]	Signal-to-Noise Ratio [dB]
195	1.000000	4.59 rad	1.17585±0.00072	64
	0.500000	2.30 rad	0.67958±0.00061	61
	0.250000	1.15 rad	0.3936±0.0012	50
	0.125000	574 mrad	0.1568±0.0013	42
	0.050000	230 mrad	0.1624±0.0042	32
	0.025000	115 mrad	0.0740±0.0035	26
500	1.000000	4.59 rad	1.07708±0.00065	64
	0.500000	2.30 rad	0.6066±0.0049	42
	0.250000	1.15 rad	0.42597±0.00061	57
	0.125000	574 mrad	0.19987±0.00061	50
	0.050000	230 mrad	0.10867±0.00079	43
	0.025000	115 mrad	0.04209±0.00065	36
1000	1.000000	4.59 rad	1.03983±0.00057	65
	0.500000	2.30 rad	0.5512±0.0040	46
	0.250000	1.15 rad	0.41987±0.00049	59
	0.125000	574 mrad	0.21210±0.00063	51
	0.050000	230 mrad	0.09519±0.00046	46
	0.025000	115 mrad	0.03782±0.00034	41
2000	1.000000	4.59 rad	0.47067±0.00026	65
	0.500000	2.30 rad	0.3231±0.0031	40
	0.250000	1.15 rad	0.1742±0.0016	41
	0.125000	574 mrad	0.09427±0.00042	47
	0.050000	230 mrad	0.04804±0.00032	43
	0.025000	115 mrad	0.03574±0.00042	39
	0.006250	28.7 mrad	0.01278±0.00061	26

Table XXXIV Least squares fit of the logarithm of the phase input A_{EFF} to the Asymmetric Digital Demodulator to achieve a given ratio S/N of signal to noise.

Frequency	Least squares curve fit
195 Hz	$\log\left(\frac{A_{EFF}}{1\ \text{rad}}\right) = [0.0392 \pm 0.0021]\frac{S}{N}_{dB} + (-1.92 \pm 0.10)$
	with r=0.994
500 Hz	$\log\left(\frac{A_{EFF}}{1\ \text{rad}}\right) = [0.0485 \pm 0.0019]\frac{S}{N}_{dB} + (-2.696 \pm 0.091)$
	with r=0.998 (excluding the first two data points)
1000 Hz	$\log\left(\frac{A_{EFF}}{1\ \text{rad}}\right) = [0.0565 \pm 0.0063]\frac{S}{N}_{dB} + (-3.22 \pm 0.31)$
	with r=0.988 (excluding the first two data points)
2000 Hz	$\log\left(\frac{A_{EFF}}{1\ \text{rad}}\right) = [0.0592 \pm 0.0078]\frac{S}{N}_{dB} + (-3.13 \pm 0.31)$
	with r=0.983 (excluding the first three data points)

Table XXXV The noise floor of the Asymmetric Digital Demodulator.

Frequency [Hz]	Noise floor [rad]	Noise floor (normalized for bandwidth)
195	12 mrad	34 mrad/√Hz
500	2.0 mrad	5.7 mrad/√Hz
1000	600 μrad	1.7 mrad/√Hz
2000	740 μrad	2.1 mrad/√Hz

connection with the harmonic distortion and the scale factor, it is gratifying to see such a large dynamic range result.

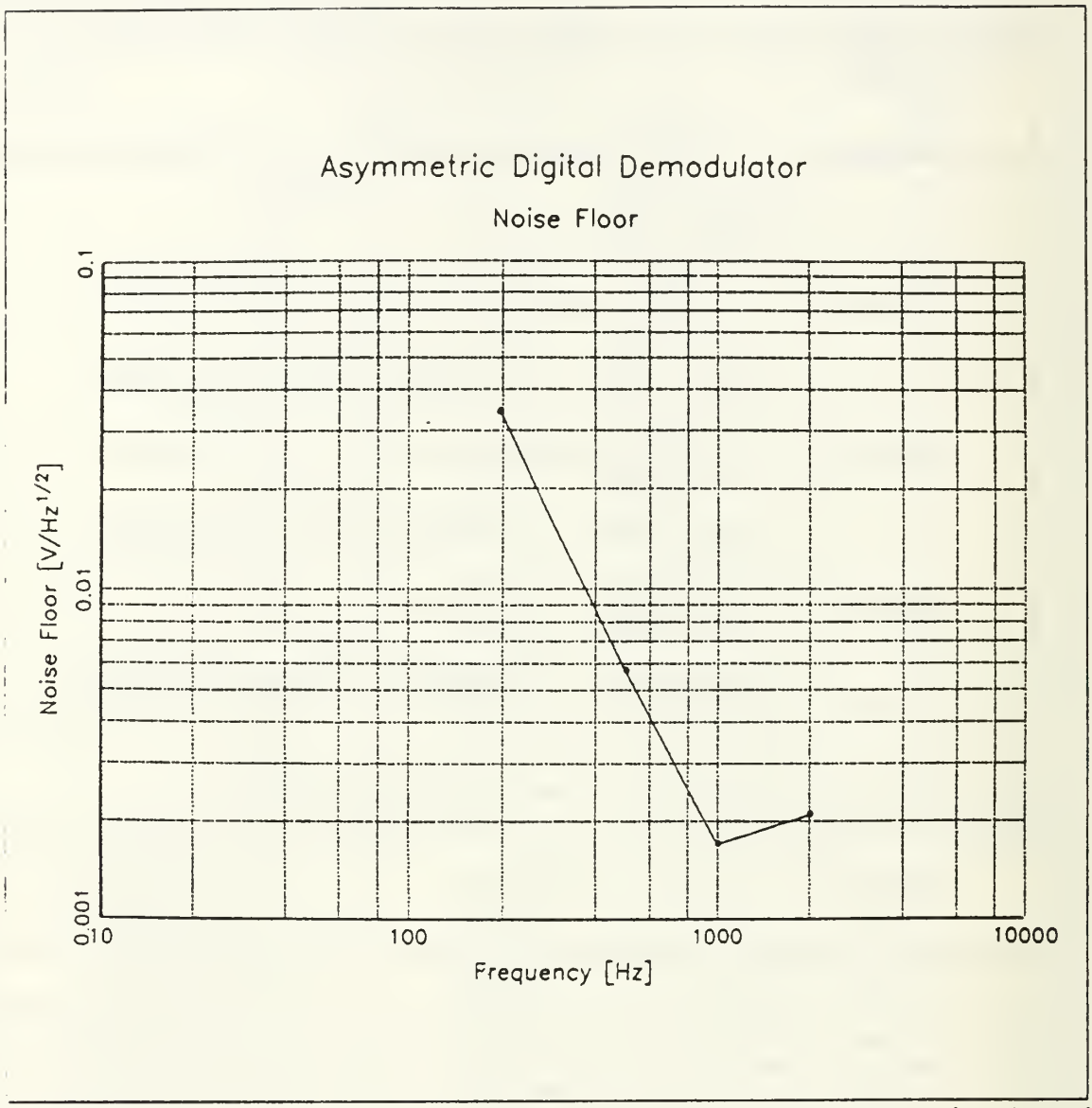

Figure 66 The noise floor of the Asymmetric Digital Demodulator as a function of frequency.

Further research should investigate causes of the difference in dynamic range between the Asymmetric Digital Demodulator and the Symmetric Analog Demodulator. How much of the difference is due to the use of digital as against analog hardware? How much is due to the use of asymmetric demodulation as against symmetric demodulation?

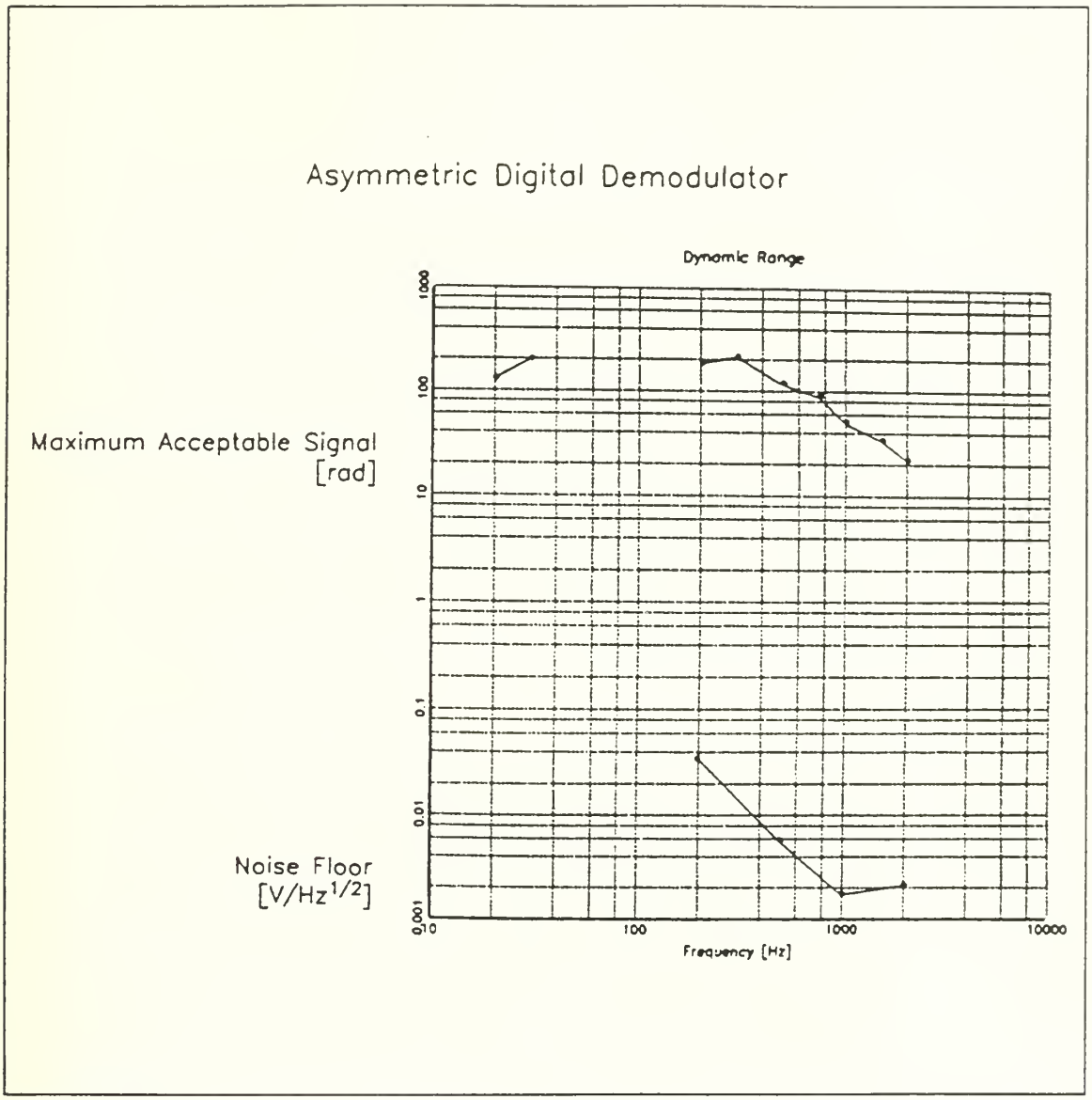

Figure 67 The dynamic range of the Asymmetric Digital Demodulator. The upper limit is taken to be where 4% total harmonic distortion results. The lower level is the noise floor in a one hertz bandwidth.

G. COMPLEXITY

The asymmetric demodulation scheme is even simpler than the symmetric demodulation scheme. However, the implementation we have chosen is much, much more complex. The use of 4-bit integrated circuits was dictated by the ease of obtaining them. Yet the wiring required to use them on a bread-board is quite staggering, as a glance at the breadboard circuit shown in Figure 68 will make abundantly clear. On the

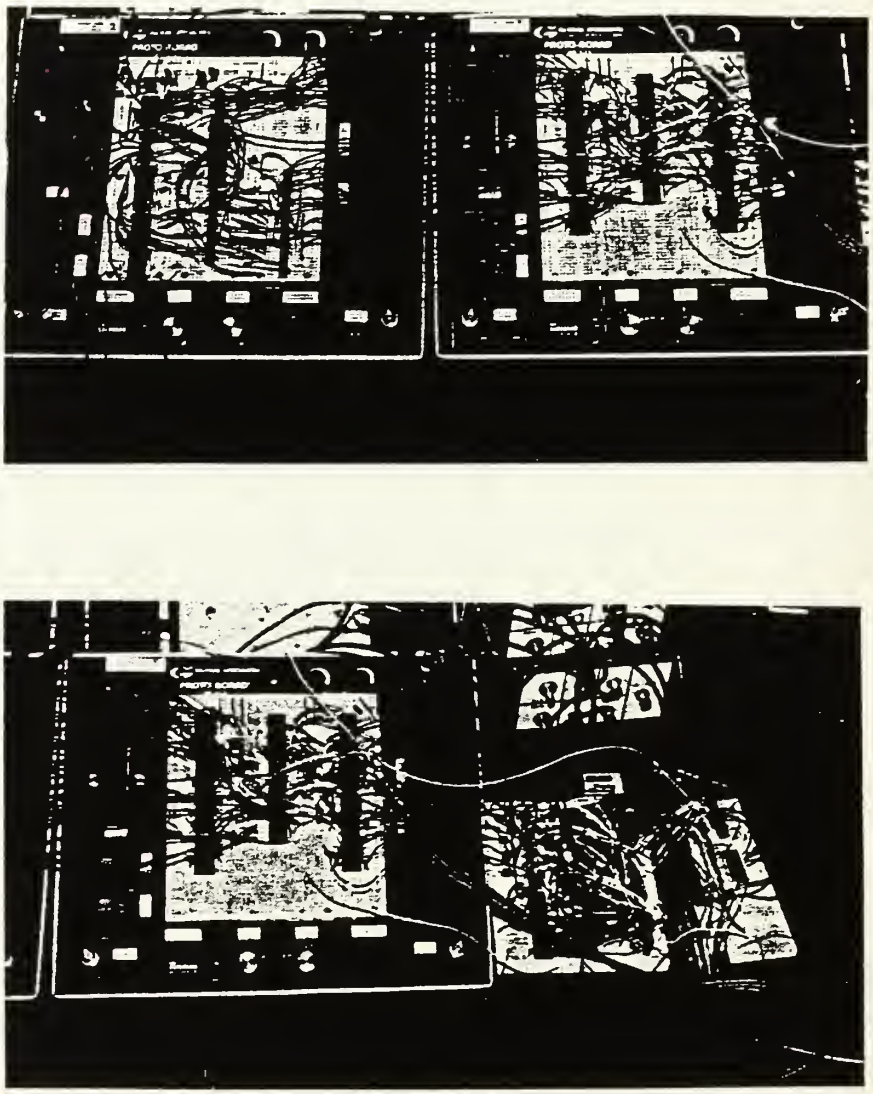

Figure 68 Breadboard implementation of the Asymmetric Digital Demodulator. The circuit on the right-hand side of the upper photograph is the same as that on the left-hand side in the lower photograph.

other hand, this scheme is highly suitable to integration on an application-specific integrated circuit (ASIC) or, possibly, a few of them.

The pipeline architecture is easily adaptable to ASIC. It has the very strong advantage of permitting the analog-to-digital (A/D) converter to operate as rapidly as possible. As mentioned in the previous chapter, a simpler implementation of the algorithm in digital hardware would entail the use of a microprocessor or a digital signal processor integrated circuit. If this could be made to operate fast enough to keep the A/D operating at full capacity, then it would be much more attractive than the brute-force approach we adopted.

Our failure to get the digital integrator working is a convincing illustration of the complexity of the circuit. Given more time, no doubt this problem could be resolved. The fact that it is a problem at all is a striking demonstration that our implementation of the Asymmetric Digital Demodulator is the most complicated of the demodulator's examined in the course of this research.

H. APPROXIMATE COST

The cost of the integrated circuits used in the construction of the Asymmetric Digital Demodulator is shown in Table XXXVI. At just over $300, it is the most costly of the demodulators considered in this research, but it is simply not as good as the Symmetric Analog Demodulator. Nearly half of the cost is due to the expensive multipliers. A fully integrated version of this algorithm, with a greater measure of success in using the full dynamic range of the A/D converters, would almost certainly result in an improved ratio of performance to price.

I. SUMMARY

In this chapter we considered the performance of a digital electronic implementation of the asymmetric demodulation algorithm. Of the three demodulators considered in this chapter, this was the most expensive and the most complicated in circuitry. Despite this fact, this circuit was able to operate over a broader dynamic range than our Fringe Rate Demodulator could. In fact, it was within 10 dB of the best performance

Table XXXVI. Calculation of the cost of the integrated circuits used in the Asymmetric Digital Demodulator.

Part ID	Description	Quantity Required	Price	Source of Price	Total Cost of Part
AD7769	LC^{2}MOS Analog I/O Port	2	$15.00	Analog Devices	$30.00
ADSP-1080A	8-Bit Multiplier	4	$37.00	Analog Devices	$148.00
AD7846	LC^{2}MOS 16-Bit Voltage Output DAC	1	$31.35	Analog Devices	$31.35
74LS04	Hex Inverter	1	$0.33	Digi-Key Corporation	$0.33
74LS83	4-Bit Binary Full Adder	12	$0.60	Digi-Key Corporation	$7.20
74LS374	Tri-State Octal D Flip-Flop	6	$0.60	Digi-Key Corporation	$3.60
74LS181	4-Bit Arithmetic Logic Unit	14	$2.84	Marvac Electronics	$39.76
OPA-111	Low-noise Op Amp	3	$11.80	Burr-Brown	$35.40
AD712	General Purpose Op Amp	2	$3.60	Analog Devices	$7.20
TOTAL		15			$302.84

a 16-bit digital-to-analog converter can deliver. We have also shown how pipe-lining can be used to provide a high rate of throughput in a digital demodulator. While this is a more complicated approach than the use of a digital signal processing (DSP) integrated circuit would entail, it is generally faster, too. Where high speed is mandatory, this approach shows considerable promise.

In the next and final chapter, we conclude this dissertation with a summary of what we have found, a comparison of the three demodulators we built and tested, and we provide some recommendations for future research.

XIV. CONCLUSION AND RECOMMENDATIONS

In this dissertation we began by looking closely at the theory of optical fiber interferometric sensors terminated with 3×3 optical fiber couplers. We considered in some detail both the workings of couplers as predicted by Maxwell's equations and their employment at the output of interferometric sensors to produce interferometric signals containing in-phase and quadrature components of the cosine of a signal of interest, the signal which impinged on the sensor in the first place. The symmetry of the operation of the couplers is such that each output is similar to the next, but with a 120° optical phase shift between them. We derived equations that will permit a study of the effects on the interferometric output of other than exactly 120° phase difference between the outputs.

We described how to build an interferometric sensor for laboratory work. We noted that the laser exhibited instabilities from time to time, and we suggested that these could be eliminated by introducing temperature control or by using an optical isolator to preclude reflections back into the laser. A sensor with more fiber wrapped on the piezoelectric cylinders and with a more powerful amplifier to drive them would permit the evaluation of the three demodulators described in this dissertation, as well as others, at higher phase amplitudes than we could achieve.

We then discussed a refinement to the Fringe Rate Demodulator proposed by Crooker [Ref. 10] and Crooker and Garrett [Ref. 11]. We found that the scale factor of this demodulator was between 105 and 120 mV/rad. The demodulator cannot function in the presence of signals generating less than $\pi/2$ rad of optical phase shift, so we were unable to express its bandwidth in the small-signal regime. For an optical phase shift of 51 rad, we found the bandwidth was 460 Hz, inasmuch as the scale factor changed by a factor of $\sqrt{2}$ at this frequency. The phase rate of the demodulator averaged 22.6 krad/s between 300 Hz and 1 kHz. The dynamic range peaked at a little over 38 dB at 100 Hz. This demodulator was both the simplest and the least expensive of the three we

investigated. However, its performance was limited. We discussed several ways in which the performance might be improved

We could use all three interferometric outputs, instead of just two, to generate the frequency signal which drives the frequency-to-voltage converter. This would reduce the minimum detectable signal to $\pi/3$ rad from $\pi/2$ rad for an extra 3.5 dB of dynamic range. The zener diode in the frequency-to-voltage converter we used could be replaced by one of 15 V. The 12 mV we measured could be reduced to the 3 mV specified as typical for the converter. These three changes would increase the dynamic range by 22 dB. The possibility of finding a better frequency-to-voltage converter than the LM2917N we used should be investigated. Very possibly a phase-locked converter would yield superior linearity.

We next turned our attention to the theory of asymmetric and symmetric passive homodyne demodulation. We considered the asymmetric scheme first, because it was simpler, and because the symmetric scheme was a natural extension of it. The symmetric scheme has the aesthetically pleasing feature that no output is discarded, as is the case in asymmetric demodulation, and all outputs are treated equally. The algorithm also automatically eliminates any dependence of the output on the optical power received, a feature not shared by the asymmetric demodulation scheme.

A detailed explanation of our analog implementation of the symmetric demodulation scheme followed next. We examined its performance and found its scale factor was 31 mV/rad, very close to the predicted value of 29 mV/rad. This agreement gave us confidence both in the theory and in the practical performance of the demodulator. The small-signal bandwidth of the Symmetric Analog Demodulator we found to be 113 kHz. The maximum acceptable signal and the noise floor both declined at the rate of 20 dB per decade of increase in frequency, as we expected them to do. This demodulator had a maximum phase rate of 65 krad/s, the highest of the three demodulators considered. The dynamic range was measured as 115 dB in a one hertz bandwidth with 4% total harmonic distortion considered acceptable at 600 Hz. This dynamic range is quite large. This demodulator was moderately complex. It cost $270.00 in integrated circuits. We suggested that the use of the new AD764 Analog Multiplier in place of the AD534

Analog Multiplier could achieve a ten-fold increase in bandwidth for a reduction in price by one half.

With its excellent performance over a broad envelope of frequencies and signal amplitudes, this new demodulator was the most successful of the three we implemented. Its price was in the middle of the prices of the other two. Its performance far surpassed the others. We included a detailed noise analysis in an appendix. We were able to identify the analog divider and the analog multipliers as the noisiest components in our implementation of the symmetric demodulation algorithm. As a result, we concluded that the receivers do not require the expensive, low-noise operational amplifiers we used. This analysis will make possible the intelligent selection of components to minimize cost and maximize performance in the future.

Our implementation of the Asymmetric Digital Demodulator was the least successful. We failed to get a digital integrator working and resorted in the end to doing the integration in analog electronics. This unappealing result needs further investigation. The performance and price of this demodulator also were arguably the worst. It had a lower minimum detectable signal than the Fringe Rate Demodulator, in that it could detect signals of less than $\pi/2$ rad optical phase shift. However, the mixture of frequencies and voltages over which it would function adequately was quite irregular. Improved performance could be obtained by using precision voltage references for the analog-to-digital and digital-to-analog converters in the Asymmetric Digital Demodulator.

The scale factor of the Asymmetric Digital Demodulator was 35 mV/rad, but this number is not particularly helpful in view of the fact that the output was produced by an analog, not a digital, integrator. The high level of distortion generated by this demodulator made a meaningful measurement of its bandwidth impossible. With further work, we believe the distortion could be reduced by taking better advantage of the dynamic range of the analog-to-digital converters. The maximum phase rate of the demodulator averaged 54 krad/s in the range from 500 Hz to 2 kHz, higher than that of the Fringe Rate Demodulator, but lower than that of the Symmetric Analog Demodulator.

In view of the increasing popularity of digital signal processing techniques, we recommend that a digital implementation of the symmetric demodulation algorithm be undertaken using very-large-scale integration (VLSI). This would greatly reduce the external circuit complexity of such a demodulator, and it should lower the cost both of construction and of components considerably. The use of pipeline-processing has been shown by our Asymmetric Digital Demodulator to be an effective way to keep the processing going as rapidly as the conversion rate will permit, and it should be a feature of a VLSI implementation. An implementation of the Asymmetric Digital Demodulator or a Symmetric Digital Demodulator should be undertaken with digital signal processing integrated circuits replacing the pipeline-processing hardware. This would help in assessing whether the reduced processing speed would be compensated for by the reduced complexity of the circuit. The large differences between the performance of the Symmetric Analogue Demodulator and the Asymmetric Digital Demodulator could be due to the difference between analog and digital processing on the one hand or symmetric and asymmetric demodulation on the other hand. This issue bears further research.

We also recommend that a new implementation of the Symmetric Analog Demodulator be built with the AD764 Analog Multiplier integrated circuit. In building this new demodulator, some trim potentiometers can be removed. Improved noise reduction should also boost the performance of this circuit at low phase rates.

The Fringe Rate Demodulator is attractive because of its low cost and its simplicity. However, it is only feasible to use it when large phase amplitudes are always present (much greater, say, than the minimum $\pi/2$ rad). The symmetric demodulation technique is superior to the asymmetric demodulation technique because dependence on received optical power is eliminated. The analog implementation of this is simple and yields a large dynamic range. However, if succeeding processing requires digital signals, then a digital implementation of the symmetric demodulation algorithm would be attractive, especially if implemented as an application-specific integrated circuit.

We conclude this dissertation with Table XXXVII, which summarizes the performance of the three demodulators we built and tested.

Table XXXVII Summary of the performance of each of the three demodulators described in this dissertation.

	Fringe Rate Demodulator	Asymmetric Digital Demodulator	Symmetric Analogue Demodulator
Phase Rate [krad/s]	23	54	65
Scale Factor [mV/rad]	105-120	35	31
Minimum Detectable Signal	$\pi/2$	4.2 mrad/$\sqrt{\text{Hz}}$ @ 600 Hz	220 μrad/$\sqrt{\text{Hz}}$ @ 600 Hz
Dynamic Range	46 dB @100 Hz	86 dB @500 Hz	115 dB @600 Hz
Complexity	Low	High	Moderate
Cost	$100	$303	$270

APPENDIX A. MISCELLANY

In this appendix, we provide a number of lemmas, theorems, derivations, and observations which are used in the body of the dissertation. These details are placed here for the sake of completeness.

A. LEMMA

$$\sum_{k=0}^{N-1} e^{\pm j\frac{k4\pi}{N}} = 0. \tag{327}$$

Proof:

Let

$$S = \sum_{k=0}^{N-1} e^{\pm j\frac{k4\pi}{N}} \tag{328}$$

$$S = \sum_{k=0}^{N-1} \left[e^{\pm j\frac{4\pi}{N}} \right]^k \tag{329}$$

$$S = \sum_{k=0}^{N-1} \alpha^k \tag{330}$$

where

$$\alpha = e^{\pm j\frac{4\pi}{N}}. \tag{331}$$

This sum is the well known geometric series, and it can be expressed in closed form as follows.

$$\alpha S = \sum_{k=0}^{N-1} \alpha^{k+1} \tag{332}$$

$$\alpha S - S = \sum_{k=0}^{N-1} \alpha^{k+1} - \sum_{k=0}^{N-1} \alpha^{k} \tag{333}$$

$$(\alpha - 1)S = \sum_{k=1}^{N} \alpha^{k} - \sum_{k=0}^{N-1} \alpha^{k} \tag{334}$$

$$(\alpha - 1)S = \alpha^{N} - \alpha^{0} \tag{335}$$

$$S(\alpha - 1) = \alpha^{N} - 1 \tag{336}$$

$$S = \frac{\alpha^{N} - 1}{\alpha - 1}. \tag{337}$$

Therefore

$$S = \frac{\left[e^{\pm j\frac{4\pi}{N}}\right]^{N} - 1}{e^{\pm j\frac{4\pi}{N}} - 1} \tag{338}$$

$$S = \frac{e^{\pm j4\pi} - 1}{e^{\pm j\frac{4\pi}{N}} - 1}. \tag{339}$$

Now

$$\begin{aligned} e^{\pm j4\pi} &= \cos(\pm 4\pi) + j\sin(\pm 4\pi) \\ &= 1 + j0 \\ &= 1. \end{aligned} \tag{340}$$

So

$$S = \frac{1-1}{e^{j\frac{4\pi}{N}}-1} \tag{341}$$

$$= 0.$$

This completes the proof of the lemma in Equation (327).

B. THEOREM

$$\sum_{k=0}^{N-1} e^{j\left[\theta-k\frac{2\pi}{N}\right]} = \sum_{k=0}^{N-1}\left\{\cos\left(\theta-k\frac{2\pi}{N}\right)+j\sin\left(\theta-k\frac{2\pi}{N}\right)\right\} = 0. \tag{342}$$

Proof:

$$\sum_{k=0}^{N-1} e^{j\left[\theta-k\frac{2\pi}{N}\right]} = e^{j\theta}\sum_{k=0}^{N-1} e^{-jk\frac{2\pi}{N}}$$

$$= e^{j\theta}\left\{\frac{e^{-jN\frac{2\pi}{N}}-1}{e^{-j\frac{2\pi}{N}}-1}\right\} \qquad \text{[Geometric series]} \tag{343}$$

$$= e^{j\theta}\left\{\frac{1-1}{e^{-j\frac{2\pi}{N}}-1}\right\}$$

$$= 0.$$

This completes the proof of the theorem.

C. THEOREM

$$\sum_{k=0}^{N-1} \cos^2\left(\phi + \frac{k2\pi}{N}\right) = \sum_{k=0}^{N-1} \sin^2\left(\phi + \frac{k2\pi}{N}\right) = \frac{N}{2} \tag{344}$$

Proof:

Let

$$S = \sum_{k=0}^{N-1} \cos^2\left(\phi + \frac{k2\pi}{N}\right) \tag{345}$$

$$S = \sum_{k=0}^{N-1} \left[\frac{e^{j\left(\phi + \frac{k2\pi}{N}\right)} + e^{-j\left(\phi + \frac{k2\pi}{N}\right)}}{2} \right]^2 \tag{346}$$

$$S = \frac{1}{4} \sum_{k=0}^{N-1} \left[e^{j2\left(\phi + \frac{k2\pi}{N}\right)} + 2e^{j\left(\phi + \frac{k2\pi}{N}\right)} e^{-j\left(\phi + \frac{k2\pi}{N}\right)} + e^{-j2\left(\phi + \frac{k2\pi}{N}\right)} \right] \tag{347}$$

$$S = \frac{1}{4} \sum_{k=0}^{N-1} \left[e^{j2\phi} e^{j\frac{k4\pi}{N}} + 2 + e^{-j2\phi} e^{-j\frac{k4\pi}{N}} \right] \tag{348}$$

$$S = \frac{1}{4} \left[e^{j2\phi} \sum_{k=0}^{N-1} e^{j\frac{k4\pi}{N}} + \sum_{k=0}^{N-1} 2 + e^{-j2\phi} \sum_{k=0}^{N-1} e^{-j\frac{k4\pi}{N}} \right]. \tag{349}$$

Now using the lemma in Equation (327), we can write

$$S = \frac{1}{4}\left[(e^{j2\phi})(0) + 2N + (e^{-j2\phi})(0)\right] \tag{350}$$

$$S = \frac{2N}{4} \tag{351}$$

$$S = \frac{N}{2}. \tag{352}$$

This completes the proof of the theorem as far as the cosine is concerned. The proof of the part concerning the sine could be proved in a similar manner, but here is a shorter proof, using a well known trigonometric identity, namely

$$\sin^2\phi + \cos^2\phi = 1. \tag{353}$$

So

$$\sum_{k=0}^{N-1}\left[\sin^2\left(\phi + \frac{k2\pi}{N}\right) + \cos^2\left(\phi + \frac{k2\pi}{N}\right)\right] = \sum_{k=0}^{N-1} 1 = N. \tag{354}$$

In view of that part of Equation (344) proved so far, we can also write

$$\sum_{k=0}^{N-1}\left[\sin^2\left(\phi + \frac{k2\pi}{N}\right) + \cos^2\left(\phi + \frac{k2\pi}{N}\right)\right] = \left[\sum_{k=0}^{N-1}\sin^2\left(\phi + \frac{k2\pi}{N}\right)\right] + \frac{N}{2}. \tag{355}$$

Comparison of Equations (354) and (355) permits us to write

$$N = \left[\sum_{k=0}^{N-1}\sin^2\left(\phi + \frac{k2\pi}{N}\right)\right] + \frac{N}{2} \tag{356}$$

$$\frac{N}{2} = \sum_{k=0}^{N-1}\sin^2\left(\phi + \frac{k2\pi}{N}\right). \tag{357}$$

This completes the remainder of the proof of the theorem of Equation (344).

D. EQUIVALENT NOISE BANDWIDTH

The equivalent noise bandwidth of a lowpass filter is the bandwidth of a hypothetical filter with total transmission below the cut-off frequency and zero transmission above it. It is a useful concept for considering the amount of white noise which a lowpass filter will permit to pass.

For a single-pole filter, the magnitude of the gain of the filter declines at the rate of 20 dB per decade of increase in frequency, *e.g.*, the gain in going from 100 Hz to 1 kHz might decline from 30 dB to 10 dB. The equivalent noise bandwidth B can be derived as follows.

The Laplace transform $H_1(s)$ of a filter with a single pole is

$$H_1(s) = \frac{1}{1+s\tau}. \tag{358}$$

The frequency response of this filter can be found by setting $s=j\omega=j2\pi f$, so

$$H_1(j2\pi f) = \frac{A}{1+j2\pi f\tau}. \tag{359}$$

The noise power experiences a transfer function given by

$$|H_1(j2\pi f)|^2 = \frac{A^2}{1+(2\pi f\tau)^2}. \tag{360}$$

To find the total noise power transferred by the filter, we must integrate this expression over all frequencies. If we let $u=2\pi f\tau$ and $du=2\pi\tau\, df$, and call the integral B, then

$$B = \int_0^\infty |H_1(j2\pi f)|^2 df = \frac{A^2}{2\pi\tau}\int_0^\infty \frac{1}{1+u^2}du. \tag{361}$$

If we now make the substitution $u=\cot\theta$, $du=-\csc^2\theta\, d\theta$, then we have

$$B = \frac{A^2}{2\pi\tau}\int_{\pi/2}^{0} \frac{-\csc^2\theta\, d\theta}{\csc^2\theta}$$

$$= \frac{A^2}{2\pi\tau}\left[-\left(0-\frac{\pi}{2}\right)\right] \tag{362}$$

$$= \frac{A^2}{4\tau}.$$

Now the point at which the gain in Equation (360) is down by one half, the −3dB frequency f_{3dB}, is given by

$$f_{-3dB} = \frac{1}{2\pi\tau}. \tag{363}$$

Also, the time constant τ is usually specified as the product of a resistance R and a capacitance C in a simple, analog filter, so

$$\tau = RC. \tag{364}$$

Hence we can write the following equivalent forms of Equation (362):

$$B = \frac{A^2}{4\tau} = \frac{A^2\pi f_{-3dB}}{2} = \frac{A^2}{4RC}. \tag{365}$$

For a two-pole filter, the magnitude of the gain of the filter declines at the rate of 40 dB per decade of increase in frequency, *e.g.*, the gain in going from 100 Hz to 1 kHz might decline from 30 dB to −10 dB. The equivalent noise bandwidth B is given by the following derivation.

The Laplace transform $H_2(s)$ of a filter with a double pole is

$$H_2(s) = \frac{1}{(1+s\tau)^2}. \tag{366}$$

The frequency response of this filter can be found by setting $s = j\omega = j2\pi f$, so

$$H_2(j2\pi f) = \frac{A}{(1+j2\pi f\tau)^2}. \tag{367}$$

The noise power experiences a transfer function given by

$$|H_2(j2\pi f)|^2 = \frac{A^2}{[1+(2\pi f\tau)^2]^2}. \tag{368}$$

To find the total noise power transferred by the filter, we must integrate this expression over all frequencies. If we let $u=2\pi f\tau$ and $du=2\pi\tau\, df$, and call the integral B, then

$$\begin{aligned} B &= \int_0^\infty |H_2(j2\pi f)|^2 df = \int_0^\infty \frac{A^2}{[1+(2\pi\tau f)^2]^2} df \\ &= \frac{A^2}{2\pi\tau}\int_0^\infty \frac{1}{[1+u^2]^2} du. \end{aligned} \tag{369}$$

If we now make the substitution $u=\cot\theta$, $du=-\csc^2\theta\, d\theta$, then we have

$$\begin{aligned} B &= \frac{A^2}{2\pi\tau}\int_0^{\pi/2} \frac{csc^2\theta\, d\theta}{csc^4\theta} \\ &= \frac{A^2}{2\pi\tau}\int_0^{\pi/2} \sin^2\theta\, d\theta. \end{aligned} \tag{370}$$

By a simple trigonometric substitution, we can rewrite this and integrate it:

$$\begin{aligned} B &= \frac{A^2}{4\pi\tau}\int_0^{\pi/2} [1-\cos 2\theta]\, d\theta \\ &= \frac{A^2}{4\pi\tau}\left[\theta - \frac{\sin 2\theta}{2}\right]_0^{\pi/2}. \end{aligned} \tag{371}$$

Evaluating the integral at the limits yields

$$B = \frac{A^2}{4\pi\tau}\frac{\pi}{2} = \frac{A^2}{8\tau}. \tag{372}$$

Now the point at which the gain in Equation (368) is down by one half, the −3dB frequency f_{3dB}, is given by

$$f_{-3dB} = \frac{1}{2\pi\tau}. \tag{373}$$

Also, the time constant τ is usually specified as the product of a resistance R and a capacitance C in a simple, analog filter, so

$$\tau = RC. \tag{374}$$

So we can write the following equivalent forms of Equation (362):

$$B = \frac{A^2}{8\tau} = \frac{A^2\pi f_{-3dB}}{4} = \frac{A^2}{8RC}. \tag{375}$$

E. ANALYSIS OF A COMPARATOR WITH HYSTERESIS

In Figure 69 we show a schematic diagram of a comparator circuit. This circuit provides hysteresis and so gives some noise immunity, that is, the output will not switch state unless the input changes by more than the amount of hysteresis provided. The analysis given here is sufficiently general that the circuit can be applied to a system with any voltage levels.

Resistors R_1 and R_2 form a resistive divider which determines the threshold level. When the input V_{IN} crosses this level, the output of the LF311 comparator changes states. However, resistor R_3 provides a small level of positive feedback to the non-inverting input of the LF311, so the threshold level is changed slightly from its nominal value by an

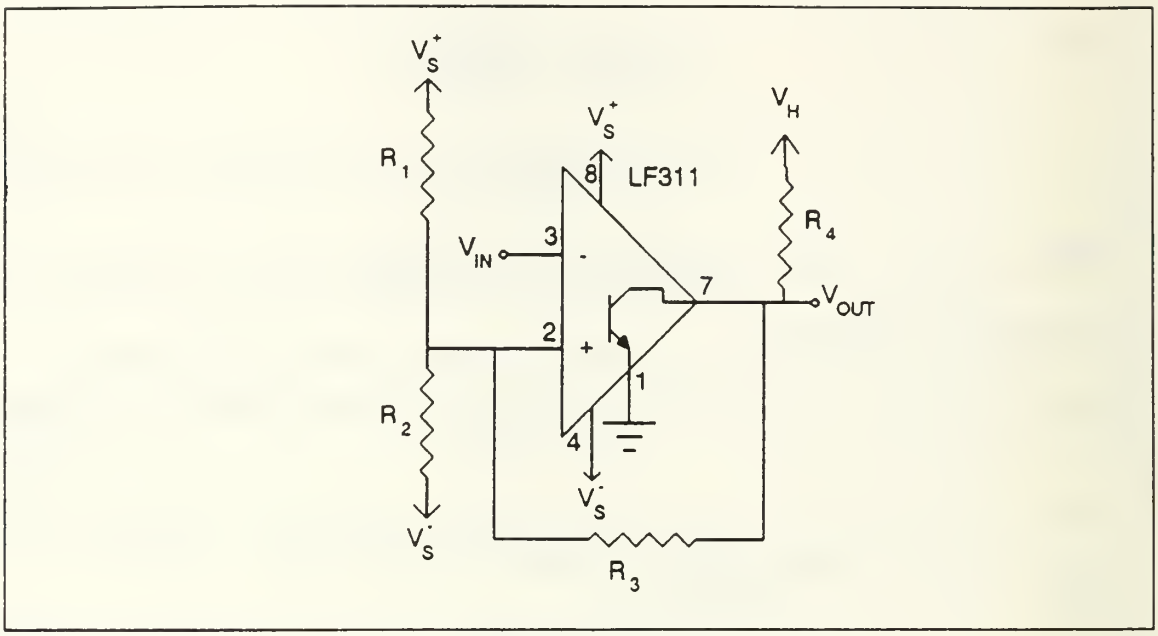

Figure 69 Schematic diagram of a comparator with hysteresis.

amount which varies with the output V_O.

Pin 7 of the LF311 is connected to an internal transistor with an open collector. Resistor R_4 tends to pull V_O to the positive voltage V_H when the transistor is cut off. The transistor pulls V_O to ground through pin 1 when it is saturated. The transistor is cut off if the voltage V_{IN} is lower than that at the non-inverting terminal of the LF311; it is saturated otherwise.

To analyze the performance of the circuit, we shall apply the principle of superposition. When the output is nearly 0 (when the transistor is saturated), the non-inverting input sees a voltage which is due to the combined effects of V_S^+ and V_S^-. This voltage is given by

$$V_{+,L} = \frac{R_2 \| R_3}{R_1 + R_2 \| R_3} V_S^+ + \frac{R_1 \| R_3}{R_2 + R_1 \| R_3} V_S^- \qquad (376)$$

If we multiply this out, we get

$$V_{+,L} = \frac{\left(\frac{R_2R_3}{R_2+R_3}\right)}{\left[R_1+\left(\frac{R_2R_3}{R_2+R_3}\right)\right]}V_S^+ + \frac{\left(\frac{R_1R_3}{R_1+R_3}\right)}{\left[R_2+\left(\frac{R_1R_3}{R_1+R_3}\right)\right]}V_S^- \quad (377)$$

This can be simplified to

$$V_{+,L} = \frac{R_2R_3}{R_1R_2+R_1R_3+R_2R_3}V_S^+ + \frac{R_1R_3}{R_1R_2+R_1R_3+R_2R_3}V_S^- \quad (378)$$

By removing the common factor R_3, we get

$$V_{+,L} = \frac{R_3\left[R_2V_S^+ + R_1V_S^-\right]}{R_1R_2+R_1R_3+R_2R_3} \quad (379)$$

When the transistor in the output of the LF311 is cut off, then R_4 enters the picture and modifies the voltage V^+ to

$$V_{+,H} = \frac{R_2\|(R_3+R_4)}{R_1-R_2\|(R_3+R_4)}V_S^+ + \frac{R_1\|(R_3+R_4)}{R_2+R_1\|(R_3+R_4)}V_S^- + \frac{R_1\|R_2}{(R_3+R_4)-R_1\|R_2}V_H \quad (380)$$

Expanding this yields

$$V_{+,H} = \frac{\left[\frac{R_2(R_3+R_4)}{R_2+R_3+R_4}\right]}{\left[R_1+\left(\frac{R_2(R_3+R_4)}{R_2+R_3+R_4}\right)\right]}V_S^+ + \frac{\left[\frac{R_1(R_3+R_4)}{R_1+R_3+R_4}\right]}{\left[R_2+\left(\frac{R_1(R_3+R_4)}{R_1+R_3+R_4}\right)\right]}V_S^- - \frac{\left[\frac{R_1R_2}{R_1+R_2}\right]}{\left[R_3+R_4+\left(\frac{R_1R_2}{R_1+R_2}\right)\right]}V^H. \tag{381}$$

This simplifies to

$$V_{+,H} = \frac{R_2R_3+R_2R_4}{R_1R_2+R_1R_3+R_1R_4+R_2R_3+R_2R_4}V_S^+ + \frac{R_1R_3+R_1R_4}{R_1R_2+R_1R_3+R_1R_4+R_2R_3+R_2R_4}V_S^- + \frac{R_1R_2}{R_1R_2+R_1R_3+R_1R_4+R_2R_3+R_2R_4}V_H. \tag{382}$$

Collecting common terms reduces this to

$$V_{+,H} = \frac{(R_3+R_4)(R_2V_S^+ + R_1V_S^-)+R_1R_2V_H}{R_1R_2+R_1R_3+R_1R_4+R_2R_3+R_2R_4}. \tag{383}$$

If we set

$$V_S^- = -V_S^+,\ R_1 \ll R_3,\ R_2 \ll R_3,\ \text{and}\ R_4 \ll R_3, \tag{384}$$

then we can approximate $V_{+,L}$ as

$$V_{+,L} \approx \frac{R_3[R_2-R_1]V_S^+}{(R_1+R_2)R_3} = \frac{R_2-R_1}{R_1+R_2}V_S^+ \tag{385}$$

and we can approximate $V_{+,H}$ as

$$V_{+,H} \approx \frac{R_3(R_2-R_1)V_S^+ + R_1R_2V_H}{(R_1+R_2)R_3}$$

$$= \frac{(R_2-R_1)}{R_1+R_2}V_S^+ + \frac{R_1 \| R_2}{R_3}V_H \qquad (386)$$

$$= V_{+,L} + \frac{R_1 \| R_2}{R_3}V_H .$$

From these two expressions, we can see that under the given assumptions, the threshold for the switching operation is

$$V_{THRESHOLD} \approx \frac{R_2-R_1}{R_1+R_2}V_S^+ \qquad (387)$$

and that this threshold rises when the output goes high by

$$V_{INCREMENTAL} \approx \frac{R_1 \| R_2}{R_3}V_H . \qquad (388)$$

Equations (387) and (388) are design criteria by which we may pick values of the four resistors which will achieve a desired lower switching level and amount of hysteresis. These equations are valid approximations only when the conditions in Equation (384) are met.

F. ANALYSIS OF A CIRCUIT FOR INTEGRATION AND DIFFERENTIATION

In Figure 70 we show a schematic for a generalized circuit which, with proper choices for the components, can function as a differentiator, an integrator, or a bandpass filter.

If we consider a signal of the form

$$s(t) = Ae^{j\omega t} = Ae^{j2\pi ft}, \qquad (389)$$

with amplitude A and frequency $\omega=2\pi f$, then it has a derivative

$$\dot{s}(t) = \frac{ds(t)}{dt} = jA\omega e^{j\omega t} = jA2\pi f e^{j2\pi ft}. \quad (390)$$

Its integral is

$$\int s(t)dt = \frac{A}{j\omega} e^{j\omega t} = \frac{A}{j2\pi f} e^{j2\pi ft}. \quad (391)$$

Neither the derivative nor the integral is a truly realizable function because, as the formulas show, they both become infinite in magnitude if the frequency goes to infinity (in the case of the derivative) or to zero (in the case of the integral). The best we can do is to approximate them over a specified band of frequencies. So what shall we do outside the region in which the approximation is acceptable? The best thing often is to let the magnitude of the approximation go to zero at extremely high and extremely low frequencies.[28]

This, of course, is just what a bandpass filter does. So if we can construct a bandpass filter whose gain characteristic has a section in which the increase in gain with frequency looks like the magnitude of the expression in Equation (390) and with a section in which the decrease in gain with frequency looks like the magnitude of the expression in Equation (391), we can make reasonable approximations to these functions.

As a bonus, of course, we will have a bandpass filter for any other purpose we might have in mind. The emphasis in this section, however, is on approximating derivatives and integrals.

Note that the capacitors in Figure 70 have been annotated with their impedances in the s-domain. After completing the analysis in this domain, we shall be interested in letting $s=j\omega$, which will give us the steady-state response of the circuit to a sinusoidal input of frequency ω.

---

[28] An alternative at low frequencies is to let the gain become a constant. This is not feasible at high frequencies, since it would require an infinite amount of energy: an impossibility.

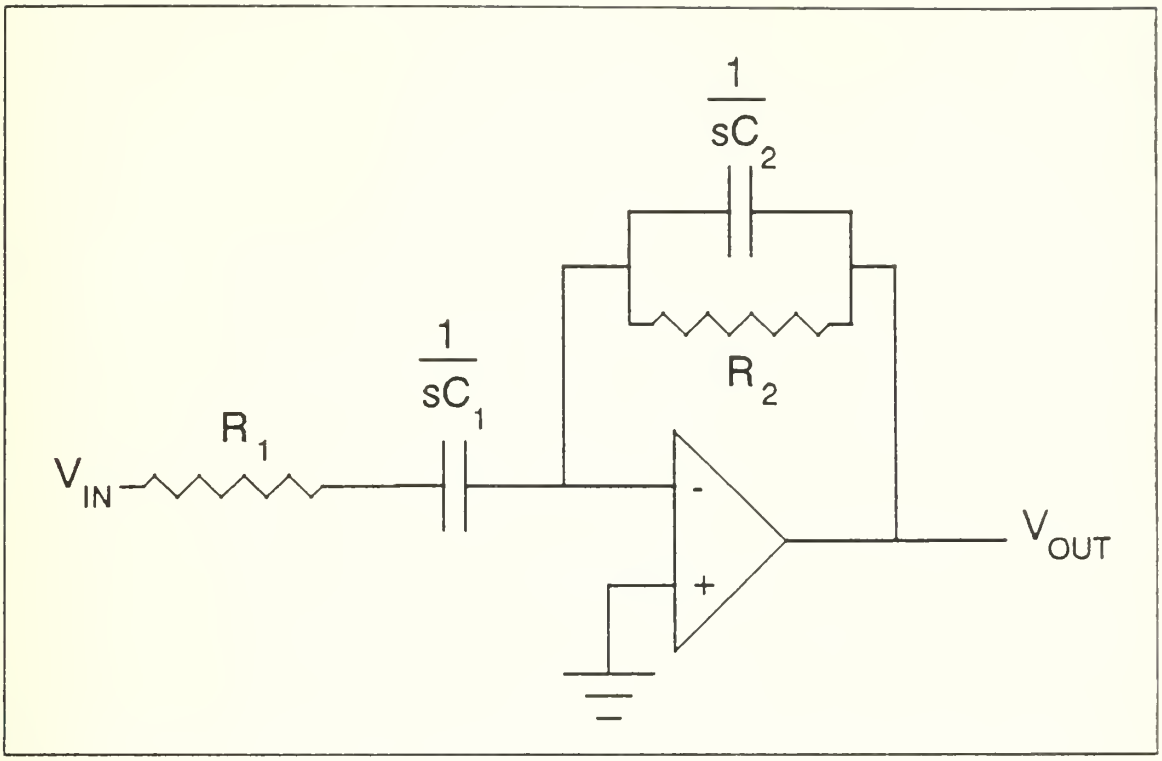

Figure 70 A general circuit for differentiation, integration, and bandpass filtering.

We can obtain the transfer function for this circuit by regarding R_1 and C_1 in series as being a single impedance and R_2 and C_2 in parallel as another impedance. At combinations of gain and frequency well below the gain-bandwidth product of the operational amplifier, the transfer function is approximately

$$\frac{V_{OUT}}{V_{IN}} = -\frac{R_2 \| \frac{1}{sC_2}}{R_1 + \frac{1}{sC_1}}. \tag{392}$$

Simplifying this, we get

$$\frac{V_{OUT}}{V_{IN}} = -\frac{\left[\dfrac{1}{\dfrac{1}{R_2}+sC_2}\right]}{\left[R_1+\dfrac{1}{sC_1}\right]}$$

$$= -\left[\frac{R_2}{1+sR_2C_2}\right]\left[\frac{sC_1}{1+sC_1R_1}\right] \tag{393}$$

$$= -\frac{sC_1R_2}{R_1R_2C_1C_2\left(\dfrac{1}{R_2C_2}+s\right)\left(\dfrac{1}{R_1C_1}+s\right)}.$$

This reduces to

$$\frac{V_{OUT}}{V_{IN}} = -\frac{s}{R_1C_2\left(\dfrac{1}{R_2C_2}+s\right)\left(\dfrac{1}{R_1C_1+s}\right)}. \tag{394}$$

Letting $s=j\omega$, we get

$$\frac{V_{OUT}}{V_{IN}}(j\omega) = -\frac{j\omega}{R_1C_2\left(\dfrac{1}{R_2C_2}+j\omega\right)\left(\dfrac{1}{R_1C_1+j\omega}\right)}$$

$$= -\frac{R_2C_1j\omega}{\left[1+\dfrac{j\omega}{\left(\dfrac{1}{R_2C_2}\right)}\right]\left[1+\dfrac{j\omega}{\left(\dfrac{1}{R_1C_1}\right)}\right]}. \tag{395}$$

Expressing this in terms of the conventional frequency $f=\omega/2\pi$,

$$\frac{V_{OUT}}{V_{IN}}(j2\pi f) = -2\pi R_2 C_1 \frac{jf}{\left[1+\frac{jf}{\left(\frac{1}{2\pi R_2 C_2}\right)}\right]\left[1+\frac{jf}{\left(\frac{1}{2\pi R_1 C_1}\right)}\right]}. \tag{396}$$

This expression is more easily grasped if we let

$$f_1 = \frac{1}{2\pi R_1 C_1} \text{ and } f_2 = \frac{1}{2\pi R_2 C_2} \tag{397}$$

for then we get

$$\frac{V_{OUT}}{V_{IN}}(j2\pi f) = -R_2 C_1 \frac{j2\pi f}{\left[1+j\frac{f}{f_1}\right]\left[1+j\frac{f}{f_2}\right]}. \tag{398}$$

Let us set $f_1=f_2=f_p$. For frequencies $f \ll f_p$, we have

$$\frac{V_{OUT}}{V_{IN}}(j2\pi f) \approx -R_2 C_1 j2\pi f. \tag{399}$$

From Equations (389) and (390),

$$\frac{\dot{s}(t)}{s(t)} = j2\pi f. \tag{400}$$

So our circuit produces $-R_2C_1$ times the derivative of the input, provided that $f \ll f_p$.

Now let us see what happens for frequencies $f \gg f_p$. We get

$$\begin{aligned}
\frac{V_{OUT}}{V_{IN}}(j2\pi f) &\approx -R_2C_1\frac{j2\pi f}{\left[j\frac{f}{f_p}\right]\left[j\frac{f}{f_p}\right]} \\
&= R_2C_1\frac{j2\pi f_p^2}{f} \\
&= -R_2C_1(2\pi f_p)^2\frac{1}{j2\pi f} \\
&= -R_2C_1\left(\frac{(2\pi)^2}{(2\pi)^2R_1R_2C_1C_2}\right)\frac{1}{j2\pi f} \\
&= -\frac{1}{R_1C_2}\frac{1}{j2\pi f}.
\end{aligned} \tag{401}$$

From Equations (389) and (391),

$$\frac{\int s(t)dt}{s(t)} = \frac{1}{j2\pi f}. \tag{402}$$

So our circuit produces $-1/R_1C_2$ times the integral of the input, provided that $f \gg f_p$.

Any time approximations are used, one is interested in knowing how good the approximation is. We have simply assumed that the frequency f is so far above f_p (in the case of the derivative) or so far below it (in the case of the integral) that errors are negligible. We can be more precise than this, however.

Let $f=\alpha f_p$. The constant α may be more or less than 1. We are interested in letting it be more than 1 in our consideration of the accuracy of our circuit for calculating derivatives and less than 1 in our consideration of the accuracy for calculating integrals. There are two sources of error. Either the magnitude of the result may be in error, or the phase may be in error.

First we will consider derivatives. The magnitude of the gain of the circuit is

$$\left|\frac{V_{OUT}}{V_{IN}}(j2\pi f)\right| = \frac{2\pi f R_2 C_1}{\sqrt{\left[1+\left(\frac{f}{f_1}\right)^2\right]\left[1+\left(\frac{f}{f_2}\right)^2\right]}}. \tag{403}$$

The fractional error in the magnitude of the gain is 1 less than the ratio of this quantity to our approximation in Equation (399). Calling this error ϵ_M, we have

$$\epsilon_M = \frac{1}{\sqrt{\left[1+\left(\frac{f}{f_1}\right)^2\right]\left[1+\left(\frac{f}{f_2}\right)^2\right]}} - 1. \tag{404}$$

If we still have equal pole frequencies ($f_p = f_1 = f_2$), then

$$\begin{aligned} \epsilon_M &= \frac{1}{\left[1+\left(\frac{f}{f_p}\right)^2\right]} - 1 \\ &= \frac{f_p^2}{f_p^2+f^2} - 1 \\ &= -\frac{1}{1+\left(\frac{f_p}{f}\right)^2}. \end{aligned} \tag{405}$$

In Table XXXVIII we have tabulated the error ϵ_M in the magnitude of the gain. As is clear from the table, less than 1% error results if we cause the pole frequency f_p to be less than 1/10 the lowest frequency of interest.

The phase of the gain of the circuit is

$$\angle\left(\frac{V_{OUT}}{V_{IN}}\right) = -\frac{\pi}{2} - 2\tan^{-1}\left(\frac{f}{f_p}\right). \tag{406}$$

The error in the phase of the gain is the difference between this angle and the phase angle of our approximation in Equation (399). Calling this error ϵ_ϕ, we have

Table XXXVIII Error in the magnitude of the gain of the differentiating circuit as a function of the ratio of signal frequency to pole frequency.

f_p/f	ϵ_M
1.00	−0.5000
5.00	−0.0385
10.00	−0.0099
50.00	−0.0004
100.00	−0.0001

$$\epsilon_P = -2\tan^{-1}\left(\frac{f}{f_p}\right). \tag{407}$$

The negative sign indicates that the magnitude of the derivative will always be understated slightly by the circuit.

In Table XXXIX we have tabulated this function in degrees for several values of the ratio of the frequency f of the signal to the pole frequency f_p.

From Table XXXVIII and Table XXXIX, we can see that the cost of acquiring greater accuracy is a necessity to restrict the frequencies f of the signal to a range well below the chosen pole frequency f_p. Generally speaking, in designing a circuit we will have in mind some specification for the accuracy in phase or magnitude of the gain. The equations developed in this section can be used to place constraints on the necessary value of f_p to meet the specifications. In addition to choosing f_p such as to meet constraints on accuracy over the range of frequencies expected, we must also choose a value for the product R_2C_1 so that the desired multiple of the derivative is obtained from the circuit. This number cannot be too big, for the amplifier will not permit it. The gain at a given frequency cannot exceed the ratio of the gain-bandwidth product of the amplifier (a published specification) and the particular frequency. For example, if we let

Table XXXIX Error in the phase of the gain of the differentiating circuit as a function of the ratio of signal frequency to pole frequency.

f/f_p	ϵ_P
1.00	−90°
0.50	−53.1°
0.10	−11.4°
0.05	−5.7°
0.01	−1.1°

GBW represent the gain-bandwidth. then at a frequency f, the gain cannot exceed GBW/f. For a differentiator, since we must operate well below the pole frequency f_p, the gain near the pole frequency will always be considerably higher than that at the frequencies we are interested in. This is just the region in which the gain-bandwidth product is likely to impose a constraint. The upshot of this is that the gain of the differentiator may need to be kept down in order to avoid driving the amplifiers too hard. The consequence of ignoring this point is reduced accuracy in the gain.

The equations for the fractional error in the magnitude of the gain of our circuit when it is used as an integrator are not quite as simple as was the case for the differentiator. In this case, we find

$$\epsilon_M = \frac{\left\{\dfrac{2\pi f R_2 C_1}{\sqrt{\left[1+\left(\dfrac{f}{f_1}\right)^2\right]\left[1+\left(\dfrac{f}{f_2}\right)^2\right]}}\right\}}{\left[\dfrac{1}{R_1 C_2 2\pi f}\right]} - 1. \tag{408}$$

We can simplify this to

$$\epsilon_M = \frac{(2\pi f)^2 R_1 R_2 C_1 C_2}{\sqrt{\left[1+\left(\frac{f}{f_1}\right)^2\right]\left[1+\left(\frac{f}{f_2}\right)^2\right]}} - 1. \tag{409}$$

From the definitions of f_1 and f_2, this can be further simplified to

$$\begin{aligned}
\epsilon_M &= \frac{f^2}{f_1 f_2 \sqrt{\left[1+\left(\frac{f}{f_1}\right)^2\right]\left[1+\left(\frac{f}{f_2}\right)^2\right]}} - 1 \\
&= \frac{f^2}{\sqrt{\left[f_1^2+f^2\right]\left[f_2^2+f^2\right]}} - 1 \\
&= \frac{f^2}{f_p^2 - f^2} - 1 \\
&= -\frac{1}{1+\left(\frac{f}{f_p}\right)^2}.
\end{aligned} \tag{410}$$

The negative sign indicates that the magnitude of the integral will always be understated slightly by the circuit. This is a very similar expression to that for the error in the gain of the differentiator. However, the ratio in the denominator here is f/f_p, whereas it was f_p/f in the case of the differentiator. Table XL looks almost identical to Table XXXVIII, except for this difference. The degree to which the frequency f of interest is far away from the pole frequency f_p, expressed as a ratio, is the key to determining the accuracy of the output.

The absolute value of the phase error is exactly the same as for the differentiator, so Table XXXIX is correct for the integrator, too.

As with the differentiator, the equations and tables in this section permit one to design an integrator if one has a required error criterion in mind and can pick components to satisfy all equations, all restraints, and the limitations on gain-bandwidth

Table XL Error in the magnitude of the gain of the integrating circuit as a function of the ratio of signal frequency to pole frequency.

f/f_p	ϵ_M
1.00	−0.5000
5.00	−0.0.385
10.00	−0.0099
50.00	−0.0004
100.00	−0.0001

product imposed by the operational amplifier. An attractive feature of this circuit to perform integration is that the gain at zero frequency is zero. Offsetting this, however, is the fact that there is high gain at frequencies just above zero, and yet there is so much phase distortion in that vicinity that the output does not look anything like a derivative. Also, to get adequate gains in an integrator, one often has to use large impedance in the feedback path, which has the effect of magnifying the effect of the operational amplifier's offset currents. These produce voltage drops across the feedback impedances that may tend to spoil the advantage of low DC gain.

G. OBTAINING LARGE RESISTANCES WITH A TEE-NETWORK

Often one needs a larger resistance than is readily available in off-the-shelf components. This is especially true in constructing integrators. It is useful, therefore, to find a way to obtain large resistances from a number of smaller resistors. In Figure 71 we show a network which achieves this. We can understand the working of this circuit by supposing that we inject a current I_1 into it and calculate what the output voltage V_O must be. The effective resistance of the network is given by

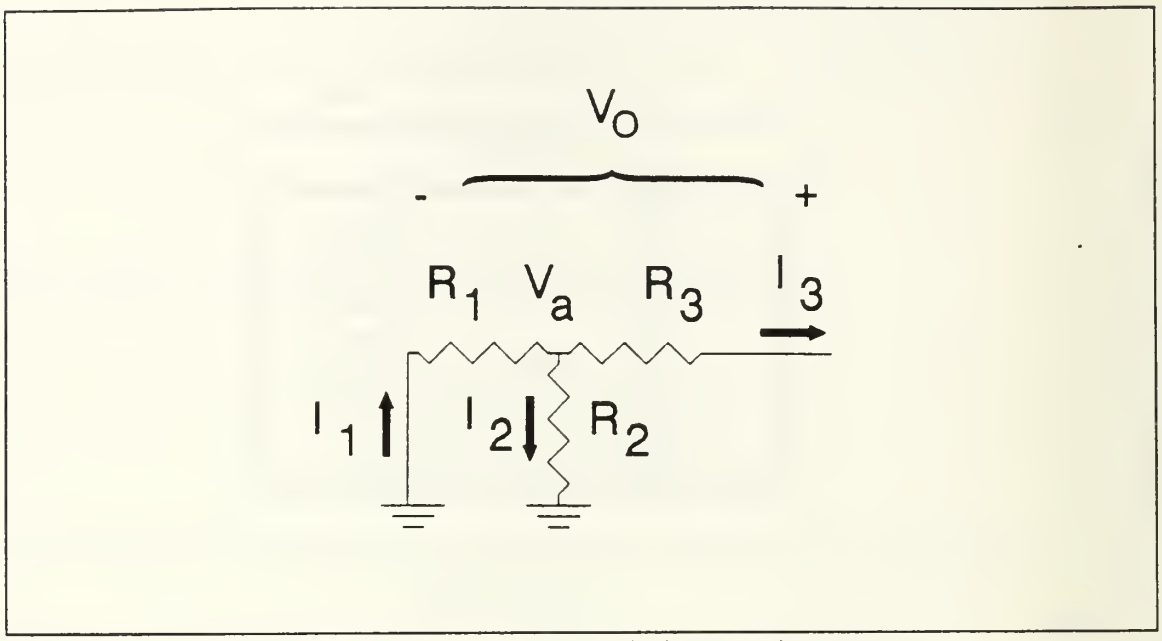

Figure 71 A Tee-network can be used to obtain large resistances.

$$R_{EFF} = \frac{V_O}{I_1}. \tag{411}$$

We shall assume that the current I_1 comes from a current source at zero volts. This is the case, for example, when the network receives its current from the virtual ground of an operational amplifier. The voltage at the junction of the Tee is given then by

$$V_a = -I_1 R_1. \tag{412}$$

Thus the current I_2 through resistor R_2 is given by

$$I_2 = \frac{V_a}{R_2} = -\frac{R_1}{R_2} I_1. \tag{413}$$

The remaining current I_3 through resistor R_3 is given by

$$I_3 = I_1 - I_2 = I_1 - \left(-\frac{R_1}{R_2} I_1\right) = \left(1 + \frac{R_1}{R_2}\right) I_1. \tag{414}$$

Knowing this, we can compute the output voltage

$$V_o = V_a - I_3 R_3 = (-I_1 R_1) - \left(1 + \frac{R_1}{R_2}\right) I_1 R_3$$

$$R_{EFF} = \frac{V_o}{I_1} = -\frac{R_1 R_2 + R_1 R_3 + R_2 R_3}{R_2}. \tag{415}$$

Now if we choose the resistances such that

$$R_1 R_2 \ll R_1 R_3 \quad \text{and} \quad R_2 R_3 \ll R_1 R_3 \tag{416}$$

then the first and third terms in the numerator can be neglected and we have the approximation

$$R_{EFF} \approx \frac{R_1 R_3}{R_2}. \tag{417}$$

We have dropped the minus sign, preferring to regard it as due to the inverting action of the amplifier in which this resistive network commonly is used. If we set $R_1 = R_3 = R$, then we get the particularly easily remembered approximation

$$R_{EFF} \approx \frac{R^2}{R_2}. \tag{418}$$

As an example, suppose we need a resistance of 3.5 GΩ. If we use a Tee-network with $R = 300$ kΩ and $R_2 = 25.5$ Ω, then the equivalent resistance is

$$R_{EFF} = \frac{R^2}{R_2} = \frac{(300\ \text{k}\Omega)^2}{25.5\ \Omega} = 3.5\ \text{G}\Omega. \tag{419}$$

In summary, a Tee-network can provide the equivalent of a single large resistor. At first glance, one might also suppose that the noise contributed by each resistor in the Tee could be added together (square root of the sum of squares) to get the total noise, and that there would be less noise from this combination than from a single larger resistor. This is wrong, however, because the noise from resistor $R_1 = R$ is multiplied approximately by the ratio R/R_2. This is a fairly large multiple if the conditions in

Equation (416) are met: certainly it is bigger than the multiple $\sqrt{2}$ which would apply (roughly) if this approach were valid.

APPENDIX B. THEORY OF OPTICAL FIBER COUPLERS

In this appendix we consider the results of applying Maxwell's equations to the operation of 2×2 and 3×3 optical fiber couplers. This material was presented in Snyder [Ref. 20] in a highly condensed form. In order to make it more comprehensible, we include many of the steps omitted in his paper. Some minor errors in Snyder's work are pointed out and corrected. Most of this chapter is highly mathematical and requires more than a passing familiarity with Maxwell's equations, calculus, and vector algebra. However, the key result is presented in the first section. This result is necessary to the analysis of the operation of 2×2 and 3×3 optical fiber couplers under specific conditions, which is in Chapter III.

A. KEY RESULT OF THE THEORY

$$\frac{da_k}{dz} + j\beta_k a_k = j\sum_{\substack{s \\ s\neq k}} a_s C_{ks}. \tag{420}$$

This differential equation gives the connection between the amplitude coefficients of the light in each of the n fibers in an optical fiber coupler where the fibers are laid parallel to each other. We consider only single-mode optical fiber. In Equation (420), β_k is the propagation constant of the light in fiber k. a_k is the amplitude of the light in fiber k. C_{ks} is the coupling coefficient between fibers k and s. The amplitude a_k actually is a function of the position z within the coupler, so $a_k(z)$ would be a more correct notation.

If we apply n initial conditions, then there is a solution to the n differential equations. Typically we shine a known amount of light into one or more of the inputs to an optical fiber coupler. This amounts to specifying the values of the $a_k(z)$ when

$z = 0$, and these specifics depend on how the coupler is to be used. We shall examine various possibilities in the next chapter.

B. MAXWELL'S EQUATIONS

Here are Maxwell's equations in point form, taken from Hayt [Ref. 1, pp. 358-359]

$$\nabla \times \mathbf{E} = -\frac{\partial \mathbf{B}}{\partial t} \tag{421}$$

$$\nabla \times \mathbf{H} = \mathbf{J} + \frac{\partial \mathbf{B}}{\partial t} \tag{422}$$

$$\nabla \cdot \mathbf{D} = \rho \tag{423}$$

$$\nabla \cdot \mathbf{B} = 0 \tag{424}$$

The following two auxiliary equations relate the electric flux density **D** to the electric field intensity **E** and the magnetic flux density **B** to the magnetic field intensity **H**.

$$\mathbf{D} = \epsilon \mathbf{E} \tag{425}$$

$$\mathbf{B} = \mu \mathbf{H} \tag{426}$$

We also need two further auxiliary equations for the current density **J**. There are two sources of current density. One is conduction current density, due to the motion of charges past a point with zero net electric charge density. This is given by

$$\mathbf{J} = \sigma \mathbf{E}. \tag{427}$$

The other source of current density is the motion of volume charge density at a velocity **v**. This is given by

$$\mathbf{J} = \rho\mathbf{v}. \tag{428}$$

In a glass fiber, we assume that the conductivity $\sigma = 0$ and that there is no net motion of the volume charge density. Therefore $\mathbf{J} = 0$ in Equation (422).

In general, the electric field intensity **E** and the magnetic field intensity **H** both are functions of time, so we would write them as $\mathbf{E}(t)$ and $\mathbf{H}(t)$. We now consider the restricted case in which the variation with time is sinusoidal. Since they both are vector quantities, we write their amplitudes in vector notation as simply **E** and **H**, separate from their dependence on time. These amplitudes may be functions of position and frequency, but not of time. $\mathbf{E}(t)$ and $\mathbf{H}(t)$ each may have some phase shift ψ_E and ψ_H, too, and these also may be functions of position and frequency, but not of time. So we have

$$\mathbf{E}(t) = \mathbf{E}\cos(\omega t + \psi_E) \tag{429}$$

and

$$\mathbf{H}(t) = \mathbf{H}\cos(\omega t + \psi_H). \tag{430}$$

These two formulas can also be written as

$$\mathbf{E}(t) = \mathrm{Re}\left[\mathbf{E}e^{j(\omega t + \psi_E)}\right] \tag{431}$$

and

$$\mathbf{H}(t) = \mathrm{Re}\left[\mathbf{H}e^{j(\omega t + \psi_H)}\right]. \tag{432}$$

To simplify the notation in what follows, we shall suppress the Re. This simplification leaves

$$\mathbf{E}(t) = \mathbf{E}e^{j(\omega t + \psi_E)} \tag{433}$$

and

$$\mathbf{H}(t) = \mathbf{H}e^{j(\omega t + \psi_H)}. \tag{434}$$

Some authors use a different convention in Equations (431) and (432). They use $-j\omega$ instead of $+j\omega$. This makes absolutely no difference in these two equations, since in taking the real part of the function in brackets, the part which depends on $\sin(\omega t + \psi)$ is the imaginary part, and it is discarded. It makes considerable difference in Equations (433) and (434), since we no longer discard anything in these formulations. It would appear that $-j\omega$ is used in Snyder's paper, although he does not explicitly so state. For if we substitute Equations (433) and (434) into Equations (421) and (422), then we obtain the following:

$$\begin{aligned} \nabla\times\mathbf{E}(t) &= -\frac{\partial\mathbf{B}}{\partial t} \\ &= -\mu\frac{\partial\mathbf{H}}{\partial t} \\ &= -j\omega\mu\mathbf{H}(t) \end{aligned} \tag{435}$$

and

$$\begin{aligned} \nabla\times\mathbf{H}(t) &= \mathbf{J} + \frac{\partial\mathbf{D}(t)}{\partial t} \\ &= 0 + \epsilon\frac{\partial\mathbf{E}(t)}{\partial t} \\ &= j\omega\epsilon\mathbf{E}(t). \end{aligned} \tag{436}$$

Snyder [Ref. 20, p. 1268] gives these equations with opposite signs, which is what one would get if the substitution of $-j\omega$ had been made for $+j\omega$.

C. APPLICATION OF MAXWELL'S EQUATIONS TO AN ARBITRARY MEDIUM

Snyder now introduces the notation $\tilde{\mathbf{E}}$ and $\tilde{\mathbf{H}}$ to refer to solutions to Maxwell's equations in a medium with permittivity $\tilde{\epsilon} = \tilde{\epsilon}(x,y,z)$. This permittivity is a function of

space. Snyder does not say so, but it also is generally a function of frequency. The material also has permeability μ. Non-magnetic materials have a value of μ which is nearly equal to μ_0, the permeability of free space, so Snyder tacitly treats the value of μ as known. Because the subject under consideration now is optical fiber, the z-axis is regarded as being along the axis of the fiber, which corresponds to the axis of propagation of light.

Snyder's goal is to find solutions for $\tilde{\mathbf{E}}$ and $\tilde{\mathbf{H}}$ in the material with permittivity $\tilde{\epsilon} = \tilde{\epsilon}(x,y,z)$ if solutions for E and H are known for a uniform lossless system with permittivity $\epsilon = \epsilon(x,y)$. This known permittivity is assumed to be independent of z. In other words, no matter where along a length of optical fiber you chance to look, you find the same permittivity.

To achieve this goal, Snyder defines a new quantity, F.

$$\mathbf{F} = \mathbf{E}\times\tilde{\mathbf{H}}^* + \tilde{\mathbf{E}}^*\times\mathbf{H}. \tag{437}$$

Hayt [Ref. 1, p 499] gives the following vector identity:

$$\nabla\cdot(\mathbf{A}\times\mathbf{B}) \equiv \mathbf{B}\cdot(\nabla\times\mathbf{A}) - \mathbf{A}\cdot(\nabla\times\mathbf{B}). \tag{438}$$

Another useful vector identity is that the divergence of the sum of two vectors is the sum of their divergences taken separately. In mathematical form, this says that

$$\nabla\cdot(\mathbf{A} + \mathbf{B}) \equiv \nabla\cdot\mathbf{A} + \nabla\cdot\mathbf{B}. \tag{439}$$

Snyder uses these two facts to obtain the divergence of Equation (437).

$$\begin{aligned}\nabla\cdot\mathbf{F} &= \nabla\cdot(\mathbf{E}\times\tilde{\mathbf{H}}^*) + \nabla\cdot(\tilde{\mathbf{E}}^*\times\mathbf{H}) \\ &= \tilde{\mathbf{H}}^*\cdot(\nabla\times\mathbf{E}) - \mathbf{E}\cdot(\nabla\times\tilde{\mathbf{H}}^*) \\ &\quad + \mathbf{H}\cdot(\nabla\times\tilde{\mathbf{E}}^*) - \tilde{\mathbf{E}}^*\cdot(\nabla\times\mathbf{H}).\end{aligned} \tag{440}$$

It is easy to show that the curl of the complex conjugate is equal to the complex conjugate of the curl, or

$$\nabla\times\mathbf{A}^* \equiv (\nabla\times\mathbf{A})^*. \tag{441}$$

Applying this fact to Equation (440), we get

$$\begin{aligned}\nabla\cdot\mathbf{F} = {} & \tilde{\mathbf{H}}^*\cdot(\nabla\times\mathbf{E}) - \mathbf{E}\cdot(\nabla\times\tilde{\mathbf{H}})^* \\ & + \mathbf{H}\cdot(\nabla\times\tilde{\mathbf{E}})^* - \tilde{\mathbf{E}}^*\cdot(\nabla\times\mathbf{H}).\end{aligned} \tag{442}$$

We can replace the factors $\nabla\times\mathbf{E}$ and $\nabla\times\mathbf{H}$ in Equation (442) by the equivalents easily obtain from Equations (435) and (436), where the presence of tildes (~) continues to signify quantities having to do with the unknown medium. This yields

$$\begin{aligned}\nabla\cdot\mathbf{F} = {} & \tilde{\mathbf{H}}^*\cdot(-j\omega\mu\mathbf{H}) - \mathbf{E}\cdot(j\omega\tilde{\epsilon}\tilde{\mathbf{E}})^* \\ & + \mathbf{H}\cdot(-j\omega\mu\tilde{\mathbf{H}})^* - \tilde{\mathbf{E}}^*\cdot(j\omega\epsilon\mathbf{E}).\end{aligned} \tag{443}$$

The constant factors can be removed from within the brackets because, for any constant k,

$$\mathbf{A}\cdot(k\ \mathbf{B}) \equiv k\mathbf{A}\cdot\mathbf{B}. \tag{444}$$

So

$$\begin{aligned}\nabla\cdot\mathbf{F} = {} & -j\omega\mu\tilde{\mathbf{H}}^*\cdot\mathbf{H} + j\omega\tilde{\epsilon}^*\mathbf{E}\cdot\tilde{\mathbf{E}}^* \\ & - j\omega\mu\mathbf{H}\cdot\tilde{\mathbf{H}}^* - j\omega\epsilon\tilde{\mathbf{E}}^*\cdot\mathbf{E}.\end{aligned} \tag{445}$$

The first and third terms in this expression are equal but of opposite signs, so they vanish. Gathering common factors, we are left with

$$\nabla\cdot\mathbf{F} = j\omega[\tilde{\epsilon}^* - \epsilon]\mathbf{E}\cdot\tilde{\mathbf{E}}^*. \tag{446}$$

This is Equation (2) in Snyder [Ref. 20, p. 1268], but with opposite sign, for the reasons we discussed above.

Next Snyder presents a formidable-looking identity without proof. Here is its derivation. The divergence theorem is

$$\int_V \nabla\cdot\mathbf{F}dV = \oint_S \mathbf{F}\cdot dS. \tag{447}$$

If we consider the volume V to be a infinitesimally thin slab of area A and thickness dz, then the slab has a differential volume element $dV = dA\ dz$. This allows us to decompose the left hand integral into two parts: a surface integral over the area of the slab, and an ordinary integral over its thickness.

The right hand integral in Equation (447) also can be decomposed into two parts. One is a surface integral of the projection of **F** onto the unit vector $\hat{z}$, perpendicular to the surface A. This surface has a differential element of area dA. The other part is a surface integral of the projection of **F** onto the unit vector $\hat{n}$, perpendicular to the rim of the slab. The circumference of this slab has a differential element of length dL, and, so, the rim as a whole has a differential element of area $dL\ dz$. The result is

$$\int_z \int_A \nabla\cdot\mathbf{F}\, dA\, dz = \int_A \mathbf{F}\cdot\hat{z}\, dA + \int_{A_{RIM}} \mathbf{F}\cdot\hat{n}\, dL\, dz. \tag{448}$$

The integral over the closed surface S is replaced here by two integrations over open surfaces. We can differentiate both sides of this equation by z. The left-hand side of the equation becomes a mere surface integral. The second term on the right-hand side is converted to a line integral along the closed contour L_A, which follows the rim of the slab. This gives us

$$\int_A \nabla\cdot\mathbf{F}\, dA = \frac{\partial}{\partial z}\int_A \mathbf{F}\cdot\hat{z}\, dA + \oint_{L_A} \mathbf{F}\cdot\hat{n}\, dL. \tag{449}$$

This is Equation (4) in Snyder. [Ref. 20, p. 1269] After some further development, which we provide here in detail, Snyder applies this identity.

If the electrical permittivity characterizing a uniform, lossless material is ϵ, then electromagnetic fields are supported in various modes with modal propagation constants β_p. These fields are of the form

$$\mathbf{E}_p(x,y,z) = \mathbf{e}_p(x,y)e^{j\beta_p z} \tag{450}$$

and

$$\mathbf{H}_p(x,y,z) = \mathbf{h}_p(x,y)e^{j\beta_p z}. \tag{451}$$

In these equations, $\mathbf{e}_p$ and $\mathbf{h}_p$ are vector functions found by solving the transverse wave equation, and they are independent of z. Also, different modes are mutually orthogonal. That is,

$$\begin{aligned} \int_{A_\infty} \hat{z}\cdot\left(\mathbf{e}_p\times\mathbf{h}_q^*\right) dA &= \pm\delta_{pq} \\ &= \begin{cases} \pm 1 \text{ if } p=q \\ 0 \text{ otherwise.} \end{cases} \end{aligned} \tag{452}$$

In this expression, A_∞ represents integration over an infinitely extensive cross-section, and δ_{pq} is the Kronecker delta function, whose definition is included in the equation. When p or q is positive, then the mode is one which propagates in the positive z direction. Conversely, when p or q is negative, then the mode is one which propagates in the negative z direction. The cross product of $\mathbf{e}_p$ and $\mathbf{h}_p$ is the Poynting vector $\mathbf{P} = \mathbf{e}_p\times\mathbf{h}_p$, and by a homophonous coincidence, it gives the direction of power flow across the cross-sectional area. So by convention, we regard $\mathbf{e}_p$ as unaffected by a change in sign of p. In contrast, $\mathbf{h}_p$ and β_p both change sign when p does. That is,

$$\mathbf{e}_{-p} = \mathbf{e}_p, \tag{453}$$

$$\mathbf{h}_{-p} = -\mathbf{h}_p, \tag{454}$$

and

$$\beta_{-p} = -\beta_p. \tag{455}$$

(If $\mathbf{e}_p$ also changed sign, then the Poynting vector would not, and so would incorrectly describe the flow of power in the negative direction along the optical fiber.)

Since $\mathbf{e}_p$ and $\mathbf{h}_p$ both are known solutions to Maxwell's equations, it is reasonable to substitute them for $\mathbf{E}$ and $\mathbf{H}$ respectively in Equation (437). If we do this, then we get

$$\begin{aligned} \mathbf{F} &= \mathbf{E}\times\tilde{\mathbf{H}}^* + \tilde{\mathbf{E}}^*\times\mathbf{H} \\ &= \left(\mathbf{e}_p e^{j\beta_p z}\right)\times\tilde{\mathbf{H}}^* + \tilde{\mathbf{E}}^*\times\left(\mathbf{h}_p e^{j\beta_p z}\right) \\ &= e^{j\beta_p z}\left(\mathbf{e}_p\times\tilde{\mathbf{H}}^* + \tilde{\mathbf{E}}^*\times\mathbf{h}_p\right). \end{aligned} \tag{456}$$

Now if we define

$$\mathbf{F} = \mathbf{F}_p e^{j\beta_p z}, \tag{457}$$

then we can divide both sides of Equation (456) by $e^{j\beta_p z}$ and so get

$$\mathbf{F}_p = \mathbf{e}_p\times\tilde{\mathbf{H}}^* + \tilde{\mathbf{E}}^*\times\mathbf{h}_p. \tag{458}$$

If we substitute Equation (450) into Equation (446), then

$$\nabla\cdot\mathbf{F} = j\omega(\tilde{\epsilon}^* - \epsilon)\mathbf{e}_p e^{j\beta_p z}\cdot\tilde{\mathbf{E}}^*. \tag{459}$$

Now we can take the integral of this expression over the cross-sectional area A and apply the identity in Equation (449).

$$\int_A j\omega(\tilde{\epsilon}^* - \epsilon)\mathbf{e}_p e^{j\beta_p z}\cdot\tilde{\mathbf{E}}^* dA$$

$$= \frac{\partial}{\partial z}\int_A e^{j\beta_p z}\mathbf{F}_p\cdot\hat{z}\,dA + \oint_{L_A} e^{j\beta_p z}\mathbf{F}_p\cdot\hat{n}\,dL \qquad (460)$$

$$= e^{j\beta_p z}\left(j\beta_p + \frac{\partial}{\partial z}\right)\int_A \mathbf{F}_p\cdot\hat{z}\,dA + e^{j\beta_p z}\oint_{L_A}\mathbf{F}_p\cdot\hat{n}\,dL.$$

We can divide through on both sides of this equation by $e^{j\beta_p z}$ and rearrange terms to get

$$\left(j\beta_p + \frac{\partial}{\partial z}\right)\int_A \mathbf{F}_p\cdot\hat{z}\,dA \qquad (461)$$

$$= j\omega\int_A(\epsilon - \tilde{\epsilon}^*)\mathbf{e}_p\cdot\tilde{\mathbf{E}}^* dA - \oint_{L_A}\mathbf{F}_p\cdot\hat{n}\,dL.$$

This is essentially the same as Equation (9) in Snyder [Ref. 20, p. 1269]. However, the difference in convention over the sign of $j\omega$ mentioned previously shows up here, too: the first term in the right hand side is the negative of that given by Snyder.

D. FINDING THE TRANSVERSE FIELDS IN AN ARBITRARY MEDIUM

Snyder next goes on to consider how to represent the transverse fields of the unknown system with permittivity $\tilde{\epsilon}^*$, since the transverse fields of the lossless cylindrical uniform system with permittivity ϵ are known. The fields within a uniform optical fiber are very well described by these solutions.

The transverse fields of the known (lossless, cylindrical, uniform) system form a complete set of orthogonal functions, so the transverse fields of the unknown system can be expressed as a linear combination of these. Hence

$$\tilde{\mathbf{E}}_t^* = \sum_q a_q(z)\mathbf{e}_{qt}^*(x,y) \qquad (462)$$

and

$$\tilde{\mathbf{H}}_t^* = \sum_q a_q(z)\mathbf{h}_{qt}^*(x,y). \tag{463}$$

The subscript t is meant to indicate the transverse field quantities. The coefficients a_q in these two equations are identical.

Snyder next substitutes these two equations into the left side of Equation (461) and integrates over the infinite cross-section A_∞. This yields

$$\begin{aligned}
&\left(\frac{\partial}{\partial z} + j\beta_p\right)\int_{A_\infty} \mathbf{F}_p \cdot \hat{z}\, dA \\
&= \left(\frac{\partial}{\partial z} + j\beta_p\right)\int_{A_\infty} \left(\mathbf{e}_p \times \tilde{\mathbf{H}}^* + \tilde{\mathbf{E}}^* \times \mathbf{h}_p\right)\cdot \hat{z}\, dA \\
&= \left(\frac{\partial}{\partial z} + j\beta_p\right)\int_{A_\infty} \left(\mathbf{e}_p \times \sum_q a_q(z)\mathbf{h}_{qt}^* + \sum_q a_q(z)\mathbf{e}_{qt}^* \times \mathbf{h}_p\right)\cdot \hat{z}\, dA.
\end{aligned} \tag{464}$$

Now we can take the summations and the factor $a_q(z)$ outside the integral, since the integral is only over the cross-section in the $x-y$ plane. Thus

$$\begin{aligned}
&\left(\frac{\partial}{\partial z} + j\beta_p\right)\int_{A_\infty} \mathbf{F}_p \cdot \hat{z}\, dA \\
&= \left(\frac{\partial}{\partial z} + j\beta_p\right)\sum_q a_q(z)\left\{\int_{A_\infty} \hat{z}\cdot\left(\mathbf{e}_p \times \mathbf{h}_{qt}^*\right) dA + \int_{A_\infty} \hat{z}\cdot\left(\mathbf{e}_{qt}^* \times \mathbf{h}_p\right) dA\right\}.
\end{aligned} \tag{465}$$

In this form, it is easy to see that we can apply the orthogonality condition expressed in Equation (452). If we do so, we get the much simplified result

$$\left(\frac{\partial}{\partial z} + j\beta_p\right)\int_{A_\infty} \mathbf{F}_p \cdot \hat{z}\, dA = \left(\frac{\partial}{\partial z} + j\beta_p\right)\left[2a_p(z)\right]. \tag{466}$$

This takes care of the left side of Equation (461). As for the right-hand side, the line integral evaluated at an infinite radius is zero. Dividing both sides by 2, we obtain

$$\frac{da_p(z)}{dz} + j\beta_p a_p(z) = \pm\frac{j\omega}{2}\int_{A_\infty} (\epsilon - \tilde{\epsilon}^*)\mathbf{e}_p \cdot \tilde{\mathbf{E}}^*\, dA. \tag{467}$$

The positive sign in the right hand side takes effect if $p > 0$ and the negative sign takes effect if $p < 0$. This equation is essentially the same as Equation (11) in Snyder [Ref. 20, p. 1269]. As usual, though, there is a difference in sign in the right-hand side.

To obtain a solution to the series expressions of Equations (462) and (463) requires finding the coefficients $a_q(z)$. These can be obtained by solving the differential Equation (467) when the perturbing field $\tilde{\mathbf{E}}^s$ in the unknown medium is specified.

E. Z-COMPONENT OF THE FIELD IN AN ARBITRARY MEDIUM

We have confined our attention so far to the transverse fields of the unknown system. It is time to include the component along the z-axis, too. We can represent the complete field as a linear combination of components in the transverse plane and along the z-axis:

$$\tilde{\mathbf{E}}^s = \tilde{\mathbf{E}}_t^s + \tilde{\mathbf{E}}_z^s \tag{468}$$

and

$$\tilde{\mathbf{H}}^s = \tilde{\mathbf{H}}_t^s + \tilde{\mathbf{H}}_z^s. \tag{469}$$

We already have the expansions for the first term, the transverse term, in each of these equations from Equations (462) and (463). We need to find the second term in each of Equations (468) and (469). We can get the z-component of $\tilde{\mathbf{E}}^s$ by projecting it onto a unit vector $\hat{z}$ in the z-direction. But we can relate $\tilde{\mathbf{E}}^s$ to $\tilde{\mathbf{H}}^s$ by the use of Equation (436). The z-component of the curl of a vector $\mathbf{A}$ is given by

$$
\begin{aligned}
[\nabla\times\mathbf{A}]_z &= [\nabla\times\mathbf{A}]\cdot\hat{z} \\
&= \frac{\partial A_y}{\partial x} - \frac{\partial A_x}{\partial y}.
\end{aligned}
\tag{470}
$$

We define the transverse divergence by

$$
\nabla_t\cdot\mathbf{A} = \frac{\partial A_x}{\partial x} + \frac{\partial A_y}{\partial y}. \tag{471}
$$

If we take the transverse divergence of the cross-product of the unit vector in the z-direction and the transverse component of $\mathbf{A}$, we get

$$
\begin{aligned}
\nabla_t\cdot(\hat{z}\times\mathbf{A}_t) &= \nabla_t\cdot(-A_y\hat{x} + A_x\hat{y}) \\
&= -\frac{\partial A_y}{\partial x} + \frac{\partial A_x}{\partial y} \\
&= -\hat{z}\cdot(\nabla\times\mathbf{A}) \\
&= -(\nabla\times\mathbf{A})_z.
\end{aligned}
\tag{472}
$$

Combining Equations (436) and (472) gives

$$
\begin{aligned}
\tilde{\mathbf{E}}_z^* &= \frac{(\nabla\times\tilde{\mathbf{H}}^*)_z}{-j\omega\tilde{\epsilon}^*} \\
&= \frac{\nabla_t\cdot(\hat{z}\times\tilde{\mathbf{H}}_t^*)}{j\omega\tilde{\epsilon}^*}.
\end{aligned}
\tag{473}
$$

This expresses the z-component of the electric field in the unknown medium in terms of the transverse component of the known magnetic field. We can substitute Equation (463) into Equation (473) to get

$$\tilde{\mathbf{E}}_z^* = \frac{\left[\nabla_t \cdot \left(\hat{z} \times \sum_q a_q(z)\mathbf{h}_{qt}\right)\right]^*}{j\omega\tilde{\epsilon}^*}. \tag{474}$$

We can expand this equation by applying Equation (438) to it.

$$\tilde{\mathbf{E}}_z^* = \frac{\left[\left(\sum_q a_q(z)\mathbf{h}_{qt}\right)\cdot(\nabla_t \times \hat{z}) - \hat{z}\cdot\left(\nabla_t \times \sum_q a_q(z)\mathbf{h}_{qt}\right)\right]^*}{j\omega\tilde{\epsilon}^*}. \tag{475}$$

The first term in the numerator is zero, for the unit vector is a constant and has no curl of any kind, let alone a transverse curl. In the second term in the numerator, we can bring the transverse curl operation inside the sum and right past the coefficient $a_q(z)$, since a function of z is a constant with respect to taking the transverse curl. Thus we have

$$\tilde{\mathbf{E}}_z^* = -\frac{\left[\hat{z}\cdot\sum_q a_q(z)(\nabla_t \times \mathbf{h}_{qt})\right]^*}{j\omega\tilde{\epsilon}^*}. \tag{476}$$

The transverse curl is parallel to $\hat{z}$, so the dot product of $\hat{z}$ with it is a nonzero scalar. By applying Equation (436) to this expression, we get

$$\tilde{\mathbf{E}}_z^* = -\frac{\left[\sum_q a_q(z) j\omega\epsilon \mathbf{e}_{qz}\right]^*}{j\omega\tilde{\epsilon}^*}. \tag{477}$$

Note that the transverse curl operation extracted only the z-component of $\mathbf{e}_q$. Dividing this out yields

$$\tilde{\mathbf{E}}_z^* = +\frac{\epsilon}{\tilde{\epsilon}^*}\sum_q a_q(z)\mathbf{e}_{qz}^* \tag{478}$$

since, for a lossless system,

$$\epsilon^* = \epsilon. \tag{479}$$

This is different from Equation (12a) in Snyder [Ref. 20, p. 1270]. Although the difference in sign we have consistently mentioned has mysteriously evaporated, Snyder's version of this equation has the permittivities inverted, *i.e.*, his version of the equation is

$$\tilde{\mathbf{E}}^* = +\frac{\tilde{\epsilon}^*}{\epsilon}\sum_q a_q(z)\mathbf{e}_{qz}^*. \tag{480}$$

This is, presumably, a typographical error.

F. COMPLETE FIELD IN AN ARBITRARY MEDIUM

We can now substitute Equation (478) into Equation (468).

$$\begin{aligned}\tilde{\mathbf{E}}^* &= \tilde{\mathbf{E}}_t^* + \tilde{\mathbf{E}}_z^* \\ &= \sum_q a_q(z)\mathbf{e}_{qt}^* - \frac{\epsilon}{\tilde{\epsilon}^*}\sum_q a_q(z)\mathbf{e}_{qz}^* \\ &= \sum_q a_q(z)\left[\mathbf{e}_{qt}^* + \frac{\epsilon}{\tilde{\epsilon}^*}\mathbf{e}_{qz}^*\right].\end{aligned} \tag{481}$$

The corresponding expression for $\tilde{\mathbf{H}}^*$ is almost identical, but because the magnetic permeabilities in glass and in free space are nearly equal, the leading ratio of permeabilities is one, and so can be suppressed.

$$\begin{aligned}\tilde{\mathbf{H}}^* &= \tilde{\mathbf{H}}_t^* + \tilde{\mathbf{H}}_z^* \\ &= \sum_q a_q(z)\mathbf{h}_{qt}^* + \sum_q a_q(z)\mathbf{h}_{qz}^* \\ &= \sum_q a_q(z)\left[\mathbf{h}_{qt}^* + \mathbf{h}_{qz}^*\right] \\ &= \sum_q a_q(z)\mathbf{h}_q^*.\end{aligned} \tag{482}$$

This expression is identical to Equation (12b) in Snyder [Ref. 20, p. 1270].

We now can substitute Equation (481) into the right side of Equation (467).

$$\begin{aligned}\frac{da_p(z)}{dz} + j\beta_p a_p(z) &= \pm\frac{j\omega}{2}\int_{A_\infty}(\epsilon-\tilde{\epsilon}^*)\mathbf{e}_p\cdot\tilde{\mathbf{E}}^*dA \\ &= \pm\frac{j\omega}{2}\int_{A_\infty}(\epsilon-\tilde{\epsilon}^*)\mathbf{e}_p\cdot\sum_q a_q(z)\left[\mathbf{e}_{qt}^* + \frac{\epsilon}{\tilde{\epsilon}^*}\mathbf{e}_{qz}\right]dA \\ &= j\sum_q a_q(z)\left[\pm\frac{\omega}{2}\int_{A_\infty}(\epsilon-\tilde{\epsilon}^*)\left(\mathbf{e}_{pt}\cdot\mathbf{e}_{qt}^* + \frac{\epsilon}{\tilde{\epsilon}^*}\mathbf{e}_{pz}\cdot\mathbf{e}_{qz}^*\right)dA\right].\end{aligned} \tag{483}$$

Again, this differs from Snyder's formulation in sign, and now, too, by the inversion of the ratio of permittivities, which we discussed earlier. We now adopt the usual expedient in dealing with a troublesomely complex equation: we define a new symbol for most of it! In keeping with Snyder's notation, we shall call everything within the square brackets C_{pq}, the coupling coefficient. The resultant differential equation is

$$\frac{da_p(z)}{dz} + j\beta_p a_p(z) = j\sum_q a_q(z)C_{pq}. \tag{484}$$

This is identical to Equation (13) in Snyder [Ref. 20, p. 1270], but of course, our definition of C_{pq} differs as already discussed. This differential equation is applicable when the optical fiber is either irregular or only slightly lossy, that is, when the perturbation to the electric fields is slight.

G. SOLUTION IN PARALLEL UNIFORM OPTICAL FIBERS

In an optical fiber coupler, we no longer have just one fiber to consider. Several nearly identical fibers are laid alongside one another and fused together. For n fibers, the modal expansion method will lead to n equations like Equation (484). Because of the similarity of the fibers and the orthogonality of the modes expressed in Equation (452), the pth mode of fiber k can only couple with the pth mode of fiber s. The coupling between fiber k and fiber s is then given by the following set of differential equations. We continue to use subscripts to denote the modes of the waves, but introduce superscripts in parentheses to denote the fiber under consideration.

$$\frac{da_p^{(k)}}{dz} + j\beta_p^{(k)} a_p^{(k)} = j\sum_{\substack{s \\ s \neq k}} a_p^{(s)} C_{pp}^{(k)(s)}. \tag{485}$$

This is identical to Equation (18) in Snyder [Ref. 20, p. 1271], except we use j for $\sqrt{-1}$, where Snyder uses i; and we use k in place of Snyder's index j. The coupling coefficient is

$$C_{pp}^{(k)(s)} = \frac{\omega}{2}\int_{A^{(s)}} (\epsilon^{(s)} - \epsilon)\mathbf{e}_p^{(j)} \cdot \mathbf{e}_p^{(s)*} dA. \tag{486}$$

The difference in permittivities that appears in this expression is that between the permittivity in fiber j and that of the surrounding medium, namely the cladding of the fiber. Because coupling is limited to the same modes p, there is no strict necessity to retain the subscripts p. (If we restrict our attention to single-mode optical fiber, which is the case under consideration, then there are no other modes anyway.) The superscripts can be moved down and become subscripts, and the result of this notational shift is

$$\frac{da_j}{dz} + j\beta_j a_j = j\sum_{\substack{s \\ s \neq k}} a_s C_{js}. \tag{487}$$

This is the key result of Snyder's work, and it is used in Chapter III for the analysis of 2×2 and 3×3 optical fiber couplers in optical fiber interferometers.

APPENDIX C. AN ANALOG INTERFEROMETRIC SIMULATOR

In this appendix, we describe an analog electronic simulator which can be used to generate a facsimile of one of the outputs of an optical fiber interferometric sensor. The idea for this simulator came from Tveten *et al.* [Ref. 21]. The implementation in this appendix is based very closely on one designed by Litton Industries. A block diagram for the simulator is shown in Figure 72. A schematic diagram for the simulator is shown in Figure 73.

A. CIRCUIT DESCRIPTION

The heart of the circuit is integrated circuit U2, which is an Analog Devices AD639 Universal Trigonometric Function Converter. It is configured in the simulator to furnish the sine of its input. An input of 1 V is treated as the equivalent of a 50° angle. To put this another way, the input scale factor of the AD639 is 50°/V = 0.873 rad/V. It is somewhat more convenient in interferometric work that the simulator have a scale factor which is an integral number of radians per volt, and 1 rad/V is the number which was chosen by Litton's designer. To obtain this scale factor we must multiply the inputs by gain 1/0.873 = 1.15.

An approximation to this necessary gain is provided by operational amplifier U1B to the main inputs to the simulator, marked SENSOR 1 and SENSOR 2. The choice of resistors R_8, R_9, and R_{10} shown in the schematic drawing actually provides a gain of 5.6 kΩ/5.1 kΩ = 1.10, a little less than the level needed. With these values, we can predict that the scale factor will be

$$\left(\frac{5.6\ \text{k}\Omega}{5.1\ \text{k}\Omega}\right)\left(\frac{50^\circ}{\text{V}}\right)\left(\frac{\pi\ \text{rad}}{180^\circ}\right) = 958\ \frac{\text{mrad}}{\text{V}}. \qquad (488)$$

The simulators we used averaged 918 mrad/V. The measurements on which we based this conclusion will be given later in this appendix.

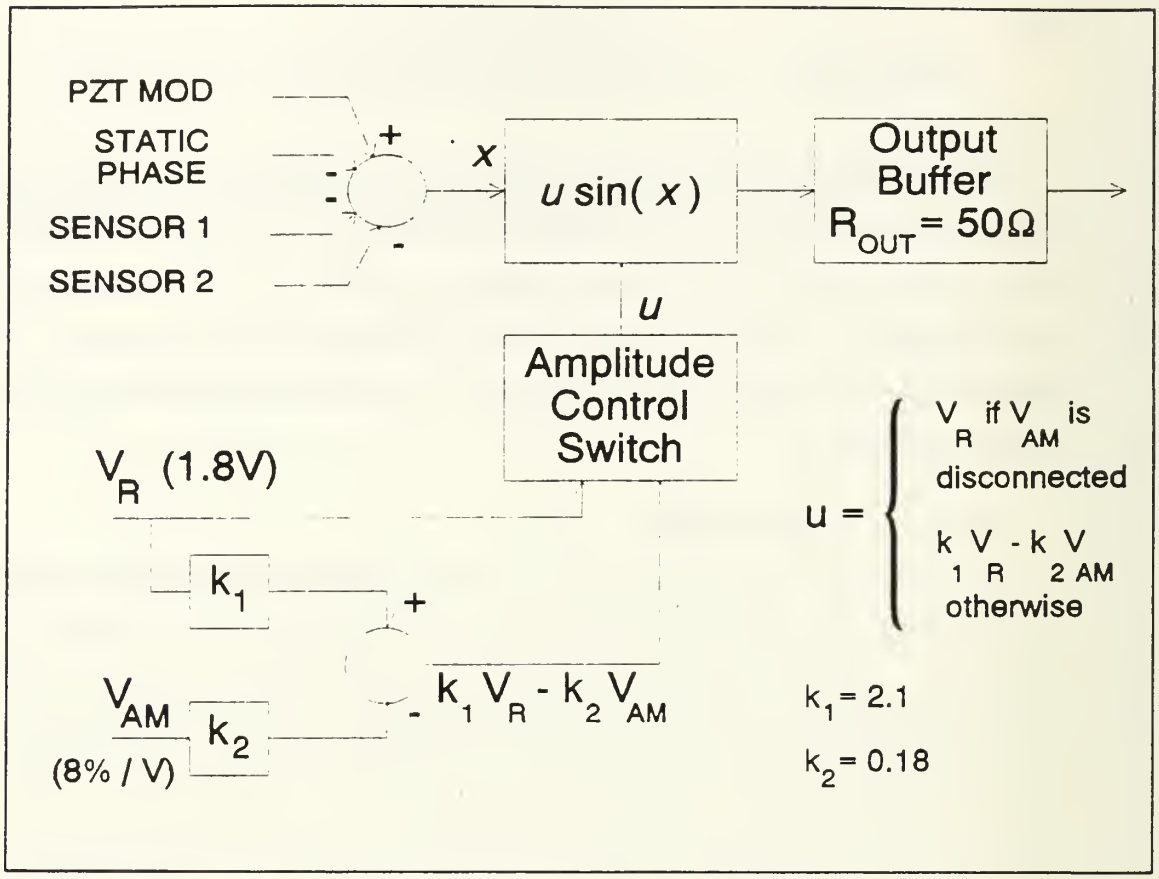

Figure 72 Block diagram of the Analog Interferometric Simulator.

Typically, one generates a test signal by applying a sine wave to one of the two sensor inputs and leaves the other one unconnected. If both inputs are used, their effects are additive, for applying a voltage to either input generates a current through either R_3 or R_9 and these currents are added at the virtual ground of operational amplifier U1B.

A third current input also is added in at this node. It is a "static phase" contribution dictated by the setting of potentiometer R16. The name was chosen by analogy with the static phase contribution in a real optical fiber interferometric sensor, which is caused by variations in temperature, pressure, and other factors. The difference is that the static phase in a real interferometer tends to drift with time, but the setting of the potentiometer in the simulator is generally set at a desired position and left there. The size of the resistors R_4 and R_5 was 1.5 kΩ in the Litton design; we reduced them to 250 Ω in order to increase the range over which the static phase might be varied. This

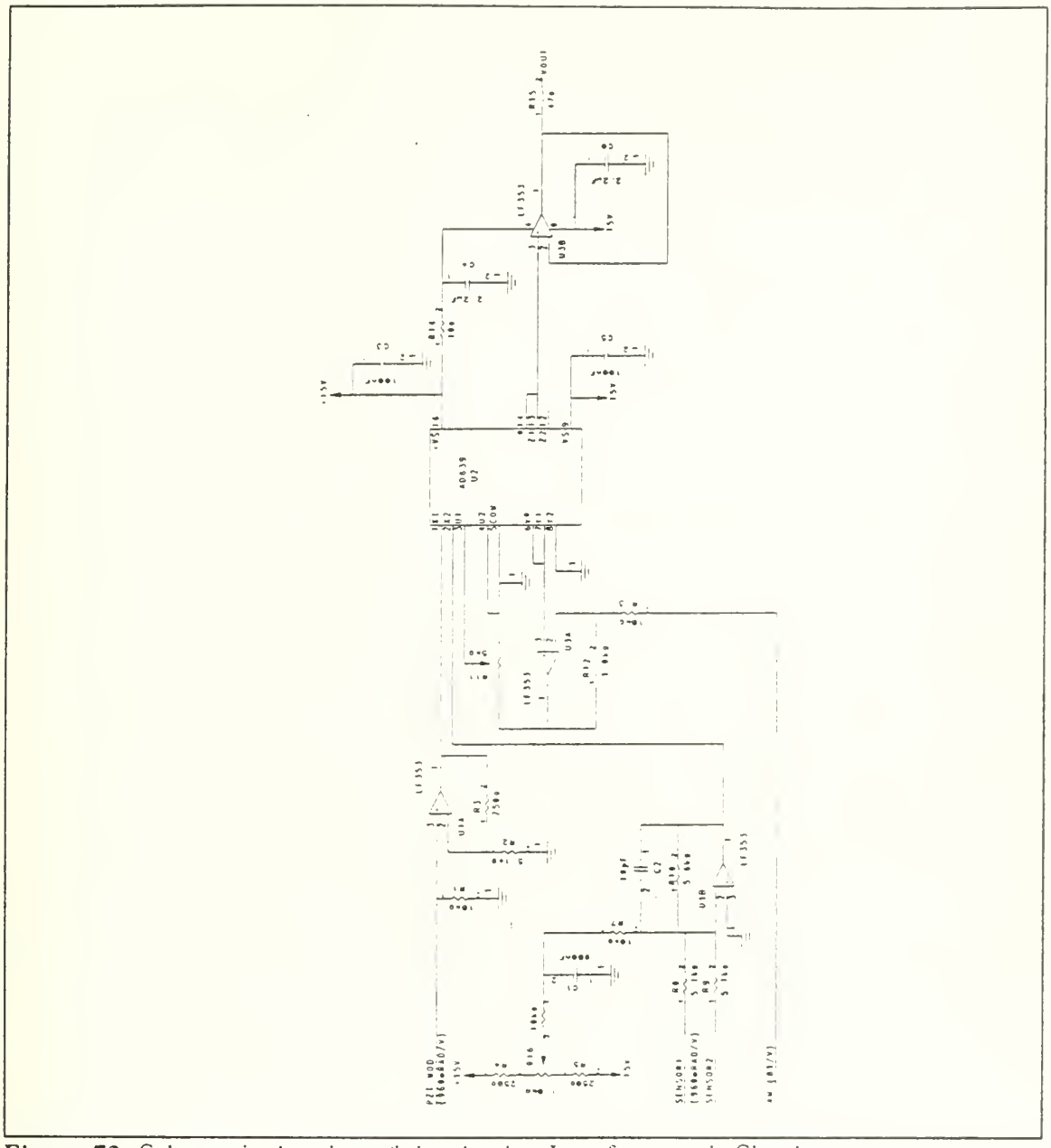

Figure 73 Schematic drawing of the Analog Interferometric Simulator.

static voltage can range between −10 V and +10 V with these smaller resistors. The DC gain of the summing amplifier for this input is 5.6 kΩ/(10 kΩ + 10 kΩ) = 0.28. Thus the output from the summing amplifier can vary between −2.8 V and +2.8 V due to changes in the setting of the static phase potentiometer. These extremes correspond to ±(2.8 V)(50°/V) = ±140° = ±2.44 rad adjustment in the static phase. This level of

variability is sufficient to permit three simulators to provide three facsimiles of an interferometric output, each one separated by 120° in phase from the next. With 1.5 kΩ resistors for R_1 and R_5, the voltage from the potentiometer is limited to ±3.75 V, which leads to ±1.05 V from the amplifier U1B, or ±52.5°, which is sufficient to provide two interferometric outputs 90° from each other, but not three outputs 120° from each other.

The other signal input to the simulator is the one marked PZT MOD on the schematic. This input is applied to operational amplifier U1A, which is configured to provide a non-inverting gain of (1+ (750 Ω/1.5 kΩ))=1.15. This, of course, is the gain we computed above to convert 1 V to the equivalent of a 1 rad input to the AD639. This signal is then provided to pin 1 of the AD639.

The AD639 actually computes the function

$$W = U\frac{\sin(X_1 - X_2)}{\sin(Y_1 - Y_2)} \tag{489}$$

when Z_1 (pin 13) and W (pin 14) are connected together, with Z_2 (pin 12) left grounded. Because Y_1 (pin 7) is connected to V_R (pin 6) at 1.8 V and Y_2 (pin 8) is grounded, the denominator in Equation (489) is 1. Input U_1 (pin 3) receives a variable voltage depending on the setting of potentiometer R_{11}, and input U_2 is grounded, so this potentiometer functions as an amplitude control for the interferometric simulation. If the final input to the simulator, the one marked AM, is left open, then operational amplifier U3A operates as a buffer of gain one, so the maximum voltage on the potentiometer R_{11} then is fixed and equal to the 1.8 V supplied by V_R (pin 6).

If the AM input is not left open, then U3A no longer functions as a unity-gain buffer. Instead, it operates on the reference voltage V_R (pin 6) with gain $1+R_{12}/R_{13}$ = 1.18 and it operates on the AM input with gain $-R_{12}/R_{13}$ = −0.18. Thus, with the AM input in use, the signal applied to potentiometer R_{11} is

$$1.18V_R - 0.18V_{AM} = 2.12 - 0.18V_{AM}. \tag{490}$$

We can interpret this to mean that a 1 V change in V_{AM} induces a $-0.18/2.12 = -8.5\%$ change in the voltage applied to resistor R_{11}, which, recall, is the maximum voltage delivered by the AD639.

The output of the AD639 is buffered by operational amplifier U3B, whose purpose is to provide current drive capability to the simulator. A 47 Ω resistor R_{15} provides roughly a 50 Ω output impedance to the circuit, to make it compatible with standard instrumentation interfaces.

B. MEASUREMENT OF THE SCALE FACTOR

The easiest way to measure the phase shift in an interferometric output is to apply two of them to the X and Y inputs of an oscilloscope. The resultant waveform is an elliptical Lissajous figure whose aspect ratio is determined by the phase shift between the two outputs. For 120° phase shift, the major axis is inclined along the 135°/−45° axis.

When more than $\pm\pi$ rad of phase shift is present, the ellipse is closed because $\sin(x)$ retraces itself if x spans at least 2π rad. The ellipse is open with less phase shift than this present. By noting how many volts we must apply to the inputs of the simulators to achieve an integral number of closures of the ellipse, we can easily obtain the scale factor of the simulator.

If we average the three slopes shown in the table, we find that the average scale factor is 918±4 mrad/V, which is the value we use in the rest of this dissertation when inferring the phase shift generated by the Analog Interferometric Simulators for a given input voltage.

The simulators proved very helpful to us before we had a real interferometer available. Generally speaking, if one's interest is confined to demodulators, the simulators are a satisfactory substitute for an interferometric source of signals only if phase shifts below around ±2 rad are required. The AD639 cannot generate phase shifts beyond this level. For measuring demodulator noise, however, where signals of small amplitude are desired anyway, the simulators are very helpful, particularly since, by

Table XLI Measurements to determine the scale factor of the three Analog Interferometric Simulators we used.

Simulator #	Number of Closures	Phase Shift	Required Input Voltage	Least-squares fit and correlation coefficient r.
1	0	0	0 V	(925±2 mrad/V) V_{IN} +(−4±10 mrad) r = 0.99997
	1	π	3.41 V	
	2	2π	6.79 V	
2	0	0	0 V	(921.3 mrad/V) V_{IN} r = 1 exactly
	1	π	3.41 V	
	2	2π	6.82 V	
3	0	0	0	(906.7±0.8 mrad/V) V_{IN} + (2±3 mrad) r = 0.9999997
	1	π	3.46 V	
	2	2π	6.93 V	

varying the static phase adjustment, the even harmonics of the fundamental frequency can be eliminated from the output.

APPENDIX D. A DIGITAL INTERFEROMETRIC SIMULATOR

In this appendix we describe briefly a new simulator of interferometric outputs. We developed this simulator in order to make interferometric signals available to a fringe-rate demodulator before we had built a real optical fiber interferometric sensor. This simulator outputs an in-phase and quadrature signal (separated by 90°, not 120°), and the waveforms are square pulses, not smoothly-rounded waves of the sort emitted by real interferometers. For a fringe-rate demodulator, this is not a limitation, since it only responds to transitions of its input (the interferometric output) through zero anyway.

Crooker [Ref. 10, p. 45] also used a simulator to produce square waves, 90° apart in phase. Hers was based on the use of a pendulum and an optical shaft encoder. Her design was limited to frequencies of one or two hertz, but could generate phase shifts of up to 100 or so radians. To get large phase shifts with this apparatus requires large displacements of the pendulum. The motion of a pendulum only approximates simple harmonic motion when the angle of displacement is very small. For large displacements, the motion becomes more complex, even chaotic. Non-linearities are introduced into the phase shift under these circumstances. A phase shift which is linear with the amplitude of the stimulus is a much more desirable characteristic of a simulator, since real sensors are designed to produce a linearly increasing phase shift with increasing amplitude of the signal of interest.

The alternative we describe here uses digital logic to produce the same effect. Central to its operation is a voltage controlled oscillator (VCO) whose output frequency is proportional to the input voltage. Figure 74 shows a block diagram of the simulator. The derivative of the signal of interest is proportional to the rate of change of the desired output phase shift. However, an interferometric output is the same whether the signal of interest is rising or falling, so we use an absolute value circuit removes the information about the direction of change. This information is required later in the circuit, however, in order to allow the digital quadrature pulse generator to decide whether the Q output

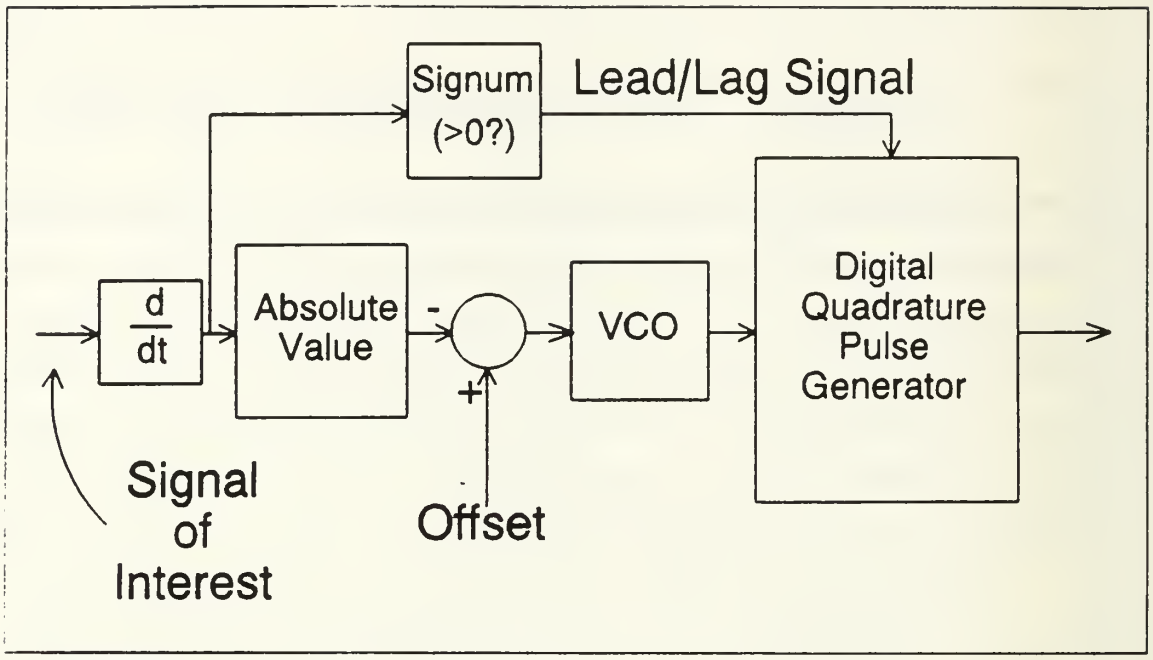

Figure 74 Block diagram of a Digital Quadrature Phase Modulation Simulator.

should lead the *I* output or *vice versa*. Consequently a *signum* circuit outputs a TRUE signal level when the derivative is positive and a FALSE signal when it is negative.

The fixed offset shown in the figure must only be added in if the VCO (such as the EXAR XR2206 that we used) requires unipolar inputs. Adding in this offset ensures that this is the case. The output of the VCO thus has a high frequency when the signal of interest is rising or falling through zero, and it has a low frequency when the signal of interest reaches an extremum. An optical fiber interferometric sensor terminated with a 2×2 optical fiber coupler produces an output whose frequency varies in this manner, too.

The digital quadrature pulse generator uses the frequency output of the VCO and the lead/lag information from the *signum* circuit to create two square pulse trains, *I* (in-phase) and *Q* (quadrature). *I* leads *Q* (that is, changes from high to low, or *vice versa* before *Q* changes) when the lead/lag signal is TRUE and it lags *Q* otherwise.

Not shown in the block diagram, but present in our implementation of it was some level-shifting and buffering circuitry following the digital quadrature pulse generator. Since its presence is not essential to understanding the technique, it is omitted in our discussions here.

While we shall not detail the implementation of the DQPMS, we shall show the logic of the digital quadrature pulse generator. This circuit was implemented with an Altera EP310 Erasable Programmable Logic Device (EPLD). Internally, the previous state of the I and Q outputs was preserved in a flip-flop. When the current state of the lead/lag signal also is present, this is enough information to generate the next I and Q data. Figure 75 shows a Karnaugh map for the generation of I and Q.

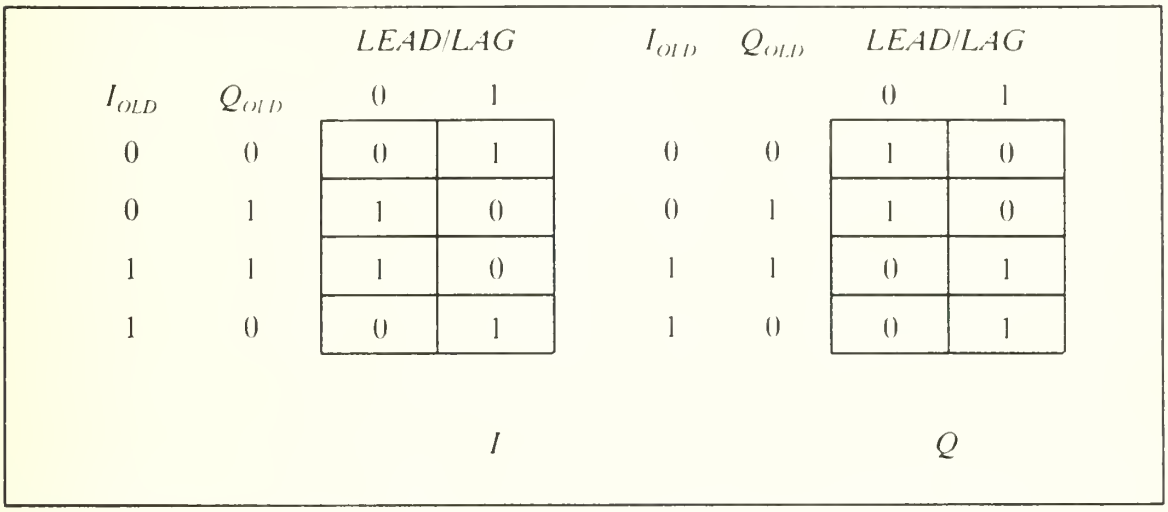

Figure 75 Karnaugh map of logic needed to generate in-phase I and quadrature Q data for the Digital Quadrature Phase Shift Modulator.

For example, suppose I presently leads Q and the old values of I and Q were 0 and 1 respectively. The *LEAD/LAG* signal was 1 before. If it stays at this level, then Q must follow I to 0 before anything else happens. We see in the Karnaugh map that the new outputs are $I=0$ and $Q=0$. But if the *LEAD/LAG* signal switches to 1, then I should follow Q now. We see in the Karnaugh map that the new outputs are $I=1$ and $Q=1$.

The other values in the map were completed in the same way. Two logical equations describing the outputs are

$$I = LL \oplus Q \qquad \text{and} \qquad Q = LL \oplus \bar{I} \tag{491}$$

The DQPMS is a useful simulator for testing fringe-rate demodulation schemes. It is not suitable for testing other demodulators because its outputs are square, not smooth. However, it is a very simple circuit and provides a much larger range of

frequencies of the signal of interest than were feasible with Crooker's pendulum-based simulator.

APPENDIX E. BEHAVIOR OF THE BESSEL FUNCTION

In this appendix, we present graphs which give some intuitive grasp of the Bessel function $J_k(A)$. Since the interferometric output resulting when a simple sinusoidal stimulus impinges on an optical fiber interferometric sensor can be expressed as a Fourier series whose coefficients are Bessel functions, it is useful to develop some feeling for how they vary with k and A.

Generally speaking, the Bessel functions are significant in magnitude only for values of k less than A. As A increases, this implies that there are more and more Bessel function coefficients which matter. In other words, there are more and more harmonies of the fundamental frequency contained in the interferometric output. In deciding how much bandwidth is required within a demodulator, then, a choice of A_{MAX} and f_{MAX} dictates the highest significant frequency components present in the interferometric output.

For example, if A were 100 rad at most, and f were 200 Hz at most, then frequencies which were integral multiples of the fundamental frequency at 200 Hz would be present, up to around $200 \times 100 = 20$ kHz.

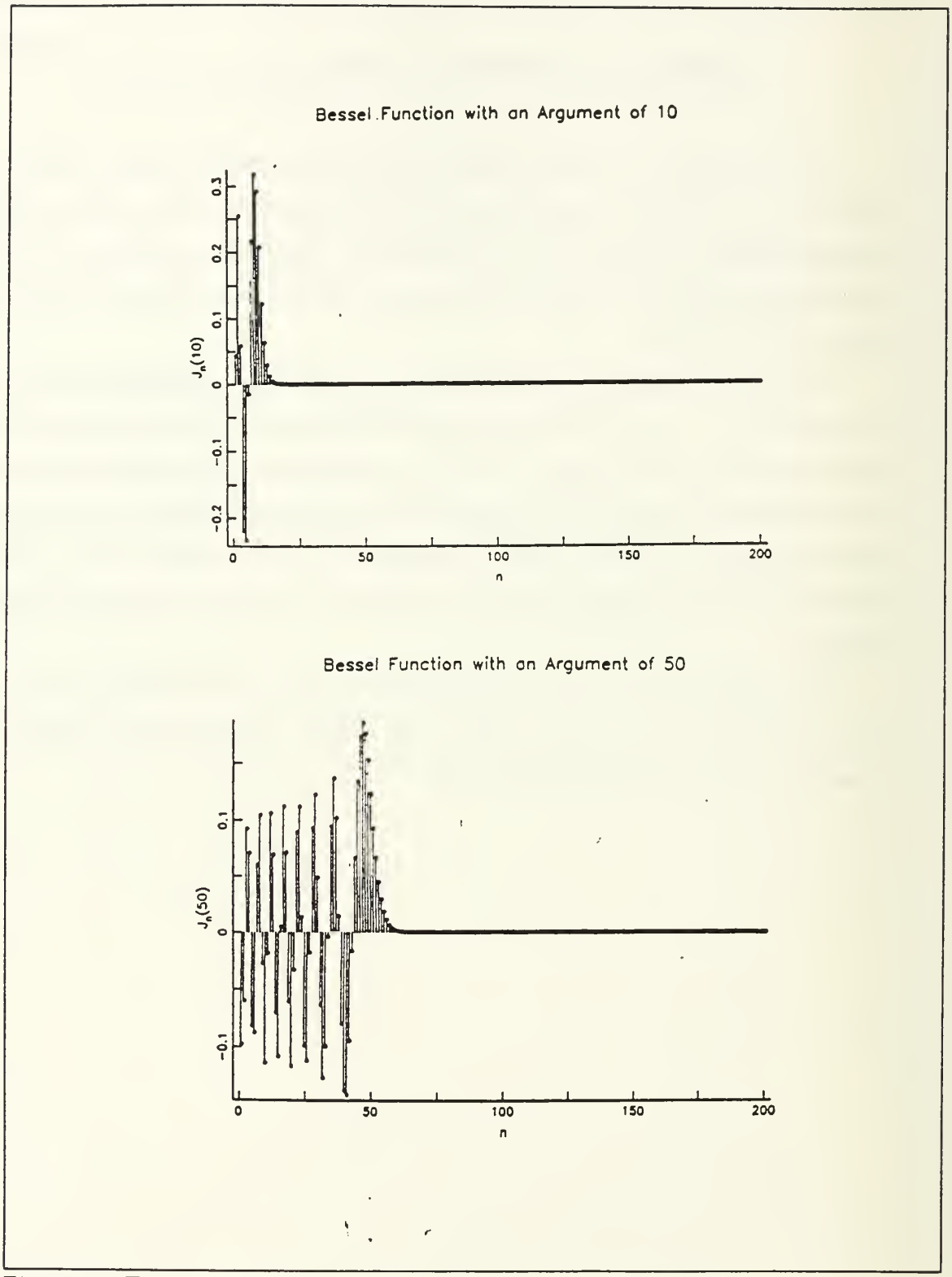

Figure 76 The Bessel functions $J_n(10)$ and $J_n(50)$ as functions of n.

Figure 77 The Bessel functions $J_n(90)$ and $J_n(100)$ as functions of n.

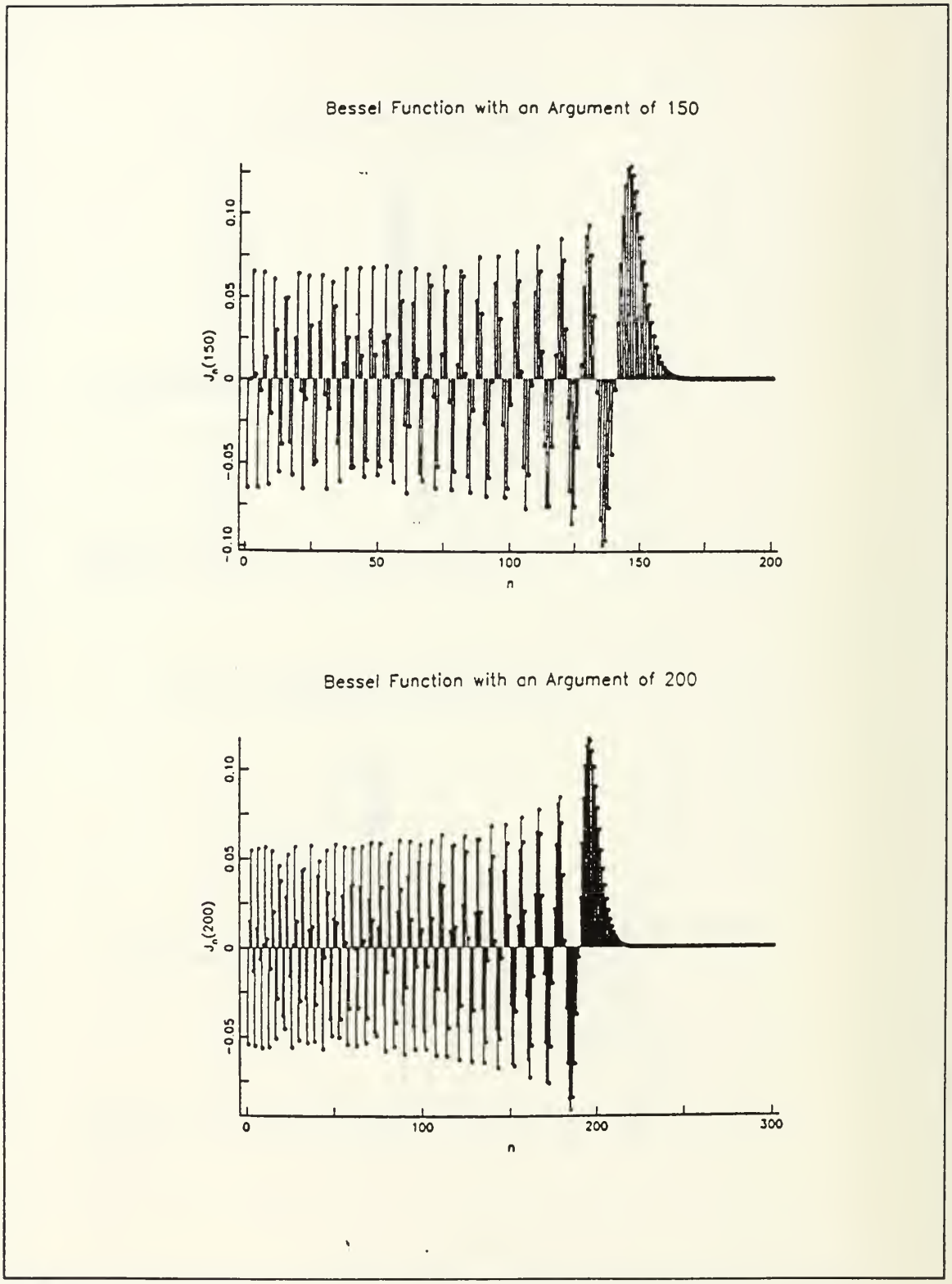

Figure 78 The Bessel functions $J_n(150)$ and $J_n(200)$ as functions of n.

APPENDIX F. NOISE ANALYSIS, SYMMETRIC ANALOG DEMODULATOR

In this appendix, we present a detailed analysis of the noise levels within the Symmetric Analog Demodulator and at its outputs. The noise sources are assumed to be Gaussian. Johnson (thermal) noise from resistors and shot noise from diodes are assumed to be white noise over the frequencies of interest. The noise sources associated with integrated circuits are generally not white. The specifications of some such circuits provide graphs, giving the noise spectral density over a continuous range of frequencies. Those for other circuits quote the noise spectral density at discrete frequencies, usually frequencies which are integral powers of 10. The operation of the demodulator itself changes what white noise there is according to the characteristics of the transfer functions which it comprises. For example, white noise is converted to "pink" noise (in which lower frequencies are enhanced and higher frequencies are attenuated) upon passing through an integrator.

The reader should refer to the schematic diagram of the Symmetric Analog Demodulator on page 134 for a complete view of the demodulator. However, we shall show each stage separately as we conduct the analysis. In the following sections, we perform general algebraic analyses of the noise performance of each of the various classes of circuits which exist in the Symmetric Analog Demodulator. After collecting the results, we apply them to the Symmetric Analog Demodulator specifically by replacing the algebraic symbols with actual values.

A brief explanation of our method of analysis generally is in order here. To avoid the cumbersome expressions associated with working with the integro-differential equations by which lumped-parameter circuits may be modelled, we work in the Laplace transform domain, the s-domain. We shall only work with resistances and capacitances. To find the quantity in the Laplace domain which is analogous to a resistance R we can take the Laplace transform of the implicit definition of R given by $v(t)=i(t)R$:

$$\mathcal{L}[v(t)] = V(s) = \mathcal{L}[i(t)R] = \int_0^\infty i(t)Re^{-st}dt = RI(s). \tag{492}$$

We see that in the Laplace domain, R is defined implicitly by the equally simple relation $R=V(s)/I(s)$.

Similarly, we can obtain the quantity in the Laplace domain which is analogous to a capacitance C by taking the Laplace transform of the equation which defines a capacitor:

$$i(t) = C\frac{dv(t)}{dt}. \tag{493}$$

The Laplace transform $F(s)$ of a wave form $f(t)$ is defined by

$$F(s) = \int_0^\infty f(t)e^{-st}dt. \tag{494}$$

Applying this definition to the definition of $i(t)$ we find

$$I(s) = \mathcal{L}[i(t)] = \int_0^\infty C\frac{dv(t)}{dt}e^{-st}dt. \tag{495}$$

This expression can be integrated by parts if we let

$$p = e^{-st} \qquad \text{and} \qquad dq = \frac{dv(t)}{dt}dt = dv(t). \tag{496}$$

Differentiating p and integrating dq yields

$$dp = -se^{-st}dt \qquad \text{and} \qquad q = v(t). \tag{497}$$

So we find

$$\begin{aligned} I(s) &= pq - \int_0^\infty q\,dp \\ &= C\left[v(t)e^{-st}\Big|_0^\infty + s\int_0^\infty v(t)e^{-st}dt\right] \\ &= C[v(0) + sV(s)]. \end{aligned} \tag{498}$$

Ultimately our interest is in steady-state solutions, *i.e.*, in the Fourier-transformed variables. These are obtained by assuming all effects due to the initial conditions $v(0)$ eventually die away, and by replacing the complex Laplace variable s by the purely imaginary frequency $j\omega = j2\pi f$. For now, we shall retain the variable s and drop the initial conditions. If we then take the ratio of $V(s)$ to $I(s)$, we obtain

$$\frac{V(s)}{I(s)} = \frac{1}{sC}. \tag{499}$$

So far, we have been careful to use lower case letters to signify variables of time t and upper case letters to signify variables of the complex frequency s. From here on, we shall not maintain this distinction. All of our analysis will be in the Laplace domain s or in the Fourier domain $s = j\omega$, so we shall feel free to use lower case letters for variables in these domains.

We also shall usually assume that the operational amplifiers are ideal. An ideal operational amplifier has infinite input impedance, zero output impedance, and has infinite gain. As a result, it will draw no current, will supply as much current as required, and keeps both its inputs at the same voltage by the operation of negative feedback. The assumption of infinite gain is fairly accurate at the low frequencies considered in this dissertation. In reality, the gain is on the order of several hundred thousand or so, and begins to decline at the rate of 20 dB per decade increase in frequency at frequencies above 10 Hz or so. The decline increases at even higher frequencies, on the order of 500 kHz to a few MHz.

Several times in this appendix, these simplifying assumptions do not make obvious the output of a circuit. When this occurs, we shall call the gain of the operational

amplifier A, ignoring its frequency dependence, and we shall express the amplifier's output as

$$v_{OUT} = A(V^+ - V^-) \tag{500}$$

where V^+ is the voltage applied to the non-inverting terminal of the operational amplifier and V^- is the voltage applied to its inverting terminal. When we have finished doing this, we shall always let A be very large, and it invariably vanishes from the results.

A. RECEIVERS WITH LOWPASS FILTERING

In Figure 79 is a schematic drawing of a receiver consisting of a photodiode with a transimpedance amplifier built around an operational amplifier. Together, they constitute a receiver with a lowpass characteristic. There are two noise voltage sources and two noise current sources in this figure.

The source $i_s^\dagger$ is a noise current due to shot noise in the photodiode of the receiver (we neglect additional effects due to dark current). Its current spectral density is given by

$$i_s^\dagger = \sqrt{2qI}. \tag{501}$$

In this expression, I is the current flowing through the diode, the current which gives rise to the shot noise in the first place, and $q = 1.602 \times 10^{-19}$ C is the charge on an electron. The current I can be expressed in terms of the responsivity $\mathcal{R}$ of the photodiode, given in units of amperes per watt of incident optical power (A/W), and the incident optical power P, given in units of watts (W). So we can rewrite Equation (501) as

$$i_s\dagger = \sqrt{2q\mathcal{R}P}. \tag{502}$$

The noise source $i_n^\dagger$ models the current noise at the inputs of the operational amplifier. We show it as acting at the inverting input.

The voltage noise source $e_n^\dagger$ models the voltage noise at the inputs of the operational amplifier. We show it as acting at the non-inverting input.

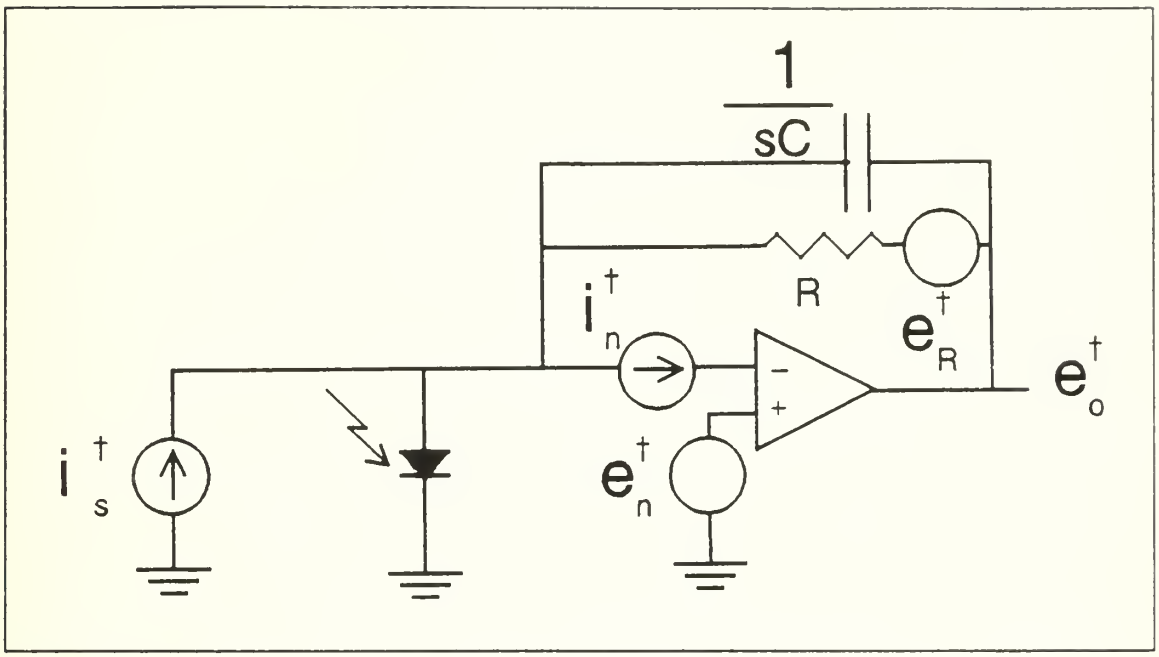

Figure 79 General schematic of an optical receiver using a photodiode and a transimpedance amplifier with lowpass filtering.

The voltage noise source $e_R^\dagger$ is due to the Johnson (thermal) noise of resistor R. It has noise voltage spectral density

$$e_R^\dagger = \sqrt{4kTR}. \tag{503}$$

The constant k is Boltzmann's constant, 1.381×10^{-23} joules per kelvin (J/K). The temperature T is measured in kelvins and we shall take it as 300 K throughout this appendix. The resistance R is measured in ohms (Ω).

We shall perform the analysis in this and all subsequent sections by suppressing every source but one, deducing the output voltage spectral density $e_o^\dagger$ due to the remaining source, and summing all these individual contributions as the square root of the sum of the squares of the individual contributions. This is appropriate if we assume all the noise sources are independent of each other and that the noise spectral density is the standard deviation (square root of the variance) of the underlying probability distribution function, for the variance of the sum of uncorrelated random variables is the sum of their individual variances.

That is, if the kth of n random variables has variance σ_k^2, then the variance σ of the sum of all n random variables is

$$\sigma^2 = \sum_{k=0}^{n} \sigma_k^2. \tag{504}$$

The standard deviation of the sum of the random variables is just the square root of this sum. (This is not the same as the standard deviation of a sampling from a single random variable.)

If we take the shot noise current source first, then we see that for an operational amplifier with very large input impedance, essentially all the noise current flows through the feedback network consisting of resistor R in parallel with capacitor C. Since the operational amplifier is in an inverting configuration, it attempts to keep the inverting terminal and the non-inverting terminal at the same voltage. With the amplifier's noise voltage source $e_n^\dagger$ suppressed, this voltage is zero. Therefore the shot noise contribution to the output noise is

$$e_{o_1}^\dagger = -\left(R \| \frac{1}{sC}\right) i_s^\dagger = -\left(\frac{R}{1+sCR}\right) i_s^\dagger = -\left(\frac{R}{1+sCR}\right) \sqrt{2q\Re P}. \tag{505}$$

Note that while we retain the negative sign here, it will be of no account when we square this noise term in computing the overall output noise due to all the noise sources.

Next we consider the noise due to the amplifier's voltage noise source acting alone. Since there is now no current available to flow through the feedback network, the voltage at the inverting terminal and the output terminal must be identical, and since the inverting and non-inverting terminals are held at essentially the same voltages by the amplifier, the output noise spectral density is

$$e_{o_2}^\dagger = e_n^\dagger. \tag{506}$$

For the operational amplifier's noise current source acting alone, all the current must pass through the feedback network. Since the voltage at both input terminals of the operational amplifier are held equal to each other at 0 V, the output noise spectral

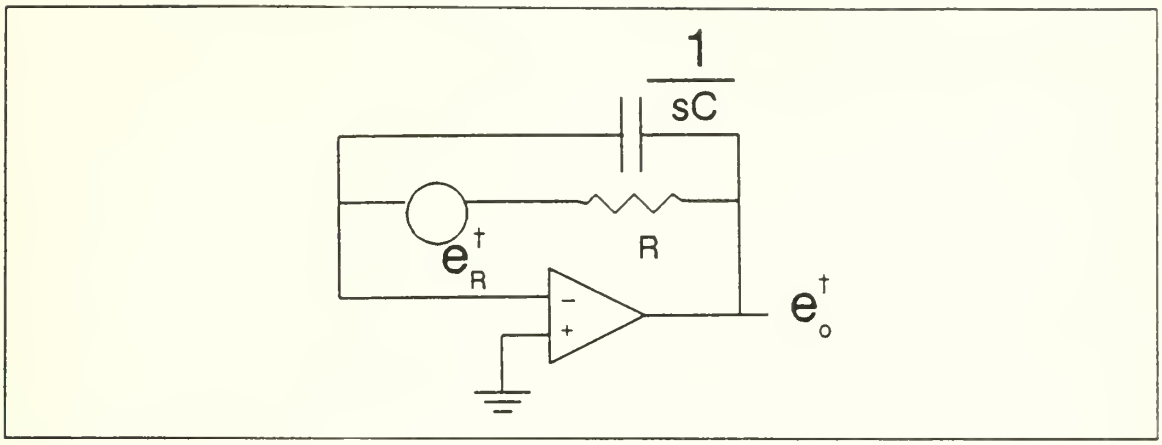

Figure 80 Noise from the transimpedance amplifier considering just the thermal noise from the feedback resistor.

density from this contribution is

$$e_{o3}^\dagger = \left(R \| \frac{1}{sC}\right) i_n^\dagger = \frac{R}{1-sCR} i_n^\dagger. \tag{507}$$

There is no negative sign here, as there was when the signal source provided a noise current, by virtue of our definition of the direction of noise current flow. Again, however, the later squaring of this contribution would eliminate a negative sign resulting from a different choice of current direction.

Finally we consider the noise due to resistor R acting alone. To do this analysis, we shall redraw the schematic as in Figure 80 with just this source acting.

Here we have interchanged the positions of the resistor and its voltage source to make it clear that the resistor and capacitor form a voltage divider. The output noise voltage spectral density is thus given by

$$e_{o_4}^{\dagger} = \frac{\left(\frac{1}{sC}\right)}{\left(R+\frac{1}{sC}\right)} e_R^{\dagger} = \frac{1}{1+sCR} e_R^{\dagger} = \frac{\sqrt{4kTR}}{1+sCR}. \tag{508}$$

When we add the effects of all four independent noise sources together, we get the total output noise voltage spectral density

$$e_o = \sqrt{\sum_{k=1}^{4} e_{o_k}^{\dagger 2}} = \sqrt{\left(2q\Re P + i_n^{\dagger 2}\right)\left(\frac{R}{1+sCR}\right)^2 + e_n^{\dagger 2} + \frac{4kTR}{(1+sCR)^2}}. \tag{509}$$

B. INVERTING SCALING ADDERS

In Figure 81 is a generalized summing amplifier with n inputs. As before, we shall consider the effects of each noise source in isolation. Note that the resistance of the source of input k is assumed to be negligible. However, if this assumption were wrong, it could be lumped in with R_k in computing transfer functions (although not in computing the thermal noise attributable to R_k itself.)

The noise due to source k is amplified by the feedback resistance R_f divided by the input resistance R_k. The sum of all such contributions is

$$e_{o_1}^{\dagger} = \sqrt{\sum_{k=1}^{n} \left[\frac{R_f}{R_k} e_{s_k}\right]^2}. \tag{510}$$

When only the amplifier's current noise source is present, there is no voltage across any of the input resistors R_k because both inputs of the operational amplifier are

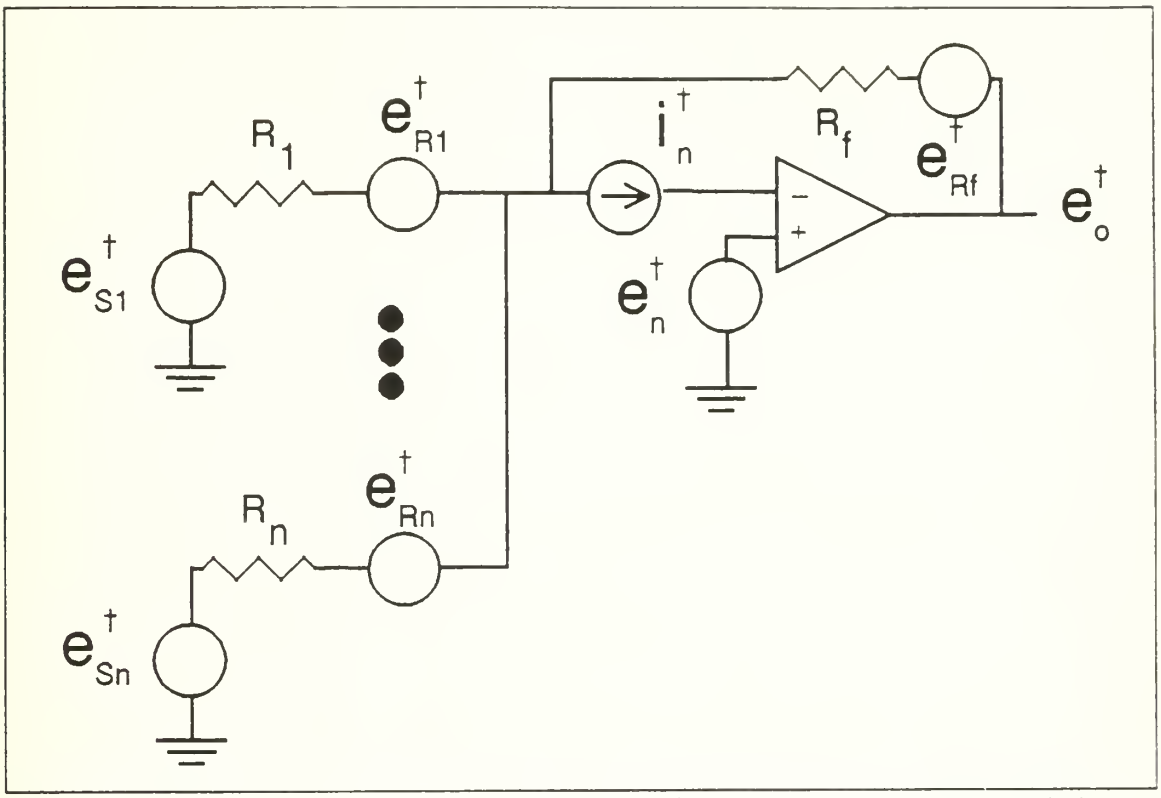

Figure 81 Schematic drawing of a summing amplifier with noise sources included.

held at zero by the amplifier's feedback. Thus all the noise current flows through the feedback resistor and the contribution to the output noise voltage spectral density is

$$e_{o_2} = R_f \, i_n^{\dagger}. \tag{511}$$

When only the amplifier's input voltage noise is present, the amplifier is configured as a non-inverting amplifier. The input resistance then is the parallel combination of all n input resistors. The contribution to the output noise is then

$$e_{o_3}^{\dagger} = \sqrt{\left[\left(1 + \frac{R_f}{\|_{k=1}^{n} R_k}\right) e_n^{\dagger}\right]^2}. \tag{512}$$

We have used here a shorthand notation for the parallel combination of all n input resistors, namely

$$R_{IN} = \prod_{k=1}^{n} R_k. \tag{513}$$

It is common to take all the input resistances as equal to each other and to the value R. We shall do this in all applications of this analysis, so the parallel resistance reduces simply to R/n and we can rewrite the noise contribution more simply as

$$e_{o_3} = \sqrt{\left[\left(1+\frac{nR_f}{R}\right)e_n^\dagger\right]^2} \tag{514}$$

When only the thermal noise due to the input resistors is present, that noise is amplified in the same manner as the source noise voltage, giving

$$e_{o_4}^\dagger = \sqrt{\sum_{k=1}^{n} 4kTR_k\left(\frac{R_f}{R_k}\right)^2} = \sqrt{4kTR_f^2\sum_{k=1}^{n}\frac{1}{R_k}}. \tag{515}$$

If, as before, we let $R_k = R$ for all k, then this can be simplified to

$$e_{o_4}^\dagger = \sqrt{4kTR_f^2\frac{n}{R}}. \tag{516}$$

The final contribution to the output noise comes from the feedback resistor. No current flows through the feedback network, so this noise contribution is felt directly at the output:

$$e_{o_5}^\dagger = \sqrt{4kTR_f} \tag{517}$$

Summing all five contributions to the noise as the square root of the sum of squares yields

$$e_o^{\dagger} = \sqrt{\left(\frac{R_f}{R}\right)^2 \sum_{k=1}^{n} e_{s_k}^{\dagger 2} + \left(R_f\, i_n^{\dagger}\right)^2 + 4kTR_f\left(1+\frac{nR_f}{R}\right) + \left[\left(1+\frac{nR_f}{R}\right)e_n^{\dagger}\right]^2} \quad . \tag{518}$$

C. INVERTING SCALING ADDERS WITH LOWPASS FILTERING

In Figure 82 is a schematic drawing very similar to the one discussed in the previous section. This one has a capacitor in parallel with the feedback capacitor, however. Its function is to provide lowpass filtering. A development similar to those in the previous two sections allows us to write the following expression for the output noise of this circuit by inspection:

$$e_o^{\dagger} = \sqrt{\left(\frac{R_f}{R(1+sCR_f)}\right)^2 \sum_{k=1}^{n} e_{s_k}^{\dagger 2} + \left(\frac{R_f}{1+sCR_f}\, i_n^{\dagger}\right)^2 + 4kTR_f\left(1+\frac{nR_f}{R(1+sCR_f)^2}\right) + \left[\left(1+\frac{nR_f}{R(1+sCR_f)}\right)e_n^{\dagger}\right]^2} \tag{519}$$

D. DIFFERENTIATORS AND INTEGRATORS

The circuit we shall use both for differentiation and integration was discussed in an earlier appendix. It is reproduced in Figure 83 with noise sources shown. We shall commence our analysis by defining two functions which will be useful in the course of the analysis. The first of these is the same transfer function we derived earlier for the entire sub-circuit. It is

$$H_1(s) = \frac{R_2 \| \frac{1}{sC_2}}{R_1 + \frac{1}{sC_1}} = \frac{\left(\frac{R_2}{1+sC_2R_2}\right)}{\left(\frac{1+sC_1R_1}{sC_1}\right)} = \frac{sC_1R_2}{(1+sC_1R_1)(1+sC_2R_2)} \quad . \tag{520}$$

The second transfer function is just the parallel combination of R_2 and C_2:

$$H_2(s) = R_2 \| \frac{1}{sC_2} = \frac{R_2}{1+sC_2R_2}. \tag{521}$$

The noise $e_s^{\dagger}$ from the input and that from the input resistor R_1 both are amplified by the transfer function $H_1(s)$. Thus their contributions to the noise are

$$e_{o_1} = H_1(s)e_s^{\dagger} \tag{522}$$

and

$$e_{o_2}^{\dagger} = \sqrt{4kTR_1}H_1(s) \tag{523}$$

respectively.

The noise source $e_n^{\dagger}$ is amplified by a non-inverting configuration of an amplifier, and so the resultant contribution at the output is

$$e_{o_3} = \sqrt{\left[(1+H_1(s))e_n^{\dagger}\right]^2}\ . \tag{524}$$

As we have seen in the last three sections, the noise from the feedback resistor R_2 shows up at the output without amplification:

$$e_{o_4} = \sqrt{4kTR_2}. \tag{525}$$

The remaining contribution to the output noise is due to the operational amplifier's input current noise, $i_n^{\dagger}$. When this is the sole source of noise, the inputs to the operational amplifier both are zero, so no current flows through the input network consisting of R_1 and C_1. All the noise current flows through the feedback network and this network has the forward transfer function $H_2(s)$, so the contribution due to the noise current source is

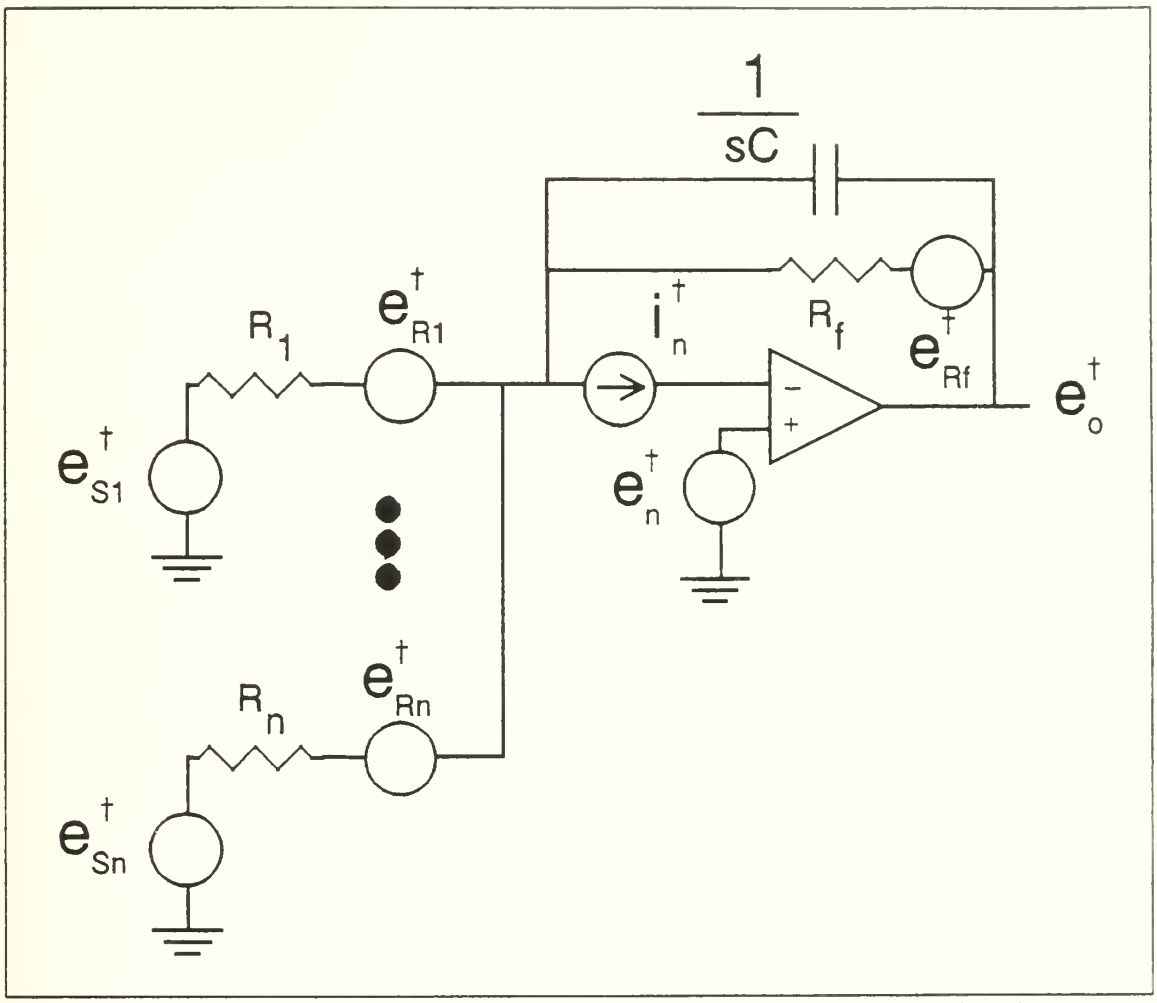

Figure 82 Schematic diagram of a scaling inverting adder with lowpass filtering.

$$e_{o_5} = i_n^{\dagger} H_2(s). \tag{526}$$

When we sum all five of these uncorrelated noise contributions, we find the output noise voltage spectral density is

$$e_o^{\dagger} = \sqrt{\left(H_1(s)e_s^{\dagger}\right)^2 + 4kTR_1H_1^2(s) + \left[\left(1 - H_1(s)\right)e_n^{\dagger}\right]^2 + 4kTR_2 + \left(H_2(s)i_n^{\dagger}\right)^2}. \tag{527}$$

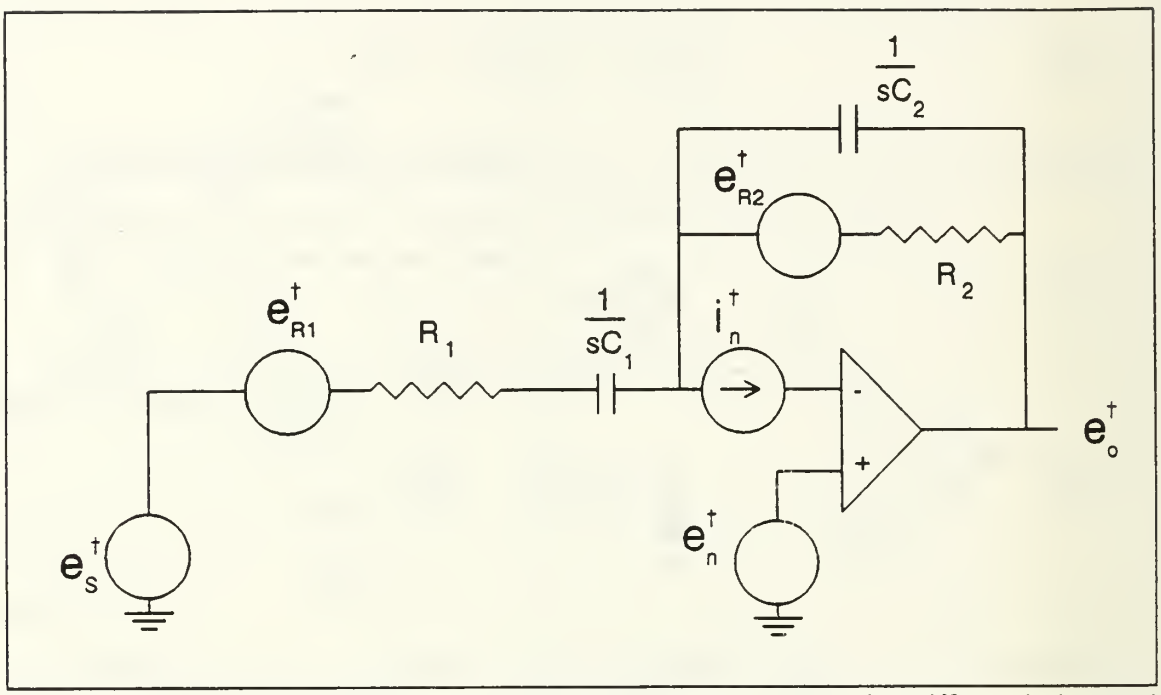

Figure 83 Schematic drawing of the standard circuit we use for differentiation and integration with noise sources shown.

E. INTEGRATORS WITH TEE-NETWORKS IN THE FEEDBACK

The output noise derived in the last section applies to integrators with a simple resistor in the feedback, as shown in Figure 83. In order to get a low-frequency cut-off characteristic, however, we often would rather use a Tee-network in the feedback, as shown in an earlier appendix, in order to get large values of effective feedback resistance without having to use other than off-the-shelf resistor values. This more elaborate version of the integrator is illustrated in Figure 84.

Two extra noise voltage spectral densities, $e_a^\dagger$ and $e_b^\dagger$ are shown in the diagram. These are not sources; rather, they are the spectral densities present at the nodes shown by the arrows.

When $R_2=R_3=R \gg R_1$, then the feedback resistance is approximately R^2/R_1. Thus we can modify the transfer function $H_1(s)$ of the last section to

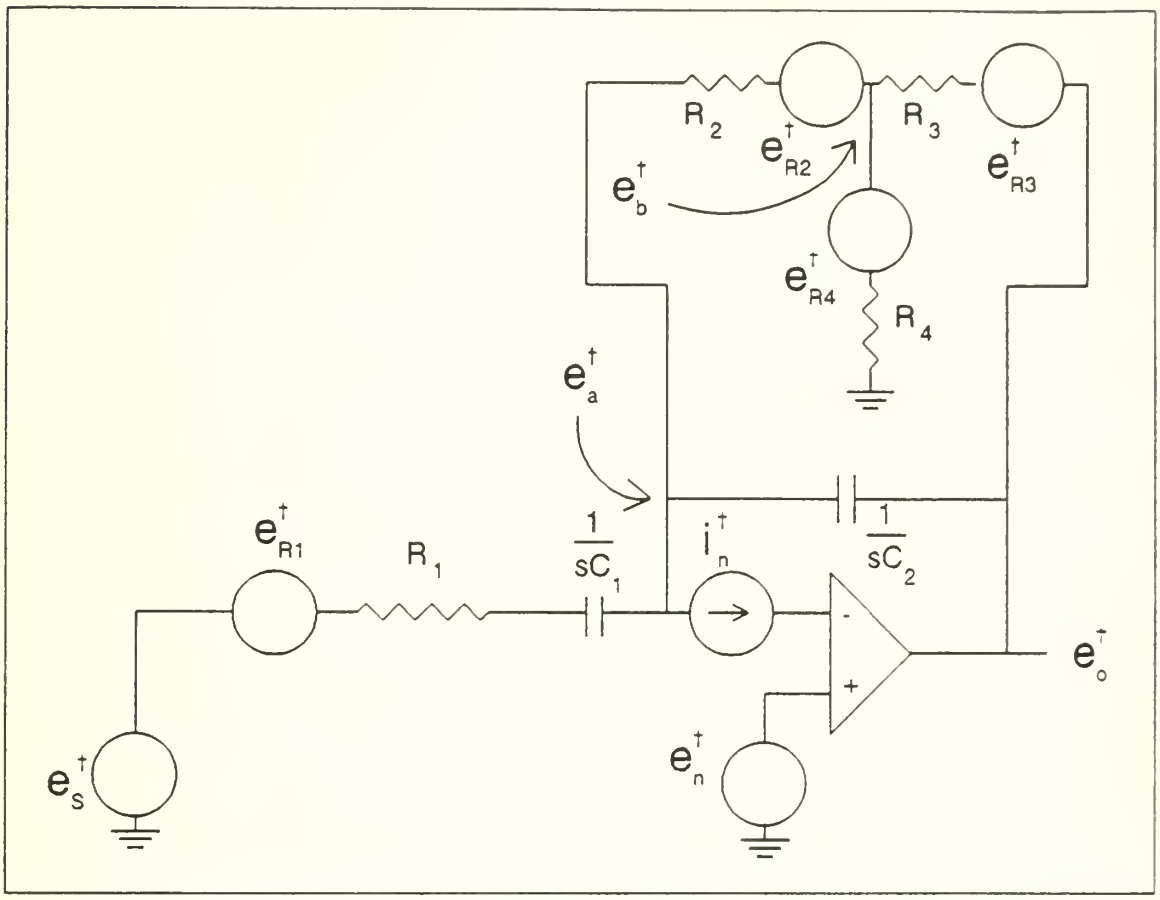

Figure 84 Schematic of an integrator with a Tee-network in the feedback and with all noise sources shown.

$$H_1(s) = \frac{\dfrac{R_2R_3}{R_4} \parallel \dfrac{1}{sC_2}}{R_1 + \dfrac{1}{sC_1}} = \frac{\left(\dfrac{\dfrac{R_2R_3}{R_4}}{1 + sC_2\dfrac{R_2R_3}{R_4}}\right)}{\left(\dfrac{1 + sC_1R_1}{sC_1}\right)} = \frac{sC_1\dfrac{R_2R_3}{R_4}}{(1 + sC_1R_1)\left(1 + sC_2\dfrac{R_2R_3}{R_4}\right)}. \tag{528}$$

Similarly, we can modify $H_2(s)$ of the last section to

$$H_2(s) = \left(\frac{R_2R_3}{R_4}\right) \| \frac{1}{sC_2} = \frac{\dfrac{R_2R_3}{R_4}}{1+sC_2\dfrac{R_2R_3}{R_4}}. \qquad \textbf{(529)}$$

The noise contributions from the source signal and the input resistors are still given by Equations (522) and (523), but of course these change upon expansion. We shall not perform the expansions, preferring to substitute numerical values for $H_1(s)$ later.

Similarly, the contribution to the noise at the output due to the input voltage noise spectral density $e_n^\dagger$ of the operational amplifier still is given by Equation (524), (526) and the contribution due to the input current spectral density $i_n^\dagger$ is still given by Equation (527).

A difference arises, however, in considering the thermal noise in the feedback network. To analyze this, we shall make explicit use of the gain A of the operational amplifier. Upon completion of the necessary algebraic manipulations, we shall use the knowledge that A is very large to simplify the results.

First we consider the thermal noise e_{R2} from resistor R_2. The voltage spectral density $e_a^\dagger$ at the inverting input of the operational amplifier induces a current $i_1^\dagger$ noise through resistor R_1 and capacitor C_1:

$$i_1^\dagger = \frac{e_a^\dagger}{R_1 + \dfrac{1}{sC_1}} = \frac{sC_1e_a^\dagger}{1+sC_1R_1}. \qquad \textbf{(530)}$$

The potential difference between the output noise voltage spectral density $e_o^\dagger$ and that at the inverting input also induces a noise current $i_2^\dagger$ through the feedback capacitor C_2:

$$i_2^{\dagger} = \frac{e_a^{\dagger} - e_o^{\dagger}}{\left(\frac{1}{sC_2}\right)} = \left[e_a^{\dagger} - \left(-Ae_a^{\dagger}\right)\right] sC_2 = (1+A)sC_2 e_a^{\dagger}. \tag{531}$$

We have taken the direction of each of these currents to be away from the inverting terminal of their operational amplifier. So their sum must flow into that terminal through the Tee-network. Calling this current $i_3^{\dagger}$, we have

$$i_3^{\dagger} = i_1^{\dagger} + i_2^{\dagger} = \left[\frac{sC_1}{1+sC_1R_1} + (1+A)sC_2\right] e_a^{\dagger}. \tag{532}$$

This current induces a voltage noise spectral density across resistor R_2 which, when added to the thermal noise spectral density caused by R_2 gives the voltage noise spectral density $e_b^{\dagger}$ at the junction of the Tee-network:

$$e_b^{\dagger} = e_a^{\dagger} + i_3^{\dagger}R_2 + e_{R_2}^{\dagger} = \left\{1 + R_2\left[\frac{sC_1}{1+sC_1R_1} + (1+A)sC_2\right]\right\} e_a^{\dagger} + e_{R_2}^{\dagger}. \tag{533}$$

Note that since the only random signal present here is due to the thermal noise $i_{R_2}^{\dagger}$, these spectral densities add directly, not as the square root of the sum of squares, which would be the case for uncorrelated noise sources acting in concert.

Knowing the voltage spectral density at the junction permits calculation of the current noise spectral density $i_4^{\dagger}$ down through resistor R_4:

$$i_4^{\dagger} = \frac{e_b^{\dagger}}{R_4} = \frac{1}{R_4}\left\{1 + R_2\left[\frac{sC_1}{1+sC_1R_1} + (1+A)sC_2\right]\right\} e_a^{\dagger} + \frac{e_{R_2}^{\dagger}}{R_4}. \tag{534}$$

The current noise spectral density $i_5^{\dagger}$ flowing through resistor R_5 into the junction of the Tee is given by

$$i_5^\dagger = i_3^\dagger + i_4^\dagger = \left[\frac{sC_1}{1+sC_1R_1} + (1+A)sC_2 + \frac{1}{R_4} + \frac{sC_1R_2}{R_4(1+sC_1R_1)} + (1+A)\frac{sC_2R_2}{R_4}\right] e_a^\dagger + \frac{e_{R_2}^\dagger}{R_4}. \quad (535)$$

We can calculate the output noise voltage spectral density $e_o^\dagger$ from

$$e_o^\dagger = e_b^\dagger + i_5^\dagger R_3 = -Ae_a^\dagger. \quad (536)$$

So

$$-Ae_a^\dagger = \left[\begin{array}{c} 1 + \dfrac{sC_1R_2}{1+sC_1R_1} + (1+A)sC_2R_2 + \dfrac{sC_1R_3}{1+sC_1R_1} \\ \\ +(1+A)sC_2R_3 + \dfrac{R_3}{R_4} + \dfrac{sC_1R_2R_3}{R_4(1+sC_1R_1)} + (1+A)\dfrac{sC_2R_2R_3}{R_4} \end{array}\right] e_a^\dagger + \frac{R_3}{R_4} e_{R_2}^\dagger. \quad (537)$$

Gathering the terms in $e_o^\dagger$ on one side and that in $e_{R_2}^\dagger$ on the other side, then multiplying by $-A$ lets us write the contribution of the thermal noise of R_2 at the output as

$$e_{o_{4a}}^\dagger = \frac{A\dfrac{R_3}{R_4}}{\left[\begin{array}{c} 1 + A + \dfrac{sC_1R_2}{1+sC_1R_1} + (1+A)sC_2R_2 + \dfrac{sC_1R_3}{1+sC_1R_1} \\ \\ +(1+A)sC_2R_3 + \dfrac{R_3}{R_4} + \dfrac{sC_1R_2R_3}{R_4(1+sC_1R_1)} + (1+A)\dfrac{sC_2R_2R_3}{R_4} \end{array}\right]} e_{R_2}^\dagger. \quad (538)$$

Now we divide numerator and denominator by A, let A tend to a large number, and neglect any numbers in which A appears only as a denominator, obtaining

$$e_{o_{4a}}^{\dagger} \approx \frac{R_3}{R_4\left(1+sC_2R_2+sC_2R_3+s\dfrac{C_2R_2R_3}{R_4}\right)}e_{R_2}^{\dagger}. \tag{539}$$

Inasmuch as R_2 and R_3 both are much smaller than their product, we can further simplify this to

$$e_{o_{4a}}^{\dagger} = \frac{R_3}{R_4\left(1+\dfrac{sC_2R_2R_3}{R_4}\right)}e_{R_2}^{\dagger}. \tag{540}$$

We now go through a similar exercise to obtain the output noise contributed by the thermal noise of resistor R_1. The development is the same up until Equation (533), which must be modified because the noise source now is in the stem of the Tee.

$$e_b^{\dagger} = e_a^{\dagger}+i_3^{\dagger}R_2 = \left[1+\frac{sC_1R_2}{1+sC_1R_1}+(1+A)sC_2R_2\right]e_a^{\dagger}. \tag{541}$$

The current noise spectral density down through R_4 must be

$$i_4^{\dagger} = \frac{e_b^{\dagger}-e_{R_4}^{\dagger}}{R_4} = \left[\frac{1}{R_4}+\frac{sC_1R_2}{R_4(1+sC_1R_1)}+(1+A)\frac{sC_2R_2}{R_4}\right]e_a^{\dagger}-\frac{e_{R_4}^{\dagger}}{R_4} \tag{542}$$

The current noise spectral density flowing left through R_5 toward the junction of the Tee then is

$$i_5^{\dagger} = i_3^{\dagger}+i_4^{\dagger} = \left[\frac{sC_1}{1+sC_1R_1}+(1+A)sC_2+\frac{1}{R_4}+\frac{sC_1R_2}{R_4(1+sC_1R_1)}+(1+A)\frac{sC_2R_2}{R_4}\right]e_a^{\dagger}-\frac{e_{R_4}^{\dagger}}{R_4}. \tag{543}$$

The contribution of the thermal noise voltage spectral density $e_{R1}^{\dagger}$ of resistor R_1 to the output voltage noise spectral density is

$$e_{o_{4b}}^{\dagger} = -Ae_a^{\dagger} = e_b^{\dagger} + i_5^{\dagger}R_3$$

$$= \left[\begin{array}{l} 1 + \dfrac{sC_1R_2}{1+sC_1R_1} + (1+A)sC_2R_2 + \dfrac{sC_1R_3}{1+sC_1R_1} \\ \\ +(1+A)sC_2R_3 + \dfrac{R_3}{R_4} + \dfrac{sC_1R_2R_3}{R_4(1+sC_1R_1)} + (1+A)\dfrac{sC_2R_2R_3}{R_4} \end{array} \right] e_a^{\dagger} - \frac{R_3}{R_4} e_{R_4}^{\dagger} \tag{544}$$

As before, we gather the terms in $e_a^{\dagger}$ on the left side, that in $e_{R4}^{\dagger}$ on the right, multiply by $-A$ and rearrange the equation to obtain

$$e_{o_{4b}}^{\dagger} = \frac{\dfrac{R_3}{R_4}A}{\left[\begin{array}{l} 1 + A + \dfrac{sC_1R_2}{1+sC_1R_1} + (1+A)sC_2R_2 + \dfrac{sC_1R_3}{1+sC_1R_1} \\ \\ +(1+A)sC_2R_3 + \dfrac{R_3}{R_4} + \dfrac{sC_1R_2R_3}{R_4(1+sC_1R_1)} - (1+A)\dfrac{sC_2R_2R_3}{R_4} \end{array} \right]} e_{R_4}^{\dagger} \tag{545}$$

Once more, we divide numerator and denominator by A, and then neglect any term in which A only appears in the denominator. This yields the approximation

$$e_{o_{4b}}^{\dagger} \approx \frac{R_3}{R_4\left(1 + sC_2R_2 + sC_2R_3 + sC_2\dfrac{R_2R_3}{R_4}\right)} e_{R_4}^{\dagger} \tag{546}$$

We can also neglect the terms in R_2 and R_3 individually, since their product is so much larger, and this gives the final approximation

$$e_{o_{4b}}^{\dagger} \approx \frac{R_3}{R_4\left(1 + sC_2\dfrac{R_2R_3}{R_4}\right)} e_{R_4}^{\dagger} \tag{547}$$

The final contribution to the output noise voltage spectral density with which we must grapple is that from the thermal noise of R_3. The analysis is the same as that for

the thermal noise from resistor R_4 down to Equation (541). The current $i_4^\dagger$ is different, however, since the noise source now is in the right-hand side of the top of the Tee:

$$i_4^\dagger = \frac{e_b^\dagger}{R_4} = \left[\frac{1}{R_4} + \frac{sC_1R_2}{R_4(1+sC_1R_1)} + (1+A)sC_2\frac{R_2}{R_4}\right] e_a^\dagger. \tag{548}$$

The current noise spectral density $i_5^\dagger$ flowing left through resistor R_5 is

$$i_5^\dagger = i_3^\dagger + i_5^\dagger = \left[\frac{sC_1}{1+sC_1R_1} + (1+A)sC_2 + \frac{1}{R_4} + \frac{sC_1R_2}{R_4(1+sC_1R_1)} + (1+A)sC_2\frac{R_2}{R_4}\right] e_a^\dagger. \tag{549}$$

Gathering like terms, multiplying by $-A$, and rearranging gives us

$$\begin{aligned} e_{o_{4c}}^\dagger &= -Ae_a^\dagger = e_b^\dagger + i_5^\dagger R_3 + e_{R_3}^\dagger \\ &= \frac{A}{\left[\begin{array}{l} 1+A+\dfrac{sC_1R_2}{1+sC_1R_1} + (1-A)sC_2R_2 + \dfrac{sC_1R_3}{1+sC_1R_1} \\ \quad + (1-A)sC_2R_3 + \dfrac{R_3}{R_4} + \dfrac{sC_1R_2R_3}{R_4(1+sC_1R_1)} + (1+A)sC_2\dfrac{R_2R_3}{R_4} \end{array}\right]} e_{R_3}^\dagger. \end{aligned} \tag{550}$$

Dividing numerator and denominator by A and neglecting terms with A only in the denominator, we find

$$e_{o_{4c}}^\dagger \approx \frac{1}{1+sC_2R_2+sC_2R_3+sC_2\dfrac{R_2R_3}{R_4}} e_{R_3}^\dagger \tag{551}$$

We also can neglect the terms in R_2 and R_3 since their product is so much larger than either of them individually:

$$e_{o_{4c}}^{\dagger} \approx \frac{1}{1+sC_2\dfrac{R_2R_3}{R_4}} e_{R_3}^{\dagger}. \tag{552}$$

We can combine all the contributions to the output noise voltage spectral density as the square root of the sum of the squares of each component:

$$e_o^{\dagger} = \sqrt{\left\{ \begin{array}{l} H_1^2(s)\left(e_s^{\dagger 2}+e_{R_1}^{\dagger 2}\right)+\left[\left(1+H_1(s)\right)e_n^{\dagger}\right]^2+\left(H_2(s)i_n^{\dagger}\right)^2 \\ +\left(\dfrac{H_2(s)}{R_2}\right)^2\left(e_{R_2}^{\dagger 2}+e_{R_4}^{\dagger 2}\right)+\left(\dfrac{R_4H_2(s)}{R_2R_3}e_{R_3}^{\dagger}\right)^2 \end{array} \right\}}. \tag{553}$$

We can expand this to explicitly give the thermal noise due to the resistors:

$$e_o^{\dagger} = \sqrt{\left\{ \begin{array}{l} H_1^2(s)\left(e_s^{\dagger 2}+4kTR_1\right)+\left[\left(1+H_1(s)\right)e_n^{\dagger}\right]^2+\left(H_2(s)i_n^{\dagger}\right)^2 \\ +H_2^2(s)4kT\left(\dfrac{1}{R_2}+\dfrac{R_4}{R_2^2}+\dfrac{R_4^2}{R_2^2R_3}\right) \end{array} \right\}}. \tag{554}$$

F. ANALOG MULTIPLIERS

The analog multipliers we used produce a noise voltage spectral density at the output which is additional to that caused by multiplying the two inputs together. We shall neglect this contribution at first and add it in later. The function performed by the multiplication function is

$$Z = k_M XY \tag{555}$$

where k_M is the scale factor (assumed to be a constant) of the multiplier and X and Y are the random variables being multiplied. We shall assume that the means of X and Y are

μ_X and μ_Y respectively, and that their variances are σ_X^2 and σ_Y^2. The expectation of the output is

$$\mathrm{E}[Z] = \mathrm{E}[k_M XY] = k_M \mathrm{E}[X]\mathrm{E}[Y]. \tag{556}$$

The separation of the mean of the products into the product of the means is valid if X and Y are statistically independent of one another, which we shall assume to be true. So

$$\mathrm{E}[Z] = k_m \mu_X \mu_Y = \mu_Z. \tag{557}$$

Next we compute the variance of the product. From the definition of the variance,

$$\mathrm{Var}[Z] = \mathrm{E}\left[(Z-\mu_Z)^2\right] = \mathrm{E}\left[Z^2 - 2\mu_Z Z + \mu_Z^2\right] = \mathrm{E}[Z^2] - \mu_Z^2. \tag{558}$$

Expanding this, we obtain

$$\mathrm{Var}[Z] = \mathrm{E}\left[k_M^2 X^2 Y^2\right] - \mu_Z^2 = k_M^2 \mathrm{E}\left[X^2\right]\mathrm{E}\left[Y^2\right] - \mu_Z^2. \tag{559}$$

This separation, too, is justified if the random variables are statistically independent. Using the identity

$$\mathrm{E}\left[X^2\right] = \mathrm{Var}[X] + \mathrm{E}^2[X] = \sigma_X^2 + \mu_X^2 \tag{560}$$

we can expand this to

$$\begin{aligned} \mathrm{Var}[Z] &= k_M^2\left(\sigma_X^2 + \mu_X^2\right)\left(\sigma_Y^2 + \mu_Y^2\right) - k_M^2 \mu_X^2 \mu_Y^2 \\ &= k_M^2\left[\sigma_X^2\sigma_Y^2 + \sigma_X^2\mu_Y^2 + \sigma_Y^2\mu_X^2 - \mu_X^2\mu_Y^2 - \mu_X^2\mu_Y^2\right] \\ &= k_M^2\left[\sigma_X^2\sigma_Y^2 + \sigma_X^2\mu_Y^2 + \sigma_Y^2\mu_X^2\right]. \end{aligned} \tag{561}$$

If the noise is small compared to the signal, then we can approximate this as

$$\mathrm{Var}[Z] \approx k_M^2\left[\mu_X^2\sigma_Y^2 + \mu_Y^2\sigma_X^2\right]. \tag{562}$$

Now that we have seen how the analysis proceeds with a simple multiplier, let us turn our attention to a multiplier with differential inputs, like the Analog Devices AD534. It implements the function

$$Z = k_M U(V-W) \tag{563}$$

where we assume that the means and variances are known, as before. First we shall compute the mean of this product.

$$\begin{aligned} \mu_Z &= \mathrm{E}[Z] = \mathrm{E}\left[k_M U(V-W)\right] \\ &= k_M\{\mathrm{E}[UV] - \mathrm{E}[UW]\} \\ &= k_M\{\mu_U\mu_V - \mu_U\mu_W\} \end{aligned} \tag{564}$$

We used the statistical independence of the three quantities U, V, and W to convert the mean of the products from the product of the means.

Next we compute the variance of the product, Z.

$$\begin{aligned} \mathrm{Var}[Z] &= \mathrm{E}\left[(Z-\mu_Z)^2\right] = \mathrm{E}[Z^2] - \mu_Z^2 \\ &= k_M^2\left\{\mathrm{E}\left[U^2V^2 - 2U^2VW + U^2W^2\right] - \mu_U^2\mu_V^2 + 2\mu_U^2\mu_V\mu_W - \mu_U^2\mu_W^2\right\} \\ &= k_M^2\left\{\begin{array}{l} \left(\sigma_U^2+\mu_U^2\right)\left(\sigma_V^2+\mu_V^2\right) - 2\left(\sigma_U^2+\mu_U^2\right)\mu_V\mu_W + \left(\sigma_U^2+\mu_U^2\right)\left(\sigma_W^2+\mu_W^2\right) \\ -\mu_U^2\mu_V^2 + 2\mu_U^2\mu_V\mu_V - \mu_U^2\mu_W^2 \end{array}\right\}. \end{aligned} \tag{565}$$

Multiplying this out and canceling equal terms with opposite signs leaves

$$\sigma_Z = \mathrm{Var}[Z] = k_M^2\left\{\sigma_U^2\left[(\mu_V-\mu_W)^2\right] + \left(\mu_U^2+\sigma_U^2\right)\left(\sigma_V^2+\sigma_W^2\right)\right\}. \tag{566}$$

Now we can add in the output noise which is specified in the data sheets:

$$\sigma_{MO} = \sqrt{k_M\left[\sigma_U^2(\mu_V-\mu_W)^2 + \left(\mu_U^2+\sigma_U^2\right)\left(\sigma_V^2+\sigma_W^2\right)\right] + \sigma_M^2}. \tag{567}$$

In general, we can relate the noise voltage spectral density e_N^2 of a random voltage variable X to the variance σ_N^2 of X by the equation

$$e_X^{\dagger} = \sqrt{\frac{\sigma_X^2}{B}} = \frac{\sigma_X}{\sqrt{B}}. \tag{568}$$

Thus the output noise spectral density of Z is

$$e_{MO}^{\dagger} = \sqrt{k_M^2\left[e_U^{\dagger 2}(\mu_V - \mu_W)^2 + \left(\mu_U^2 + e_U^{\dagger 2}B\right)\left(e_V^{\dagger 2} + e_W^{\dagger 2}\right)\right] + e_M^{\dagger 2}}. \tag{569}$$

To get the output noise spectral density of a squaring device whose function is described by

$$Z = k_M U^2 \tag{570}$$

we shall use a slightly different approach. We shall assume that the mean of U is zero, as is the case in the Symmetric Analog Demodulator at the input to the squaring circuit. Taking U as $U = \mu_U \pm \sigma_U$, we have

$$\begin{aligned} Z &= k_M(\mu_U \pm \sigma_U)^2 = k_M\left(\mu_U^2 \pm 2\sigma_U\mu_U + \sigma_U^2\right) \\ &= k_M\mu_U^2 \pm 2k_M\sigma_U\mu_U + k_M\sigma_U^2. \end{aligned} \tag{571}$$

The first term in this result is what we would expect the output to be if noise were not present. We shall identify the second two terms as a reasonable approximation to the standard deviation, that is,

$$\sigma_Z \approx \sqrt{4k_M^2\mu_U^2\sigma_U^2 + k_M^2\sigma_U^4}. \tag{572}$$

Because we have assume that the mean of U is zero, this can be simplified to

$$\sigma_Z \approx k_M\sigma_U^2 = k_M e_X^{\dagger 2}B. \tag{573}$$

Expressing the output as a voltage noise spectral density, and including the noise added by the multiplier, we have the following expression for the output voltage noise spectral density of a squaring device:

$$e_{MO}^{\dagger} \approx \sqrt{\left(k_M e_X^{\dagger 2}\right)^2 B + e_M^{\dagger 2}}. \tag{574}$$

G. ANALOG DIVIDERS

In general, a divider will provide some voltage spectral noise density at the output in addition to that caused by the operation of division on the two inputs. We shall approximate the standard deviation as follows.

The operation we want to compute with the divider is

$$Z = k_d \frac{X}{Y} \tag{575}$$

where

$$X = k_1 E^2 \dot{\xi} \pm \sigma_X, \tag{576}$$

$$Y = k_2 E^2 \pm \sigma_Y, \tag{577}$$

$$k_1 = \frac{3}{2}\sqrt{3} k_{A_3} k_{A_1}^2 k_M k_D, \text{ and} \tag{578}$$

$$k_2 = \sqrt{3} k_M k_{A_1}^2 k_{A_2}. \tag{579}$$

Recall that the definitions of k_1 and k_2 arose in the body of the dissertation in the development of the symmetric demodulation algorithm. These constants depend on the choice of scaling constants at each stage of the demodulator.

We can write the product, then, as roughly

$$
\begin{aligned}
Z &= k_d \frac{X}{Y} = k_d \left[\frac{k_1 E^2 \dot{\xi} \pm \sigma_X}{k_2 E^2 \pm \sigma_Y} \right] \\
&\approx k_d \left[\left(k_1 E^2 \dot{\xi} \pm \sigma_X \right) \left(\frac{1}{k_2 E^2} \mp \frac{\sigma_Y}{\left(k_2 E^2 \right)^2} \right) \right] \\
&= k_d \frac{k_1 E^2 \dot{\xi}}{k_2 E^2} \left[1 \pm \frac{\sigma_X}{k_1 E^2 \dot{\xi}} \right] \left[1 \mp \frac{\sigma_Y}{k_2 E^2} \right] \\
&\approx k_d \frac{k_1}{k_2} \dot{\xi} \pm k_d \frac{\sigma_X}{k_2 E^2} \mp k_d \frac{k_1 \dot{\xi} \sigma_Y}{k_2^2 E^2}.
\end{aligned}
\tag{580}
$$

In the last line, we have dropped the products of variances as they can be assumed to be negligible. We therefore can approximate the standard deviation as

$$
\sigma_Z \approx \sqrt{\frac{k_d^2 \sigma_X^2}{\left(k_2 E^2 \right)^2} + k_d^2 \frac{\left(k_1 \dot{\xi} \right)^2}{\left(k_2 E \right)^4} \sigma_Y^2}. \tag{581}
$$

Now we can include the noise of the divider itself, and convert all the standard deviations into voltage noise spectral densities:

$$
e_Z^{\dagger} \approx \sqrt{\left(\frac{k_d e_X^{\dagger 2}}{k_2 E^2} \right)^2 + \left(\frac{k_d k_1 \dot{\xi} e_Y^{\dagger 2}}{k_2^2 E^2} \right)^2 + e_D^{\dagger 2}}. \tag{582}
$$

H. CALCULATING THE NOISE: RECEIVERS

To calculate the actual noise voltage spectral density output by the receivers, we apply Equation (509). Since we are using Burr-Brown OPA-111s in the receivers, the input noise voltage spectral density for the operational amplifier is

$$e_n^{\dagger} = \begin{cases} 40 \ \dfrac{\text{nV}}{\sqrt{\text{Hz}}} \text{for } f\text{=40 Hz;} \\ 15 \ \dfrac{\text{nV}}{\sqrt{\text{Hz}}} \text{for } f\text{=100 Hz;} \\ 8 \ \dfrac{\text{nV}}{\sqrt{\text{Hz}}} \text{for } f\text{=1 kHz; and} \\ 6 \ \dfrac{\text{nV}}{\sqrt{\text{Hz}}} \text{for } f\text{=10 kHz.} \end{cases} \tag{583}$$

The noise current spectral density for this operational amplifier is given as 500 aA/$\sqrt{\text{Hz}}$. Resistor R in the equation is resistor $R_1=R_2=R_3=64.9$ kΩ in the schematic drawing shown in Figure 33 on page 133 and capacitor C in the equation is capacitor $C_1=C_2=C_3=10$ pF in the schematic. We shall take the responsivity $\mathcal{R}=370$ mA/W, and the optical power $P=150$ μW. The optical power used here is an average value around which the instantaneous power fluctuates. We find that

$$e_{REC}^{\dagger} = \begin{cases} 52 \ \dfrac{\text{nV}}{\sqrt{\text{Hz}}} \text{for } f\text{=10 Hz;} \\ 36 \ \dfrac{\text{nV}}{\sqrt{\text{Hz}}} \text{for } f\text{=100 Hz;} \\ 34 \ \dfrac{\text{nV}}{\sqrt{\text{Hz}}} \text{for } f\text{=1 kHz; and} \\ 33 \ \dfrac{\text{nV}}{\sqrt{\text{Hz}}} \text{for } f\text{=10 kHz.} \end{cases} \tag{584}$$

The capacitors have no appreciable effect on the noise at these low frequencies. We ignored the fluctuations in power around the central value $D=P$. This proved reasonable, for the noise was totally dominated by the contributions from the input noise voltage spectral density of the operational amplifier and the thermal noise voltage spectral density from the feedback resistor. The shot noise and the noise from the input noise current spectral density of the operational amplifier were entirely negligible.

I. CALCULATING THE NOISE: SUMMING AMPLIFIER U4A

To calculate the actual noise voltage spectral density output by integrated circuit U4A in the Symmetric Analog Demodulator, we apply Equation (519). The feedback resistor R_f in the equation is resistor R_7=34.8 kΩ in the schematic. The input resistors whose magnitude is R in the equation are R_1=R_5=R_6=102 kΩ in the schematic. We switched to using Analog Devices AD712s for all the sub-circuits except the receivers. These devices have a specified noise voltage spectral density at their inputs of

$$e_n^{\dagger} = \begin{cases} 45 \ \dfrac{\text{nV}}{\sqrt{\text{Hz}}} \text{ for } f\text{=40 Hz;} \\ 22 \ \dfrac{\text{nV}}{\sqrt{\text{Hz}}} \text{ for } f\text{=100 Hz;} \\ 18 \ \dfrac{\text{nV}}{\sqrt{\text{Hz}}} \text{ for } f\text{=1 kHz; and} \\ 16 \ \dfrac{\text{nV}}{\sqrt{\text{Hz}}} \text{ for } f\text{=10 kHz.} \end{cases} \tag{585}$$

Their noise current spectral density is specified as 10 fA/$\sqrt{\text{Hz}}$ at 1 kHz; no data is given for other frequencies, so we shall apply this same specification at each of the four frequencies we use in our calculations. Using the results already found for the noise from the receivers in Equation (584), we find

$$e_{U4A}^{\dagger} = \begin{cases} 54 \ \dfrac{\text{nV}}{\sqrt{\text{Hz}}} \text{ for } f\text{=10 Hz;} \\ 22 \ \dfrac{\text{nV}}{\sqrt{\text{Hz}}} \text{ for } f\text{=100 Hz;} \\ 18 \ \dfrac{\text{nV}}{\sqrt{\text{Hz}}} \text{ for } f\text{=1 kHz; and} \\ 16 \ \dfrac{\text{nV}}{\sqrt{\text{Hz}}} \text{ for } f\text{=10 kHz.} \end{cases} \tag{586}$$

The noise from this circuit was entirely dominated by the input noise voltage spectral density of the AD712 operational amplifier; all other sources were negligible by comparison.

J. CALCULATING THE NOISE: SUBTRACTORS U5A, U6A, U7A

To calculate the actual noise voltage spectral density output by integrated circuits U5A, U6A, and U7A in the Symmetric Analog Demodulator, we apply Equation (518). (Recall that the purpose of these four sub-circuits is to remove the offset D from the interferometric outputs.) The feedback resistor R_f in the equation is equal to resistors $R_{10}=R_{13}=R_{16}=51.1$ kΩ in the schematic diagram. The input resistors R_k in the equation are all the same; in the schematic they are R_8, R_9, R_{11}, R_{12}, R_{14}, and R_{15}, with the value 13.7 kΩ. We still are using the AD712 here, with values for input noise voltage and current given above. The inputs come from one of the receivers and from the summing amplifier U4A. The results of the computations are

$$\left.\begin{matrix} e^{\dagger}_{U5A}, \\ e^{\dagger}_{U6A}, \\ e^{\dagger}_{U7A} \end{matrix}\right\} = \begin{cases} 480 \ \dfrac{\text{nV}}{\sqrt{\text{Hz}}} \text{ for } f=10 \text{ Hz}; \\ 260 \ \dfrac{\text{nV}}{\sqrt{\text{Hz}}} \text{ for } f=100 \text{ Hz}; \\ 230 \ \dfrac{\text{nV}}{\sqrt{\text{Hz}}} \text{ for } f=1 \text{ kHz; and} \\ 210 \ \dfrac{\text{nV}}{\sqrt{\text{Hz}}} \text{ for } f=10 \text{ kHz}. \end{cases} \tag{587}$$

As in the previous sub-circuits considered, most of the noise was contributed by the operational amplifier's voltage noise input. The next largest contributors were the noise from the previous stages and the thermal noise from the feedback resistors. The current noise had a negligible effect.

K. CALCULATING THE NOISE: DIFFERENTIATORS U5B, U6B, U7B

To calculate the actual noise voltage spectral density output by integrated circuits U5B, U6B, and U7B in the Symmetric Analog Demodulator, we apply Equation (527). The input resistor R_1 in the equation corresponds to resistors R_{17}, R_{19}, and R_{21} in the schematic, all with the value 464 Ω. The input capacitor C_1 in the equation corresponds to capacitors C_4, C_6, and C_8 in the schematic, all with the value 470 pF. The feedback resistor R_2 in the equation corresponds to resistors R_{18}, R_{20}, and R_{22} in the schematic

diagram, and they all have the value 1.91 kΩ. The feedback capacitor C_2 in the equation corresponds to capacitors C_5, C_7, and C_9 in the schematic diagram. The operational amplifier is an AD712 with the noise specifications given above. The results of the computations are

$$\left.\begin{matrix} e^{\dagger}_{U5B}, \\ e^{\dagger}_{U6B}, \\ e^{\dagger}_{U7B} \end{matrix}\right\} = \begin{cases} 45 \ \dfrac{\text{nV}}{\sqrt{\text{Hz}}} \text{for } f\text{=10 Hz;} \\ 23 \ \dfrac{\text{nV}}{\sqrt{\text{Hz}}} \text{for } f\text{=100 Hz;} \\ 19 \ \dfrac{\text{nV}}{\sqrt{\text{Hz}}} \text{for } f\text{=1 kHz; and} \\ 21 \ \dfrac{\text{nV}}{\sqrt{\text{Hz}}} \text{for } f\text{=10 kHz.} \end{cases} \tag{588}$$

All noise sources except the voltage noise spectral density of the operational amplifiers were completely negligible in these calculations, except for the thermal noise in the feedback resistors, which was still a factor of four smaller than the noise injected by the operational amplifier.

L. CALCULATING THE NOISE: CROSS-MULTIPLIERS U11, U12, U13

To calculate the actual noise voltage spectral density output by integrated circuits U11, U12, and U13 in the Symmetric Analog Demodulator, we apply Equation (569). Because of the operation of integrated circuits U5A, U6A, and U7A in removing the fixed offset D from the signals, the means of all the inputs in the equation are zero when the signal of interest generates significantly more than π rad of optical phase shift. (In the case of the differentiated signals, this is always true. It is not generally true for smaller undifferentiated signals, however.) The gain constant of the AD534 multipliers is K_M=0.1 V^{-1}. Their own contribution to the output noise is specified as between 1.1 $\mu V/\sqrt{Hz}$ at 10 Hz and 800 $nV/\sqrt{Hz}$ at 10 kHz.

For the bandwidth B in the equation, we used 1.3 MHz. This figure was arrived at by taking the gain (3.73) of the subtractor circuits U5A, U6A, and U7A whose gain-bandwidth product is 3 MHz. The ratio of these two gives a 3 dB bandwidth of 804 kHz.

When multiplied by $\pi/2$ to yield the equivalent noise bandwidth, the result was 1.3 Mhz. The results of the calculations are

$$\left.\begin{matrix} e_{U11}^{\dagger}, \\ e_{U12}^{\dagger}, \\ e_{U13}^{\dagger} \end{matrix}\right\} = \begin{cases} 1.1\ \mu\dfrac{\text{V}}{\sqrt{\text{Hz}}} \text{ for } f\text{=10 Hz;} \\ 900\ \dfrac{\text{nV}}{\sqrt{\text{Hz}}} \text{ for } f\text{=100 Hz;} \\ 800\ \dfrac{\text{nV}}{\sqrt{\text{Hz}}} \text{ for } f\text{=1 kHz; and} \\ 800\ \dfrac{\text{nV}}{\sqrt{\text{Hz}}} \text{ for } f\text{=10 kHz.} \end{cases} \tag{589}$$

The output noise is entirely dominated by the multiplier noise. One implication of this fact is that there was no need to use very-low-noise operational amplifiers in the receivers. Since these low-noise amplifiers are expensive, this is an area of potential savings if quieter multipliers cannot be found.

M. CALCULATING THE NOISE: SQUARING MULTIPLIERS U8, U9, U10

To calculate the actual noise voltage spectral density output by integrated circuits U8, U9, and U10 in the Symmetric Analog Demodulator, we apply Equation (574). The multipliers are the same AD534s just described. The results of the computations are

$$\left.\begin{matrix} e_{U8}^{\dagger}, \\ e_{U9}^{\dagger}, \\ e_{U10}^{\dagger} \end{matrix}\right\} = \begin{cases} 1.1\ \dfrac{\mu\text{V}}{\sqrt{\text{Hz}}} \text{ for } f\text{=10 Hz;} \\ 900\ \dfrac{\text{nV}}{\sqrt{\text{Hz}}} \text{ for } f\text{=100 Hz;} \\ 800\ \dfrac{\text{nV}}{\sqrt{\text{Hz}}} \text{ for } f\text{=1 kHz; and} \\ 800\ \dfrac{\text{nV}}{\sqrt{\text{Hz}}} \text{ for } f\text{=10 kHz.} \end{cases} \tag{590}$$

The noise from these circuits is exactly the same as the noise from the cross-multiplying circuits. The input noise contributions are totally negligible by comparison.

N. CALCULATING THE NOISE: SCALING ADDER U14A

To calculate the actual noise voltage spectral density output by integrated circuit U14A in the Symmetric Analog Demodulator, we apply Equation (518). The feedback resistor R_f in the equation now corresponds to resistor R_{50} in the schematic and is 4.99 kΩ. The input resistors $R_k = R$ in the equation correspond to resistors R_{11}, R_{15}, and R_{19} in the schematic diagram and they all are equal to 14.0 kΩ. We again are using an AD712 operational amplifier with noise specifications mentioned above.

The results of the calculations are

$$e^{\dagger}_{U14A} = \begin{cases} 690 \ \dfrac{\text{nV}}{\sqrt{\text{Hz}}} \text{ for } f = 10 \text{ Hz}; \\ 560 \ \dfrac{\text{nV}}{\sqrt{\text{Hz}}} \text{ for } f = 100 \text{ Hz}; \\ 500 \ \dfrac{\text{nV}}{\sqrt{\text{Hz}}} \text{ for } f = 1 \text{ kHz; and} \\ 500 \ \dfrac{\text{nV}}{\sqrt{\text{Hz}}} \text{ for } f = 10 \text{ kHz}. \end{cases} \tag{591}$$

The multiplier noise from the previous sub-circuit still is dominant, although its magnitude has been reduced somewhat. The reason for this is that the gain of the adder is less than one.

O. CALCULATING THE NOISE: SCALING ADDER U4B

To calculate the actual noise voltage spectral density output by integrated circuit U4B in the Symmetric Analog Demodulator, we apply Equation (519) again. The feedback resistor R_f of the equation corresponds to resistor $R_{37} = 14.0$ kΩ in the schematic diagram. The feedback capacitor C of the equation corresponds to capacitor $C_{10} = 1.0$ μF in the schematic diagram. The input resistors $R_k = R$ in the equation correspond to resistors R_{26}, R_{30}, and R_{35} in the schematic diagram, each of which provides 10.5 kΩ resistance. Again we are using the AD712. The results of the calculations are

$$e_{U4B}^{\dagger} = \begin{cases} 1.9\dfrac{\mu V}{\sqrt{Hz}} \text{ for } f=10 \text{ Hz;} \\ 240\ \dfrac{nV}{\sqrt{Hz}} \text{ for } f=100 \text{ Hz;} \\ 28\ \dfrac{nV}{\sqrt{Hz}} \text{ for } f=1 \text{ kHz; and} \\ 16\ \dfrac{nV}{\sqrt{Hz}} \text{ for } f=10 \text{ kHz.} \end{cases} \tag{592}$$

An interesting aspect of these numbers is the way the noise drops off with increasing frequency. The feedback capacitor was used in order to achieve this effect. The very large noise at low frequencies is due to the noise of the three multipliers which precede this sub-circuit. At the high frequencies, the noise of the operational amplifier U4B finally dominates the multiplier noise, which is attenuated at these frequencies by the capacitor.

P. CALCULATING THE NOISE: THE DIVIDER U15

To calculate the actual noise voltage spectral density output by integrated circuit U15B in the Symmetric Analog Demodulator, we apply Equation (582). The constants implicit in the equation are $k_{\cdot}=10$ V, $k_{A_1}=3.73$, $k_{A_3}=7.2$, $k_{A_2}=1.33$, $k_M=0.1$ V^{-1}, $E=1.3$ V, $k_D=901$ ns, $A=100$ rad, and $f=200$ Hz. Recall that A is the optical phase amplitude of a simple sinusoidal test signal and f is the frequency of the test signal. The derivative $\dot{\xi}$ will never exceed $A2\pi f$, which is the upper limit we use in the calculations. The divider has its own contribution to the output noise voltage spectral density. This is $e_d^{\dagger}=8.0\ \mu V/\sqrt{Hz}$, a number an order of magnitude large than that of the multipliers, which up to this point have been the noisiest components in the demodulator. The results of the calculations are

$$e_{U15}^{\dagger} = \begin{cases} 8.7 \ \dfrac{\mu V}{\sqrt{Hz}} \text{ for } f=10 \text{ Hz;} \\ 8.1 \ \dfrac{\mu V}{\sqrt{Hz}} \text{ for } f=100 \text{ Hz;} \\ 8.1 \ \dfrac{\mu V}{\sqrt{Hz}} \text{ for } f=1 \text{ kHz; and} \\ 8.1 \ \dfrac{\mu V}{\sqrt{Hz}} \text{ for } f=10 \text{ kHz.} \end{cases} \tag{593}$$

These results show very clearly that, to this point at least, the divider creates the largest contribution to noise of any sub-circuit in the Symmetric Analog Demodulator.

Q. CALCULATING THE NOISE: THE INTEGRATOR U14B

To calculate the actual noise voltage spectral density output by integrated circuit U14B in the Symmetric Analog Demodulator, we apply Equation (553), using the definitions of $H_1(s)$ and $H_2(s)$ of Equations (528) and (529). The input resistor R_1 and capacitor C_1 of the equations correspond to resistor $R_{51}=309$ kΩ and $C_{10}=1.0$ μF in the schematic diagram. The feedback capacitor C_2 in the equations corresponds to capacitor $C_{17}=470$ pF in the schematic. The three resistors R_2, R_3, and R_4 in the equations correspond to resistors $R_{52}=76.8$ kΩ, $R_{53}=76.8$ kΩ, and $R_{54}=10.2$ Ω respectively in the schematic. The noise spectral densities of the operational amplifier are those of the AD712 given earlier. The results of the calculations are

$$e_{U15}^{\dagger} = \begin{cases} 15.7 \ \dfrac{\mu V}{\sqrt{Hz}} \text{ for } f=10 \text{ Hz;} \\ 1.57 \ \dfrac{\mu V}{\sqrt{Hz}} \text{ for } f=100 \text{ Hz;} \\ 158 \ \dfrac{nV}{\sqrt{Hz}} \text{ for } f=1 \text{ kHz; and} \\ 15.8 \ \dfrac{nV}{\sqrt{Hz}} \text{ for } f=10 \text{ kHz.} \end{cases} \tag{594}$$

By dividing these voltage noise spectral densities by the scale factor 31 mV/rad, we can infer the equivalent phase noise which would have to appear at the input to the demodulator to produce this effect. Doing so yields

$$\text{Equivalent input phase noise spectral density} = \begin{cases} 510 \ \frac{\mu\text{rad}}{\sqrt{\text{Hz}}} \text{for } f\text{=10 Hz;} \\ 51 \ \frac{\mu\text{rad}}{\sqrt{\text{Hz}}} \text{for } f\text{=100 Hz;} \\ 5.1 \ \frac{\mu\text{rad}}{\sqrt{\text{Hz}}} \text{for } f\text{=1 kHz; and} \\ 510 \ \frac{\text{nrad}}{\sqrt{\text{Hz}}} \text{for } f\text{=10 kHz.} \end{cases} \quad (595)$$

The noise declines by 20 dB per decade increase in frequency, just as we would expect from the integration of white noise. However, a comparison with Table XXIII on page 198 reveals that the observed noise is an order of magnitude higher than the predicted noise. Although the reasons for this are unclear, it suggests that considerable improvement in the noise performance of the Symmetric Analog Demodulator should be possible without a major redesign. The possibility of contamination from nearby circuits, ground loops, or other causes should be investigated.

R. SUMMARY

In this appendix, we have performed a detailed noise analysis of the Symmetric Analogue Demodulator. This rather tedious exercise has revealed that the most significant sources of noise, in descending order of importance, are the analog divider and the six analog multipliers. If these could be replaced by quieter equivalents, then it might become possible to justify the use of expensive, low-noise operational amplifiers in the receivers of the circuit. However, as matters stand presently, these amplifiers deliver much quieter signals than necessary. In the absence of a reduction in the noise from the divider and multipliers, this is a needless expense.

The equations derived in this appendix also make it feasible to compute a new prediction of the noise if different components are substituted into the circuit. In fact, the equations make it possible to explore various strategies for lowering the noise floor--with a consequent increase in dynamic range--without implementing them in a circuit. Thus it should be possible to fine-tune the performance of the Symmetric Analogue Demodulator by applying these equations.

LIST OF REFERENCES

1. Hayt, W. H., *Engineering Electromagnetics*, McGraw-Hill Book Company, New York, 1981.

2. The Chemical Rubber Co., *Handbook of Chemistry and Physics*, 52nd Edition, edited by Weast, R. C., 1971.

3. Telephone conversation between Mr. Herb Mohler of Sharp Electronics and the author, 5 June 1991.

4. Grob, B., *Basic Electronics*, McGraw-Hill, Inc., New York, 1977.

5. Giallorenzi, T. G., Bucaro, J. A., Dandridge, A., Sigel, G. H., Jr., Cole, J. H., and Rashleigh, S. C., "Optical Fiber Sensor Technology", *IEEE Journal of Quantum Electronics*, Volume QE-18, pp. 626-666, April, 1982.

6. Busurin, V. I., Semenov, A. S., and Udalov, N. P., "Optical and Fiber-optic Sensors (Review)", *Soviet Journal of Quantum Electronics*, Volume 15, Number 5, pp. 595-621, May, 1985.

7. Dandridge, A., Tveten, A. B., and Giallorenzi, T. G., "Homodyne Demodulation Scheme for Fiber Optic Sensors Using Phase Generated Carrier", *IEEE Journal of Quantum Electronics*, Volume QE-18, Number 10, October, 1982.

8. Dandridge, A., and Tveten, A. B., "Phase Compensation in Interferometric Fiber-optic Sensors", *Optics Letters*, Volume 7, pp. 279-281, 1982.

9. Cole, J. H., *et al.*, "Synthetic-Heterodyne Interferometric Demodulation", *IEEE Journal of Quantum Electronics*, Volume QE-18, Number 4, April, 1982.

10. Crooker, C. M., *Two Demodulators for High Sensitivity Fiber Optic Interferometric Sensors*, Master's Thesis, Naval Postgraduate School, Monterey, California, December 1987.

11. Crooker, C. M., and Garrett, S. L., "Fringe Rate Demodulator for Fiber Optic Interferometric Sensors", *SPIE Vol. 838, Fiber Optics and Laser Sensors V (1987)*, pp. 329-331.

12. Sheem, S. K., "Fiber-optic Gyroscope with [3×3] Directional Coupler", *Applied Physics Letters*, Volume 37, Number 10, pp. 869-871, 15 November, 1980.

13. Sheem, S. K., "Optical Fiber Interferometers with [3×3] Directional Couplers: Analysis", *Journal of Applied Physics*, Volume 52, Number 6, pp. 3865-3872, June, 1981.

14. Telephone conversation between Dr. Sang K. Sheem, Lawrence Livermore National Laboratory and the author, 5 June 1991.

15. National Semiconductor Corporation, *Special Purpose Linear Devices*, Santa Clara, California, 1989.

16. Koo, K. P., Tveten, A. B., and Dandridge, A., "Passive Stabilization Scheme for Fiber Interferometers Using (3×3) Fiber Directional Couplers", Appl. Phys. Lett. **41**(7), 616-618, 1 October 1982.

17. Sedra, A. S., and Smith, K. C., *Microelectronic Circuits*, Holt, Rinehart and Winston, 1982.

18. Abramowitz, M. and Stegun, I.A., *Handbook of Mathematical Functions with Formulas, Graphs and Mathematical Tables*, National Bureau of Standards, AMS-55, U. S. Government Printing Office, 1974.

19. Strum, R. D., and Kirk, D. E., *First Principles of Discrete Systems and Digital Signal Processing*, Addison-Wesley Publishing Company, Inc., 1989.

20. Snyder, A. W., "Coupled-Mode Theory for Optical Fibers", *Journal of the Optical Society of America*, Volume 62, Number 11, November 1982, pp. 1267-1277.

21. Tveten, A. B., Kersey, A. D., McGarry, E. C., and Dandridge, A., "Electronic Interferometric Sensor Simulator/Demodulator" (unpublished paper), Optical Techniques Branch, Naval Research Laboratory, Wsashington, DC.

BIBLIOGRAPHY

1. Ambrózy, A., *Electronic Noise*, McGraw-Hill, 1982.

2. Analog Devices, Inc., *Data Conversion Products Databook*, Norwood, Massachusetts, 1989.

3. Analog Devices, Inc., *DSP Products Databook*, Norwood, Massachusetts, 1989.

4. Analog Devices, Inc., *Linear Products Databook 1990*, Norwood, Massachusetts, 1990.

5. Analog Devices, Inc., *Nonlinear Circuits Handbook*, Norwood, Massachusetts, 1976.

6. Bennett, W. R., *Electrical Noise*, McGraw-Hill, 1960.

7. Bennett, W. R., "Methods of Solving Noise Problems", *Proceedings of the IRE*, Volume 44, pp. 609-638.

8. Bucaro, J. A., Lagakos, N., Cole, J. H., and Giallorenzi, T. G., "Fiber Optic Acoustic Transduction", *Physical Acoustics*, Volume XVI, edited by Maso, W. P., and Thurston, R. N., Academic Press, Inc., 1982.

9. Buckingham, M. J., *Noise in Electronic Devices and Systems*, Ellis Horwood, 1983, Chapter 5.

10. Burr-Brown Corporation, *Burr-Brown Integrated Circuits Data Book*, Volume 33, Tucson, Arizona, 1989.

11. Burr-Brown Corporation, *The Handbook of Linear IC Applications*, Tucson, Arizona, 1987.

12. Carlson, A. B., *Communication Systems*, McGraw-Hill Book Company, 1986.

13. Carome, E. F., "Acousto-optic Transduction in Optical Fibers and in Fiber Optic Devices", *Frontiers in Physical Acoustics*, edited by D. Sette, Società Italiana di Fisica, Bologna, 1986, pp. 476-505.

14. Clarke, A. B., and Disney, R. L., *Probability and Random Processes for Engineers and Scientists*, John Wiley and Sons, Inc., 1970.

15. Couch, L. W., *Digital and Analog Communication Systems*, Second Edition, Macmillan Publishing Company, 1983.

16. Dandridge, A., Tveten, A. B., Miles, R. O., and Giallorenzi, T. G., "Laser Noise in Fiber-optic Interferometer Systems", *Applied Physics Letters*, Volume 7, Number 6, p. 526, 1980.

17. Dandridge, A., and Tveten, A. B., "Phase Noise of Single-mode Diode Lasers in Interferometer Systems", *Applied Physics Letters*, Volume 39, Number 7, p. 530, 1981.

18. Dandridge, A., Tveten, A. B., Miles, R. O., Jackson, D. A., and Giallorenzi, T. G., "Single-mode Diode Laser Phase Noise", *Applied Physics Letters*, Volume 38, pp. 77-78, 1981.

19. Frederiksen, T. M., *Intuitive Op Amps*, National Semiconductor Corporation, Santa Clara, California, 1984.

20. Gardner, F. M., *Phaselock Techniques*, John Wiley and Sons, 1966.

21. Ghausi, M. S., and Laker, K. R., *Modern Filter Design*, Prentice-Hall, Inc., 1981.

22. Gower, J. *Optical Communication Systems*, Prentice-Hall International, Inc., 1984.

23. Gray, P. R. and Meyer, R. G., *Analysis and Design of Analog Integrated Circuits*, Wiley, 1977.

24. Hecht, E., *Optics*, Second Edition, Addison-Wesley Publishing Company, 1987.

25. Hewlett-Packard Company, *HP5316A 100 MHz Universal Counter Manual*, Santa Clara, California, 1981, pp. 3-4 and 3-25.

26. Horowitz, P. and Hill, W., *The Art of Electronics*, 2nd Edition, Cambridge University Press, 1989.

27. Howard, R. M., Jeffery, R. D., and Hullett, J. L., "On the Noise of High-transimpedance Amplifiers for Long-wavelength Pulse OTDRs", *Optical and Quantum Electronics*, Volume 19, 1987, pp. 123-129.

28. Irvine, R., *Operational Amplifier Characteristics and Applications*, Prentice-Hall, Inc., 1981.

29. Motchenbacher, C. D., and Fitchen, F. C., *Low-Noise Electronic Design*, Wiley, 1973.

30. National Semiconductor Corporation, *CMOS Logic Databook*, Santa Clara, California, 1988.

31. National Semiconductor Corporation, *Data Acquisition Linear Devices Databook*, Santa Clara, California, 1989.

32. National Semiconductor Corporation, *General Purpose Linear Devices Databook*, Santa Clara, California, 1989.

33. National Semiconductor Corporation, *Linear Applications Handbook*, Santa Clara, California, 1986.

34. National Semiconductor Corporation, *LS/S/TTL Logic Databook*, Santa Clara, California, 1989.

35. Parzen, E., *Modern Probability Theory and Its Applications*, John Wiley and Sons, Inc., New York, 1960.

36. Parzen, E., *Stochastic Processes*, Holden-Day, Inc., San Francisco, 1962.

37. Research and Education Association, *Handbook of Mathematical, Scientific, and Engineering Formulas, Tables, Functions, Graphs, Transforms*, Piscataway, NJ, 1989.

38. Rice, S. O., "Mathematical Analysis of Random Noise", *Bell System Technology Journal*, Volume 23, pp. 282-332 and Volume 24, 1947, pp. 46-156.

39. Rice, S. O., "Statistical Properties of a Sine-Wave plus Random Noise", *Bell System Technology Journal*, Volume 27, 1947, pp 109-157.

40. Rich, A., "Shielding and Guarding", *Analog Dialogue*, Analog Devices, Inc., Cambridge, Massachusetts, Volume 17, Number 1, 1983.

41. Rich, A., "Understanding Interference-Type Noise", *Analog Dialogue*, Analog Devices, Inc., Cambridge, Massachusetts, Volume 16, Number 3, 1982.

42. Robinson, F. N., *Noise and Fluctuations in Electronic Devices and Circuits*, Clarendon Press, 1974.

43. Saff, E. B., and Snider, A. D., *Fundamentals of Complex Analysis for Mathematics, Science, and Engineering*, Prentice-Hall, Inc., 1976.

44. Sharp Corporation, *Laser Diode User's Manual*, Osaka, Japan, 1986.

45. Sheem, S. K., Giallorenzi, T. G., and Koo, K., "Optical Techniques to Solve the Signal Fading Problem in Fiber Interferometers", *Applied Optics*, Volume 21, Number 4, 689-693, 1982.

46. Smith, L., and Sheingold, D.H., "Noise and Operational Amplifier Circuits", *Analog Dialogue*, Analog Devices, Inc., Cambridge, Massachusetts, Volume 3, Number 1, March, 1969.

47. Tarnow, V., "The Lower Limit of Detectable Sound Pressures", *Journal of the Acoustical Society of America*, Volume 82, pp. 379-381, 1987.

48. Van der Ziel, A., *Noise: Sources, Characterization, Measurement*, Prentice-Hall, 1970.

INITIAL DISTRIBUTION LIST

1.	Defense Technical Information Center Cameron Station Alexandria, VA 22304-6145	2
2.	Library, Code 52 Naval Postgraduate School Monterey, CA 93943-5002	2
3.	Chairman, Department of Electrical and Computer Engineering, Code EC Naval Postgraduate School Monterey, CA 93943-5000	1
4.	LCDR Charles B. Cameron USS John F. Kennedy (CV-67) FPO New York, NY 09538-2800	2
5.	Prof. Steve Garrett, Code PH/Gx Naval Postgraduate School Monterey, CA 93943-5000	10
6.	Prof. John Powers, Code EC/Po Naval Postgraduate School Monterey, CA 93943-5000	1
7.	Prof. Sherif Michael, Code EC/Mi Naval Postgraduate School Monterey, CA 93943-5000	1
8.	Prof. Donald Gaver, Code OR/Gv Naval Postgraduate School Monterey, CA 93943-5000	1
9.	Prof. Tri T. Ha, Code EC/Ha Naval Postgraduate School Monterey, CA 93943-5000	1

10. Commanding Officer — 1
Office of Naval Research
ATTN: Dr. L. Hargrove
Physics Division (Code 1112)
800 N. Quincy Street
Arlington, VA 22217-5000

11. Commanding Officer — 1
Space and Naval Warfare Systems Command
PD80
ATTN: RADM R. Witter, Code PD-80
Washington, DC 20363-5100

12. Commanding Officer — 2
Office of Naval Technology
ATTN: Dr. P. Selwyn (Code 20)
Library
800 N. Quincy Street
Arlington, VA 22217-5000

13. Commanding Officer — 3
Naval Sea Systems Command
ATTN: CAPT M. Kosonowska, Code 06KR
Mr. C. Jacobson, Code 06KR22
Mr. G. Kamilakis, Code 06UR4
Washington, DC 20362-5102

14. Commanding Officer — 3
Naval Research Laboratory
ATTN: Dr. A. Dandridge (Code 6574)
Dr. A. Tveten (Code 6535)
Dr. J. Bucaro (Code 5130)
4555 Overlook Avenue
Washington, DC 20375-5000

15. Commanding Officer — 1
Naval Underwater Systems Center
ATTN: Mr. R. Maple (Code 2133)
New London, CT 06320-5594

16. Commanding Officer — 1
Naval Research Laboratory
ATTN: Dr. R. Timme (Code 5870)
Orlando, FL 32856-8337

17. National Center for Physical Acoustics — 1
ATTN: Dr. H. Bass
P. O. Box 847
University of Mississippi
Oxford, MI 38677

18. Sperry Marine Inc. — 1
ATTN: Dr. D. L. Gerdt
1070 Seminole Trail
Charlottesville, VA 22906

19. Optical Technologies, Inc. — 1
ATTN: Mr. C. Davis
360 Herndon Parkway
Suite 1200
Herndon, VA 22070

20. Raytheon Company — 1
Submarine Signal Division
ATTN: Mr. D. Korff
1847 W. Main Road
Portsmouth, RI 02871-1087

21. Litton, Guidance and Control Systems — 3
ATTN: Dr. E. Moore
Mr. J. Bunn
Mr. D. Meyer
5500 Canoga Avenue
Woodland Hills, CA 91367-6698

22. McDonnell Douglas Electronic Systems Company — 1
ATTN: Dr. S. Wantanabe
0201 Greensbore Drive
Suite 400
McLean, VA 22102

23. Alliant Tech Systems — 1
ATTN: Mr. M. Young
6500 Harbour Heights Parkway
Everett, WA 98204-8899

24.	Honeywell, Inc. ATTN: Mr. J. Lenz Mr. A. L. Darbut P. O. Box 1361 (MN65-2600) Minneapolis, MN 55418	2
25.	International Transducer Corporation ATTN: Mr. W. Bunker 469 Ward Drive Santa Barbara, CA 93111	1
26.	Donovan Associates ATTN: Mr. J. Donovan 1515 Jefferson Davis Highway Suite 1221 Arlington, VA 22202	1
27.	General Dynamics Electric Boat Division ATTN: Mr. E. Rothenberg 75 Eastern Point Road Groton, CT 06340-4980	1
28.	Hazeltine Corporation ATTN: Mr. J. Franzini Greenlawn, NY 11740	1
29.	Systron Donner ATTN: Mr. M. Layton Inertial Division 2700 Systron Drive Concord, CA 94518-1399	1
30.	Magnavox ATTN: Mr. D. V. Conte 1313 Production Road Fort Wayne, IN 46808	1
31.	LT Daphne Kapolka, Code 30 Naval Postgraduate School Monterey, CA 93943-5000	1

32. Mr. Jeff Bush 1
Optiphase, Unit A-2
16555 Sherman Way
Van Nuys, CA 91406

33. Dr. David Brown, Code PH 1
Naval Postgraduate School
Monterey, CA 93943-5000

34. LCDR David Gardner, Code PH 1
Naval Postgraduate School
Monterey, CA 93943-5000

35. Mr. David Bartlett, Code 30 1
Naval Postgraduate School
Monterey, CA 93943-5000

36. LT Martha Van der Kamp, Code 34 1
Naval Postgraduate School
Monterey, CA 93943-5000

37. Commanding Officer 1
Naval Weapons Center
ATTN: Mr. Stephen Church, Code 006
China Lake, CA 93555-6001

38. Commanding Officer, NOPF 1
ATTN: LCDR C. M. Crooker
Dam Neck, VA